MAGNETIC NANOPARTICLES FOR BIOMEDICAL APPLICATIONS

DIPAK MAITY

Dissertation submitted to the Faculty of Engineering, National University of Singapore in partial fulfillment of the requirements for the degree of

DOCTOR of PHILOSOPHY

in

MATERIALS SCIENCE AND ENGINEERING

NUS
National University
of Singapore

July 2011

Keywords: Nanoparticles, Iron oxide, Magnetite, Superparamagnetic, Ferrofluids, Thermal decomposition, MRI, Hyperthermia

This dissertation is dedicated in memory of my Parents

VITA

May 1999	B.Sc. in Chemistry, Calcutta University, India
June 2002	B.Tech. in Chemical Technology, Calcutta University, India
June 2004	M.Tech. Materials Science, Indian Institute of Technology (IIT) Kanpur, India.

PUBLICATIONS

1. **D. Maity**, P. Pradhan, P. Chandrasekharan, S.N. Kale, B. Shutter, S-S. Feng, D. Bahadur, J-M. Xue, J. *Ding, "Synthesis of hydrophilic superparamagnetic magnetite nanoparticles via thermal decomposition of Fe(acac)$_3$ in 80 Vol% TREG+20 Vol% TREM"* **J. Nanosci. Nanotechnol.** 11 (2011) 2730.
2. P. Chandrasekharan, **D. Maity**, C-T. Yang, K-H. Chuang, J. Ding, S-S. Feng, "*Vitamin E (D-alpha-tocopheryl-co-poly(ethylene glycol) 1000 succinate) micelles-superparamagnetic iron oxide nanoparticles for enhanced thermotherapy and MRI*" **Biomaterials** 32 (2011) 5663.
3. Y. F. Tan, P. Chandrasekharan, **D. Maity**, Y. Cai Xian, K-H Chuang, Y. Zhao, S. Wang, J. Ding, S-S Feng "*Multimodal tumor imaging by iron oxides and quantum dots formulated in poly(lactic acid)-D-alpha-tocopheryl polyethylene glycol 1000 succinate nanoparticles*" **Biomaterials** 32 (2011) 2969.
4. **D. Maity**, P. Chandrasekharan, C-T Yang, K-H Chuang, B. Shuter, J-M Xue, J. Ding, S-S. Feng, "*Facile synthesis of water-stable magnetite nanoparticles for clinical MRI and magnetic hyperthermia applications*" **Nanomedicine** 5 (2010) 1571.
5. P. Chandrasekharan, **D. Maity**, C-T. Yang, K-H. Chuang, J. Ding, S-S. Feng, "*Superparamagnetic iron oxide - loaded poly (lactic acid)–D-α-tocopherol polyethylene glycol 1000 succinate copolymer nanoparticles as MRI contrast agent*" **Biomaterials** 31 (2010) 5588.
6. P. Chandrasekharan, **D. Maity**, C-T. Yang, K-H. Chuang, J. Ding, S-S. Feng, "*Formulation of iron oxides by nanoparticles of poly-lactide-co-D-α-tocopherol-polyethylene glycol 1000 succinate biodegradable polymer for magnetic resonance imaging*" **J. Appl. Phys.** 107 (2010) 09B309.
7. **D. Maity**, P. Chandrasekharan, S-S. Feng, J-M. Xue, J. Ding, "*Polyol-based synthesis of hydrophilic magnetite nanoparticles*" **J. Appl. Phys.** 107 (2010) 09B3010.
8. **D. Maity**, S.N. Kale, R. Kaul-Ghanekar, J-M Xue, J. Ding, "*Studies of magnetite nanoparticles synthesized by thermal decomposition of iron (III) acetylacetonate in tri(ethylene glycol)*" **J. Magn. Magn. Mater.** 321 (2009) 3093.
9. **D. Maity**, S-G. Choo, J. Yi, J. Ding, J-M. Xue, "*Synthesis of magnetite nanoparticles via a solvent-free thermal decomposition route*" **J. Magn. Magn. Mater.** 321 (2009) 1256.
10. **D. Maity**, J. Ding, J-M. Xue, "*One pot synthesis of hydrophilic and hydrophobic ferrofluid*" **Int. J. Nanosci.** 8 (2009) 65.
11. **D. Maity**, J. Ding, J-M. Xue, "*Synthesis of magnetite nanoparticles by thermal decomposition: time, temperature, surfactant and solvent effects*" **Func. Mater. Lett.** 1 (2008) 189.

CONFERENCE PRESENTATIONS

1. D. Maity, P. Chandrasekharan, K-H Chuang, S-S. Feng, J-M Xue, J. Ding, *Synthesis of hydrophilic Fe_3O_4 nanoparticles and their bio-medical applications*, **MRS-S Trilateral 2010, IMRE, Singapore (Best Poster Award)**

3. D. Maity, P. Chandrasekharan, K-H Chuang, S-S. Feng, J-M Xue, J. Ding, *Facile synthesis of superparamagnetic magnetite nanoparticles for Biomedical Applications*, **ICONSAT 2010, IITB, India (Best Poster Award)**

2. D. Maity, P. Chandrasekharan, S-S. Feng, J-M Xue, J. Ding, *Functionalized Magnetite Nanoparticles for Cancer Hyperthermia Application*, **ICONN 2010, Sydney, Australia.**

4. D. Maity, P. Chandrasekharan, S-S. Feng, J-M Xue, J. Ding, *Polyol-based Synthesis of Hydrophilic Magnetite Nanoparticles for Hyperthermia Application*, **MMM-Intermag 2010, Washington DC, USA.**

5. D. Maity, P. Chandrasekharan, K-H Chuang, S-S. Feng, J-M Xue, J. Ding, *Magnetite Nanoparticles for Biomedical Applications,* **1st Nano Today 2009, Biopolis, Singapore.**

6. D. Maity, P. Chandrasekharan, K-H Chuang, S-S. Feng, J-M Xue, J. Ding, *Superparamagnetic Iron Oxide Nanoparticles for Biomedical Applications,* **ICMAT 2009, Suntec City, Singapore.**

7. D. Maity, J-M Xue, J. Ding, *One Pot Synthesis of Hydrophobic and Hydrophilic Ferrofluid,* **AsiaNANO 2008, Biopolis Singapore.**

8. **D. Maity**, J-M Xue, J. Ding, *Functionalized Magnetic Nanoparticles for Biomedical Applications,* **3rd MRS-S 2008, IMRE, Singapore.**

Acknowledgements

I would like to express my heartfelt gratitude to Prof. Jun Ding for his patience, excellent guidance and constant encouragement throughout my PhD study and research work in NUS.

I would also like to express my sincere gratitude to Dr. Jun-Min Xue for his guidance and support throughout my PhD research work.

I would like to express my earnest appreciation to Prof. Si-Shen Feng and Prof. S.N. Kale for their great help and kind suggestions for my research work. Also, I deeply appreciate to Dr. Borys, Dr. Chang-Tong Yang and Dr. Kai-Hsiang Chuang for their help in MRI measurements.

I would like to especially thank to my friend, Mr. Prashant Chandrasekharan for his continuous help, support, and engaging discussions throughout my PhD research work.

I am very grateful to Dr. Jiabao, Dr. Kai, Dr. Lina, Eugene, Yuwei and other lab mates, batch mates and all stuffs of our department and NUS for their kind assistance in various aspects.

Finally, I would like to thank to my family members, for their continuous support, encouragement and sacrifice during my PhD study in NUS.

Abstract

Superparamagnetic nanoparticles have been under intensive investigation in various biomedical applications. However, it is still a challenge to synthesize high quality water stable ultrafine magnetite nanoparticles for better magnetic performance and less side effects in clinical MRI and thermotherapy (magnetic hyperthermia). In this work, monodispresed and control sized hydrophobic superparamagnetic magnetite (Fe_3O_4) nanoparticles have been synthesized by thermal decomposition method optimizing the reaction parameters like temperature, time, solvent and surfactant effects. These hydrophobic Fe_3O_4 nanoparticles are converted into hydrophilic (i.e. water soluble) by functionalization and polymeric encapsulation to make them useful for biomedical applications. Direct synthesis of hydrophilic Fe_3O_4 nanoparticles and nanoclusters with high saturation magnetization (Ms ~ 73 - 86 emu/g) have also been performed using one-step polyol method. The Fe_3O_4 nanoparticles and nanoclusters are systematically characterized to identify their structure, surface coating, magnetic properties, cytotoxicity, cellular uptake, magnetic resonance imaging (MRI) contrast and specific absorption rate (SAR) properties. *In vitro* experiments have demonstrated high cellular uptake and low cytotoxicity and the AC magnetic field heating experiments showed effectiveness in temperature rise and 60-74% cancer cell death due to magnetic hyperthermia. The Fe_3O_4 nanoclusters yielded high specific absorption rate (SAR~500 Watt/g) values as compared to the Fe_3O_4 nanoparticles (SAR~135 Watt/g) upon exposure to AC magnetic field. The Fe_3O_4 nanoparticles have showed high r_2* relaxivity (617.5 $s^{-1}mM^{-1}$) and very promising contrast i*n vivo* tumor imaging. Thus, the Fe_3O_4 nanoparticles are proficient for MRI imaging and magnetic hyperthermia applications.

Abbreviations

AC	Alternating current
AMF	Alternative magnetic field
APTES	3-aminopropyltriethoxysilane
BET	Benzyl ether
CT	Critical temperature
DC	Direct current
DCC	Dicyclohexylcarbodiimide
DCM	Dichloromethane
DEA	Diethanol amine
DEG	Di(ethylene glycol)
DLS	Dynamic Light Scattering
DMAAm	*N,N'*-dimethylacrylamide
DMEM	Dulbecco's Modified Eagle Medium
DMF	Dimethylformamide
DPA	Dopamine
D_s	Critical single-domain size
EA	Ethanol amine
FBS	Fetal bovine serum
FC	Field cooling
$Fe(acac)_3$	Iron(III) acetylacetonate
FTIR	Fourier transform infrared spectroscopy
H_c	Coercivity

HDA	Hexadecylamine
HRTEM	High resolution transmission electron microscopy
HT	Hyperthermia
ICP-MS	Inductively coupled plasma mass spectrometry
IEP	Isoelectric Point
IO	Iron oxide
JCPDS	Joint Committee on Powder Diffraction Standards
LA	Lauric acid
LCST	Lower critical solution temperature
LH	Local hyperthermia
LNP	Luminescence Nanoparticle
LSS	Liquid–solid–solution
OA	Oleic acid
ODE	1-Octadecene
OM	Oleylamine
MCF-7	Michigan Cancer Foundation-7
MCL	Magnetic cationic liposome
MDT	Magnetic drug targeting
MFN	Multifunctional nanoparticle
MNP	Magnetic Nanoparticle
MPS	Mononuclear phagocytic system
M_r	Magnetic remenance
MRI	Magnetic resonance imaging

M_S	Saturation magnetization
MTT	3-(4,5-Dimethylthiazol-2-yl)-2,5-diphenyltetrazolium bromide
NHS	*N*-hydroxysuccinimide
PAA	Poly(acrylic acid)
PBS	Phosphate buffered saline
PCL	Poly (ε-caprolactone)
PDA	Poly(ethylene glycol) dopamine acid
PDI	Polydispersity index
PDT	Photodynamic therapy
PEG	Poly(ethylene glycol)
PEGDA	Poly(ethylene glycol) diacid
PET	Phenyl ether
PLA	Poly(lactide)
PNIPAAm	Poly (N-isopropylacrylamide)
PNP	Polymer Nanoparticle
PTFE	Polytetrafluoroethylene
RES	Reticulo-endothelial system
RH	Regional hyperthermia
SAED	Selected area electron diffraction
SAR	Specific absorption rate
SCID	Severe combined immune deficiency
SDS	Sodium dodecyl sulphate
SNR	Signal to noise ratio

SPION	Superparamagnetic iron oxide nanoparticle
SPM	Superparamagnetic
SQUID	Superconducting quantum interference device
SSM	Solvent and/or surfactant mixture
T	Tesla
TEA	Triethanol amine
TEG	Tri(ethylene glycol)
TEM	Transmission electron microscopy
TGA	Thermogravimetric analysis
THF	Tetrahydrofuran
TOPO	Tri-octyl phospine oxide
TPGS	D-α-tocopherol polyethylene glycol 1000 succinate
TTEG	Tetra(ethylene glycol)
VSM	Vibrating sample magnetometer
WBH	Whole body hyperthermia
XPS	X-ray photoelectron spectra
XRD	X-ray diffraction
ZFC	Zero field cooling

Table of Contents

List of Tables

List of Figures

CHAPTER 1

Background

1.1. Brief Introduction on Magnetism

Magnetism originates from electron spins and electron movement. Electrons in an atom govern magnetic properties in two different ways: 1) electron acting as a spinning charged sphere. The spin is a quantum mechanical property and can be oriented in one of two directions, in the Up. (↑) direction or the Down. (↓) direction; 2) the effect of the electron circulating around the nucleus of the atom, which resembles a current loop. The flow of charge in a circular current loop produces magnetic lines of force known as a dipole [1]. There are various forms of magnetism that arise depending on how the dipoles interact with each other. Figure 1.1 shows a schematic representation of the different types of arrangements of magnetic dipoles in ferro-, antiferro- and ferrimagnetic materials below a "critical temperature". Above this temperature, the magnetic moments randomize due to thermal energy and hence the material displays paramagnetic behavior. This temperature is known as **Néel temperature** (T_N) for antiferromagnetic materials and **Curie temperature** (T_C) for ferromagnetic and ferrimagnetic materials. It is to note that ferromagnetic and ferrimagnetic substances are important for commercial applications.

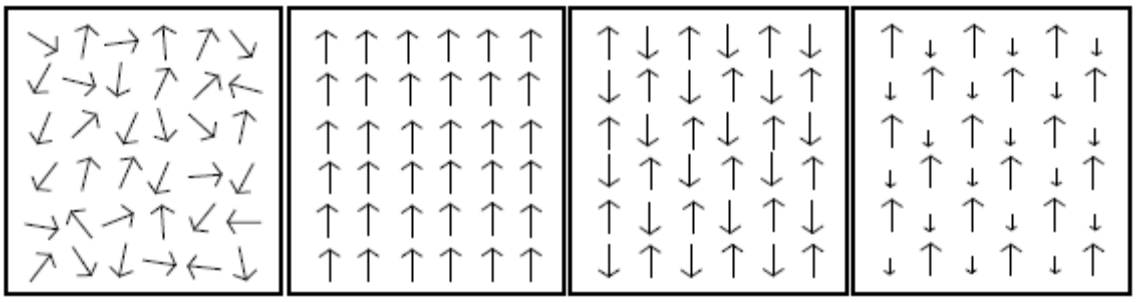

(a) (b) (c) (d)

Figure 1.1. Different orientations of magnetic dipoles: (a) paramagnetic, (b) ferromagnetic, (c) antiferromagnetic, and (d) ferrimagnetic [2].

To minimize the energy, a ferromagnet or ferrimagnet is split up into *domains* in which all dipoles are ordered along a preferential direction (Figure 1.2). This direction changes from domain to domain, and hence the bulk magnetic materials may as a whole be unmagnetized, even though they are magnetized on the length scale of the domains. When placed in the presence of a sufficiently large external magnetic field, the spins in each domain rotate parallel to the direction of the applied magnetic field until all the dipoles are aligned to give the saturation magnetization (Ms). When the applied field is decreased, the magnetization decreases. In multi-domain bulk materials, demagnetization occurs primarily via spin rotation through the domain walls. If the demagnetization curve, during the removal of the applied field, does not follow the initial magnetization curve, the material displays hysteresis, which is the lag observed in Figure 1.3. Remanence magnetization (M_r) is the magnetization remaining at zero applied field (H = 0). The magnetic field applied in the negative direction required to return the magnetization to zero is the coercive force (H_c).

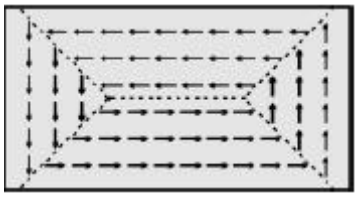

Figure 1.2. Dipole alignments in bulk ferromagnetic materials [2].

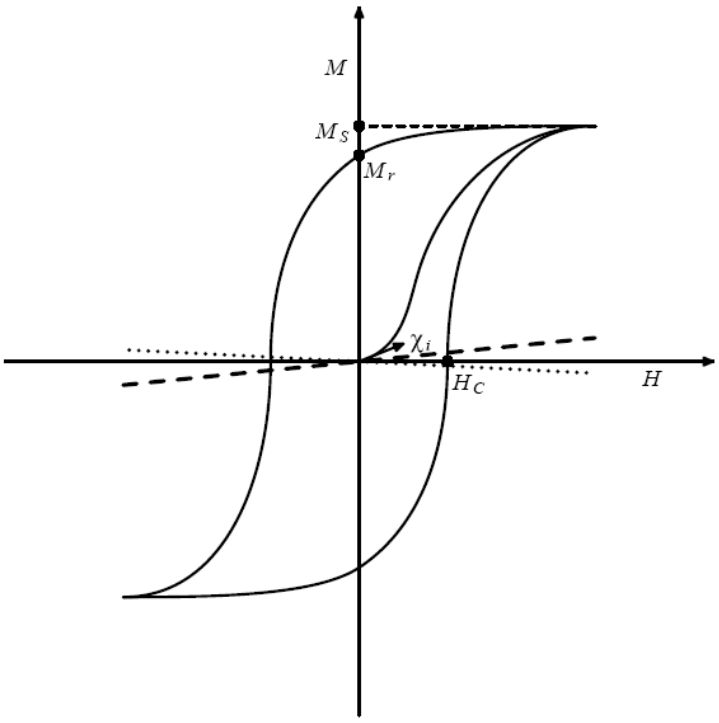

Figure 1.3. Magnetization (M) vs. applied field (H) for ferromagnetic (solid line), paramagnetic (broken line), and diamagnetic materials (dotted line). H_c represents the coercive field of the material, M_S the saturation magnetization, M_r the remanent magnetization, and χ_i the initial susceptibility [2].

1.2. Magnetism of Nanosized Particles

Nanosized particles have physical and chemical properties that are characteristic of neither the atom nor the bulk counterparts. Quantum size effects and the large surface area of magnetic nanoparticles dramatically change some of the magnetic properties and exhibit superparamagnetic phenomena, surface magnetism and quantum tunnelling of magnetization, because each particle can be considered as a single magnetic domain [3].

1.2.1. Single Domain Particles

In large magnetic particles, it is well known that there is a multidomain structure, where regions of uniform magnetization are separated by domain walls. The width of a domain wall (δ′) is a function of the magnetocrystalline anisotropy (K), the exchange energy (E_{ex}) and lattice spacing (a) of the crystal structure (Equation 1.1).

$$\delta' = \left(\frac{\pi^2 E_{ex}}{2aK} \right)^{\frac{1}{2}} \quad \text{---------- (1.1)}$$

The formation of the domain walls is a process driven by the balance between the magnetostatic energy (ΔE_{MS}), which increases proportionally to the volume of the materials and the domain-wall energy (E_{dw}), which increases proportionally to the interfacial area between domains. If the sample size is reduced, there is a critical volume below which it costs more energy to create a domain wall than to support the external magnetostatic energy of the single-domain state. The critical size of a spherical particle, D_s, below which it exists in a single-domain state is reached when $\Delta E_{MS} = E_{dw}$, which implies $D_s \approx 18 \frac{\sqrt{E_{ex} K}}{\mu_0 M^2}$, where μ_0 is the vacuum permeability, and M is the saturation magnetization [4]. Thus, the particles having size below the critical size (D_s, single domain size) is considered as single domain particles. This D_s typically lies in the range of a few tens of nanometers and depends on the material. It is influenced by the contribution from various anisotropy energy terms. Typical values of D_s for some important magnetic materials are listed in Table 1.1 [4-6].

Table 1.1. Estimated maximum single-domain size (D_s) for spherical particles [4-6].

Material	D_s (nm)
Fe	14
hcp Co	15
fcc Co	7
Ni	55
Fe_3O_4	128
$\gamma - Fe_2O_3$	166

Table 1.2. The influence of the shape of Fe particles on the coercivity [8].

Aspect ratio (c/a)	H_c (Oe)
1:1	820
1:5	3300
2:1	5200
5:1	9000
10:1	10100

The demagnetization is dependent on coherent rotation of the spins, which results in large coercivity in small nanoparticles [7]. The large coercive force in single domain particles is not only due to the magnetocrystalline anisotropy but also the shape anisotropies for nonspherical particles. The shape anisotropy increases as the aspect ratio of a particle

increases (Table 1.2). Therefore, elongated single-domain particles display large coercive forces. The coercive force is also dependent on particle size as shown in Figure 1.4. As the size of these single domain particles decreases, the coercive force decreases.

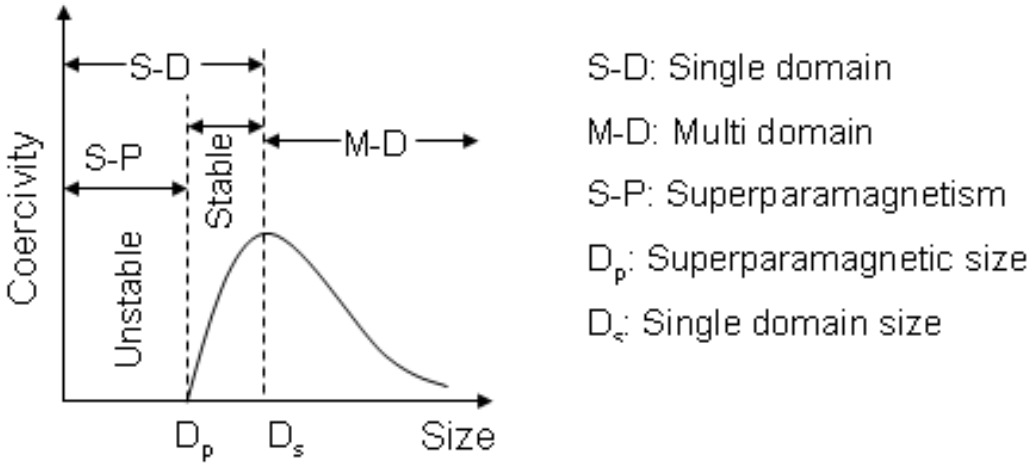

Figure 1.4. Coercivity as a function of particle size (D_p is the superparamagnetic size and D_s is the single domain particle size) [8].

1.2.2. Superparamagnetism

The superparamagnetism can be understood by considering the behavior of a well-isolated single-domain particle. The magnetic anisotropy energy per particle which is responsible for holding the magnetic moments along a certain direction can be expressed as follows: $E(\theta) = KV\sin^2\theta$, where V is the particle volume, K is the anisotropy constant and θ is the angle between the magnetization and the easy axis [4]. The energy barrier KV separates the two energetically equivalent easy directions of magnetization. With decreasing particle size, the thermal energy, k_BT, exceeds the energy barrier KV

(Equation 1.2) and the magnetization is easily flipped i.e. there is no more preferential orientation of the moment in the particle.

$$KV < 25k_BT \text{ ---------- (1.2)}$$

The magnetic moment of the particle may fluctuate behaving as a paramagnet. Thus, a single domain particle appears to be superparamagnetic when temperature is over the critical temperatures as given in equation 1.2 (Figure 1.5) [9]. Such a system has no hysteresis and the data of different temperatures superimpose onto a universal curve of M versus H/T [1].

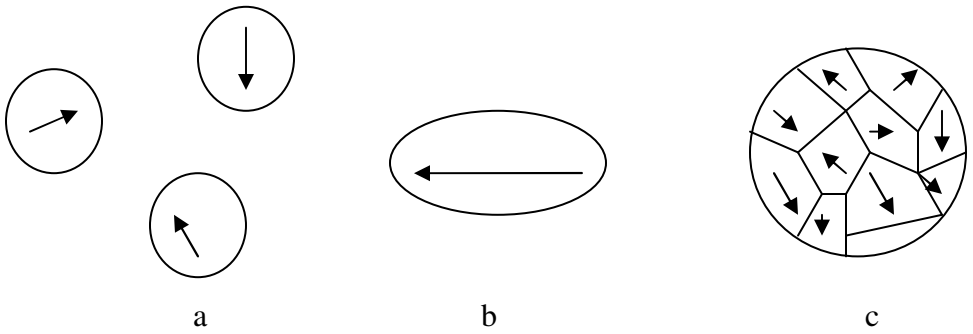

Figure 1.5. Domain structures observed in magnetic particles: (a) superparamagnetic; (b) single domain particle; (c) multi-domain particle [9].

1.2.3. Magnetic Relaxation

Considering particles in a carrier liquid under the influence of an external magnetic field, it can be shown that when the applied magnetic field is removed the magnetization of the particles is reversed. There are two main mechanisms for the magnetization reversal: *spin rotation or particle rotation*, which describe whether the change in direction of the magnetic moment of the particle is due to the reversal of the magnetic spin of the particle or the actual physical rotation of the particle. The time required for the reversal of the

magnetic moment of the particle (spin rotation) is related to the magnetic anisotropy of the material, Néel relaxation time, τ_N. The mathematical expression of Néel relaxation time is shown by Equation 1.3 [4].

$$\tau_N = \tau_0 \exp\left(\frac{KV}{k_B T}\right);\ \tau_0 \approx 10^{-9}\text{s} \text{ ---------- (1.3)}$$

The characteristic time for the randomization of the magnetization due mainly to the thermal motion of the particle is known as Brown relaxation time, τ_B, expressed by Equation 1.4.

$$\tau_B = \frac{3V_H \eta}{k_B T} \text{ ---------- (1.4)}$$

For a superparamagnetic material $\tau_N << \tau_B$, which means that the magnetization reversal occurs by rotation of the magnetic axis. Alternatively, when the magnetic moment of the particle is locked to a given crystallographic direction (easy axis), the particle is thermally blocked and $\tau_B << \tau_N$.

If the particle magnetic moment reverses at times shorter than the experimental time scales, the system is in a superparamagnetic state, if not, it is in the so-called blocked state. The critical temperature, which separates these two regimes, is called blocking temperature, T_B. Thus, beside the dependence of the magnetization on the particle size and composition, the magnetic properties depend greatly on the temperature. Above T_B ferro- or ferrimagnetic particle will behave as superparamagnetic. It is possible to calculate T_B using Equation 1.5. The blocking temperature depends on the anisotropy constant, the size of the particles, the applied magnetic field, and the experimental measuring time.

$$T_B = \frac{KV}{25k_B} \text{ ---------- (1.5)}$$

Thus under certain circumstances of particle size and temperature, ferro- or ferrimagnetic particles may be considered superparamagnetic. The criterion of superparamagnetism is regularly assumed considering particles with a relaxation time lower than 100 s. In the case of Fe_3O_4 with an anisotropy constant, K = 4.4 $\times 10^4$ Jm^{-3}, the critical superparamagnetic particle size at room temperature, T = 290 K, is between 9 and 17 nm [10].

A simple and rapid way to estimate the blocking temperature (T_B) is provided by DC magnetometry (SQUID) measurements, in which a zero-field-cooling (ZFC) and field-cooling (FC) procedure is employed. Briefly, the sample is cooled from room temperature in zero magnetic field (ZFC) and in a magnetic field (FC). Then a small magnetic field is applied (about 100 Oe) and the magnetization is recorded on warming. As temperature increases, the thermal energy disturbs the system and more moments acquire the energy to be aligned with the external field direction. The number of unblocked, aligned moments (i.e. the ZFC magnetization curves) reaches a maximum at the blocking temperature (T_B). Above the T_B the thermal energy is strong enough to randomize the magnetic moments leading to a decrease in magnetization. In the case of FC procedure, magnetization monotonically increases as the temperature decreases. For a single magnetic domain, the FC and ZFC curves diverge below T_B due to the existence of magnetic anisotropy barriers. Above T_B the sample is superparamagnetic and below is ferro- or ferrimagnetic. At T_B the thermal energy becomes comparable to the energy barrier gained in external magnetic field.

1.2.4. Dependence of Magnetization on Particle Size

The magnetization of bulk magnetic materials is inherently larger than for nanoparticles of the respective materials. Experimental values for the saturation magnetization of magnetite (Fe_3O_4) nanoparticles have been reported in the range of 30-60 emu/g which is lower than theoretical saturation magnetization (92 emu/g) of bulk magnetite [11-13]. Several researchers using a variety of techniques have investigated the causes for the observed reduction in magnetization in fine magnetic particles. In 1968 Berkowitz et al observed that the saturation magnetization, M_S (293K) depends upon the average crystallite size (Figure 1.6) [14]. The values of M_S (293K) for the samples (γ-Fe_2O_3 particles) with the largest crystallite sizes were very close to the theoretical saturation magnetization (74 emu/g) of bulk maghemite (γ-Fe_2O_3) while a sharp decrease of M_S occurred for the samples with the smallest crystallite sizes. They gave several reasons for the decreasing of M_S:

(1) the presence of either α-Fe_2O_3 or γ-$Fe_2O_3.H_2O$

(2) the magnetostatic interactions among all the crystallites in a particle, as well as the interactions between the particles

(3) the magnetocrystalline anisotropy of γ-Fe_2O_3 and

(4) the consequence of crystallite sizes that depart from the critical size of 400Å.

Many other researchers also observed the decrease in saturation magnetization (M_S) of Fe_3O_4 and γ -Fe_2O_3 nanoparticles from the corresponding M_S value of bulk material. The reported possible reasons for the decreasing of M_S of particles are [12, 15-16]:

(a) existence of noncollinear spin and magnetically dead layer (about ~1 nm thick) which formed by asymmetric environment effect of the surface atoms.

(b) high effective anisotropy fields in the surface, nonmagnetic grain boundaries and hydrogen in the lattice.

(c) particle surface defects and order-disorder structural characteristics because of their amorphous nature

(d) smaller crystalline magnetic anisotropy energy constant, K.

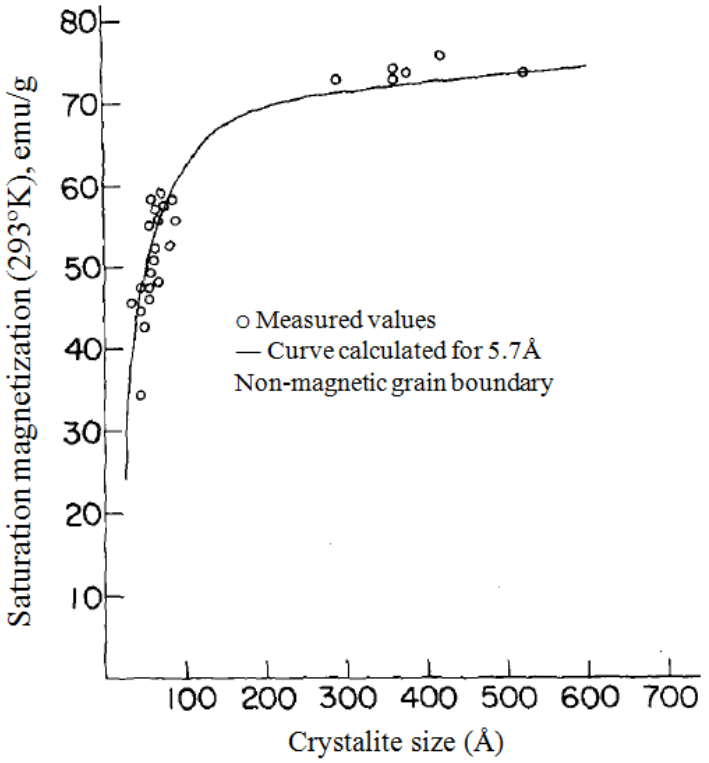

Figure 1.6. Saturation magnetization as a function of the crystallite size of acicular γ-Fe_2O_3 particles [14].

1.3. Magnetic Nanoparticles for Biomedical Applications

Nano-science and nanotechnology have generated tremendous opportunities in many biological and technical fields of applications because of the unique chemical and physical properties of nanomaterials in comparison to the bulk materials. Magnetic nanoparticles have been attracted in the bio-medical field to a large extent in recent years.

This is due to a number of beneficial factors: First, they have sizes that place them at dimensions comparable to those of a virus (20–500 nm), a protein (5–50 nm) or a gene (2 nm wide and 10–100 nm long) [17]. Second, the nanoparticles are magnetic, which means that they can be manipulated by an external magnetic field. As for example, magnetic nanoparticles can be guided to a chosen site using a localized magnetic field gradient, hold them there until the therapy is complete and then remove them. Third, nanoparticles have a large surface area that can be properly modified to attach biological agents. Finally, since the particles are very small, there is a possibility of ubiquitous tissue accessibility.

Applications in biotechnology impose strict requirements on the particles' physical, chemical, thermal, mechanical, and pharmacological properties, including chemical composition, granulometric uniformity, crystal structure, magnetic behavior, surface structure, adsorption properties, solubility and low toxicity [17]. Based on their unique properties, magnetic nanoparticles offer a high potential for several biomedical applications, such as [18-22]:

(a) cellular labelling/call separation;

(b) tissue repair;

(c) targeted drug delivery;

(d) magnetic resonance imaging (MRI);

(e) hyperthermia;

(f) magnetofection; etc.

For all of these applications, the effectiveness of the magnetic particles depends upon their (a) magnetic susceptibility; (b) magnetic saturation; (c) superparamagnetic

behaviour; (d) size and monodispersity; (e) biocompatibility and toxicity; (f) chemical stability and (g) tailored surface chemistry such as availability of interactive functions at their surface of bio-molecules like antibody; protein; drug; gene etc.

Magnetic hyperthermia is promising therapy for cancer treatment in which the cancerous organs or tissues are preferentially heated to temperatures between 42°C and 46°C [18-20]. The heating helps to shrink tumors by damaging cells or depriving them of substances they need to live. Moreover, magnetic resonance imaging (MRI) has been recognized as one of the best noninvasive imaging modalities in both clinical and research fields. In this thesis, we have focused the magnetic hyperthermia and MRI imaging of the magnetic nanoparticles for the diagnostic and therapeutic (theronestic) application.

1.4. Hyperthermia

Cancer is a group of diseases characterized by abnormal regulation of cellular growth and reproduction [23]. Cancer cells can be characterized by some basic features that include uncontrolled cell proliferation, decreased cellular differentiation, ability to invade the surrounding tissue and ability to establish new growth at ectopic sites [24]. Cancer cells are characterized by essential alterations in cell physiology that collectively dictate malignant growth. These are: i) self-sufficiency in growth signals, ii) insensitivity to growth-inhibitory (antigrowth) signals, iii) evasion of programmed cell death and metastasis [25]. As per the National Center for Health Statistics, cancer is one of the second leading (second only to heart diseases) cause of death in the U.S. and many other

industrialized countries [26]. It kills approximately 500,000 people each year in the United States and costs our society more than 100 billion dollars annually. The American Cancer Society estimates 1,437,180 new cancer cases and 565,650 deaths (at a rate of 1500 people a day) related to cancer in 2008 [27].

Up to date, the best known methods for curing cancer are surgery, radiotherapy and chemotherapy. Although radiation and surgical interventions have increased the five-year survival rate in cancer patients, it has been suggested that neither may be able to kill or remove all cancerous tissue due to the irregular shape of the tumor. Not to mention the very invasive nature of a surgery and the collateral damage that is inevitable in radiotherapy. In chemotherapy, drugs that are injected either systematically or locally stop the reproduction of cancerous cells [28]. However, chemotherapy attacks all sorts of cells without discerning between cancerous and normal cells. Therefore, many side effects are attributed to chemotherapy. Hair, skin, mouth, stomach and intestines cells are attacked by this method resulting in hair loss, sores in mouth and throat, dry skin, nausea, vomiting, and diarrhea [27]. Moreover, both radiation therapy and chemotherapy are known to cause "the second cancers". For instance, chemotherapy is a high risk in causing leukemia.

Within the past decade, hyperthermia has been widely used in a variety of therapeutic procedures, either as a singular therapy or as an adjuvant therapy with radiation and drugs in cancer treatments. Since it is associated with few complications [27], hyperthermia is preferable for patients suffering from inoperable or surgically complex tumors, or for patients who are looking for an alternative to the costly and risky surgical procedures [29].

1.4.1. Types, Methods and Principles of Hyperthermia

Hyperthermia (HT) is a minimally invasive method for selective heat treatment in which the target tissues are heated to about 42-46°C [30-36]. HT is usually applied as one of three different treatment strategies: local hyperthermia (LH), which restricts the application of heat to the tumor site, regional hyperthermia (RH) which is applied to treat an entire organ or limb and whole body hyperthermia (WBH), which applies heat to the entire body [37]. Since its inception, different methods have been used in hyperthermia to generate thermal energy or heat in tumors including microwaves, high-frequency radiowaves, special radiant-heat systems, temperature controlled water baths, high energy magnets, ultrasound, capacitive heating using RF electric field, as well as interstitial and intracavitary probes [37-39].

Cancer cells are more susceptible to effects of heat at temperatures above 41°C as compared to normal cells [40]. Therefore, in a hyperthermia treatment, thermal energy is delivered to tumors to raises the intratumoral temperature above 42°C for duration of more than 60 minutes, while maintaining the temperatures in the surrounding normal tissue below 42°C [41]. Death of the tumor cells occur due to a heat-induced cytotoxic response and/or increased cytotoxic effects of radiation and drugs at such an elevated temperatures. Both the direct cell-killing effects of heat and the sensitization of other agents by heat are phenomena strongly dependent on the achieved distribution of the temperature increase and duration of heating.

1.4.2. Magnetic Nanoparticles for Hyperthermia

Magnetic nanoparticle hyperthermia has attracted growing research interests in malignant tumor treatment due to its simple implementation, low cost, and reduced complication. A major concern with the hyperthermia treatments is difficulty in heating the local tumor region to the intended temperature without causing harm to the normal tissues [42-43]. To overcome this, the idea of magnetic particles based intracellular hyperthermia was first proposed for the treatment of deep-seated tumors more than fifty years ago. In this method, micron sized magnetic particles were delivered to the tumor tissue or blood vessels induce localized heating when exposed to an alternating magnetic field, leading to irreversible thermal damage to the tumor [44]. This method enables adequate heat to be generated within tumor tissue without necessitating heat penetration through the skin surface, thus eliminating the consequent side effects of excessive collateral thermal damage. Magnetic nanoparticles have been exploited as miniature heat generators in tissue to address the limitations of conventional hyperthermia approaches. It is an effective and clinically safe therapeutic alternative for cancer treatment because of its ability to provide sufficient and localized heating in tumors, its versatility in treating tumors of irregular shapes that are unsurpassed by traditional non-invasive heating approaches, and its maneuverability to be incorporated into other treatment routes to achieve optimized therapeutic effect. The critical properties of magnetic nanoparticles which are used for heat generation include non-toxicity, biocompatibility, injectability, high-level accumulation in the target tumor and effective absorption of the energy of the AC magnetic field [42]. To date, the magnetite (Fe_3O_4) and maghemite (γ-Fe_2O_3)

nanoparticles are most frequently studied in hyperthermia due to their excellent biocompatibilty [45-46].

Nanoparticles have undergone rapid growth as site-specific carriers for the delivery of therapeutic, imaging, and sensing agents [28]. Nanoparticles loaded with anti-cancer agents are used to target tumor cells selectively to reduce drug intake by healthy tissue. The multifunctional nanoparticles have been developed by encapsulating the magnetic nanoparticles (MNPs) and anticancer drugs (Ads) to combine the magnetic hyperthermia with the chemotherapy [47]. The site-specific targeting of the nanoparticles enhance selective uptake of the MNPs and Ads by the target cells and thereby potentially restrict the hyperthermic and chemotherapeutic effects to a particular diseased areas avoiding various side effects to the surrounding normal tissues [48]. Thus, the combined therapy of magnetic hyperthermia and chemotherapy using the nanoparticles offer better therapeutic efficacy for cancer treatment.

1.4.3. Mechanism of Heat Generation by Magnetic Nanoparticles

Ferromagnetic materials are commonly known to dissipate heat by hysteresis when exposed to an alternating (AC) magnetic field [35]. The heating by hysteresis is enhanced as the size of the ferromagnetic particles decreases to nanoscale. Ferrofluid consisting of extremely fine particles with diameter around 10 nm have superparamagnetic properties. The magnetization of a superparamagnetic ferrofluid relaxes back to zero when it is removed from a magnetic field, due to the ambient thermal energy of its environment [49]. This relaxation either corresponds to the physical rotation of the particles themselves within the fluid (known as Brownian rotation), or rotation of the atomic

magnetic moments across an effective anisotropy barrier within each particle (known as Néel relaxation) [40,49]. The relaxation phenomena strongly depend on the size of the particles. For the smaller particles the Néel relaxation process dominates, while large particles relax following Brownian rotation [40]. For magnetite the critical size for the transition from Neel to Brown relaxation is about 13 nm [40]. When ferrofluid is exposed to an external AC magnetic field, magnetic particles generate heat mainly due to the Néel relaxation mechanism and/or Brownian rotation of the particles [35,50]. The heat induced by the ferrofluid is termed magnetic fluid hyperthermia. In Neel relaxation mechanism, thermal energy is released when the initial permanent magnetic moment of magnetic nanoparticles changes with the alternating magnetic field [51]. In this case, the Eddy current heating is negligible [50]. On the other hand, the heat is generated in Brown relaxation mechanism due to friction between the moving particles and liquid. One of the main advantages of fine superparamagnetic nanoparticles is that they are able to produce an impressive level of heating at relatively low magnetic fields and frequencies (less than 1 MHz) [51]. At such small frequency levels, the induced electric fields are negligible [52]. The specific amount of heat known as the specific loss power (*SLP*) generated by magnetic nanoparticles was derived and evaluated by Rosenweig (2002) (Equation 1.6) [50]:

$$SLP = \pi\mu_0\chi_0 H^2 f \frac{2\pi f\tau}{1+(2\pi f\tau)^2}\varphi \quad \text{---------- (1.6)}$$

$$\chi_0 = \chi_i \frac{3}{\xi}\left(\coth\xi - \frac{1}{\xi}\right),\ \chi_i = \frac{\mu_0 M_d^2 V_p}{3K_bT},\ \xi = \frac{\mu_0 M_d H V_p}{K_bT}$$

$$\frac{1}{\tau} = \frac{1}{\tau_B} + \frac{1}{\tau_N},\ \tau_N = \tau_0 e^{\frac{KV_p}{K_bT}},\ \tau_B = \frac{3\eta V_p(1+\delta/R_p)^3}{K_bT}$$

where H and f are the magnetic field strength and frequency respectively, φ is the concentration (volume of nanoparticles per unit volume of tissue), η is the liquid viscosity, K_b is Boltzmann constant, M_d and K are two parameters that depend on the nanoparticles material, T is the temperature, R_p is the nanoparticle radius and V_p is the nanoparticle volume.

1.5. Magnetic Resonance Imaging Contrast Agents

Magnetic resonance imaging (MRI) has been recognized as a powerful noninvasive diagnostic technique to visualize the fine structure of a human body in a high spatial resolution [53]. MR images of biological tissue are constructed by applying a static magnetic field to the tissue, exciting the magnetic moments of protons in the tissue with a radio frequency pulse, and spatially resolving the density and/or relaxation times of the excited protons. Compared to other medical imaging modalities, MR images possesses high spatial resolution but have limited sensitivity (poor contrast) with anatomical or pathological features that possess similar proton relaxation times, such as small liver metastases [54]. In such poor contrast features, the sensitivity of MRI can be effectively increased by the use of MRI contrast agents, which locally increases image contrast by shortening proton relaxation times. The use of MR contrast agents enables achievement of clear images for accurate diagnosis, by exerting an influence on the longitudinal ($T1$) or transverse ($T2$) relaxation time of the surrounding tissue. For example, paramagnetic complexes containing gadolinium (Gd^{3+}) or manganese (Mn^{2+}) ions induce the local relaxation change of the nearby water protons and mainly reduce $T1$, providing positive contrast (bright signal) on $T1$-weighted MR image [55-56]. On the other hand, the

superparamagnetic iron oxide (SPIO) nanoparticles function as MRI contrast agents by shortening the spin-spin proton relaxation (T2 relaxation) of nearby water protons. The shortened T2 relaxation is manifested as negative contrast (darkening) in the MR image, thus increasing the contrast of the tissue containing SPIO nanoparticles [57]. Iron oxide is an attractive material as a biocompatible contrast agent as it is readily sequestered and metabolized by the body [58]. Superparamagnetic magnetite nanoparticles have been widely utilized as ultrasensitive dark negative contrast for stem cell tracking and early detection of cancers due to their strong *T*2 shortening effect [59-61].

The ability of magnetite nanoparticles to generate MR contrast is influenced by the particles size, crystallographic structure and presence of contaminants. While maghemite (γ-Fe_2O_3) nanoparticles are sometimes used as MRI contrast agents, magnetite is preferred due to a higher saturation magnetization (mass normalized maximum magnetic moment) compared to maghemite. The influence of the size and composition of magnetite nanoparticles and other Fe-based spinels on the MR contrast has been studied recently [62-63]. These studies demonstrated that with increasing size of the nanoparticles within the size range of 6 to 12 nm the MR contrasts increases as shown in Figure 1.7. A higher MR contrast of larger magnetite nanoparticles is reasonable, because faster spin-spin relaxation processes of the water molecules are induced by materials with a larger magnetization [64]. Nevertheless, superparamagnetism is an important property of SPIO MRI contrast agents due to the inherent absence of remnant magnetization in the nanoparticle after applying an external magnetic field, as remnant magnetization would lead to undesirable magnetic aggregation of the nanoparticles. The small size of the magnetite nanoparticles is important for MRI contrast applications

because the iron oxide particles become superparamagnetic at diameters <30 nm, the maximum size for a single magnetic domain particle [65]. Therefore, it has yet to be determined what size range is optimum for highest MR contrast without losing the superparamagnetic properties of the nanoparticles.

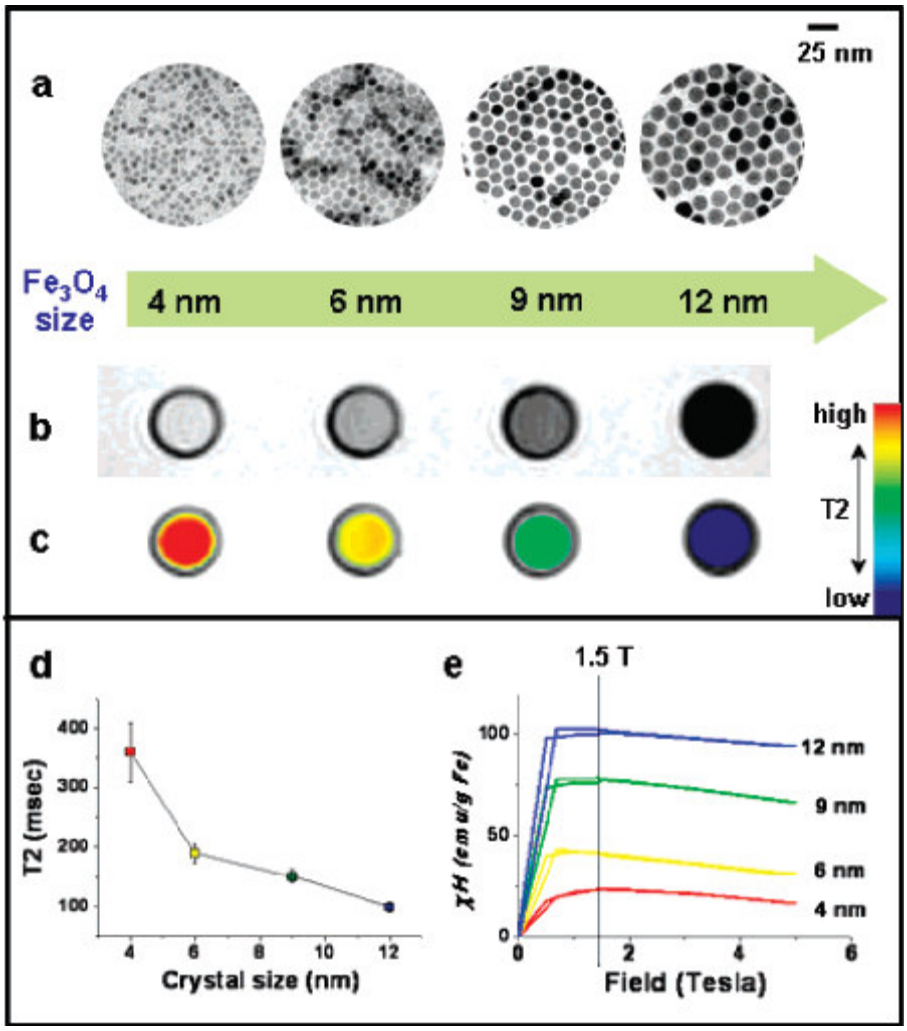

Figure 1.7. Nanoscale size effect of Fe_3O_4 nanocrystals on magnetism and induced MR signals. (a) TEM images of Fe_3O_4 nanocrystals of 4 to 6, 9, and 12 nm. (b) Size-dependent *T*2-weighted MR images of Fe_3O_4 nanocrystals in aqueous solution at 1.5 T. (c) Size-dependent changes from red to blue in color-coded MR images based on *T*2

values. (d) Graph of *T*2 value versus Fe_3O_4 nanocrystal size. (e) Magnetization of Fe_3O_4 nanocrystals measured by a SQUID magnetometer [62].

The commercial T2 contrast agents are synthesized by coprecipitation and coated by different polymers or molecules [66]. The hydrodynamic size and coating determine the nanoparticle biodistribution and the desired organ or tissue to be imaged [67-68]. For example, iron oxide nanoparticles coated by dextran (Feridex, Guerbet) or carboxidextran (Resovist, Schering) with a high hydrodynamic size have been used to image the liver [69-70]. However, magnetic nanoparticles coated by the same polymers but with a low hydrodynamic size (Sinerem, Guerbet and Supravist, Schering) have been used as blood pool agents to image macrophages or lymph nodes [71].

There are two different strategies to improve the quality of the contrast agents. One is related to the nanoparticle synthesis method, and the other is related to the coating and the hydrodynamic size. The coprecipitation method presents several problems, such as the poor control of the size and size distribution and the lack of crystallinity of these particles due to the presence of defects in the structure and the lack of symmetry of the iron ions at the surface [66]. As a consequence of that, these nanoparticles present poor magnetic properties which are in detriment of the contrast in the MR images. Uniform and high crystalline magnetite nanoparticles would be highly desirable for this application. In relation to the coating and the hydrodynamic size, an important effort should be done to developed contrast agents with covalently bonded ligands and small hydrodynamic sizes to enhance the blood half-life time. Polymers or small molecules are usually bonded to the nanoparticle surface by adsorption forces, and when the particles

are introduced to the body, they are desorbed due to dilution, facilitating its aggregation and uptake by the macrophages [66].

The use of magnetic nanoparticles as MRI contrast agents can be divided into molecularly targeted approaches, which rely on equipping the nanoparticles with specific ligands to recognize specifically the target markers and the passive approaches. The passive approaches are based on the non-specific accumulation of the nanoparticles into the tissues to be imaged, for instance the organs of the RES system such as liver and spleen following intravenous injection of the nanoparticles. Dextran-coated magnetite nanoparticles have been clinically used as MRI contrast agents for more than a decade and commercially available products are available with different sizes and surface chemistry. Imaging of the lymph node system has also been achieved through either intravenous or subcutaneous injection of dextran-coated nanoparticles.

Currently, there is wide interest in using targeted SPIO nanoparticles in diagnostic imaging applications, with a number of recent studies demonstrating the clinical potential for cancer diagnosis and tumor detection. Molecularly targeted approaches are more challenging but promising *in vivo* results have been reported, enabling MR imaging of rare molecular events at the cellular and subcellular level. For this, the SPIO nanoparticles are conjugated with targeting vectors or biomarkers (i.e. antibodies, small molecular ligands, aptamers), to target them at a specific site. Monoclonal antibody and peptide sequences have been conjugated to magnetite nanoparticles and used to target them to pathologic areas such as tumors, myocardial infarction, or beta-amyloid plaques [66, 72]. Magnetite nanoparticles conjugated with the synaptotagmin I protein that bind to anionic phospholipids expressed in apoptotic cells have for instance been used to

detect with MRI apoptotic tumor cells following treatment with chemotherapeutics in a murine lymphoma model [73]. Herceptin-conjugated nanoparticles could also be used to detect cancer cells implanted in mice *in vivo* in T2 weighted MRI sequences [74]. Recent years have witnessed an explosion of work in molecular imaging by MRI and interested readers are referred to recent reviews [72, 75-77].

In addition to bioconjugation, SPIO nanoparticle material properties can be manipulated by changes in size and surface chemistry. These approaches enable "tuning" of the colloidal magnetic properties [74]. Specifically, the local T2 proton relaxivity of SPIO nanoparticles can be modified via interfacial surface chemistry to induce aggregation or dispersion in the colloid, thus providing control of the ultimate nanoparticle aggregate size and magnetic properties, with the end goal being the optimization of the colloid for a specific imaging application.

1.6. Biocompatibility, Biodistribution and Clearance of Magnetic Nanoparticles

The important properties which determine the biocompatibility and toxicity of magnetic nanoparticles are the nature of the magnetically responsive component, such as iron, nickel or cobalt [78-79]. But, cobalt and nickel are highly toxic and susceptible to oxidation, and thereby they are of little interest [79]. Iron oxide nanoparticles such as magnetite (Fe_3O_4) or maghemite (γ-Fe_2O_3) are most commonly used in biomedical applications. The biocompatibility of iron oxide nanoparticles has been proven in previous studies on the humans [66] through toxicological and pharmacological tests. Iron oxides in a human body can be degraded in blood pools rich in iron such as

hemoglobin after 7 days and thereby it is considered as nontoxic. However, excessive amounts of iron are harmful to the function of liver; the upper limit of the iron concentration is 4 mg/g of wet liver tissue [80].

Magnetic nanoparticles are small enough to be considered as biological entities and can cross vascular barriers and migrate in the extracellular space without causing embolic phenomena [28, 81]. Due to their small size, nanoparticles cause no blood coagulation on their surface but they are likely to be consumed through phagocytosis [82]. However, the blood vessels in tumors are very "leaky" relative to normal blood vessels and the endothelial barriers are diminished; therefore nanoparticles have a better chance to enter the local tumor cells rather than being drained to the lymphatic glands. The phenomenon is known as EPR, for "Enhanced Permeability and Retention" and it is enhanced through coating the nanoparticles with a protein layer [83]. Not everything in the blood stream will invade a tumor by this route, but on the whole it is a fairly non-specific mechanism that works for a wide range of nanoparticles, as long as the nanoparticle of interest is able to circulate long enough. A more specific method to target a tumor is to attach molecules to the surface of the nanoparticle that improves its ability to attach to the surface of a tumor or to penetrate into the cancerous cells. These molecules can be sugars, small molecules, antibodies, or small peptides; folic acid is one of the most commonly employed small molecules, which targets the folate receptor present on the surface of many tumor cells [47, 84].

Probably the most important factor in the design of any nanoparticle for in-vivo application is the biocompatibility of the device. The term “biocompatibility” has many meanings. In some cases the mere demonstration of water solubility is cited as evidence

of biocompatibility. In other cases "biocompatible" means that the nanoparticle must display limited toxicity to the organism at its effective dose, it must be able to perform its function without interference from the organism's healthy mechanisms, and it must be able to circulate long enough to accomplish its intended task. Shape, size, and charge are all factors in determining how long a given nanoparticle will circulate before being eliminated by the liver, kidneys, or spleen. A key requirement for intravenously administered nanoparticles is that they have an ability to circulate in the bloodstream for > 2 hours; if it is filtered out by the liver or the kidneys it can't make it to the tumor.

What happens to Nanoparticles after Intravenous Injection?

One of the most important pathways for clearance of nanoparticles *in vivo* is the mononuclear phagocytic system (MPS), alternatively known as reticulo-endothelial system (RES). After particles are injected into the bloodstream they are rapidly coated by components (opsonins) of the circulation, such as plasma proteins (immunoglobulins, complement proteins, fibronectin, etc.) [21,33]. This process is known as opsonisation. Body's major defence system, the RES is a diffuse system of specialized cells that are phagocytic (i.e. engulf inert material) associated with the connective tissue framework of the liver (Kupffer cells), spleen and lymph nodes [21]. These macrophages easily recognize the opsonized particles and rapidly clear them from the blood circulation. The fate of nanoparticles following intravenous (iv) administration, is indicated in Figure 1.8. Therefore, the first step for achieving long circulation of the nanoparticle is development of a strategy to minimize or delay the nanoparticle uptake by the MPS or RES or phagocytes.

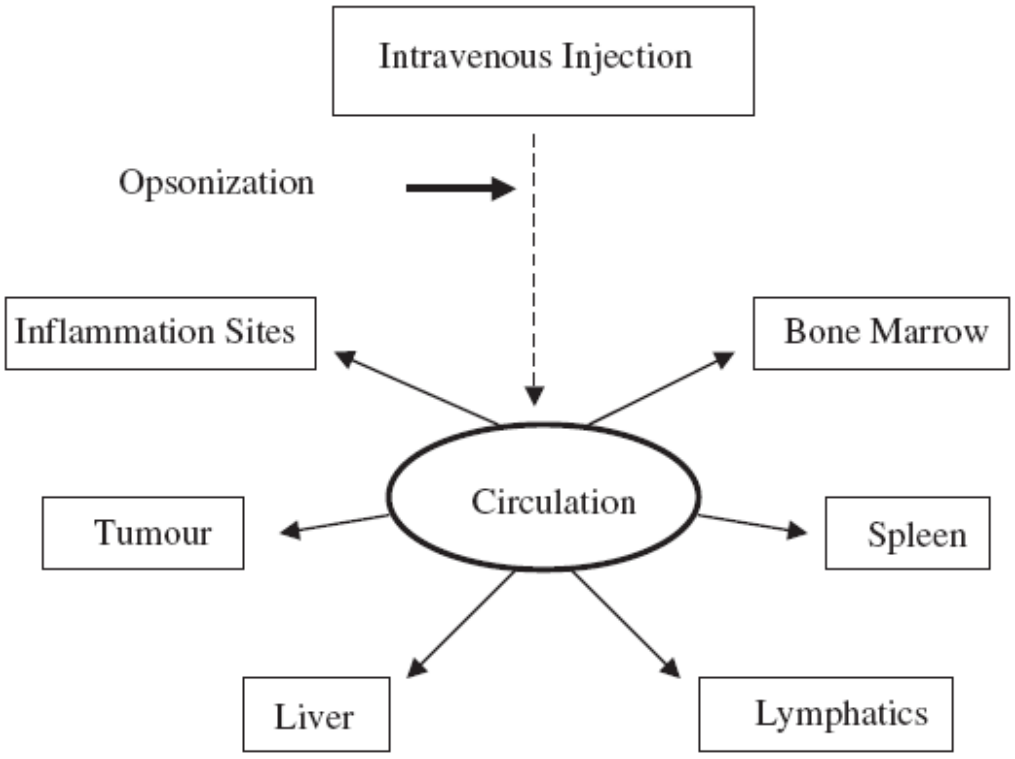

Figure 1.8. Biodistribution of nanoparticles following intravenous injection [21].

The size, morphology, charge, and surface chemistry of magnetic particles could strongly influence their biodistribution. The smaller, more neutral and more hydrophilic particle surface are responsible for the longer its plasma half-life i.e. longer circulation time [33]. Particles that have a largely hydrophobic surface are efficiently coated with plasma components and thus rapidly removed from the circulation, whereas particles that are more hydrophilic can resist the opsonisation process and are cleared more slowly [85]. This has been used to the advantage when attempting to synthesize RES evading particles by sterically stabilizing the particles with a layer of hydrophilic polymer chains [86]. In the literature the most common coatings are derivatives of dextran, polyethylene glycol (PEG), polyethylene oxide (PEO), poloxamers and polyoxamines [87]. The role of the

dense brushes of polymers is to inhibit opsonization, thereby permitting longer circulation times [88-90]. A further strategy in avoiding the RES is by reducing the particle size [91-92]. Particles below 100 nm are small enough both to overcome the RES uptake of the body as well as penetrate the very small capillaries within the body tissues [91]. Despite all efforts, however, complete evasion of the RES by these coated nanoparticles has not yet been possible [85]. Thus, a pre-requisite to the widespread use of nanoparticles *in vivo* is their ability to resist non-specific adsorption of opsonins i.e. to avoid the RES uptake. In this thesis, the *in vivo* biodistribution of nanoparticles are studied using mice and rat to evaluate their bold circulation time.

1.7. Iron Oxide Nanoparticles: Building Block of Ferrofluids

Magnetic nanoparticles are comprised of metals and metal oxides including Ni, Co, Fe, iron oxide (γ-Fe_2O_3, Fe_3O_4 etc) and other ferrites ($MnO{\cdot}Fe_2O_3$, $CoO{\cdot}Fe_2O_3$ $NiO{\cdot}Fe_2O_3$). Although, the ferromagnetic transition metal (Fe, Co and Ni) particles have high saturation magnetization value but it is very difficult to produce their nanoparticles in stable form due to rapid oxidation on their surface. For example, nanoscale Fe particles are so unstable that they will spontaneously burst into flames when exposed to air. Ni and Co particles are less reactive but an oxide coating will still form if exposed to air. Also, cobalt and nickel are toxic, making them unsuitable for in vivo applications [22]. In contrast, iron oxide nanoparticles are easily fabricated due their chemical stability. Iron oxide consist of iron (Fe^{2+} or Fe^{3+}) ions which are the component of blood hemoglobin and essential for metabolism of red blood cells and thereby it is considered as nontoxic (toxicity can arise when overdose). Iron oxide nanoparticles are superparamagnetic; that

is, they do not show any magnetism in the absence of an external magnet, but develop a magnetic moment when an external magnet is applied. In addition, they have relatively high saturation magnetization and high initial susceptibility. Therefore, iron oxide particles such as magnetite (Fe_3O_4) or maghemite (γ-Fe_2O_3) are most commonly employed in the biomedical applications for past decades. In biomedical applications, the iron oxide nanoparticles are generally used in ferrofluid form. A ferrofluid (also known as *magnetic fluid or magnetic colloid or magnetic liquid*) is a stable and homogeneous colloidal suspensions of single-domain magnetic particles dispersed in appropriate carrier liquid which is either polar (e.g. water) or non-polar (e.g. hydrocarbon) [93-94]. The advantage of the ferrofluid is that it is possible to control its flow using an external magnetic force as shown in Figure 1.9.

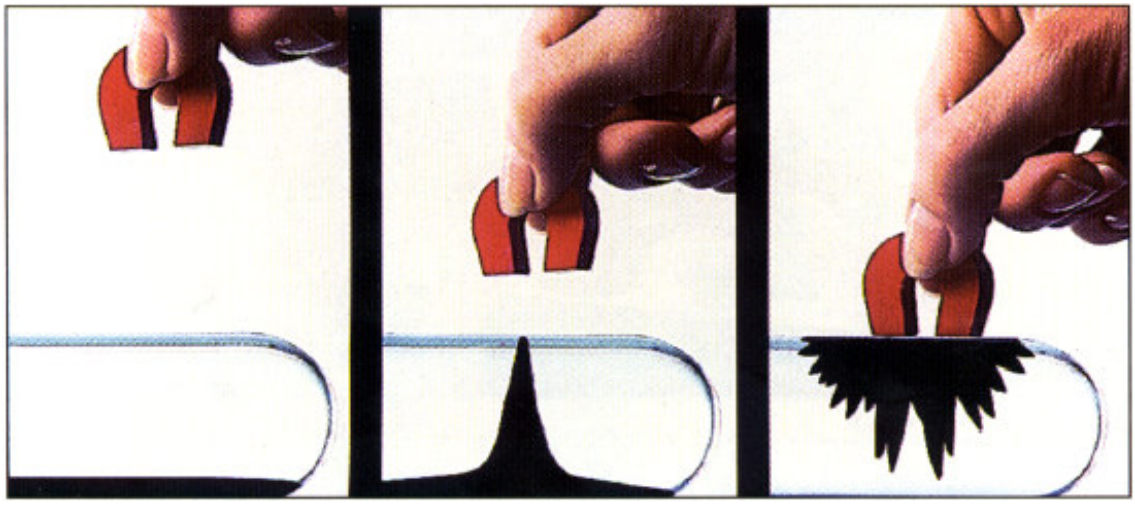

Figure 1.9. Flow of ferrofluid in presence of a permanent magnet.

Ferrofluid contains colloidal ferro- or ferrimagnetic particles with a typical size of 10 nm dispersed in a carrier liquid. Because of their small size, these magnetic colloid particles contain a single magnetic domain, and therefore have a permanent magnetic moment

proportional to their volume. In the absence of an external magnetic field, the magnetic moments of each single particle are randomized and the materials are not magnetized and hence magnetic fluids are paramagnetic in behavior. On the other hand, since the particle sizes are so small, their magnetic moments can freely rotate essentially instantaneously along an applied magnetic field gradient and this can significantly enhance the strength of the applied field. Thus like ferromagnets magnetic fluids can easily approach their saturation magnetization. Hence magnetic fluids are called *superparamagnetic* that means although they are ferromagnetic on the molecular scale, they resemble a paramagnet on the colloidal scale, with the major difference that the magnetic moments of magnetic colloids are much larger than the moments in a paramagnet (typical values are 10^{-19} Am^2 for magnetic colloids and 10^{-23} Am^2 for paramagnets). A schematic drawing of the properties of a superparamagnetic fluid is shown in Figure 1.6. Further, *superparamagnetic fluids* differ from ordinary paramagnetic fluids in that they have high magnetic susceptibility (χ) and are able to be saturated in moderate fields. In addition, they also differ from typical ferromagnetic materials in that they do not exhibit magnetic hysteresis (zero coercive force).

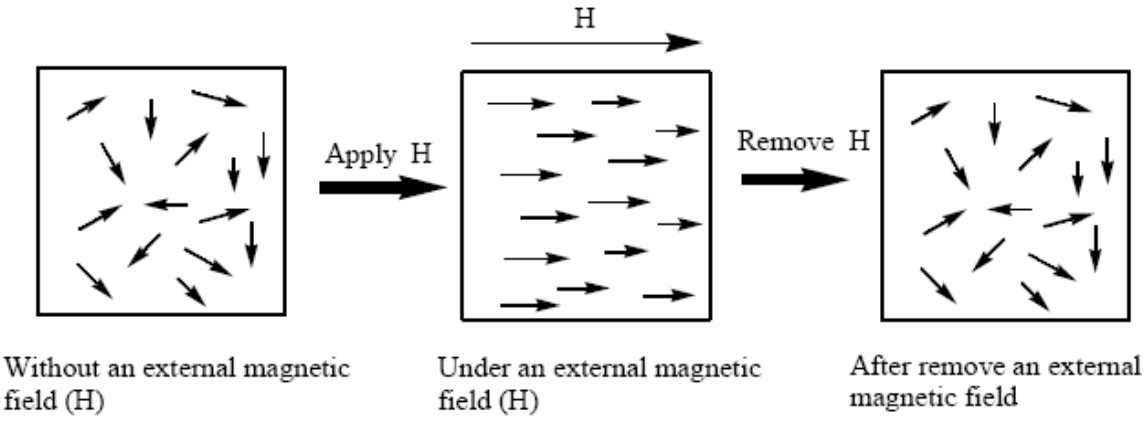

Figure 1.10. A schematic diagram of the properties of superparamagnetic fluids [95].

In ferrofluid, the sizes of colloidal magnetic particles are so small (~10 nm) that particles are subject to Brownian motion (Figure 1.11). Collision of particles would eventually lead to coagulation and sedimentation due to the van der Waal's forces (Figure 1.12). This process is also speeded up due to magnetic dipole-dipole interactions. Due to the van der Waals force of attraction and magnetic dipole-dipole attractive interactions, the magnetic nanoparticles tend to coagulate irreversibly. Hence a suspension of bare magnetic particles in a carrier liquid will not be stable against agglomeration.

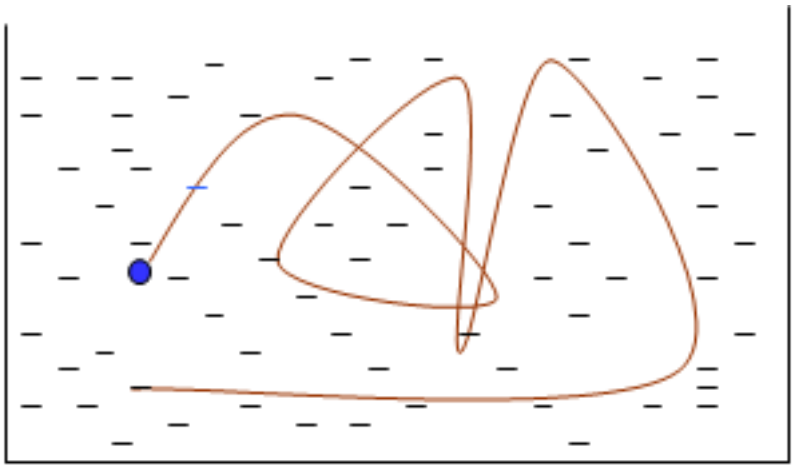

Figure 1.11. Brownian motion of a particle in a colloidal suspension.

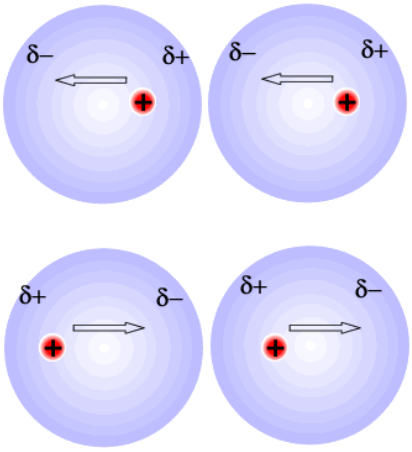

Figure 1.12. van der Waal's interaction between particles in a colloidal suspension.

1.8. Stability of Ferrofluids

For technical and biomedical uses and scientific studies, the most important property of magnetic colloid is its stability i.e. stability against sedimentation and agglomeration of the particles. Such sedimentation and agglomeration is due to gravitational and magnetic forces. The particles do not sediment and the suspension remains well dispersed if the thermal energy due to Brownian motion of the particles $E_T = k_B T$ (k_B: Boltzmann's constant, T: absolute temperature) is high enough to provide sufficient mixing of the suspensions [93-94]. Therefore it needs to be higher than the energy of the particles in the gravitational field or in a magnetic field respectively.

1.8.1. Stability in a Magnetic-Field Gradient

Sedimentation of particles due to an external magnetic field can be avoided if thermal energy (E_T) of the particles is greater than the magnetic energy (E_H) i.e.

$$\frac{E_T}{E_H} = \frac{k_B T}{\mu_0 m H} > 1 \quad \text{---------- (1.7)}$$

where m (= $M_0 V$) is the magnetic moment of the particle, M_0 is the spontaneous magnetization of the magnetic material of the particles, μ_0 is the permeability of free space, and volume $V = \frac{\pi}{6} d^3$ for a spherical particle of diameter d.

Thus the expression for the maximum size of the particles is:

$$d < \left(\frac{6 k_B T}{\mu_0 M_0 \pi H} \right)^{\frac{1}{3}} \quad \text{---------- (1.8)}$$

For stability of magnetite particles in a magnetic field, actual size of the particles is in the order of 10 nm [93-94].

1.8.2. Stability against Settling in a Gravitational Field

Due to gravitational energy (E_g), particles tend to settle down while thermal energy (E_T) counteracts the gravitational force and prevents the sedimentation of the particles. Gravitational energy of the particles in the gravitational field is

$$E_g = \Delta\rho g h \pi d^3/6 \text{ ---------- (1.9)}$$

where $\Delta\rho$ is the density difference between the particles and the carrier liquid, g is the gravitational acceleration and h the height of particle of diameter d from the bottom of a container. For gravitational stability of magnetite particles, maximum size of particles is in the order of 10 nm [93-94].

1.8.3. Stability against Magnetic Agglomeration

Due to magnetic dipole-dipole interaction, particles tend to agglomerate while thermal energy provides motion which prevents agglomeration of particles. Expression for the magnetic dipole interaction energy (E_{dd}) is

$$E_{dd} = \frac{\pi}{9}\frac{\mu_0 M_0^2 d^3}{(l+2)^3} \text{ ---------- (1.10)}$$

where $l = 2\delta / d$, with δ the surface-to-surface separation distance of particles.

For particles to escape agglomeration, the thermal energy of the two interacting particles should be greater than the magnetic dipole interaction energy i.e.

$$2k_B T > \frac{\pi\mu_0 M_0^2 d^3}{9(l+2)^3} \text{ ---------- (1.11)}$$

The interaction energy reaches its maximum when the particles come into contact ($l = 0$) and thus the expression for the maximum size of the particles is

$$d \leq \left(\frac{144 k_B T}{\pi \mu_0 M_0^2 d^3} \right)^{\frac{1}{3}} \text{ ---------- (1.12)}$$

To avoid the agglomeration due to magnetic dipole-dipole interaction, size of the magnetite particles should be in the order of 10 nm [93-94]. Thus the thermal energy of magnetite particles with 10 nm diameter is efficient to avoid sedimentation or agglomeration due to gravity or magnetic dipole interaction respectively. However, there is an additional problem as discussed later.

1.8.4. Stability against the van der Waals Attractive Force

Always there is van der Waals force of attraction between the particles and this van der Waal's interaction energy for spherical particles of diameter d with the surface-to-surface separation distance δ is expressed as below [93]

$$|E_{v.d.W.}| = \frac{A}{6}\left[\frac{2}{l^2 + 4l} + \frac{2}{(l+2)^2} + \ln\left(\frac{l^2 + 4l}{(l+2)^2} \right) \right] \text{ ---------- (1.13)}$$

where l (= 2δ/d) is the normalized distance and A is the Hamaker constant.

In order to achieve colloidal stability in the system, the van der Waals attractive force between the particles has to be avoided. The stabilization of the suspension can be achieved by incorporating steric repulsion into the system and for that the particles are coated with a layer of surfactant of long chained molecules (Figure 1.13). The steric repulsive energy, comes out from the interaction of the long tails of surfactant molecules, can be expressed as below [93]

$$E_{steric} = \frac{k_B T \pi d^2 \xi}{2}\left[2 - \frac{l+2}{t}\ln\left(\frac{1+t}{1+l/2}\right) - \frac{l}{t}\right] \text{---------- (1.14)}$$

where ξ is the surface concentration of the surfactant molecules, t (= 2s/d) is the normalized surfactant thickness with s the thickness of surfactant layer.

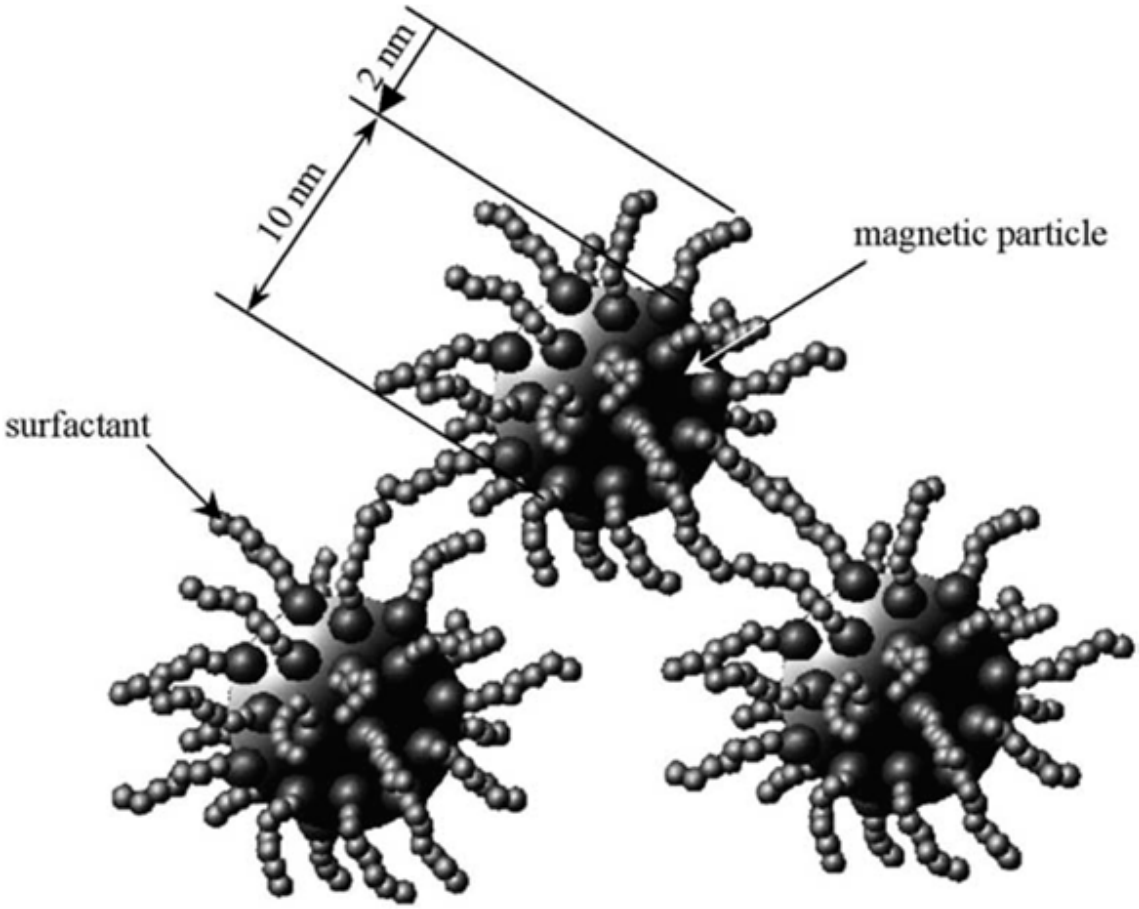

Figure 1.13. Schematic sketch of the surfactant coated colloidal magnetic particles in a ferrofluid [94].

1.8.5. Net Interaction Curve

For magnetite particles with diameter, d = 10 nm and a surface density ς = 1 nm^{-2} with 2 nm surfactant layer thickness different interaction energies are plotted as a function of the

interparticle (surface-to-surface separation) distance, δ (Figure 1.14). Thus a surfactant thickness of 2 nm provides an energy barrier of about 20 k_BT between the particles, being sufficient to avoid their agglomeration due to van der Waals attraction and magnetic dipole-dipole interactions [94].

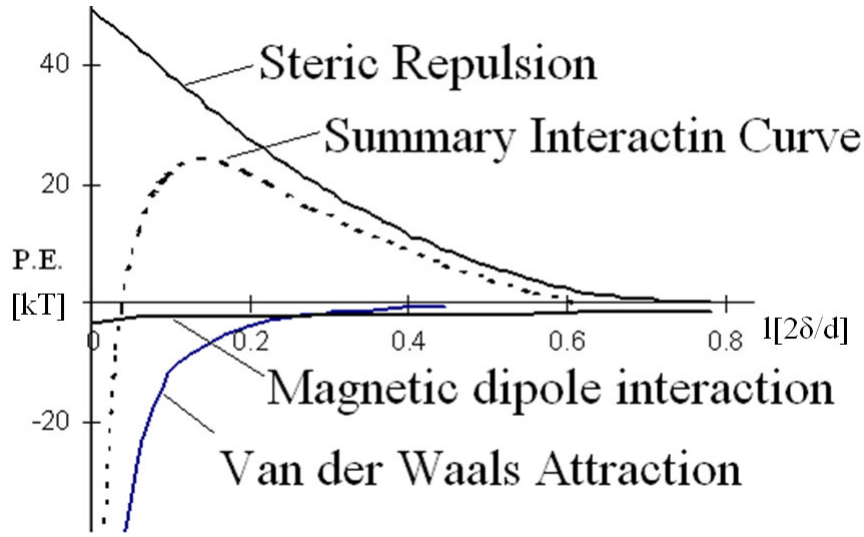

Figure 1.14. Potential energy versus interparticle distance between the surfacted magnetite particles of 10 nm diameter [94].

The iron oxide nanoparticles are usually stabilized in an organic solvent (e.g. hexane, toluene etc) or in polar solvent like water using the hydrophobic (e.g. oleic acid, oleyl amine) or hydrophilic (e.g. dextran, ethylene glycol) coating to their surface, respectively. A schematic drawing of a ferrofluid, seen on three length scales, is shown in Figure 1.15.

Iron oxides exist in a variety of chemical compositions and with different magnetic properties (Table 1.3) [96]. However, the magnetite (Fe_3O_4) nanoparticles are commonly used as building blocks of ferrofluid due to their biocompatibility, high saturation magnetization and high chemical stability [18, 97]. Moreover, magnetite

nanoparticles have been considered an ideal candidate for biological applications, both as a tag for sensing and imaging, and as an activity agent for antitumor therapy [98-102].

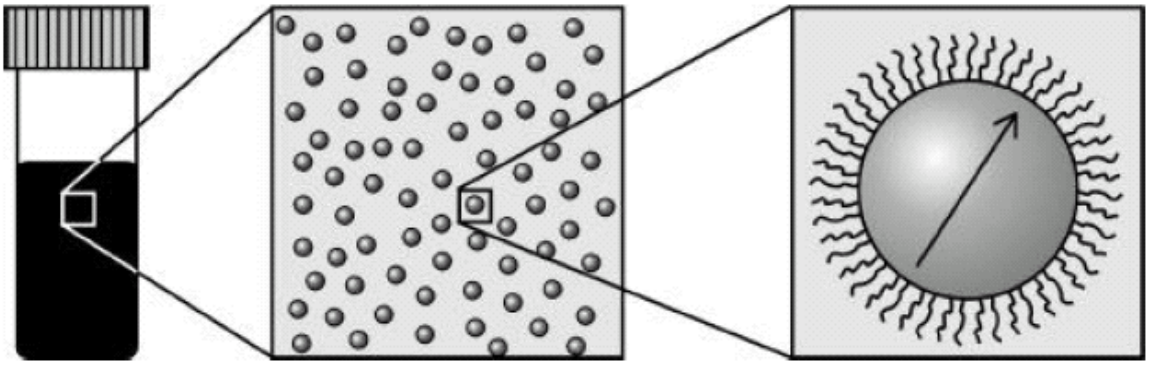

Figure 1.15. Schematic drawing of a ferrofluid on three length scales. On the macroscopic length scale (left), it resembles an ordinary liquid. On the colloidal length scale (middle), the fluid is appears to consist of small solid particles dispersed in a liquid. Each particle consists of a single domain iron oxide core, and a surface grafted with surfactant or polymer chains (right) [95].

Table 1.3. Iron oxyhydroxide and iron oxide species [96]

Mineral	Formula	Magnetic response
Goethite	α - FeOOH	antiferromagnetic
Akaganeite	β - FeOOH	antiferromagnetic
Lepidocrocite	γ - FeOOH	antiferromagnetic
Feroxyhyte	δ - FeOOH	ferrimagnetic
Ferrihydrite	$Fe_3HO_8\,4H_2O$	antiferromagnetic
Hematite	α Fe_2O_3	ferrimagnetic
Maghemite	γ – Fe_2O_3	weakly ferrimagnetic
Magnetite	Fe_3O_4	ferrimagnetic

1.9. Crystal Structure of Iron Oxide

Magnetite (Fe_3O_4) has an inverse spinel crystal structure with face centered cubic unit cell where oxygen ions are located regularly in cubic close packed positions along the [111] axis [96]. Figure 1.16 shows the unit cell of magnetite, typical inverse spinel ferrites. The unit cell is comprised of 56 atoms: 32 O^{2-} anions, 16 Fe^{3+} cations and 8 Fe^{2+} cations, respectively [8]. The chemical formula of magnetite is Fe_3O_4, however more appropriately it is defined as $FeO{\cdot}Fe_2O_3$ (molar ratio of Fe^{2+}:Fe^{3+} = 1:2). The inverse spinel structure is arranged such that half of the Fe^{3+} ions are occupying interstitial 8 tetrahedral (A-sites) positions and the remaining half of Fe^{3+} and all of the Fe^{2+} are occupying 16 octahedral (B-sites) positions.

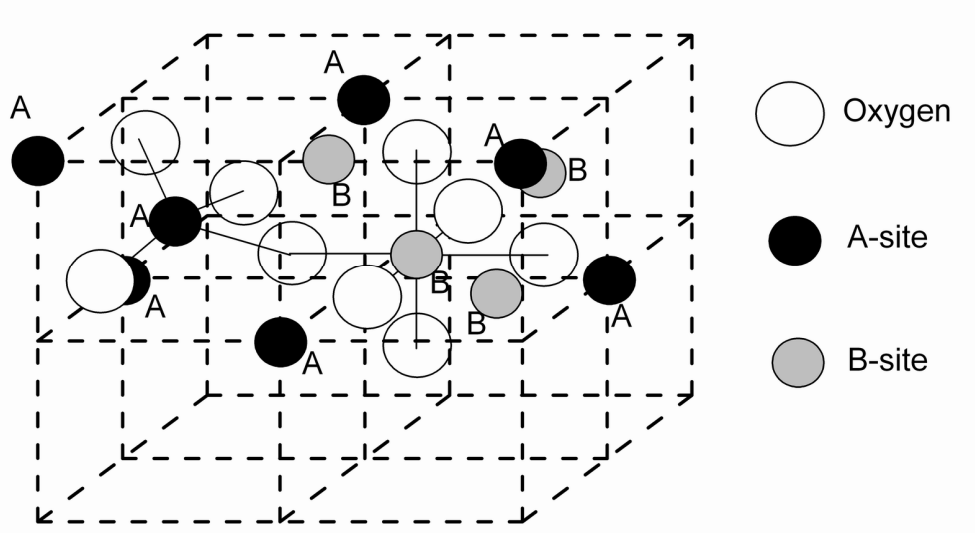

Figure 1.16. Representation of the inverse spinel structure of magnetite.

Maghemite (γ-Fe_2O_3) has a structure similar to that of magnetite, only differs in that all of the Fe is in the trivalent state (Fe^{3+}). Cation vacancies (□) compensate for the oxidation of

Fe^{2+} to Fe^{3+} cations (Equation 1.17). Due to the small difference in crystal structure, magnetite and maghemite have quite similar physical properties (Table 1.4).

$$\text{Magnetite } (FeO.Fe_2O_3) \xrightarrow{\text{Oxidation}} \text{Maghemite } (\gamma\text{-}Fe_2O_3)$$
$$(Fe_8^{3+})_A[Fe_8^{2+}Fe_8^{3+}]_B O_{32} \quad \Rightarrow \quad (Fe_8^{3+})_A[(Fe_{5.3}^{3+}\square_{2.7})Fe_8^{3+}]_B O_{32}$$

---------- (1.15)

Table 1.4. Physical properties of magnetite and maghemite [93,96,103]

Mineral	Crystal system	Cell Dimensions (Å)	Density (g/cm^3)	Color	Magnetic saturation (emu/g)	Curie Temperature (K)
Fe_3O_4	cubic	a_0= 8.39	5.26	black	90-98	850
γ-Fe_2O_3	cubic or tetragonal	a_0= 8.34	4.87	reddish-brown	76-81	820-986

1.10. Synthesis of Iron Oxide Nanoparticles

It has long been of scientific and technological challenge to synthesize controlled size, phase pure, controlled shaped magnetic nanoparticles with narrow size distribution. Wet chemical methods have been widely used to produce iron oxide nanoparticles because they are very straightforward, tractable and very efficient methods for producing large quantities of the final product with appreciable control over size, composition and sometimes even the shape of the nanoparticles [18]. A brief revision of some of the most frequently used wet chemical routes is described below.

1.10.1. Co-Precipitation

Co-precipitation has been widely used to synthesize the iron oxides (either Fe_3O_4 or γ-Fe_2O_3) due to its ease and large volume capability. Conventionally, magnetite is prepared by adding a base (NH_4OH or NaOH) to an aqueous mixture of Fe^{2+} and Fe^{3+} salts (e.g. chlorides, sulphates, nitrates etc.) at a 1:2 molar ratio under inert atmosphere at temperature range of 60-95°C [104-106]. The precipitated magnetite is black in color. The chemical reaction may be written as follows [107-108]:

$$Fe^{2+} + 2Fe^{3+} + 8OH^- \rightarrow Fe_3O_4 + 4H_2O \text{ ---------- (1.16)}$$

The precipitation of Fe_3O_4 is carried out between pH = 9-14 while maintaining a molar ratio of Fe^{3+}:Fe^{2+} = 2:1 under an inert environment [108-109]. The non-oxidizing oxygen-free inert (N_2 or Ar) environment is necessary to avoid the oxidation as shown in Equation 1.16 and Equation 1.17 [4, 16].

$$Fe_3O_4 + 0.25\ O_2 + 4.5\ H_2O \rightarrow 3Fe(OH)_3 \text{ --------- (1.17)}$$

$$4\ Fe_3O_4 + O_2 \rightarrow 6\ \gamma\text{-}Fe_2O_3 \text{ ---------- (1.18)}$$

In order to prevent the possible oxidation in air as well as from agglomeration, Fe_3O_4 nanoparticles are usually coated with organic or inorganic molecules during the precipitation process [109-110].

Genesis of the particles in the solution under optimum synthetic conditions takes place by the formation of tiny crystalline nuclei in a supersaturated medium, followed by crystal growth [111]. The latter process is controlled by mass transport and by the surface equilibrium of addition and removal of individual monomers, i.e., atoms, ions, or molecules. Hereby, the driving force for monomer removal (dissolution) increases with

decreasing particle size. Thus, within an ensemble of particles with slightly different sizes, the large particles will grow at the cost of the small ones. This mechanism is called Ostwald ripening and is generally believed to be the main path of crystal growth. The major disadvantage of the precipitation route is that the control of size, shape and composition of nanoparticles very much depends on the type of salts used, Fe^{2+} and Fe^{3+} ratio, precipitation temperature, pH and ionic strength of the precipitation medium [104-107]. As a matter of fact, the magnetite nanoparticles synthesized using this method are usually polydisperse in size and heavily aggregated, leading to a poor colloidal stability. As a result, the production of significant quantities of controlled sized nanoparticles with narrow size distribution remains a significant challenge using this method.

1.10.2. Microemulsion

A microemulsion can be defined as a thermodynamically stable isotropic dispersion of two immiscible liquids consisting of nanosized domains of one or both liquids in the other, stabilized by an interfacial film of surface-active molecules [17-18]. In water-in-oil microemulsions, the aqueous phase is dispersed as microdroplets or microcavities (typically 1–50 nm in diameter) surrounded by a monolayer of surfactant molecules in the continuous hydrocarbon phase (Figure 1.17) [18]. This surfactant-stabilized microcavity provides a confinement effect that limits particle nucleation, growth, and agglomeration [17]. The size of the reverse micelle is determined by the molar ratio of water to surfactant [112]. By mixing two identical water-in-oil microemulsions containing the desired reactants, the microdroplets will continuously collide, coalesce, and break again, and finally a precipitate forms in the micelles [18]. By the addition of solvent, such as acetone or ethanol, to the microemulsions, the precipitate can be

extracted by filtering or centrifuging the mixture. Recent developments have been focused in the use of microemulsions for the preparation of highly monodispersed magnetic nanoparticles useful in biomedical applications. The principle advantage of utilizing this type of microemulsion system for nanoparticle formation is that the size of nanoparticles can be controlled by modulating the size of aqueous micellar core [18]. Although many types of magnetic nanoparticles have been synthesized in a controlled manner using the microemulsion method, the particle size and shapes usually vary over a relative wide range [10]. Moreover, the working window for the synthesis in microemulsions is usually quite narrow and the yield of nanoparticles is low compared to other methods, such as thermal decomposition and coprecipitation. Large amounts of solvent are necessary to synthesize appreciable amounts of material. It is thus not a very efficient process and also rather difficult to scale-up.

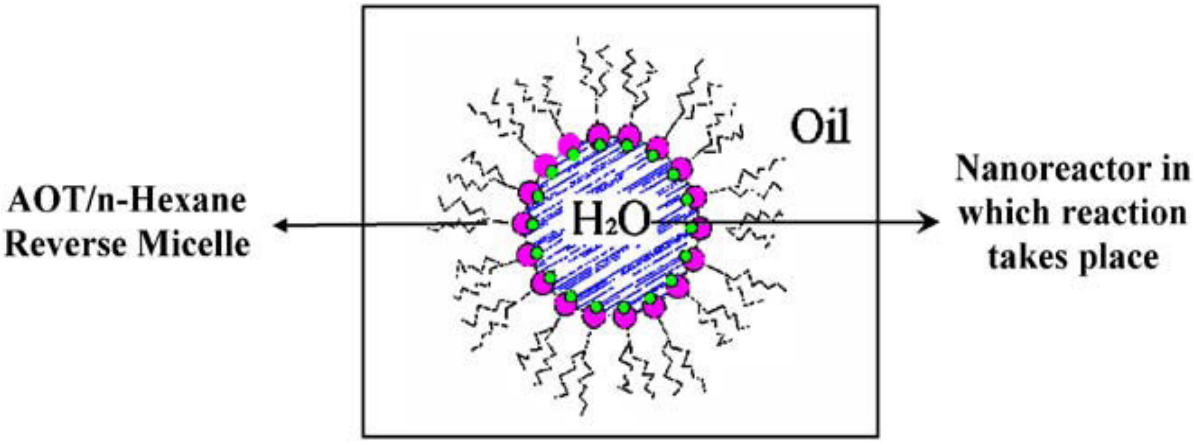

Figure 1.17. Structure of reverse micelles formed by dissolving, a surfactant, in a hydrocarbon. [18].

1.10.3. Thermal Decomposition

Thermal decomposition method have been widely used to synthesize high-quality (single-crystalline, monodisperse, well-shaped, and phase pure) quantum dot and rare earth oxide nanocrystals [113-117]. In the similar way, monodisperse iron oxide nanocrystals with smaller size can essentially be synthesized through the thermal decomposition of organometallic compounds in high-boiling organic (non-aqueous) solvents containing stabilizing surfactants. The organometallic precursors e.g. iron(III) acetyleacetonate ($Fe(AcAc)_3$), iron(II) acetate ($Fe(Ac)_2$), iron pentacarbonyl ($Fe(CO)_5$) and iron oleate ($Fe(OA)_3$), surfactants such as oleic acid (OA, RCOOH), lauric acid (LA), oleyl amine (OM, RNH_2), tri-octyl phospine oxide (TOPO) and hexadecylamine (HDA) and organic solvents like diphenyl ether (Ph_2O, bp 265ºC), 1-hexadecene (bp 274°C), dioctyl ether (bp 287ºC), benzyl ether (bp 300ºC), 1-octadecene (bp 330ºC), 1-eicosene (bp 330°C) and trioctylamine (bp 365°C), are widely used for the synthesis of iron oxide nanoparticles using this technique [118-125]. Typical thermal decomposition synthesis of Fe_3O_4 nanoparticles are shown in Figure 1.18.

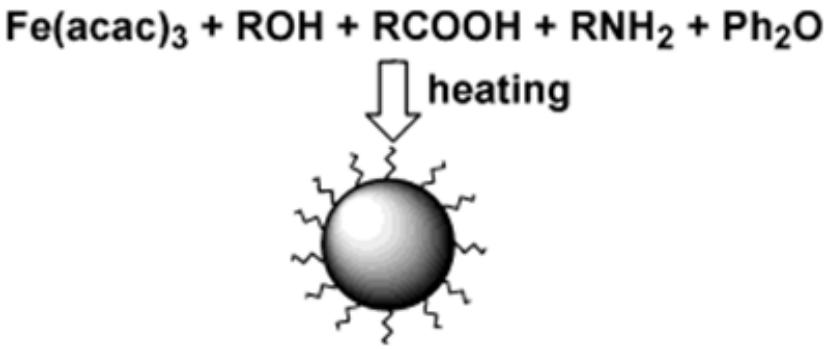

Figure 1.18. Schematic representation of thermal decomposition synthesis of Fe_3O_4 nanoparticles (Ph_2O is diphenyl ether) [123].

In principle, the ratios of the starting reagents including organometallic compounds, surfactant and solvent are the decisive parameters for the control of the size and morphology of magnetic nanoparticles. The reaction temperature, reaction time, as well as aging period may also be crucial for the precise control of size and morphology. The size and shape of the nanocrystals can also be controlled by variation of the reactivity and concentration of the precursors. The reactivity can be tuned by changing the chain length and concentration of the fatty acids. Generally, the shorter the chain length, the faster the reaction rate is. Alcohols or primary amines could be used to accelerate the reaction rate and lower the reaction temperature.

If the metal in the precursor is zero valent, such as in carbonyls, thermal decomposition initially leads to formation of the metal, but two-step procedures can be used to produce oxide nanoparticles as well. For instance, iron pentacarbonyl can be decomposed in a mixture of octyl ether/trioctyl amine and oleic acid at 100-300ºC, subsequent addition of trimethylamine oxide $(CH_3)_3NO$ or Pyridine *N*-Oxide $(C_5H_5)NO$ as a mild oxidant at elevated temperature, results in formation of monodisperse γ-Fe_2O_3 nanocrystals with a size of approximately 5-16 nm [118-121]. Decomposition of precursors with cationic metal centers leads directly to the oxides, that is, to Fe_3O_4, if the $Fe(acac)_3$ is decomposed in the presence of 1,2-hexadecanediol, oleylamine, and oleic acid in phenol ether [121-124]. A 4-6 nm-sized magnetite particles can be directly obtained through the decomposition of $Fe(acac)_3$ while larger ones can be synthesized through subsequent seed-mediated growth [123]. Direct thermal decomposition of iron-surfactant complex has also been demonstrated to fabricate monodisperse 5-22 nm magnetite nanoparticles successfully depending upon the decomposition temperature and

aging period [121, 125]. In this method, iron(III) chloride and sodium oleate are reacted in situ to generate an iron oleate complex which was then decomposed at temperatures between 274 to 365ºC in different solvents, such as 1-hexadecene, octyl ether, 1-octadecene, 1-eicosene, or trioctylamine. The thermal decomposition of iron pentacarbonyl at relatively low temperature induces nucleation while the decomposition of the iron oleate complex at a higher temperature leads to growth. Peng and co-workers reported a general decomposition approach for the synthesis of size- and shape-controlled magnetic oxide nanocrystals based on the pyrolysis of metal fatty acid salts in non-aqueous solution [126]. The reaction system was generally composed of the metal fatty acid salts, the corresponding fatty acids (decanoic acid, lauric acid, myristic acid, palmitic acid, oleic acid, stearic acid), a hydrocarbon solvent (octadecene (ODE), n-eicosane, tetracosane, or a mixture of ODE and tetracosane), and activation reagents. Nearly monodisperse Fe_3O_4 nanocrystals, with sizes adjustable over a wide size range (3–50 nm) could be synthesized, with controlled shapes, including dots and cubes. This method can be explained by the classical LaMer mechanism. That is, a short burst of nucleation from a supersaturated solution is followed by the slow growth of particles without any significant additional nucleation, thereby achieving a complete separation of nucleation and growth [127].

The above-mentioned nanoparticles are dispersible in organic solvents. However, water soluble magnetic nanoparticles are more desirable for biomedical applications. In addition, the use of toxic solvents and surfactants may reduce the biocompatibility of the produced nanoparticles, although iron oxide itself is considered a biocompatible material.

Therefore, several groups have been tried to modify the thermal decomposition method to synthesize water soluble magnetite nanoparticles without sacrificing their biocompatibility. Gao et al have reported one step synthesis of water-soluble 5 nm iron oxide nanocrystals by thermal decomposition of $Fe(acac)_3$ or $FeCl_3 \cdot 6H_2O$ in 2-pyrrolidone at 245 ºC [128-129]. In this method, 2-pyrrolidone is used both as solvent and stabilizer since it has strong polarity, high boiling point, and coordination capacity with transition metal ions (Figure 1.19).

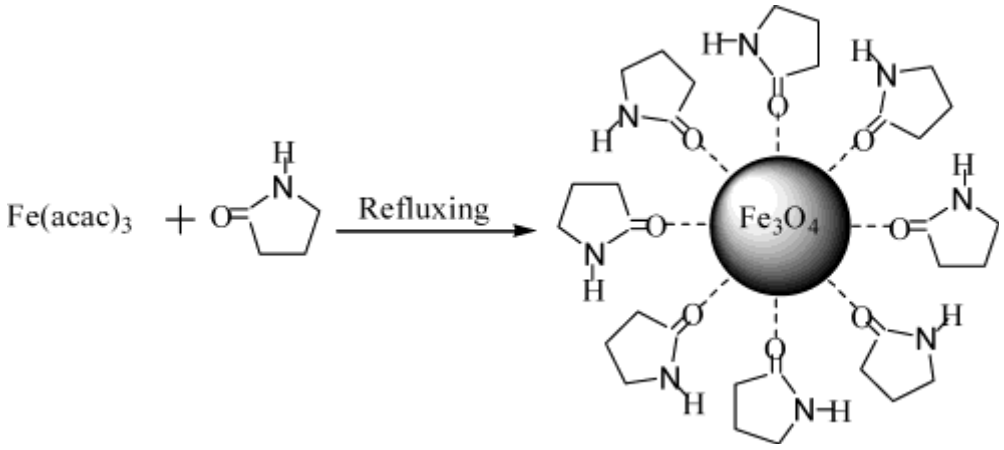

Figure 1.19. Coordination of 2-pyrrolidone with the Fe ions of Fe_3O_4 nanoparticles [128].

Kim et al have also reported one-pot synthesis of water-soluble 5 nm magnetite nanoparticles by the thermal decomposition of $Fe(acac)_3$ in presence of polyvinylpyrrolidone polymeric surfactant [130]. Recently, synthesis of water soluble 6-25 nm magnetite nanoparticles by the decomposition of $Fe(acac)_3$ in liquid polyols e.g. benzyl alcohol (bp 205ºC), diethylene glycol (bp 245ºC), tri ethylene glycol (bp 280ºC) and tetra ethylene glycol (bp 300ºC) have been reported [131-133]. The advantage of this

approach is the possibility to kinetically control of experimental conditions and easily to scale-up.

1.10.4. Hydrothermal Synthesis

Li et al. reported a generalized hydrothermal method for synthesizing a variety of different nanocrystals by a liquid–solid–solution (LSS) reaction [134]. This strategy is based on a general phase transfer and separation mechanism occurring at the interfaces of the liquid, solid, and solution phases present during the synthesis (Figure 1.20). The system consists of metal linoleate (solid), an ethanol–linoleic acid liquid phase (liquid), and a water–ethanol solution (solution) at different reaction temperatures under hydrothermal conditions.

After the aqueous solution of noble metal ions, sodium linoleate (or another sodium stearate) and the mixture of linoleic acid (or another fatty acid) and ethanol were added into the vessel in order. Three phases formed in this system: sodium linoleate (solid), the liquid phase of ethanol and linoleic acid (liquid), and the water–ethanol solution containing noble metal ions (solution). A phase transfer process of the noble metal ions occurred spontaneously across the interface of sodium linoleate (solid) and the water–ethanol solution (solution) based on ion exchange, which led to the formation of noble metal linoleate and the entering of the sodium ions into the aqueous phases. Then at a designated temperature, the ethanol in the liquid and solution phases reduced the noble metal ions at the liquid–solid or solution–solid interfaces. Along with the reduction process, the in-situ generated linoleic acid absorbed on the surface of the noble metal nanocrystals with the alkyl chains on the outside, through which the produced metal

nanocrystals will gain hydrophobic surfaces. A spontaneous phase-separation process then occurred because of the weight of the metal nanocrystals and the incompatibility between the hydrophobic surfaces and their hydrophilic surroundings, and the noble metal nanocrystals can be easily collected at the bottom of the container.

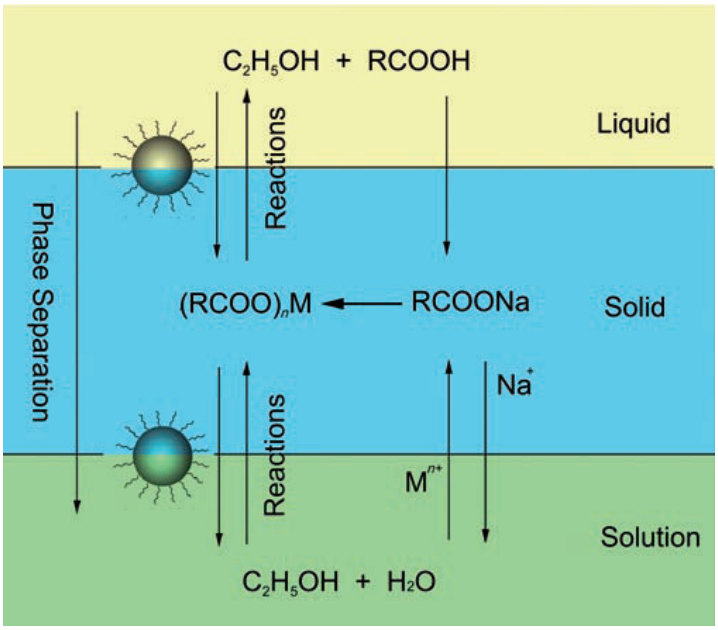

Figure 1.20. Scheme of liquid–solid–solution (LSS) phase transfer synthetic strategy [134].

This LSS phase transfer and separation process can generate nanocrystals with a large variety of nanocrystals such as noble metal, magnetic/dielectric, semiconducting, rare-earth fluorescent, and polymer nanoparticles with different chemistries and properties and with low dispersity [134]. The phase transfer process can occur for nearly all the transitional or main group metal ions, which gives flexibility to the reactions at the interfaces. After the phase transfer process of the metal ions from aqueous solution to the solid phase of $(RCOO)_nM$, under designated reaction conditions, the M^{n+} dehydrates into

oxides (to yield for example, TiO_2, CuO, ZrO_2, SnO_2 or ZnO) and/or composite oxides (to yield for example, MFe_2O_4 (M represents Fe, Co, Mg, Zn or Mn) and $MTiO_3$ (M represents Ba or Sr) through co-precipitation). Li et al. have synthesized ~ 10 nm sized nanocrystals of magnetic spinel MFe_2O_4 through the coprecipitation reactions of Fe^{2+} ions and Fe^{3+}, Co^{2+}, Mg^{2+}, Mn^{2+} and Zn^{2+} ions following this LSS phase transfer and separation method. Li et al. also reported a synthesis of monodisperse, hydrophilic, singlecrystalline ferrite microspheres by hydrothermal reduction [135]. A mixture, consisting of $FeCl_3$, ethylene glycol, sodium acetate, and polyethylene glycol, was stirred vigorously to form a clear solution, then sealed in a Teflon-lined stainless-steel autoclave, and heated to and maintained at 200 ℃ for 8–72 h. In this way, monodisperse ferrite spheres were obtained with tunable sizes in the range of 200–800 nm. In this method, ethylene glycol was used as a high-boiling-point reducing agent, which is known from the polyol process to produce monodisperse metal or metal oxide nanoparticles; sodium acetate as electrostatic stabilizer to prevent particle agglomeration, and polyethylene glycol as a surfactant against particle agglomeration.

The advantages and disadvantages of the four above mentioned synthetic methods are briefly summarized in Table 1.5. In terms of simplicity of the synthesis, co-precipitation is the preferred route. In terms of size and morphology control of the nanoparticles, thermal decomposition seems the best method developed to date. As an alternative, microemulsions can also be used to synthesize monodispersed nanoparticles with various morphologies. However, this method requires a large amount of solvent. Hydrothermal synthesis is a relatively little explored method for the synthesis of magnetic nanoparticles, although it allows the synthesis of high-quality nanoparticles. To date,

thermal decomposition is the best method to prepare high quality magnetic nanoparticles on a large scale.

Table 1.5. Summary comparison of the synthetic methods [4,18].

Synthetic method	Co-precipitation	Microemulsion	Thermal decomposition	Hydrothermal synthesis
Synthesis	very simple, ambient conditions	complicated, ambient conditions	simple, inert atmosphere	complicated, high pressure
Reaction temp.	20–90 ℃	20–50℃	100–330℃	200–220℃
Reaction period	minutes	hours	hours-days	hours ca. days
Solvent	water	organic compound	organic compound	water-ethanol
Surface-capping agents	needed, added during or after reaction	needed, added during reaction	needed, added during reaction	needed, added during reaction
Size distribution	relatively narrow	relatively narrow	very narrow	very narrow
Shape control	not good	good	very good	very good
Yield	high/ scalable	low	high/ scalable	medium
Remarks	Less control over the size, polydispersity and oxidation of magnetite nanoparticles	Surfactants are difficult to remove from the synthesized magnetite nanoparticles	High quality monodispersed magnetite nanoparticles can be synthesized	Require very high pressure which is not safe for longer synthesis of nanoparticles

1.11. References

1. C. Kittel, Introduction to Sol. St. Phys., Wiley, New York, (1976).
2. W.D. Callister, Materials science and engineering, John Wiley, (1985).
3. G.F. Goya, T.S. Berquo, F.C. Fonseca, J Appl. Phys. 94 (2003) 3520.
4. A-H. Lu, E.L. Salabas, F. Schüth, Angew. Chem. Int. Ed. 46 (2007) 1222.
5. D.L. Leslie-Pelecky, R.D. Rieke, Chem. Mater. 8 (1996) 1770.
6. C. Kittel, Phys. Rev., 70 (1946) 965.
7. T. Iwaki, Y. Kakihara, T. Toda, M. Abdullah, K. Okuyama, J. Appl. Phys. 94 (2003) 6807.
8. C.M. Sorensen, Magnetism in Nanoscale Materials in Chemistry (Ed.: K. J. Klabunde), Wiley-Interscience Publication, New York, (2001).
9. M. Ozaki, in Fine Particles: Synthesis, Characterization, and Mechanisms of Growth, Vol. 92 (Ed.: T. Sugimoto), Marcel Dekker, Inc., New York, (2000).
10. S-A. German, PhD thesis, Synthesis, Characterisation and Applications of Iron Oxide Nanoparticles, Materials Science and Engineering, KTH, Stockholm, Sweden, (2004).
11. D.J. Craik, Structure and Properties of Magnetic Materials, Pion Limited, London (1971).
12. T. Sato, T. Iijima, M. Sekin, N. Inagaki, J. Magn. Magn. Mater. 65 (1987) 252.
13. J. Popplewell, L. Sakhnini, J. Magn. Magn. Mater. 149 (1995) 72.
14. A.E. Berkowitz, W.J. Schuele, P.J. Flanders, J. Appl. Phys. 39 (1968)1261.
15. J.M.D. Coey, Phys. Rev. Lett. 27 (1971) 1140.

16. M.P. Morales, M. Andres-Verges, S. Veintemillas-Verdaguer, M. I. Montero, C.J. Serna, J. Magn. Magn. Mater. 203 (1999) 146.
17. P. Tartaj, M.P. Morales, T. Gonzalez-Carreno, S. Veintemillas-Verdaguer and C.J. Serna, J. Magn. Magn. Mat. 290-291(2005) 28.
18. A.K. Gupta, M. Gupta, Biomaterials 26 (2005) 3995.
19. S. Mornet, S. Vasseur, F. Grasset, P. Veverka, G. Goglio, A. Demourgues, J. Portier, E. Pollert, E. Duguet, Prog. Solid State Chem. 34 (2006) 237.
20. Q.A. Pankhurst, N.K.T. Thanh, S.K. Jones, J. Dobson, J. Phys. D: Appl. Phys. 42 (2009) 224001.
21. C.C. Berry, A.S.G. Curtis, J. Phys. D: Appl. Phys. 36 (2003) R198.
22. P. Tartaj, M. P. Morales, S. Veintemillas-Verdaguer, T. González-Carren˜o, C. J. Serna J. Phys. D: Appl. Phys. 36 (2003) R182.
23. V.T. DeVita, S. Hellman, S. Rosenberg, Principles and Practice of Oncology. Philadelphia: Lippincott Williams and Wilkins (1997).
24. R.T. Dorr, D. VonHoff, Cancer Chemotherapy Handbook: Appleton & Lange (1994).
25. D. Hanahan, R.A. Weinberg, Cell 100 (2000) 57.
26. A. Jemal, R. Siegel, E. Ward, Y. Hao, J. Xu, T. Murray, M.J. Thun, CA Cancer J Clin 58 (2008) 71.
27. American Cancer Society: Information and Resources for Cancer: Breast, Colon, Prostate, Lung. www.cancer.org
28. D.S. Kohane, Biotechnol. Bioeng. 96 (2007) 203.

29. M.W. Dewhirst, L. Prosnitz, D. Thrall, D. Prescott, S. Clegg, C. Charles, J. MacFall, G. Rosner, T. Samulski, E. Gillette, S. LaRue, Semin. Oncol. 24 (1997) 616.
30. J. Qin, S. Laurent, Y.S. Jo, A. Roch, M. Mikhaylova, Z.M. Bhujwalla, R.N. Muller, M. Muhammed, Adv. Mater. 19 (2007) 1874.
31. P. Pradhan, J. Giri, G. Samanta, H.D. Sarma, K.P. Mishra, J. Bellare, R. Banerjee, D. Bahadur, J. Biomed. Mater. Res. Part B: Appl. Biomater. 81B (2007) 12.
32. M. Kawashita, M. Tanaka, T. Kokubo, Y. Inoue, T. Yao, S. Hamada, T. Shinjo, Biomaterials 26 (2005) 2231.
33. S. Mornet, S. Vasseur, F. Grasset, E. Duguet, J. Mat. Chem. 14 (2004) 2161.
34. M. Andrés Vergés, R. Costo, A.G. Roca, J.F. Marco, G.F. Goya, C.J. Serna, M.P. Morales, J. Phys. D: Appl. Phys. 41 (2008) 134003.
35. R. Hertg, W. Andrä, C.G. d'Ambly, I. Hilger, W.A. Kaiser, U. Richter, H. G. Schmidt, IEEE Trans. Magn. 34 (1998) 3745.
36. A. Jordan, R. Scholz, P. Wust, H. Fahling, R. Felix, J. Magn. Magn. Mater. 201 (1999) 413.
37. R.B. Campbell, Nanomed. 2 (2007) 649.
38. F. Matsuoka, M.Shinkai, H. Honda, T.Kubo, T.Sugita, T. Kobayashi, Biomagn. Res. Technol. 2 (2004) 3.
39. J. Motoyama, N. Yamashita, T. Morino, M. Tanaka, T. Kobayashi, H. Honda, Biomagn. Res. Technol. 6 (2008) 2.
40. A.K. Silva, E.L. Silva, A.S. Carrico, E.S. Egito, Curr. Pharm. Des. 13 (2007) 1179.
41. K. Engin, Neoplasma. 41(1994) 277.
42. M. Shinkai, J Biosci. Bioeng. 94 (2002) 606.
43. A. Ito, M. Shinkai, H. Honda, T. Kobayashi, J Biosci. Bioeng. 100 (2005) 1.

44. R.K. Gilchrist, R. Medal, W.D. Shorey, R.C. Hanselman, J.C. Parrott, C.B. Taylor, Ann. Surg. 146 (1957) 596.
45. I. Hilger, R. Hergt, W.A. Kaiser, J. Magn. Magn. Mater. 293 (2005) 314.
46. P. Moroz, S.K. Jones, B.N. Gray, Int. J. Hyperthermia. 18 (2002) 267.
47. J.M.C. Bull, Cancer. Res. 44 (1984) 4853.
48. D.L. Johnson, J. Chem. Phys. 7 (1982) 1531.
49. Q.A. Pankhurst, J. Connolly, S.K. Jones, J. Dobson J. Phys. D: Appl. Phys. 36 (2003) R167.
50. R.E. Rosensweig, J. Magn. Magn. Mater. 252 (2002) 370.
51. Y. Lv, Z.Deng, J. Liu, IEEE T. Nanobiosci. 4 (2005) 284.
52. B. Batell, A. Ferstl, Am. J. Phys. 71(2003) 925.
53. M. Rudin, R.Weissleder, Nat. ReV. Drug Discov. 2 (2003) 123.
54. S. Saini, et al., Gastrointestinal Radiology, 11 (1986) 296.
55. T.J. Meade, A.K. Taylor, S.R. Bull, Curr. Opin. Neurobiol. 13 (2003) 597.
56. J.W.M. Bulte, D.L. Kraitchman, NMR Biomed. 17 (2004) 484.
57. M.G. Harisinghani, K.S. Jhaveri, R. Weissleder, W. Schima, S. Saini, P.F. Hahn, P.R. Mueller, Clin. Radiol., 56 (2001) 714.
58. M. Babincova, , P. Sourivong, D. Leszczynska, P. Babinec, Medical Hypotheses, 55 (2000) 459.
59. J.W.M. Bulte, S.-C. Zhang, P. Van Gelderen, V. Herynek, E.K. Jordan, I.D. Duncan, J.A. Frank, Proc. Natl. Acad. Sci. U.S.A. 96 (1999) 15256.
60. L. Josephson, C.H. Tung, A. Moore, R. Weissleder, Bioconj. Chem. 10 (1999) 186.

61. H. Lee, E. Lee, D.K. Kim, N.K. Jang, Y.Y. Jeong, S. Jon, J. Am. Chem. Soc. 128 (2006) 7383.

62. Y.W. Jun, Y.M. Huh, J.S. Choi, J.H. Lee, H.T. Song, S. Kim, S. Yoon, K.S. Kim, J.S. Shin, J.S. Suh, J. Cheon, J. Am. Chem. Soc. 127 (2005) 5732.

63. J.H. Lee, Y.M. Huh, Y.W. Jun, J.W. Seo, J.T. Jang, H.T. Song, S. Kim, E.J. Cho, H.G. Yoon, J.S. Suh, J. Cheon, Nat. Med. 13 (2007) 95.

64. S.H. Koenig, K.E. Kellar, Magn. Reson. Med. 34 (1995) 227.

65. Gorbik, P., et al., Cryosynthesis of single-domain magnetite particles. Journal of Surface Investigation: X-ray, Synchrotron and Neutron Techniques, 2 (2008) 142.

66. C. Corot, P. Robert, J.M. Ide´e, M. Port, Adv. Drug Deliv. Rev. 58 (2006) 1471.

67. O. Cle´ment, N. Siauve, C.A. Cue´nod, G. Top. Frija, Magn. Reson. Imaging 9 (1998) 167.

68. P. Reimer, C. Marx, E.J. Rummeny, M. Müller, M. Lentschig, T. Balzer, K.H. Dietl, U. Sulkowski, T. Berns, K. Shamsi, P.E. Peters, J. Magn. Reson. Imaging 7 (1997) 945.

69. S.J. McLachlan, M.R. Morris, M.A. Lucas, R.A. Fisco, M.N. Eakins, D.R. Fowler, R.B. Scheetz, A.Y. Olukotun, J. Magn. Reson. Imaging 4 (1994) 301.

70. G.H. Simon, J. Von Vopelius-Feldt, Y. Fu, J. Schlegel, G. Pinotek, M.F. Wendland, M.H. Chen, H.E. Daldrup-Link, Invest. Radiol. 41 (2006) 45.

71. R. Weissleder, G. Elizondo, J. Wittenberg, A.S. Lee, L. Josephson, T.J. Brady, Radiology 175 (1990) 494.

72. D.E. Sosnovik, and R.Weissleder, Curr. Opin. Biotechnol. 18 (2007) 4.

73. M. Zhao, D.A. Beauregard, L. Loizou, B. Davletov, K.M. Brindle, Nature Med. 7 (2001) 1241.

74. Y. M. Huh, Y.W. Jun, H.T. Song, S. Kim, J.S. Choi, J.H. Lee, S. Yoon, K.S. Kim, J.S. Shin, J.S. Suh, J. Cheon, J. Am. Chem. Soc. 127 (2005) 12387.

75. S.A.Wickline, A.M. Neubauer, P.M.Winter, S.D. Caruthers, G.M. Lanza, J. Magn. Reson. Imaging, 25 (2007) 667.

76. A. Jasanoff, Trends Neurosci., 28 (2005) 120.

77. P.M. Winter, S.D. Caruthers, S.A. Wickline, G.M. Lanza, Curr. Cardiol. Rep., 8 (2006) 65.

78. U.O. Hafeli, Int. J. Pharm. 277 (2004) 19.

79. P. Tartaj, M.P. Morales, T. Gonzalez-Carreno, S. Veintemillas-Verdaguer, C.J. Serna, J. Phys. D: Appl. Phys. 36 (2003) R182.

80. Bacon, B.R., Tavill, A.S. Hemochromatosis: Hepatology. 6 (1986) 142.

81. C. Wilhelm, J.P. Fortin, F.J. Gazeau, Nanosci. Nanotechnol. 7 (2007) 2933.

82. K. Arshady, K.Kono, Smart Nanoparticles in Nanomedicine. The MML Series Volume 8, Kentus Books; London, (2006).

83. A. Curtis, Europhys, News. 34 (2003) 210.

84. J.-H. Park, G. von Maltzahn, L. Zhang, M.P. Schwartz, E. Ruoslahti, S.N. Bhatia, M. J. Sailor, Adv. Mater. 20 (2008) 1630.

85. U. Gaur, S.K. Sahoo, T.K. De, P.C. Ghosh, A Maitra, P.K. Ghosh, Int. J. Pharm.202 (2000) 1.

86. E. Allemann, J.C. Leroux, R. Gurny E. Doelker, Pharm. Res. 10 (1993) 1732.

87. L.M. Lacava, Z.G.M. Lacava, M.F. Da Silva, O. Silva, S.B. Chaves, R.B. Azevedo, F. Pelegrin, C. Gansau, N. Buske, D. Sabolovic, P.C. Morais, Biophys. J. 80 (2001) 2483.

88. T.T. Shen, A. Bogdanov, A. Bogdnaov, K. Poss, T.J. Brady, R. Weisleder, Bioconjugate Chem. 7 (1996) 311.

89. D. Portet, B. Denoit, E. Rump, J.J. Lejeunne P. Jallet, J. Coll. Inter. Sci. 238 (2001) 37.

90. I. Brigger, C. Dubernet, P. Couvreur, Adv. Drug Del. Rev. 54 (2002) 631.

91. S.M. Moghimi, A.C. Hunter, J.C. Murray Pharm.Rev. 53 (2001) 283.

92. R. Gref., Y. Minamitake, M.T. Peracchia, V. Trubetskoy, V. Torchilin, R. Langer, Science 263 (1994) 1600.

93. R.E. Rosensweig, Ferrohydrodynamics, Cambridge University Press, Cambridge, (1985).

94. S. Odenbach, Magnetoviscous Effects in Ferrofluids, Springer: Bremen (2001).

95. G.A. van Ewijk, PhD thesis, Phase behavior of mixtures of magnetic colloids and nonadsorbingv polymer, University of Utrecht (2001).

96. R.M. Cornell, U. Schertmann, The iron oxides: structure, properties, reactions, occurrence and uses, VCH Publishers, Weinheim (2003).

97. R. Weissleder, D.D. Stark, B.L. Engelstad, B.R. Bacon, C.C. Compton, D.L. White, P. Jacobs, J. Lewis, Am. J. Rentgenol. 152 (1989) 167.

98. J.M. Perez, T.O._Loughlin, F.J. Simeone, R. Weissleder, L. Josephson, J. Am. Chem. Soc. 124 (2002) 2856.

99. J.M. Perez, F.J. Simeone, A. Tsourkas, L. Josephson, R. Weissleder, Nano Letter., 4 (2004) 119.

100. J.M. Perez, L. Josephson, T.O._Loughlin, D. Hogemann, R. Weissleder, Nat. Biotechnol. 20 (2002) 816.

101. A.Y. Louie, M.M. Huber, E.T. Ahrens, U. Rothbacher, R.Moats, R.E. Jacobs, S.E. Fraser, T.J. Meade, Nat. Biotechnol. 18 (2000) 321.

102. U. Häfeli, W. Schütt, J. Teller, M. Zborowski, Scientific and Clinical Application of Magnetic Carriers, Plenum, New York, (1997).

103. R.S. Tebble, D.J. Craik, Magnetic Materials, John Wiley & Sons Ltd (1969).

104. D.K. Kim, Y. Zhang, W. Voit, K.V. Rao, M. Muhammed, J. Magn. Magn. Mater. 225 (2001) 30.

105. K.T. Wu, P.C. Kuo, Y.D. Yao, E.H. Tsai, IEEE Trans. Magn. 37 (2001) 2651.

106. G.W. Reimers, S.E. Khalafalla, Preparing magneticfluids by a peptizing method, US Bureau Mines Tech Rep 59 (1972).

107. R.M. Cornell, U. Schertmann, Iron oxides in the laboratory; preparation and characterization, Weinheim: VCH; (1991).

108. F.A. Cotton, G. Wilkinson In: Advanced inorganic chemistry, New York: Wiley Interscience (1988).

109. A. Wooding, M. Kilner, D.B. Lambrick, J. Colloid Int. Sci. 144, 236 (1991).

110. L. Shen, P.E. Laibinis, T.A. Hatton, Langmuir 15 (1999) 447.

111. G.C. Hadjipanayis, R.W. Siegel, Nanophase materials: synthesis, properties and applications NATO ASI Series, Applied Sci., E260 Dordrecht: Kluwer; (1993).

112. B.K. Paul, S.P. Moulik, Curr. Sci. 80 (2001) 990.

113. C.B. Murray, D.J. Norris, M.G. Bawendi, J. Am. Chem. Soc. 115 (1993) 8706.

114. X. Peng, J. Wickham, A.P. Alivisatos, J. Am. Chem. Soc. 120 (1998) 5343.

115. S. O'Brien, L. Brus, C.B. Murray, J. Am. Chem. Soc. 123 (2001) 12085.

116. R. Si, Y.-W. Zhang, L.-P. You, C.-H. Yan, Angew. Chem. Int. Ed. 44 (2005) 3256.

117. R. Si, Y.-W. Zhang, H.-P. Zhou, L.-D. Sun, C.-H. Yan, Chem. Mater. 19 (2007) 18

118. T. Hyeon, S.S. Lee, J. Park, Y. Chung, H.B. Na, J. Am. Chem. Soc. 123 (2001) 12798.

119. J. Park, E. Lee, N.-M. Hwang, M. Kang, S.C. Kim, Y. Hwang, J.-G. Park, H.-J. Noh, J.-Y. Kim, J.-H. Park, T. Hyeon, Angew. Chem. 117 (2005) 2931; Angew. Chem. Int. Ed. 44 (2005) 2872.

120. F.X. Redl, C.T. Black, G.C. Papaefthymiou, R.L. Sandstrom, M. Yin, H. Zeng, C.B. Murray, S.P. O'Brien, J. Am. Chem. Soc. 126 (2004) 14583.

121. A.G. Roca, M.P. Morales, C.J. Serna, IEEE Trans. Mag. 42 (2006) 3025.

122. S. Sun, H. Zeng, J. Am. Chem. Soc. 124 (2002) 8204.

123. S. Sun, H. Zeng, D.B. Robinson, S. Raoux, P.M. Rice, S.X. Wang, G. Li, J. Am. Chem. Soc. 126 (2004) 273.

124. J. Xie, C. Xu, N. Kohler, Y. Hou, S. Sun, Adv. Mater. 19 (2007) 3163.

125. J. Park, K. An, Y. Hwang, J.-G. Park, H.-J. Noh, J.-Y. Kim, J.-H.Park, N.-M. Hwang, T. Hyeon, Nat. Mater. 3 (2004) 891.

126. N.R. Jana, Y. Chen, X. Peng, Chem. Mater. 16 (2004) 3931.

127. V.K. LaMer, R.H. Dinegar, J. Am. Chem. Soc. 1950, 72, 4847.

128. Z. Li, H. Chen, H. Bao, M. Gao, Chem. Mater. 16, (2004) 1391.

129. Z. Li, Q. Sun, M. Gao, Angew. Chem. 117 (2005) 125; Angew. Chem. Int. Ed. 44 (2005) 123.

130. H-L Liu, S.P. Ko, J-H Wu, M-H Jung, J.H. Min, J.H. Lee, B.H. An, Y.K. Kim, J. Magn. Magn. Mater. 310 (2007) e815.

131. N. Pinna, S. Grancharov, P. Beato, P. Bonville, M. Antonietti, M. Niederberger, Chem. Mater. 17 (2005) 3044.

132. W. Cai, J. Wan, J. Colloid Int. Sci. 305 (2007) 366.

133. J. Wan, W. Cai, X. Meng, E. Liu, Chem. Commun., 47 (2007) 5004.

134. X. Wang, J. Zhuang, Q. Peng, Y. Li, Nature, 437 (2005) 121.

135. H. Deng, X. Li, Q. Peng, X. Wang, J. Chen, Y. Li, Angew. Chem. 117 (2005) 2841; Angew. Chem. Int. Ed. 44 (2005) 2782.

CHAPTER 2

Motivation and Work Plan

2.1. Motivation

There are huge demands in biomedical field for the high quality magnetic nanoparticles consisting of following properties:

1. water soluble
2. monodisperse
4. biocompatible
5. superparamagnetic and
6. high saturation magnetization, M_S

Although, ferromagnetic (Fe, Co and Ni) have high M_S however, unstable Fe nanoparticles can be spontaneously oxidized and less reactive Ni and Co nanoparticles are very toxic. And as a consequence Fe, Co and Ni nanoparticles are not suitable for bio-applications. Therefore, iron oxide particularly magnetite (Fe_3O_4) and maghemite (γ-Fe_2O_3) nanoparticles have been commonly used in biomedicine because of their low toxicity and high chemical stability. The major difficulty in the synthesis of ultrafine iron oxide particles is to control the particle size and its distribution at the nanosized scale. This difficulty arises from the fact that the nanoparticles form aggregates and continuously grow to minimize the overall surface free energy. Therefore, the search for facile and flexible synthetic routes which are able to produce iron oxide nanoparticles with the desired size, acceptable size distribution without particle aggregation is of extremely importance to realize the full potential of these materials in biomedicine.

Several synthesis methods including co-precipitation, microemulsion and thermal decomposition methods have been employed to synthesize iron oxide nanoparticles. Among these methods, the thermal decomposition of organometallic compounds has been well accepted as a promising technique which is able to produce high quality monodispersed superparamagnetic iron oxide nanoparticles. The size distribution of iron

oxide nanoparticles should be monodisperse for their better performance in biomedical applications. High quality (high crystallinity, monodispersed, high Ms and phase pure) magnetite nanoparticles can be synthesized by the high temperature thermal decomposition of iron (III) acetylacetonate, $Fe(acac)_3$ in presence of oleic acid and/or oleylamine. However, the obtained magnetite nanoparticles are only suspendable in non-polar (organic) solvent which makes them inappropriate for biomedical applications. Therefore, further surface modifications on these hydrophobic nanoparticles are necessary to optimize their water suspensibility and biocompatibility for *in vivo* applications. Various surface coating materials such as lipids, surfactants, polymers, silica and Au have been attempted to convert the hydrophobic magnetite nanoparticles to be hydrophilic. However, it has been noted that these surface modification procedures are usually very complicated, tedious and time consuming. Moreover, the surface modified magnetite nanoparticles are not preferred for long term applications due to the risk of dissociation of the coating layers, which leads to agglomeration of the nanoparticles. In addition, the use of toxic solvents and chemicals during the surface modifications may reduce the biocompatibility of the surface modified nanoparticles, although iron oxide itself is considered a biocompatible material. Thus, direct one pot synthesis of hydrophilic magnetite nanoparticles is extremely important to realize the full potential of these materials in biomedicine.

In recent years, magnetite nanoparticles have been focused on the simultaneous therapeutic and diagnostic (i.e. theronestic) applications on a large extend. Magnetic hyperthermia based on the magnetite nanoparticles is promising therapy for cancer treatment in which the cancerous organs or tissues are preferentially heated to

temperatures between 42°C and 46°C. The heating helps to shrink tumors by damaging cells or depriving them of substances they need to live. Magnetic resonance imaging (MRI) based on the magnetite nanoparticles has been recognized as one of the best noninvasive imaging modalities in both clinical and research fields. The strong superparamagnetism of magnetite nanoparticles allows the visualization of the target diseased tissue in any plane of body using T2- weighted magnetic resonance imaging.

Magnetite (Fe_3O_4) nanoparticles have received a great deal of attention in the biomedical field in past two decades due to their superparamagnetic behavior, relatively high saturation magnetization (M_S, 92 emu/g for bulk Fe_3O_4), nontoxicity, good chemical stability and excellent biocompatibility. Moreover, thermal decomposition technique has been recognized as one of the best method to prepare high quality monodispersed nanoparticles on a large scale. Therefore, the objective of this project is to develop size controlled hydrophilic magnetite nanoparticles with well controlled sizes and size distributions using the thermal decomposition technique and then characterization of their structure and properties relevant to magnetic hyperthermia and magnetic resonance imaging to evaluate efficacy of the magnetite nanoparticles for a feasible therapeutic and diagnostic applications.

2.2. Plan of Work

In this thesis, we have planned to develop high quality superparamagnetic magnetite nanoparticles by thermal decomposition of organometallic precursors and then to explore

the feasibility of their use in magnetic hyperthermia and as MRI contrast agent. We had planned our work in the following approaches:

A. Preparation and characterizations of hydrophobic magnetite nanoparticles using thermal decomposition technique and study of time, temperature, surfactant and solvent effect to optimize the reaction parameter for obtaining monodispersed superparamagnetic nanoparticles with high saturation magnetization (Ms).
B. Conversion of hydrophobic to hydrophilic nanoparticles and characterization of their structure and properties.
C. Direct one step synthesis of hydrophilic magnetite nanoparticles using polyol based synthesis technique and optimization of the reaction parameter to develop monodispersed superparamagnetic nanoparticles with high saturation magnetization (Ms).
D. Direct one step synthesis of hydrophilic magnetite nanoclusters with high saturation magnetization (Ms) and then characterizations of their structure and properties.
E. Evaluation of *in vitro b*iocompatibility using normal and cancer cell lines.
F. Evaluation of *in vitro* cellular uptake efficacy using cancer cell lines.
G. Magnetic hyperthermia (Ac magnetic field heating) and MRI relaxivity studies of hydrophilic magnetite nanoparticles *in vitro*.
H. Evaluation of *in vitro* therapeutic efficacy using cancer cell lines.
I. Evaluation of *in vivo* MRI imaging efficacy in animal surface tumor models.
J. Evaluation of localization, retention and bioavailability of hydrophilic nanoparticles *in vivo*.

Work Plan Flow chart

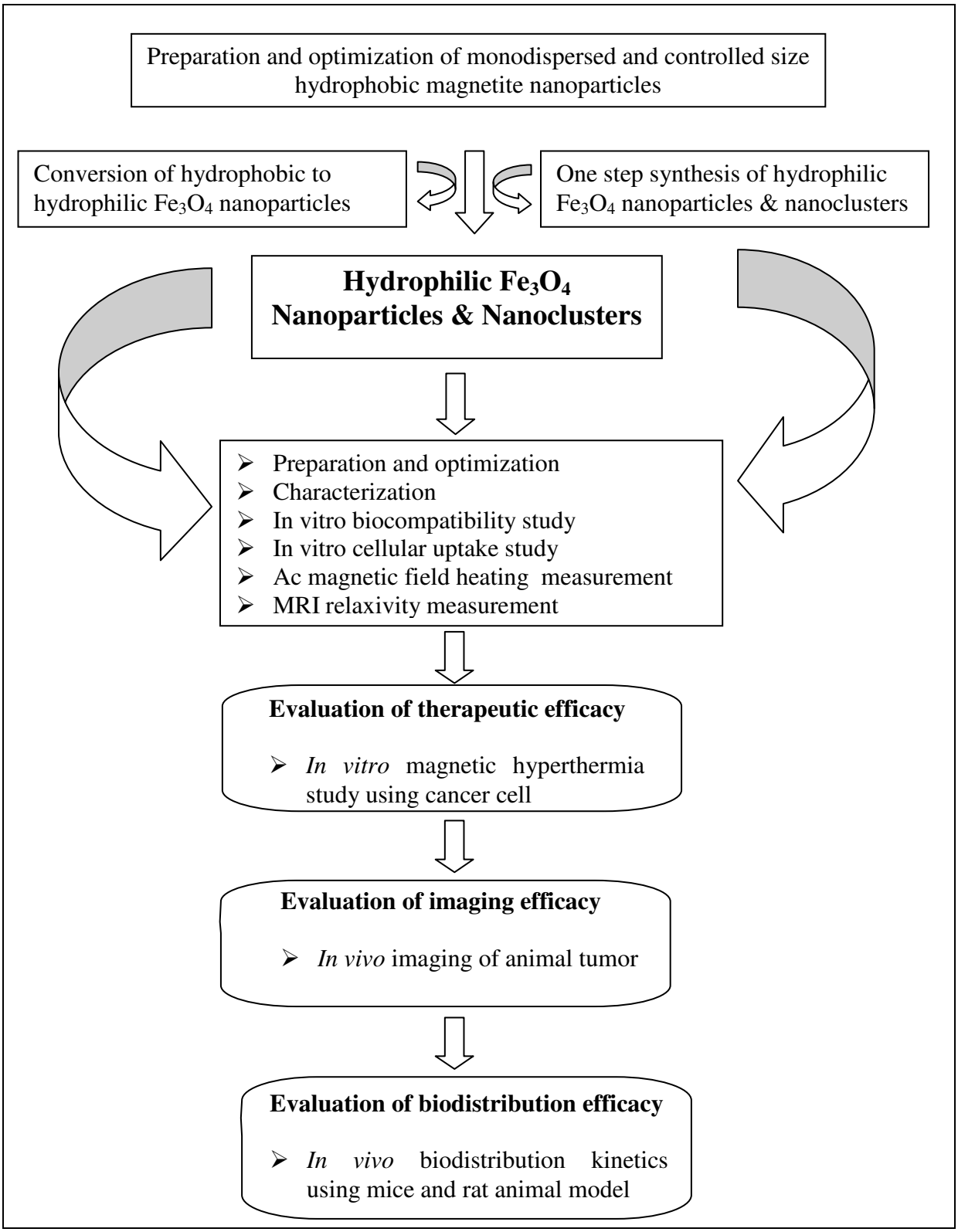

CHAPTER 3

Characterization Techniques

3.1. Characterization Techniques

The as-synthesized magnetite particles were either dispersed in a carrier liquid to obtain ferrofluid suspension (liquid) or dried at 40°C in an oven for overnight to obtain dry powders. Both the powder and ferrofluid samples were characterized using a series of characterization tools or methods to study their structure, morphology, magnetic properties. All the characterization tools are listed in Table 3.1. Cytotoxicity, cellular uptake, AC field induced magnetic hyperthermia and magnetic resonance imaging (MRI) studies of the ferrofluid samples were carried out to evaluate efficacy of the as-prepared nanoparticles for diagnostic and therapeutic applications.

Table 3.1. Instruments used for characterizations

Characterization Tool	**Company and Model**
X- ray diffraction (XRD)	Bruker D8 Advance
Fourier transform infrared spectroscopy (FTIR)	Varian 3100
X-ray photoelectron spectroscopy (XPS)	Kratos AXIS Ultra DLD
Transmission electron microscopy (TEM)	JEOL 2010 and 3010
Thermogravimetric analysis (TGA)	DMSE SDTQ600
Zetasizer	Malvern Nano-ZS
Vibrating sample magnetometer (VSM)	Lakeshore, Model 665
Superconducting quantum interference device (SQUID)	Quantum Design, MPMS XL
Inductively coupled plasma mass spectrometry (ICP-MS)	Agilent ICP-MS 7500 Series

3.1.1. X-ray Diffraction (XRD)

When a beam of monochromated X-ray impinges on a crystal composed of atoms arranged periodically in three dimensions, it will be scattered by the atoms within the crystal. The coherently scattered X-rays, having the same frequency and definite

phase difference, interfere with each other either constructively or destructively. A diffraction pattern is generated when the scattered rays mutually reinforce one another [1].

The principle of X-ray diffraction is governed by the well-known Bragg's Law [2]:

$$n\lambda = 2d \sin\theta \text{ ---------- (3.1)}$$

Where n = order of reflection i.e. an integer corresponding to the order of diffraction plane (n =1 for first order of reflection), λ = wavelength of incident X-ray, d = interplanar spacing i.e. the distance between two diffraction plane and θ = diffraction angle i.e. angle between the incident X-ray and the diffraction plane (Figure 3.1).

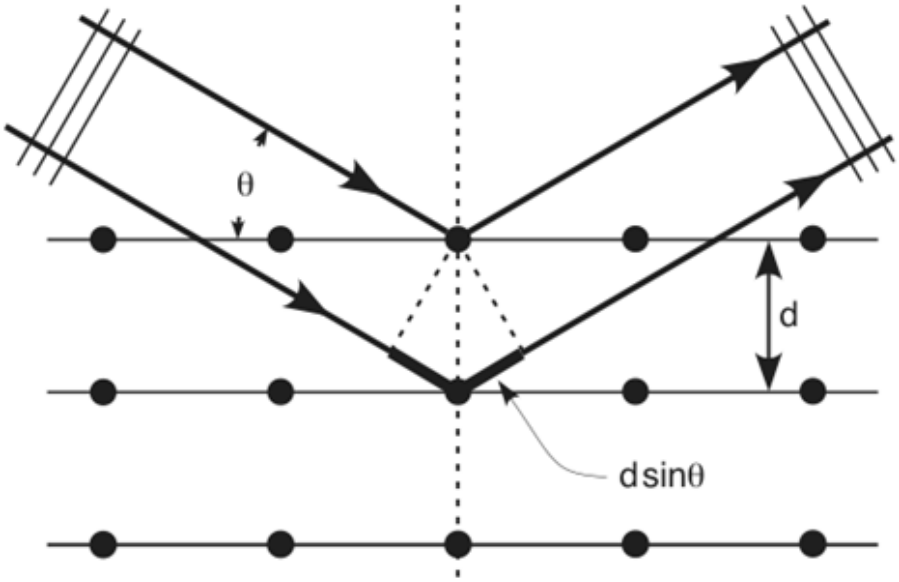

Figure 3.1. Bragg X-ray diffraction.

In this work, X-ray diffraction experiments were performed to identify the crystallographic structure of nanoparticles. XRD patterns of the powder samples were taken using a diffractometer (Bruker AXS Powder, D8 Advance) with Cu-K_α

(λ=1.5418Å) radiation source. The powders of the requisite sample were packed on a glass plate to make the specimens and the surface of the powder was smoothened by pressing another glass plate over it. The x-ray diffraction plot of the samples was taken between $2\theta = 10^0$ and $2\theta = 80^0$.

A computer recorded all intensity versus angle data via an interface and produced a plot. The position of peak, corresponding relative intensities and the interplanar spacing (d) were obtained from the computer. The phase analysis and indexing of the peaks were done by matching the peak positions and relative intensities with standard powder diffraction files (PDF) compiled by the Joined Committee of Powder Diffraction Standards (JCPDS) [3].

The average crystallite size of the powder was determined using Scherrer formula [2]:

$$D_c = \frac{\kappa\lambda}{B\cos\theta} \quad \ldots\ldots\ldots\ldots\ldots \quad (3.2)$$

where D_c = mean crystallite size, κ = particle shape factor (for spherical particles, κ = 0.9), λ= X-ray wavelength (Å), B = peak width measured at half intensity, FWHM (radian) and θ = diffraction angle (degree).

The relative intensity and corresponding two theta values, which were retrieved for each plot from the computer, were replotted and analyzed using graphical (origin) software. The uncorrected FWHM (B) measured from the plot has several components other than broadening due to crystallite size. They were instrumental broadening and broadening due to stress in the crystal. Therefore, the corrected FWHM (B_C) was calculated using the Warren's formula [2]:

$$B_C^2 = B_M^2 - B_S^2 \quad \ldots\ldots\ldots\ldots\ldots \quad (3.2)$$

Where B_M = measured full width at half-maximum intensity, and B_S = peal width of the standard silicon material.

3.1.2. Fourier Transform Infrared Spectroscopy (FTIR)

Molecular bonds vibrate at various frequencies depending upon the elements and the type of bonds. For any given bond, there are several specific frequencies at which it can vibrate. According to quantum mechanics, these frequencies correspond to the ground state (lowest frequencies) and several excited states (higher frequencies). One way to cause the frequency of a molecular vibration to increase is to excite the bond by absorbing light energy. For any given transition between two states the light energy (determined by the wavelength) must exactly equal the energy difference between the two states (usually ground state (E0) and the first excited state (E1)), as shown in the following equation:

$$E_1 - E_0 = \frac{hc}{\lambda} \text{ ……..(3.3)}$$

Where h = Plank's constant, c = speed of light, and λ = the wavelength of light.

The energy corresponding to these transitions between molecular vibration states is generally 1-10 kilocalories/mole that corresponds to the infrared portion of the electromagnetic spectrum. FTIR is a powerful tool for identifying types of chemical bonds (functional groups). The wavelength of light absorbed is characteristic for the chemical bond. By interpreting the infrared absorption spectrum, the chemical bonds in a molecule can be determined.

In infrared spectroscopy, IR radiation is passed through a sample (Figure 3.2). Some of the infrared radiation is absorbed by the sample and some of it is passed through (transmitted). The resulting spectrum represents the molecular absorption and transmission, creating a molecular fingerprint of the sample. Like a fingerprint no two unique molecular structures produce the same infrared spectrum.

In this work, powder samples were characterized FTIR (Varian 3100) to investigate structure of the particles especially to indentify adsorbed coating molecules onto their surface. Samples were prepared by following steps:

(1) First less than 0.1 mg particles were mixed with 25 mg KBr powder (highly transparent substance in IR range) using spatula.

(2) Then the resulting mixture was pounded with a pestle.

(3) Finally a thin pallet was formed under a press.

IR spectra of the samples were recorded on a computerized spectrophotometer (FTIR, Varian 3100) in wave number range of 4000-400 cm^{-1}.

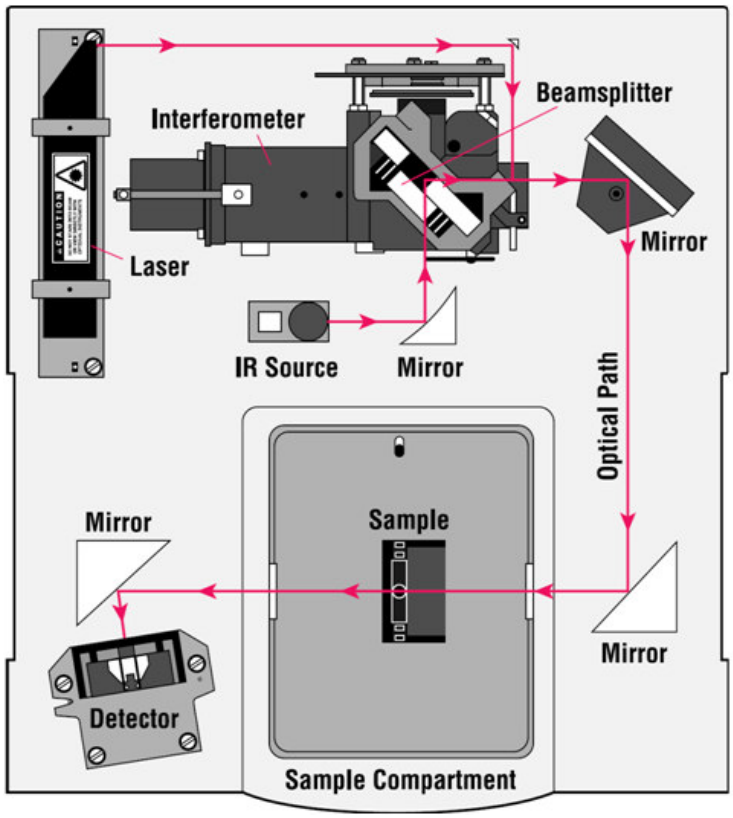

Figure 3.2. A simple FTIR spectrometer layout.

3.1.3. X-ray Photoelectron Spectroscopy (XPS)

X-ray photoelectron spectroscopy (XPS) is a quantitative spectroscopic technique that measures the elemental composition, empirical formula, chemical state and electronic state of the elements that exist within a material. A sample maintained under ultra high vacuum (UHV) is bombarded with X-rays. The X-rays penetrate a substantial distance into the sample and excites electron (referred to as photoelectrons). A small fraction of these photoelectrons (from the top 1 to 10 nm on the surface) escape from the sample. The kinetic energy of these photoelectrons is measured by an analyzer (Figure 3.1).

Because the energy of a particular X-ray wavelength is known, the electron binding energy of each of the emitted electrons can be determined by using an equation:

$$E_{binding} = E_{photon} - E_{kinetic} - \Phi \quad \text{.....(3.4)}$$

where where $E_{binding}$ is the binding energy of the electron, E_{photon} is the energy of the X-ray photons being used, $E_{kinetic}$ is the kinetic energy of the electron as measured by the instrument and Φ is the work function of the spectrometer (not the material).

A typical XPS spectrum is a plot of the number of electrons detected (intensity) (Y-axis, ordinate) versus the binding energy of the electrons detected (X-axis, abscissa). Each element produces a characteristic set of XPS peaks at characteristic binding energy values that directly identify each element that exist in or on the surface of the material being analyzed. These characteristic peaks correspond to the electron configuration of the electrons within the atoms, e.g., 1s, 2s, 2p, 3s, etc. The number of detected electrons in each of the characteristic peaks is directly related to the amount of element within the area (volume) irradiated. To generate atomic percentage values,

each raw XPS signal must be corrected by dividing its signal intensity (number of electrons detected) by a "relative sensitivity factor" (RSF) and normalized over all of the elements detected.

In this work, powder samples were analyzed using XPS (Kratos AXIS Ultra DLD) to investigate adsorbed organic coating on to the surface of the nanoparticles.

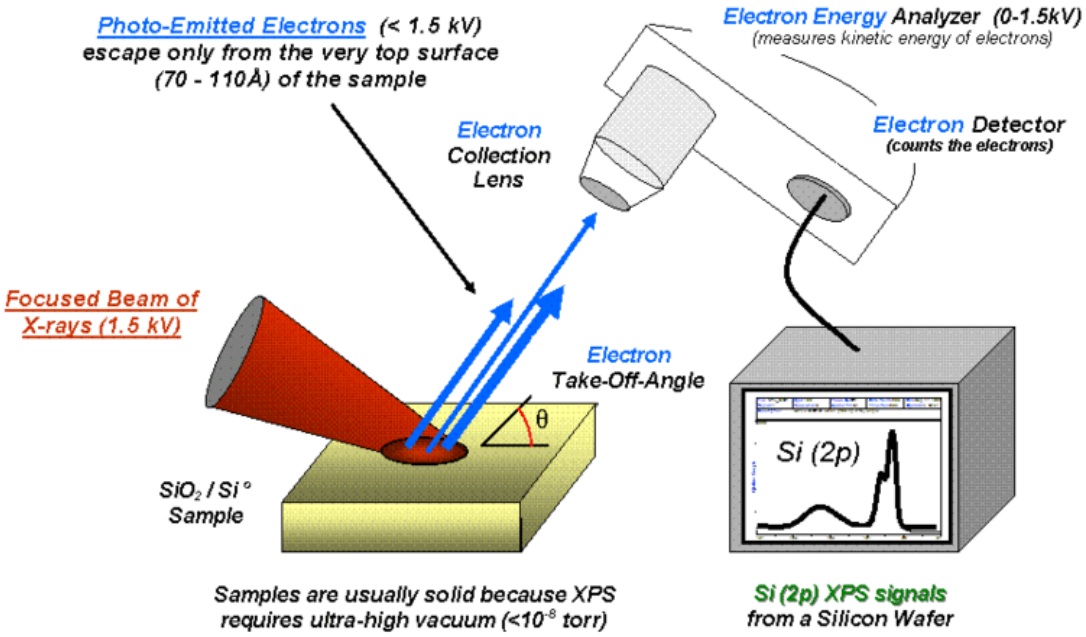

Figure 3.3. Basic components of a monochromatic XPS system.

3.1.4. Transmission Electron Microscopy (TEM)

Transmission electron microscopy (TEM) is a very powerful tool for obtaining morphology and crystallographic information of materials. The main components of a TEM include an electron gun, a condenser lens system, a specimen chamber, objective and intermediate lenses, projector systems for producing images and

diffraction patterns, and vacuum/computer systems. Electron beams with high energy transmitted through the specimen, and an image formed, further magnified and detected by an camera. For the most common types of TEM, the electron energy employed is in the range of 60-300 kV. The appropriate electron energy depends on the nature of the specimen and the information required. Much higher electron energy is suggested if the specimen is relatively thick or very high resolution is required. To satisfy different research interests, three basic appearances of TEM image are taken.

A. Bright field image

In bright field image, only the undeflected electrons contribute to the formation of image. In the absence of a specimen, a bright background is observed. Regions of the specimen that are thicker or of higher density will scatter more strongly (i.e. more electrons will be deflected) and will appear darker image. This technique is suitable for all specimens (amorphous or crystalline, biological or metallic), provided the specimen is thin enough.

B. Dark field image

In dark field image, only the part of the specimen that diffracts electrons contributes to the image. It has the reverse contrast to the bright field image. The background appears dark in the absence of a specimen. To obtain a dark field image with better resolution, the primary electron beam has to be tilted so that the chosen diffracted beam travels along the optical axis and pass through the centered aperture. This technique is suitable to detect the crystalline grains and defects in specimen, which cannot be clearly observed in bright field image.

C. Diffraction image

In diffraction image, only the diffracted rays contribute to the formation of a diffraction pattern in the back focal plane of the objective lens. After applying a selected area only a small area enclosed by the aperture contributes to the diffraction pattern. If a single crystal specimen is oriented such that several sets of planes are parallel to the beam, this will give rise to a diffraction pattern consisting of a regular array of spots. If the specimen contains many crystals of random orientation as in a polycrystalline specimen, then the diffraction pattern is the sum of the individual patterns forming a ring patterns. This technique provides information about the crystal structure and lattice spacing of the samples.

In this work, TEM (JEOL 2010 and 3010, LaB_6) was used to investigate structure, size, morphology, and size distribution of nanoparticles. The microstructure of a single particle was characterized using HRTEM. Samples for TEM were prepared by diluting ferrofluid sample with the additional corresponding carrier fluids (hexane, water etc) to obtain the color of "weak tea." The solutions were cast onto a carbon-coated grid and the carrier fluid was evaporated.

3.1.5. Thermogravimetric Analysis (TGA)

Themogravimetric analysis (TGA) is an analytical method by means of thermal energy to measure the amount and rate of weight change in a material, either as a function of increasing temperature, or isothermally as a function of time, in a controlled atmosphere. This technique can be used to characterize any material that exhibits a weight change due to decomposition, oxidation or dehydration. TGA curves can provide information concerning the thermal stability and the composition of the initial sample, any intermediate compounds formed and the residue.

In this work, TGA (DMSE SDTQ600) was used to determine amount of organic coating adsorbed on to the surface of the nanoparticles and amount of magnetic core (Fe_3O_4) of the nanoparticles. TGA experiments were carried by placing 5-25 mg dry powder samples in a standard alumina pan under N_2 atmosphere and then scanning from room temperature to 800 °C with a heating rate of 20 °C min^{-1}.

3.1.6. Zeta Potential Measurements

A charged particle will move in an applied electric field. The mobility of the particle is related to some exterior factors, such as dielectric constant and viscosity of the suspending liquid. It also depends on the electrical potential at the boundary between the moving particle and the liquid. This boundary is called slip plane and is usually defined as the point where Stern layer and diffuse layer meet. Stern layer consists of ions tightly bound to the particle (Figure 3.4). Diffuse layer consists of free ions that rapidly exchange with ions in Stern layer and it can be visualized as a charged atmosphere surrounding the particle. Stern layer and diffuse layer together are called double layer. The electrical potential at the slip plane is related to the mobility of the particle and is called Zeta potential. It is the measurable potential of a solid surface and is a function of particle surface charge density.

The magnitude of the zeta potential gives an indication of the potential stability of the colloidal system. If all the particles in suspension have a large negative or positive zeta potential then they will tend to repel each other and there will be no tendency for the particles to come together (flocculate). However, if the particles have low zeta potential values then there will be no force to prevent the particles coming together and flocculating. The general dividing line between stable and unstable suspensions is generally taken at either +30 or -30 mV. Particles with zeta potentials more positive

than +30 mV or more negative than -30 mV are normally considered stable. The most important factor that affects zeta potential is **pH**. A zeta potential value on its own without a quoted pH is a virtually meaningless number. A typical plot of zeta potential versus pH is shown in Figure 3.5. The point where the plot passes through zero zeta potential is called the **Isoelectric point** and is very important from a practical consideration. It is normally the point where the colloidal system is least stable.

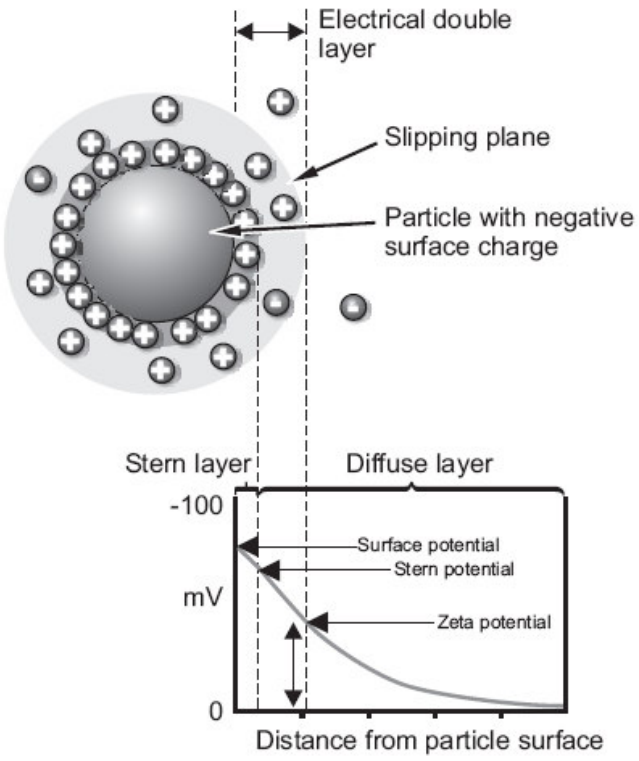

Figure 3.4. Schematic representation of zeta potential.

Zeta potential is derived from measuring the mobility distribution of a colloidal dispersion of charged particles as they are subjected to an electric field. Thus, it is the electrophoretic mobility that we measure directly with the conversion to zeta potential being inferred from theoretical considerations. The technique used to measure the electrophoretic mobility in Malvern's Zetasizer Nano series of instruments is **Laser**

Doppler Velocimetry. The essence of a classical micro-electrophoresis system is a cell with electrodes at either end to which a potential is applied (Figure 3.6). Particles move towards the electrode of opposite charge, their velocity is measured and expressed in unit field strength as their mobility.

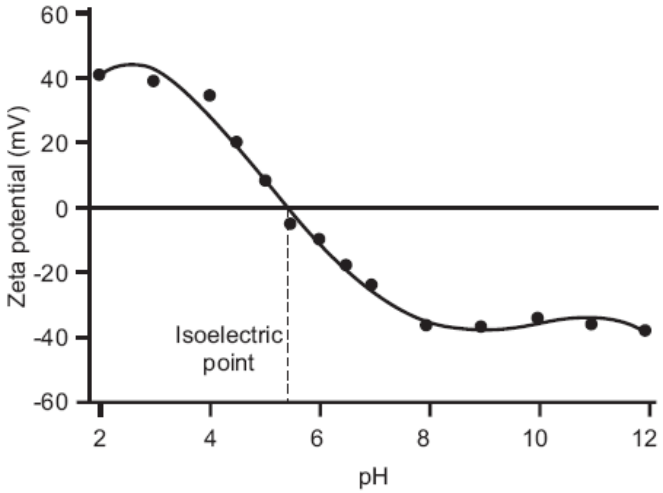

Figure 3.5. Zeta potential vs. pH curve.

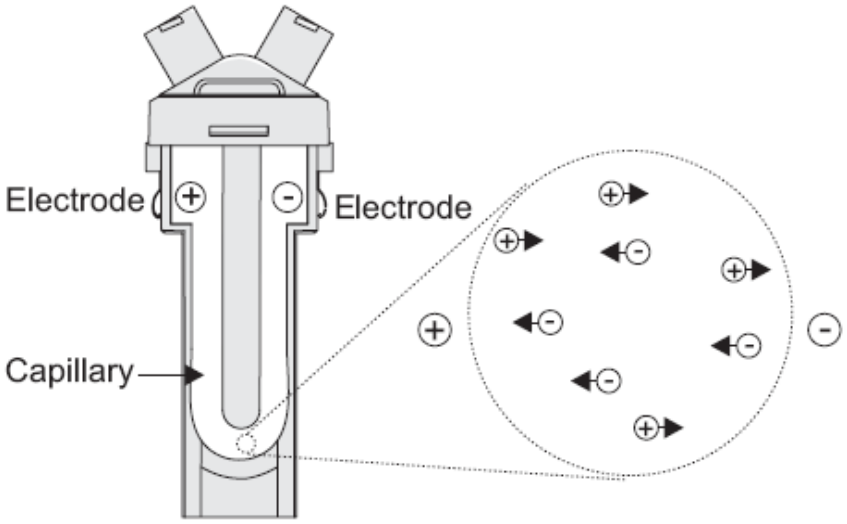

Figure 3.6. Schematic diagram of a sample holder (electrophoretic cell) which is used measure the Zeta potential by Malvern Zetasizer instrument.

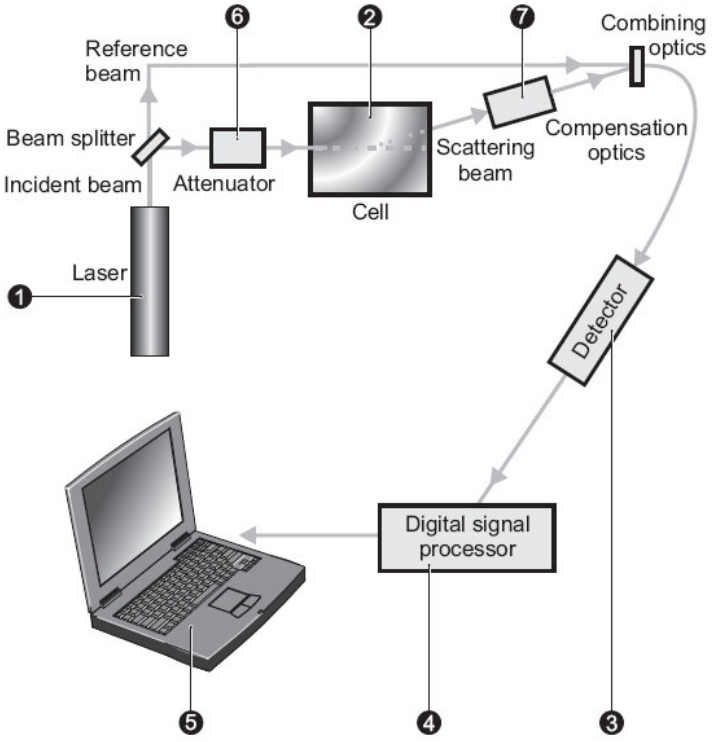

Figure 3.7. Basic components of a Malvern zetasizer instrument.

A zeta potential measurement system comprises of six main components (Figure 3.7). First of all a **laser (1)** is used to provide a light source to illuminate the particles within the sample; for zeta potential measurements this light source is split to provide an incident and reference beam. The reference beam is also 'modulated' to provide the doppler effect necessary. The laser beam passes through the centre of the sample **cell (2)**, and the scattering at an angle of 17° is detected. On insertion of the cell into the cell holder, the cell terminals allow the system to recognise the type of zeta potential cell fitted, and configures the software to use the correct measurement sequence. When an electric field is applied to the cell, any particles moving through the measurement volume will cause the intensity of light detected to fluctuate with a frequency proportional to the particle speed. A **detector (3)** sends this information to a **digital signal processor (4)**. This information is then passed to a **computer (5),**

where the Zetasizer Nano software produces a frequency spectrum from which the electrophoretic mobility and hence the zeta potential information is calculated.

In this work, Zeta potential of diluted ferrofluid samples were measured Zetasizer (Malvern Nano-ZS) to determine surface charge adsorbed on to the surface of the nanoparticles. The samples were prepared by diluting ferrofluid sample with the additional corresponding carrier fluids to obtain the color of "weak tea."

3.1.7. Vibrating Sample Magnetometer (VSM)

Vibrating sample magnetometer (VSM) was used to characterize the magnetic properties of the material. It is based on vibrating a sample in a magnetic field to produce an alternating electromagnetic field in the pickup coils. A schematic diagram of VSM is shown in Figure 3.8. Sample is placed between two electromagnet poles which are attached to pickup coils. The electromagnets produce a high magnetic field (~90 kOe) to saturate the sample. The sample vibrates vertically and the oscillation induces an AC signal (i.e. e.m.f. according to the Faraday's law) in the pickup coils. The amplitude of this signal is proportional to the magnetic moment of the sample. A M-H hysteresis loop is obtained by slowly sweeping the applied field from a maximum positive field, through zero, to a maximum negative field and reversing to the maximum positive field.

In this work, VSM (Lakeshore, Model 665) was used to determine the saturation magnetization (M_S) of the nanoparticles. VSM experiments were carried by placing 10-20 mg dry powder samples (wrapped with aluminum foil) in a VSM sample holder and then scanned from 2T to -2T (Tesla, 1 T = 10^4 Gauss) at the room temperature. A small piece of nickel was used as a standard sample to calibrate the VSM before all the VSM measurements.

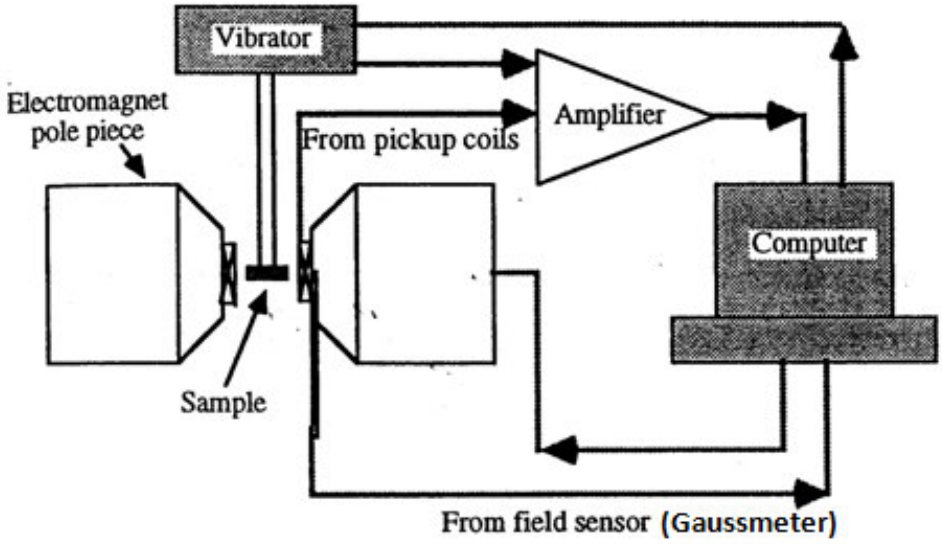

Figure 3.8. Schematic diagram of a VSM.

3.1.8. Superconducting Quantum Interference Devices (SQUID)

Superconducting Quantum Interference Devices (SQUID) is an instrument which converts magnetic flux (which is difficult to measure) into voltage (which is easy to measure). As a result, SQUID magnetometer can be used to detect and measure small magnetic fields. The magnetization can be measured over wide temperature range from that of liquid helium (~4K) up to four hundred degrees.

In this work, SQUID (Quantum Design, MPMS XL) was used to get magnetic information at low temperature. Superparamagnetic characteristics of the nanoparticles were investigated by the zero field cooling (ZFC) and field cooling (FC) procedures. Temperature dependence of magnetization was measured using SQUID between 5 K and 300 K in the applied field of 50-100 Oe.

3.1.9. ICP-MS Analysis

The Fe concentration of the ferrofluid samples (water suspension of Fe_3O_4

nanoparticles) was determined by ICP-MS analysis. A known volume of ferrofluid samples were put in a glass test tube and dried in oven. Then 1-2 ml of concentrated nitric acid was added. The tube was then heated to 110°C for 45 min and the samples were analyzed using ICP-MS (Agilent ICP-MS 7500 Series) after sufficient dilution with milli-Q water. The analysis of sample was done in comparison with the ICP-MS standard (Sigma).

3.1.10. In vitro Cytotoxicity Studies

In vitro biocompatibility of the nanoparticles was evaluated by cytocompatilibility studies with MCF-7 mammalian breast cancer cells (Michigan Cancer Foundation-7) and NIH-3T3 mouse fibroblast cell lines (3-day transfer, inoculum 3 x 10^5 cells) using MTT assay (3-(4,5-Dimethylthiazol-2-yl)-2,5-diphenyltetrazolium bromide). The MCF-7 and NIH-3T3 cells were seeded in 96-well plates (Costar, IL, USA) at the density of 5000 viable cells/well and incubated 24 hours (48 hours in case of NIH-3T3) to allow cell attachment. The MCF-7 and NIH-3T3 cells were incubated for 24 h with media containing nanoparticles at different concentrations. Wells without the nanoparticles treatment were used as control. 10µl of MTT was added into the 96 well plates at five hours prior to the time point. The cells were incubated till the time point. After incubation, the media solution was removed from the wells, leaving the precipitate. Dimethylsulphoxide (100 µl) was added to the wells to dissolve the formazan crystals which were formed. Finally, the absorbance in each well was measured using a microplate reader (GENios, Tecan, Switzerland) at 550 nm. The cell viability was then calculated (n=8) by:

$$\% \text{ Cell viability} = \frac{\text{Absorbance of sample well}}{\text{Absorbance of control well}} \times 100$$

3.1.11. In vitro Cellular Uptake Studies

3.1.11.1. Qualitative Analysis of In Vitro Cellular Uptake

To assess the cellular uptake qualitatively, the MCF-7 cancer cells were grown in 175 cm^2 culture flask at a cell density of 1 x 10^6 cells/ml. After 24 hours, the media was replaced by fresh media containing the nanoparticles with 2 mmol of Fe/L concentration. After 24 hours of incubation, the media was removed; the cells were washed 4 times with PBS (Phosphate buffered saline, Table 3.2), and fixed with 2.5% glutaraldehyde at 37^oC. After 2 hours, the glutaraldehyde solution was removed and the cells were washed with PBS. The cells were then scraped and pelleted at 3500 rpm for 10 minutes. The pellet was post-fixed using 1% Osmium tetroxide at PH 7.4 for 1 hour, followed by washing with PBS two times. The cell pellet was then fixed in 6% gelatin followed by a series of dehydration process using ethanol and acetone. Finally, the cell pellet was embedded in araldite resin. The embedded cell samples were then sectioned into thin films of 100 nm thickness. The sections were stained using lead citrate prior to the observation of the samples using Transmission Electron Microscope (JEOL, JEM- 1220).

Table 3.2: PBS contains the following constituents

Salt	**Concentration (mmol/L)**	**Concentration (g/L)**
NaCl	137	8.00
KCl	2.7	0.20
$Na_2HPO_4 \bullet 2\ H_2O$	8.1	1.44
KH_2PO_4	1.76	0.24
pH	7.4	7.4

3.1.11.2. Quantitative Evaluation of In Vitro Cell Uptake

MCF-7 cancer cells were seeded in 24 well plates (Costar, IL, USA) at a density of 5000 viable cells/well (n = 3). The cells were allowed to grow for 24 hours. The

media in the plates were then replaced by fresh media. To the fresh media 100 µl of the nanoparticles with 43-142 mg of Fe/L concentrations (final concentrations of 4-14 µg of Fe/well) was added. Cancer cells with 100 µl of PBS were used as control. After 24 hours, the media was removed and the plates were washed 4 times with 500µl each of fresh PBS. The cells were then trypsinized and 10 µl of the solution was used to count the number of cells. The cell suspension was centrifuged at 2000 rpm for 5 minutes. 2 ml of concentrated nitric acid was added to the cell pellet followed by heating at 80^{o}C for 1 hour to dissolve the cell pellet and eventually to convert the iron oxide nanoparticles taken up by the cell into the corresponding Fe ions. The resulting solution was diluted using MilliQ water, and then filtered using a 0.45 µm PTFE filter. Finally the filtered solution was analyzed by Inductively Coupled Plasma-Mass Spectrometer (Agilent ICP MS 7500). The cell uptake at different Fe loading was represented in terms of Fe uptake in picogram (pg) per cell.

3.1.12. Magnetic Hyperthermia Studies

AC magnetic field induced heating ability of the as prepared magnetite nanoparticles was determined from the time-dependent calorimetric measurements using a RF generator (EASYHEAT-5060, Ameritherm, Figure 3.9) operating at different frequency (240 & ~400 kHz). Samples were placed in the centre of the water cooled copper tubing coil (Figure 3.9). One milliliter of ferrofluid samples (aqueous suspension of magnetite nanoparticles) with the Fe concentration in the range of 0.5 – 10 mg/ml were subjected to 89 kA/m AC field and time dependent temperature rise was monitored for different times using an optical fibre based temperature probe (FLUOTEMP Series, FTP-LN2). The specific absorption rate (SAR) was calculated

using the following equation [5]:

$$SAR = C\frac{\Delta T}{\Delta t}\frac{1}{m_{Fe}}$$

where C is the specific heat of solvent (here C_{water}= 4.18 J/g °C), $\Delta T/\Delta t$ is the initial slope of the time-dependent temperature curve and m_{Fe} is weight fraction of magnetic element (i.e. Fe) in the sample.

Figure 3.9. Instrument for generating hyperthermia: EasyHeat-5060 (Source: Ameritherm Inc., NY).

In magnetic hyperthermia application, the alternative magnetic field (AMF) causes the heating of magnetic nanoparticles to provide therapeutic effect. However, the AMF could act for non-selective heating of both, cancerous as well as healthy tissue due to generation of eddy currents. The energy (E) absorbed due to eddy current is proportional to the area ($\pi D^2/4$) of the exposed tissue i.e. $E \sim D^2$. Therefore, a strict limitation $H \times f < C$ (f = frequency, H = field amplitude and C = constant) are followed for a particular induced current loop diameter. Hergt and Dutz (2007) have used a coil with a diameter of 0.1 m and found a limit of $H \times f = 5 \times 10^9$ $Am^{-1}S^{-1}$ [90]. In this

work, we have used a coil with a diameter of 0.034 m (for 240 kHz) and 0.032 m (for ~400 kHz) which is about 1/3 of the diameter of the coil of Hertz and Dutz and thus we could use a limit of 9 times of that reported by Hertz and Dutz (5×10^9 $Am^{-1}S^{-1}$) i.e. $H \times f = 4.5 \times 10^{10}$ $Am^{-1}S^{-1}$. Therefore, the potentiality of the nanoparticles for the magnetic hyperthermia applications has been evaluated using the combinations of either H = 18 - 134 kA/m & f = 240 or H = 17 - 104 kA/m & f = ~400 kHz i.e. $H \times f = 0.4 – 4.2 \times 10^{10}$ $Am^{-1}S^{-1}$.

3.1.13. In vitro Hyperthermia

For in *vitro* cellular hyperthermia, 1×10^6 exponentially growing MCF-7 cancer cells in DMEM cell culture medium (Dulbecco's Modified Eagle Medium) containing 10% FBS (Fetal bovine serum) and 1 % antibiotic antimycotic solution were taken in 15 ml sterile polypropylene tubes and centrifuged at 1000 rpm for 5 minutes to get cell pellet. Then, the cells were re-suspended in 1 ml DMEM medium containing iron oxide (IO) nanoparticles having 1 mg of total iron (i.e. 1 mg/ml Fe concentration) in 15 ml polypropylene tubes. The tubes were subjected to an initial AC field of 89 kA/m field using the RF generator operating at 240 kHz frequency and temperature rise of the cell suspension was monitored using the optical fibre based temperature probe. After the temperature reached to 45°C, the field was adjusted (by decreasing the field) to maintain about 45°C temperature of the cell suspension for 1 hr magnetic hyperthermia treatment. For comparison, same numbers of cells as above were treated using only the magnetic field (without using nanoparticles) and another with only the IO nanoparticles (without using magnetic field) with 1 mg of Fe/ml concentration. Cells without any treatment were used as control.

After the treatment, the cells were centrifuged and washed with PBS for 2 times. Then, 2×10^4 cells were placed in a 96 well plate in 16 replicates and following 48 hrs of incubation in 5% CO_2 incubator. MTT assay was performed to evaluate the cell viability. For this purpose, the cell culture supernatants were replaced with 100 µl each of fresh medium containing 10 µl of 5 mg/ml MTT each. The plates were then incubated for 5 hours at 37°C. The purple formazan crystals were dissolved in 50% DMF in water solution containing 20% SDS (sodium dodecyl sulphate). Thereafter, the absorbance was measured at 550 nm wavelength in a plate reader. The percentage of cell viability was calculated using the following equation:

$$\text{Cell viability}\,(\%) = \frac{\text{Absorbance from the well treated with IO or magnetic filed or both}}{\text{Absorbance from the well without any treatment}} \times 100$$

3.1.14. MRI Relaxivity Studies

The longitudinal (T1) and transverse (T2 and $T2^*$) relaxation times of ferrofluid samples containing various Fe concentrations were measured at 20°C using a Siemens Symphony 1.5T MRI and a Varian 9.4T MRI scanner with a head coil. Gradient echo images for calculation of T2* were acquired at 4 to 5 echo times (TE) for individual bottles as single 2D coronal slices (FOV: 6.4cm; Matrix: 64x64; Voxel dimensions (VD): 1mm x 1mm x 5mm; repetition time (TR): 1.6s; TE: 5ms to 60ms/; flip angle: 90°). T2 relaxation times were determined from a multi-echo spin-echo sequence of all bottles (32 echoes; TR: 1600 ms; TE: 15–480 ms; FOV: 18cm; Matrix: 256x256; VD: 0.7mm x 0.7mm x 5mm). T1 relaxation times were determined from a saturation recovery experiment using spin-echo images obtained with a number of TRs (7 TRs; TR: 100–6400 ms; TE: 15 ms; FOV: 18cm; Matrix: 256x256; VD: 0.7mm x 0.7mm x

5mm). The T1, T2 and $T2^*$ relaxation time was computed using in-house software (MATLAB V7) by fitting appropriate exponential functions. Based on the T1, T2 and $T2^*$ values, the specific relaxivities (r1, *r*2, and $r2^*$), which are a measure of the induced change of the spin-lattice relaxation rate ($T1^{-1}$), spin-spin relaxation rate ($T2^{-1}$and $T2^{*-1}$) per unit concentration of Fe, were calculated. The T1, T2 and $T2^*$ relaxation times of ferrofluid samples containing various Fe concentrations were also measured using a Varian 9.4T MRI scanner (Palo Alto, CA, USA). The T2 and $T2^*$ were measured using multiple spin echo sequence at TR=10000 ms and TE=5.69 ms while the T1 was measured by using inversion recovery spin echo sequence.

3.1.15. In vivo MRI Imaging

In vivo animal studies were approved by the A*STAR Institutional Animal Care and Use Committee (IACUC). The contrast agent kinetics were studied on healthy Wistar rats (male, weight 320-340 g) under 2% isoflurane anaesthesia using a Varian 9.4T MRI and a 72 mm volume coil. The magnetite nanoparticles were injected at a dosage of 5 mg [Fe]/kg body weight through tail vein. T2-weighted images were acquired every 48 s for 32 min with a fast spin echo sequence (TR/TE = 1000/28 ms, field of view = 8 cm, thickness = 2 mm, intersection gap = 0.3 mm, matrix = 256 x 192, under fat saturation and respiratory trigger; respiration rate = 60 /min). The coronal and axial sections of the whole body of the rat were imaged at different time periods. The SNR (signal to noise ratio) from the liver and kidney and the normalized contrast (%) were calculated and plotted against time.

$$\text{SNR} = \frac{\text{Mean signal from the region of interest}}{\text{Background standard deviation}}$$

$$\text{Normalized contrast (\%)} = \frac{\text{SNR change at any time t}}{\text{SNR at time zero before contrast}} \times 100$$

Xenograft tumor model was developed using severe combined immune deficiency (SCID) mice (female, weight 20 g). MCF-7 cancer cells were injected into the subcutaneous part of the mice near the right flank. The tumor was allowed to develop to a volume of 150-200 mm^3. The tumor-bearing SCID mice were imaged using a Bruker 7T Clinscan MRI. Contrast agent was injected (dosage: 5 mg of [Fe]/ Kg body weight) through tail veins of the mice under 1% isoflurane anesthesia. T2-weighted images were acquired at various time points within 12 hours after injection using fast spin-echo sequence (TR/TE = 1500/36 ms, resolution=100 μm, thickness = 1 mm). ROI (region of interest) was taken from the tumor and the signals were normalized by the signal of a phantom filled with saline. Normalized contrast (%) was calculated as above.

3.2. References

1. E. Lifshin, X-ray Characterization of Materials, Weinheim: Wiley-VCH, (1999).
2. B.D. Cullity, Elements of X-Ray Diffraction, Addison-Wesley Company, Massachusetts, USA (1978).
3. Powder Diffraction File, Inorganic volume, JCPDS, U.S.A. (1987).
4. C.D. Wagner Riggs W.M., Davis L.E. Moulder J.F. and Muilenberg G.E., Handbook of X-ray Photoelectron Spectroscopy, Perkin-Elmer Corporation (1979).
5. I. Hilger, K. Frühauf , W. Andrä, R. Hiergeist, R. Hergt, W.A. Kaiser, Acad. Radiol. 9 (2002) 198.

CHAPTER 4

Synthesis of Hydrophobic Magnetite Nanoparticles

4.1. Introduction

To meet the increasing demand of high quality magnetite nanoparticles for various applications, synthesis of magnetite nanoparticles with fine size and uniform size distribution, high crystallinity and precise composition control has been intensively studied in the last decade. The major difficulty in the synthesis of ultrafine magnetite particles is to control the particle size and its distribution at the nanometric scale. This difficulty arises because during the synthesis, the magnetic nanoparticles form aggregates and continuously grow to minimize the overall surface free energy. Moreover, the saturation magnetization (M_S) value of the nanosized magnetic particles significantly decreases from that of the bulk materials (briefly explained in Chapter 1, Section 1.6.4). Therefore, the search for facile and flexible synthetic routes which are able to produce magnetic nanoparticles with the desired size, acceptable size distribution with high M_S value is of extremely importance to realize the full potential of magnetite nanoparticles for their biomedical applications. Several synthesis procedures like chemical coprecipitation, microemulsion and thermal decomposition method (described in Chapter 1, Section 1.7) have been adopted to achieve this goal. Among these methods, the thermal decomposition of organometallic compounds in a high boiling point organic solvent containing stabilizing surfactant is a very promising technique to produce monodispersed magnetite nanoparticles without particle aggregation [1-5].

The M_S of the magnetic particles depends upon their size and crystallinity which are linearly varied with the reaction temperature and reaction time of the thermal decomposition. Thus, the M_S of the magnetite particles could be are improved using higher reaction temperature and reaction time; however, the size and distribution of the

particles would be affected with the reaction time and temperature. Therefore, synthesizing nanosized magnetite particles with high M_S using higher reaction time and temperature without affecting their size and size distribution is still a big challenge. In this work, we have studied the time, temperature, surfactant and solvent effects on the size, distribution and magnetic properties of Fe_3O_4 nanoparticles prepared by thermal decomposition method. The surfactant or solvent effect has been adopted over the temperature and time effect to produce magnetite nanoparticles with high M_S value while maintaining their size smaller with an acceptable size distribution.

4.2. Experimental

Absolute ethanol, hexane, toluene and tetrahydrofuran (THF) were used without purification. oleylamine (OM, ≥70%), oleic acid (OA, 90%), phenyl ether (PET, 99%), benzyl ether (BET, ≥98%), 1-octadecene (ODE, 90%) and iron(III) acetylacetonate ($Fe(acac)_3$, 97%) were purchased from Sigma-Aldrich. Chemical structure of $Fe(acac)_3$, OM and OA are shown in Figure 4.1.

4.2.1. Synthesis of Hydrophobic Magnetite Nanoparticles

Magnetite nanoparticles were prepared by thermal decomposition of $Fe(acac)_3$ precursor in presence of solvent and surfactant (OA+OM) mixture [6-7]. Our experimental reaction setup for the synthesis of magnetite nanoparticles are shown in Figure 4.2. The magnetite particles are immediately coated with OA and OM surfactant as soon as they nucleated from the decomposition of $Fe(acac)_3$ precursor. The OA and OM are amphiphilic molecules which consist of hydrophilic polar head (–COOH or $–NH_2$) and hydrophobic

nonpolar (CH_3-$(CH_2)_7$-CH=CH-$(CH_2)_7$–) tail (Figure 4.3). The hydrophilic head part reacts with the surface OH groups of Fe_3O_4 particles and thus chemically bonded to the Fe_3O_4 particles while the hydrophobic tail help them to be stabilized in a nonpolar carrier liquids like hydrocarbons (hexane, dodecane etc) to produce oil based ferrofluid suspension (Figure 4.4).

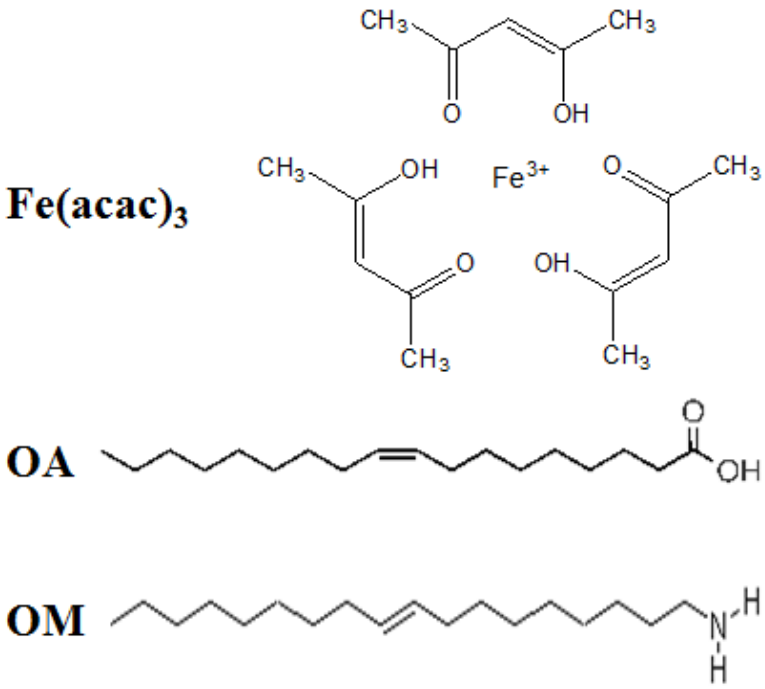

Figure 4.1. Chemical structure of iron(III) acetylacetonate ($Fe(acac)_3$), oleic acid (OA), and oleylamine (OM).

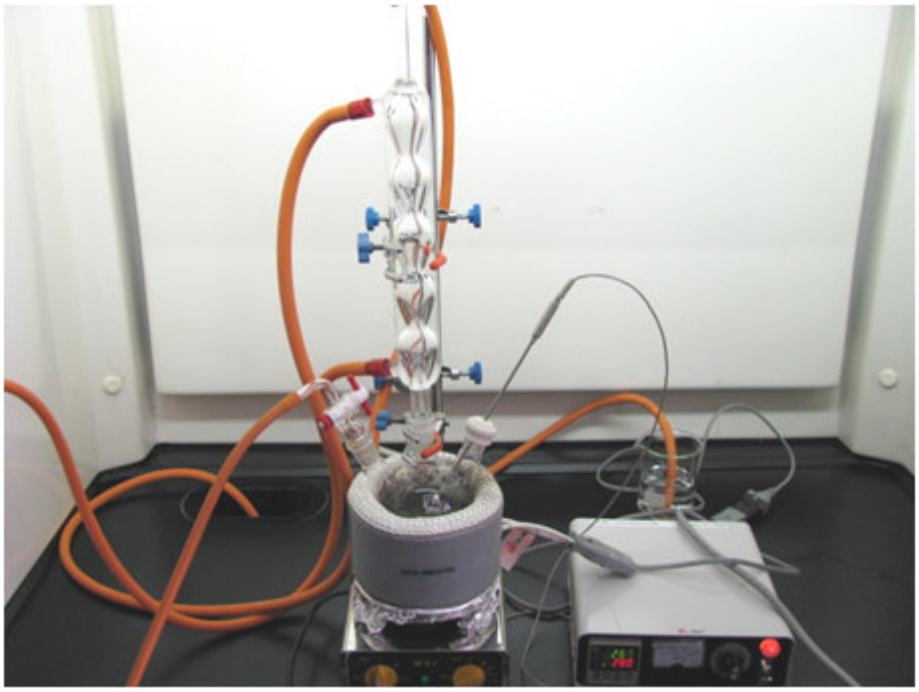

Figure 4.2. Reaction setup for synthesis of magnetite particles using the thermal decomposition method.

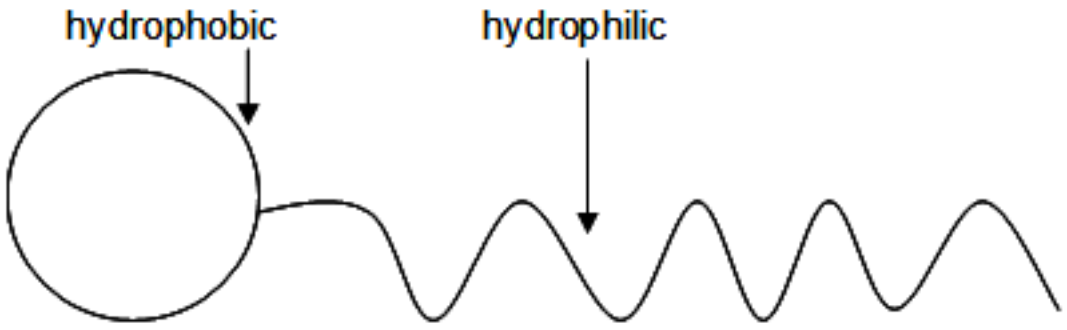

Figure 4.3. Schematic sketch of OA and OM surfactant molecules.

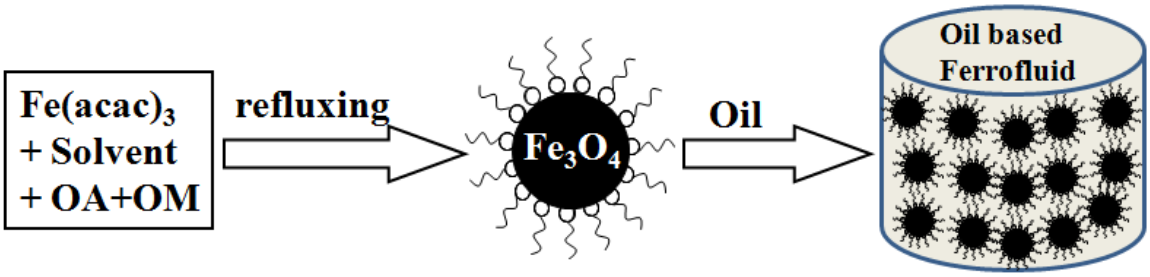

Figure 4.4. Schematic representation of synthesis of hydrophobic magnetite nanoparticles and their ferrofluid suspension.

The flow chart of the synthesis procedure is shown in Figure 4.5. Typically, a 2 mmol (~0.7 g) of $Fe(acac)_3$ was dissolved in a 20 ml solvent and/or surfactant mixture (SSM in Table 4.1) into a three necked round bottom flask (RBF) and the resulting mixture solution was magnetically stirred under a flow of argon. The solution was dehydrated at 120 °C for 1 h, and then quickly heated to a certain temperature (220-330ºC) and kept at this temperature for a certain time (1/2 - 24 h). The resulting black supernatant solution was cooled to room temperature by removing the heat source. A 20 mL of ethanol was added into the supernatant solution and the precipitated particles were collected by centrifugation at 10000 rpm. The precipitated particles were three times washed with ethanol (to remove excess surfactants) followed by the centrifugation. Finally, one half of the washed hydrophobic particles were dispersed in an organic solvent (e.g. hexane, THF, toluene etc) to fabricate ferrofluid and the other half was dried overnight in oven (at 40°C) to obtain dry magnetite powder.

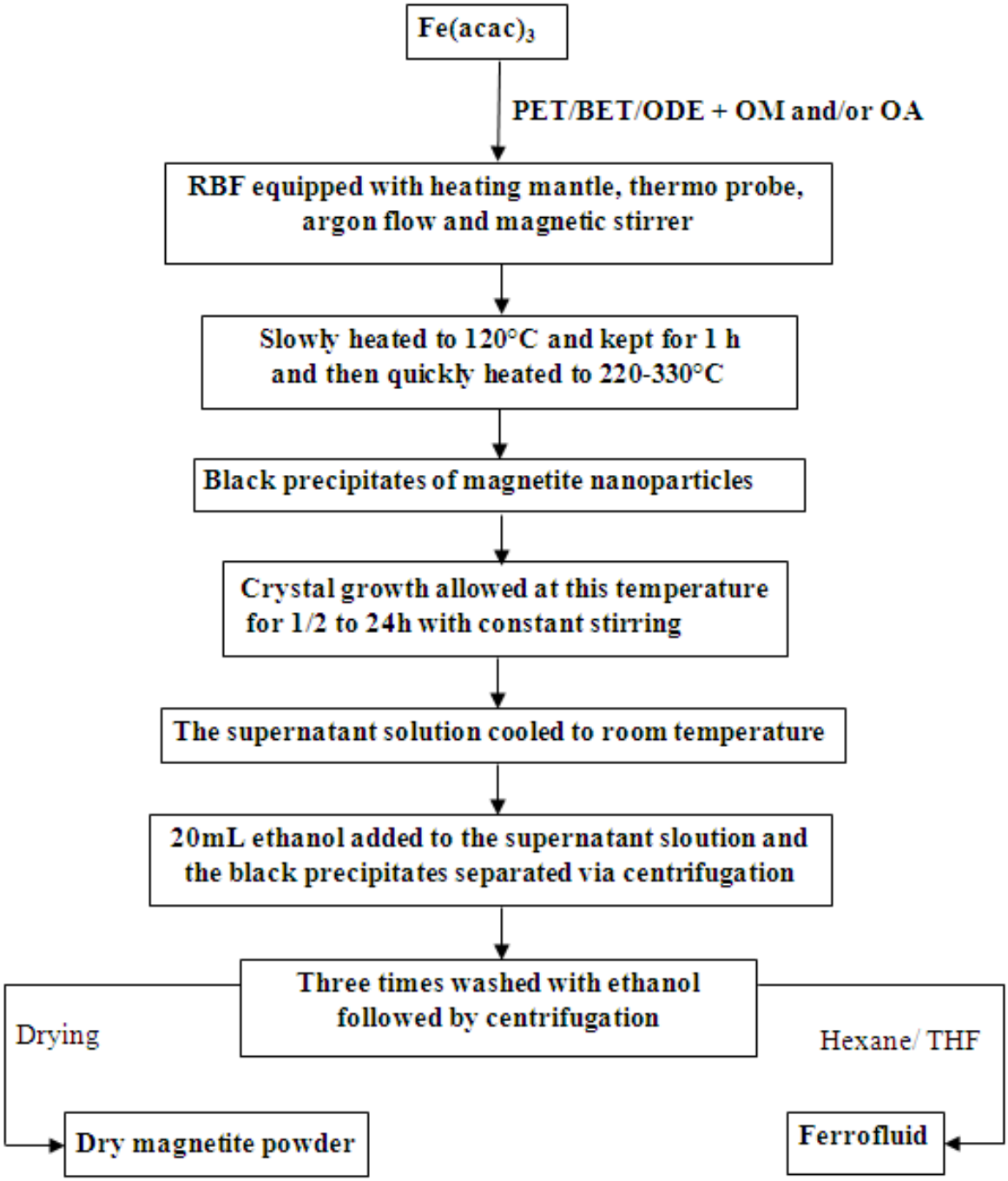

Figure 4.5. Flow chart for synthesis of magnetite nanoparticles by thermal decomposition.

The stability of the as prepared ferrofluid samples were tested by exposing the ferrofluid to a strong permanent magnet and no phase separations of particles were observed on exposure the magnet indicating the formation of stable ferrofluid suspension. The flow of the ferrofluid in presence of a magnet is shown in shown in Figure 4.6. All of the samples prepared using different reaction conditions are given in Table 4.1.

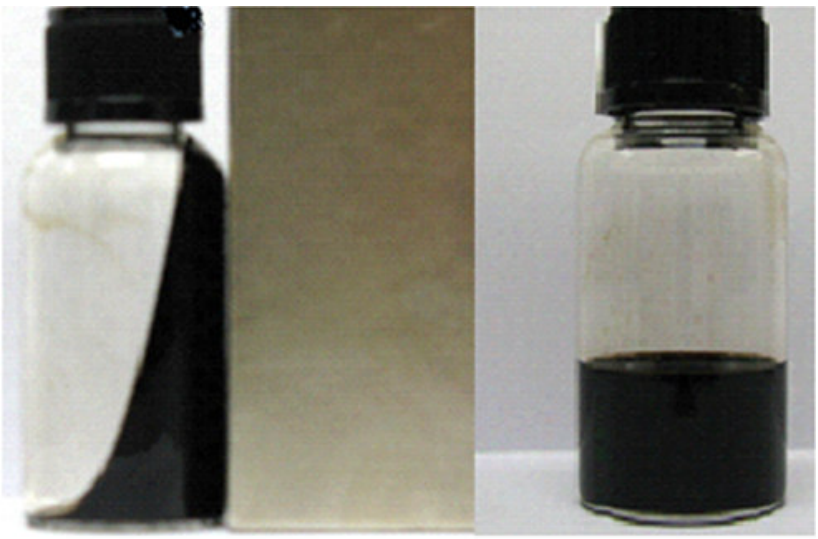

Figure 4.6. Photo of hydrophobic ferrofluid (Right) and flow of the ferrofluid in presence of a permanent magnet (Left).

4.2.2. Characterization of Nanoparticles

The ferrofluid (nanoparticles suspended in hexane) samples were characterized by transmission electron microscopy (TEM, JEOL 2010) while dry powder samples were characterized by X-ray diffraction (XRD, Bruker D8 Advance), Fourier transform infrared spectroscopy (FTIR, Varian 3100), X-ray photoelectron spectra (XPS, Kratos AXIS Ultra DLD), thermogravimetric analysis (TGA, DMSE SDTQ600). superconducting quantum interference device (SQUID, Quantum Design, MPMS XL)

and vibrating sample magnetometer (VSM, Lakeshore, Model 665) measurement. Crystal structure of the as-synthesized nanoparticles was identified by XRD while their size and morphology were investigated by TEM. The organic coating adsorbed to the particle surface was determined by FTIR, XPS and TGA measurements. Magnetic properties of the particles were studied using VSM and SQUID measurement.

Table 4.1. Hydrophobic magnetite nanoparticles samples and corresponding results.

Sample code	Preparation condition			Average Particle Size		Size Distribution	M_S (emu/g)	Remarks
	Temp. (ºC)	Time (h)	SSM	XRD (nm)	TEM (nm)			
A1	220	2	BET + OM	4.9	3	narrow	46	Temp. effect
A2	265	2	PET + OM	5.8	5	narrow	51	
A3	300	2	BET + OM	9.4	9	relatively wide	60	
A4	330	2	ODE +OM	14.3	24	very wide	74	
B1	300	1/2	BET + OM	----	7	relatively narrow	57	Time effect
B2	300	4	BET + OM	----	12	very wide	65	
C1	300	1/2	BET + OM + OA	----	6	very narrow	----	Surfactant effect (addition of OA)
C2	300	2		----	8	very narrow	----	
C3	300	4		----	14	very narrow	67	
D1	300	1/2	OM + OA	----	5	narrow	----	Solvent effect (absence of solvent)
D2		2		----	6	narrow	58	
D3		4		----	7	narrow	----	
D4		24		----	11	relatively narrow	71	
D5	330	1/2	OM + OA	----	6	narrow	----	
D6		2		----	7	relatively narrow	----	
D7		4		----	9	relatively narrow	76	
D8	300	1/2	OM	----	8	narrow	----	
D9		2		----	10	relatively narrow	----	
D10		4		----	10	relatively narrow	65	

4.3. Results and Discussion

4.3.1. Effect of Temperature

To study the effect of reaction temperature, the samples A1, A2, A3 and A4 were prepared using different reaction temperature (220, 265, 300 and 330ºC respectively) at

2h of reaction time (Table 4.1). Figure 4.7 (a), (b), (c) and (d) are the XRD patterns of the A1, A2, A3 and A4 samples, respectively. Position of the diffraction peaks which are assigned to the (111), (220), (311), (222), (400), (422), (511), (440) and (533), match well with the standard XRD data for bulk magnetite (JCPDS file No. 19-0629) and corresponding which indicating the formation of Fe_3O_4 phase. It can be seen that broadness of the peaks decrease with increasing the reaction temperature which could be due to the increase of either the particle size or the crystallinity of the particles. The average crystallite sizes are calculated using Scherrer's equation [8] as 4.9, 5.8, 9.4 and 14.3 nm (Table 4.1). This result demonstrates that the particle size increases with increasing the reaction temperature and the reason for this could be the increase of growth rate with the increase of reaction temperature.

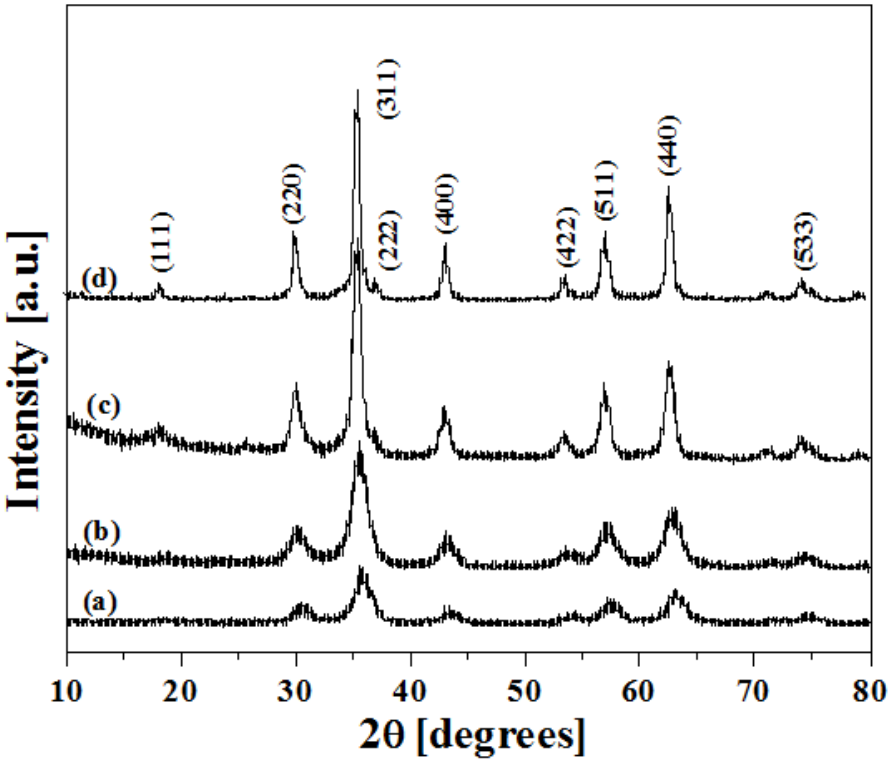

Figure 4.7. XRD patterns of the samples (a) A1, (b) A2, (c) A3 and (d) A4.

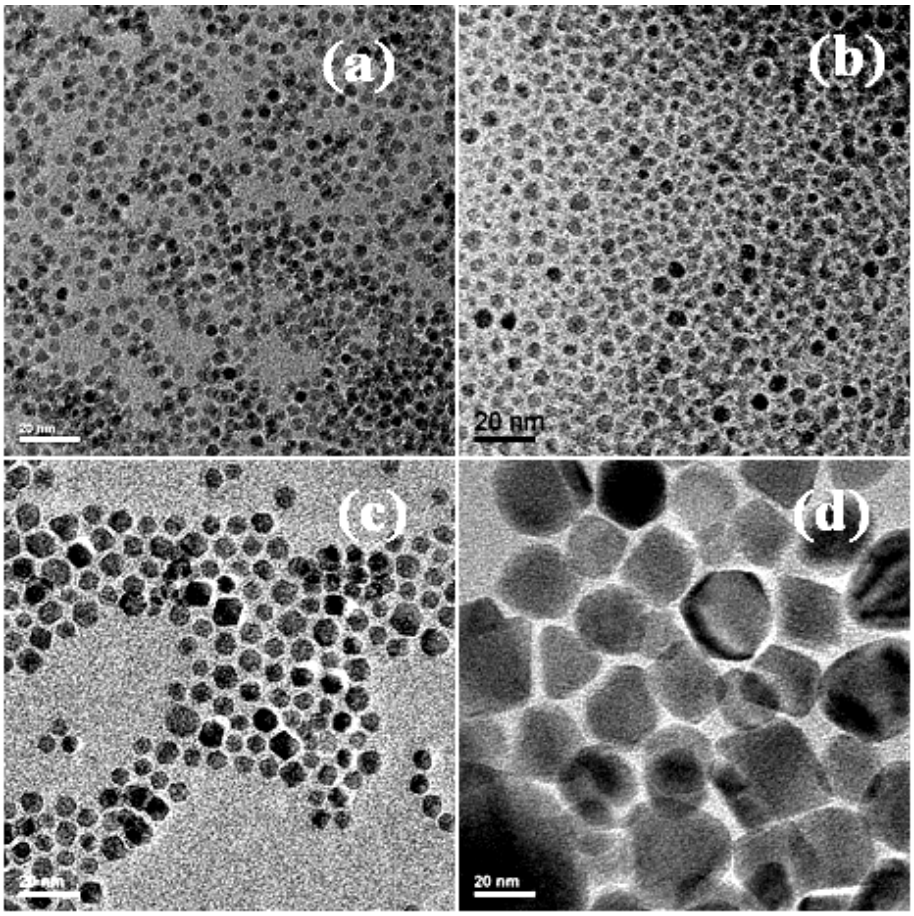

Figure 4.8. TEM images of the samples (a) A1, (b) A2, (c) A3 and (d) A4 (scale bar - 20 nm).

Figure 4.8 (a), (b), (c) and (d) show the TEM images of the A1, A2, A3 and A4 samples, respectively. It can be seen that the size distribution of the magnetite particles prepared at lower reaction temperature such as 220 and 265ºC are quite narrow (Figure 4.8 (a) and (b)). However, the particle size distribution becomes very wide when they prepared at higher reaction temperature such as 300 and 330ºC. The wider particle size distribution indicates that the crystal growth of the nanoparticles at the higher reaction temperature is very much uncontrolled. The average particle sizes are measured from the TEM images are about 3, 5, 9 and 24 nm for the particles prepared using the reaction temperature 220,

265, 300 and 330ºC respectively which further demonstrates that size of the particle increases with the reaction temperature.

Figure 4.9 (a), (b), (c) and (d) depict the magnetization (M-H) curves of the A1, A2, A3 and A4 samples, respectively. It can be seen that the M_S increases from 46 to 74 emu/g with increasing the reaction temperature from 220 to 330ºC. The increase of M_S with increasing the reaction temperature could be due to the increase of either particle size or crystallinity of the particles.

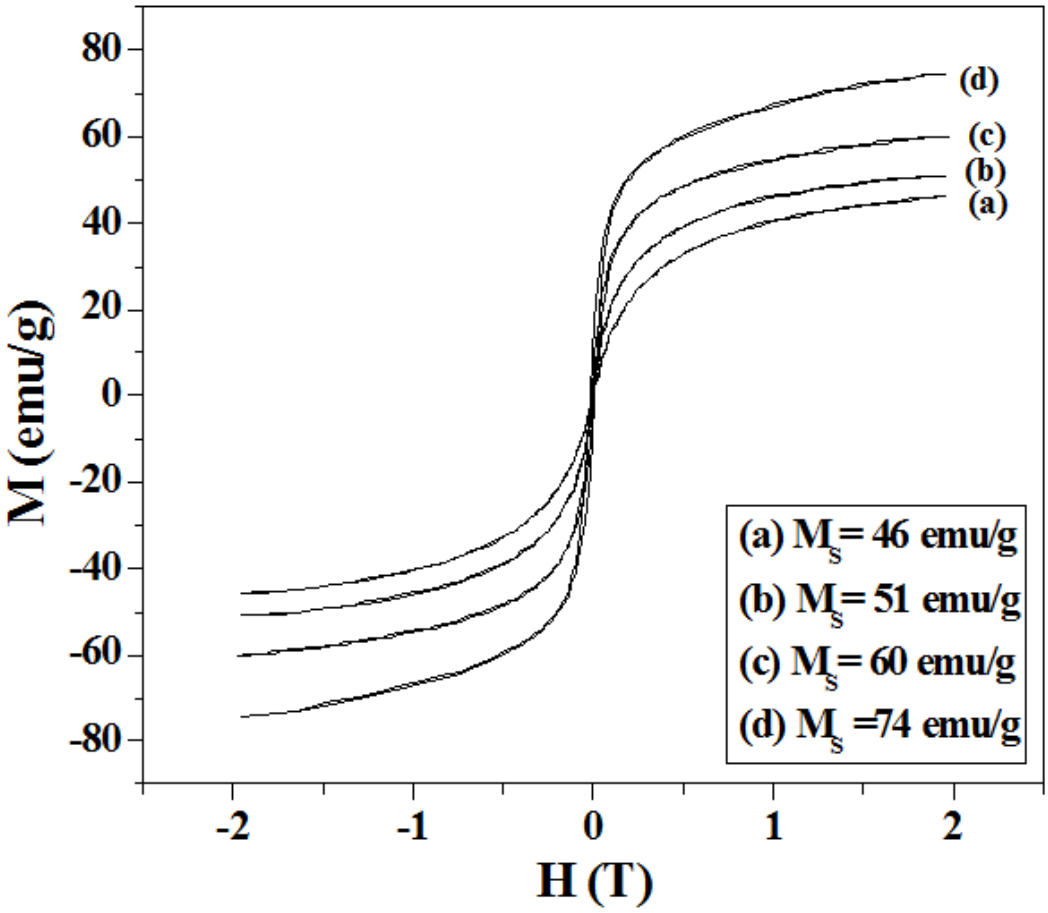

Figure 4.9. Magnetization (M-H) curves of the samples (a) A1, (b) A2, (c) A3 and (d) A4.

4.3.2. Effect of Time

To study the effect of reaction time, the samples B1 and B2 were prepared using different reaction time intervals (1/2 and 4 h respectively) at 300ºC (Table 4.1). Figure 4.10 (a) and (b) show the TEM images of B1 and B2 samples, respectively. It can be seen that average size of the particles again increase from 7 to 12 nm and size distribution of the particles becomes wider with increasing the reaction time from 1/2 to 4 h. This is simply because of the "Ostwald ripening" i.e. small particles becomes smaller and large particle becomes larger with prolonging the reaction time.

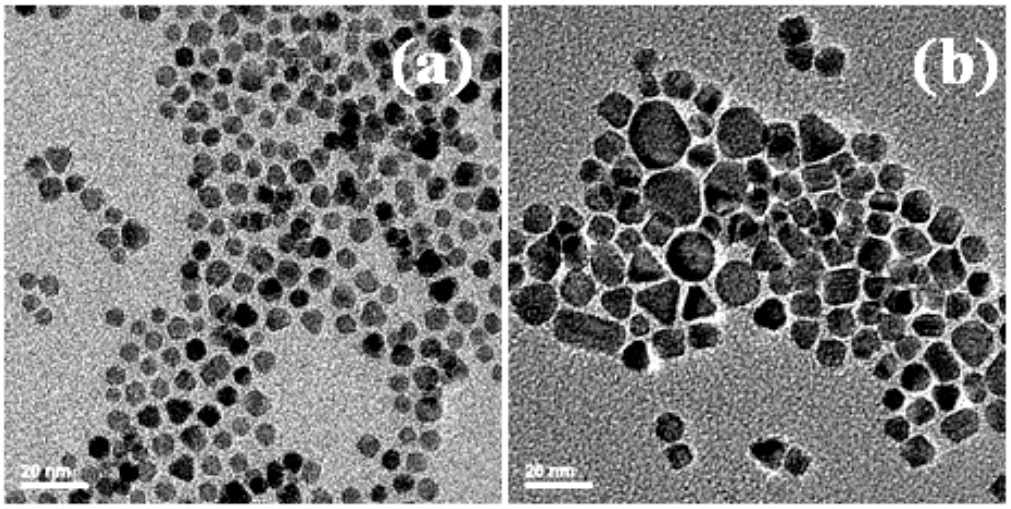

Figure 4.10. TEM images of the samples (a) B1 and (b) B2 (scale bar - 20 nm).

Figure 4.11 (a) and (b) are the M-H curves of the B1 and B2 samples, respectively. The M_S value again increases from 57 to 65 emu/g with increasing the reaction time from 0.5 to 4h. The increase of M_S with increasing the reaction time also could be due to the increase of either particle size or crystallinity of the particles.

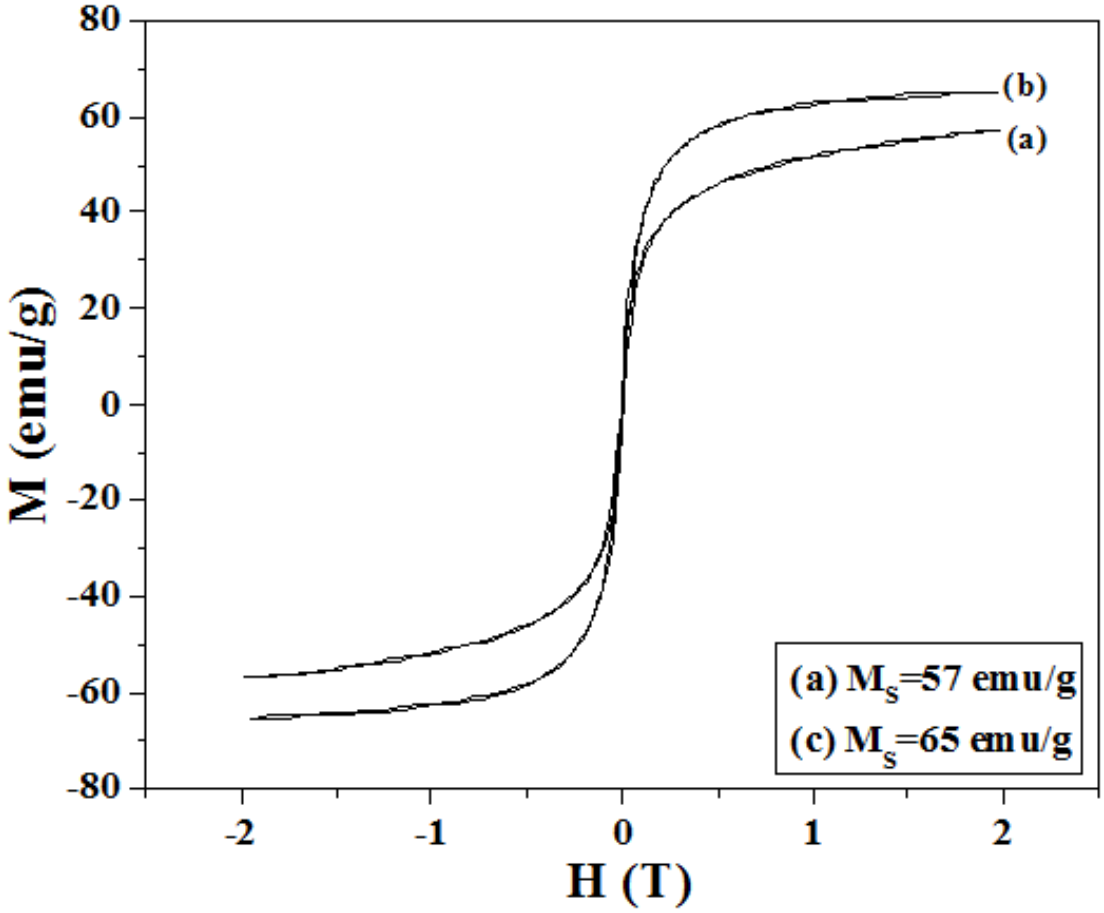

Figure 4.11. Magnetization curves of the samples (a) B1 and (b) B2.

In summary, The M_S of the particles can be increased using higher reaction temperature and longer reaction time during the thermal decomposition of $Fe(acac)_3$. However, the increase in reaction temperature and/or reaction time resulted in unwanted particle size increase and undesirable particle size distribution. Therefore, the surfactant and solvent effect is adopted for controlling the above time and temperature dependent size and dispersity to obtain narrow size distribution magnetite nanoparticles with the desired size and higher M_S value.

4.3.3. Effect of Surfactant

To study the surfactant effect, the samples C1, C2 and C3 were prepared using different reaction time intervals (1/2, 2 and 4 h respectively) at 300ºC mixing one additional surfactant OA to the previous solvent surfactant mixture (SSM) (Table 4.1). Figure 4.12 (a), (b) and (c) depict the TEM images of the C1, C2 and C3 samples, respectively. It can be seen that the particle size distribution is very narrow in presence of OA even at the higher reaction temperature of 300ºC using longer reaction time interval (4h). The narrow size distribution in presence of OA is due to the selective adsorption of coordinating OA surfactant to the particle surface which controls the particles to grow very uniformly (Figure 4.13) [9]. However, average size of the particles increases from 6 to 14 nm with increasing the reaction time from 1/2 to 4h. This indicates that although the size distribution of particles improved in presence of OA but the particles continuously grow with the reaction time. Therefore, the solvent effect is adopted to confine the particles growth with the reaction time.

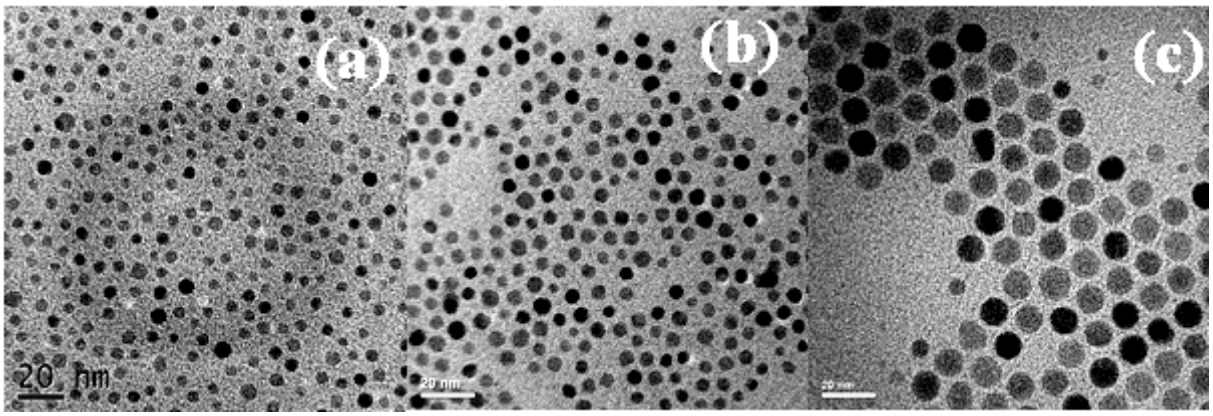

Figure 4.12. TEM images for the samples (a) C1, (b) C2 and (c) C3 (scale bar - 20 nm).

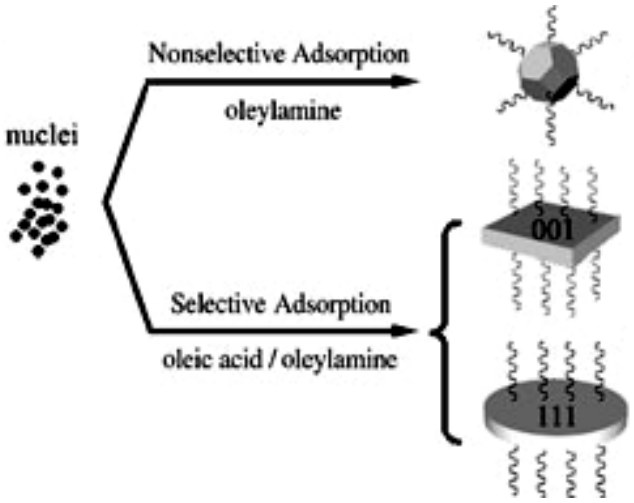

Figure 4.13. Schemetic mechanism for the formation of particle in presence of OA and OM [9].

4.3.4. Effect of Solvent

To study the solvent effect, D1 to D10 samples are prepared varying the reaction temperature (300 to 330ºC) and reaction time interval (1/2 to 24h) removing the solvent from the previous solvent surfactant mixture (SSM) (Table 4.1). Figure 4.14 (a), (b), (c) and (d) show the TEM images of D1, D2, D3 and D4 samples and Figure 4.15 (a), (b) and (c) depict the TEM images of D5, D5 and D7 samples, respectively. It can be seen that the particle size increases from 5 to 11 nm and 6 to 9 nm with increasing the reaction time from 1/2 to 24h and 1/2 to 4h at two different reaction temperature 300 and 330ºC respectively. Thus, the size of the particles increases very slowly with increasing the reaction time if they are decomposed in absence of solvent. The TEM image shown in Figure 4.14 (d), indicates that there is no obvious abnormal crystal growth even when the reaction period is 24 h, suggesting that ‘‘Ostwald ripening’’ does not happen in the reaction system

which does not have solvent. Moreover, the particles prepared in absence of solvent have relatively narrow size distribution even at higher reaction temperature (300 and 330ºC). This indicates that the growth of the particles has been confined in absence of the solvent. The possible reason is that in absence of solvent, the particles are surrounded with very dense stabilizing surfactant environment which restrain the growth of the particles.

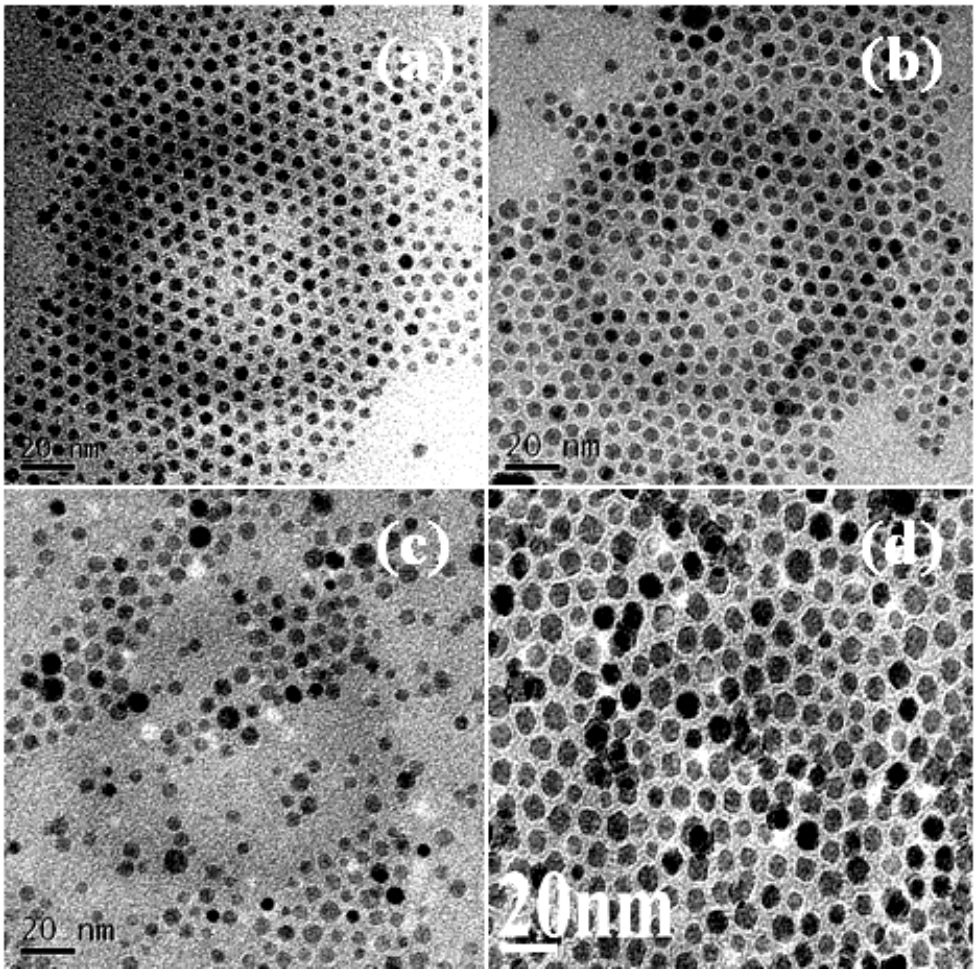

Figure 4.14. TEM images for the samples (a) D1, (b) D2, (c) D3 and (d) D4(scale bar - 20 nm).

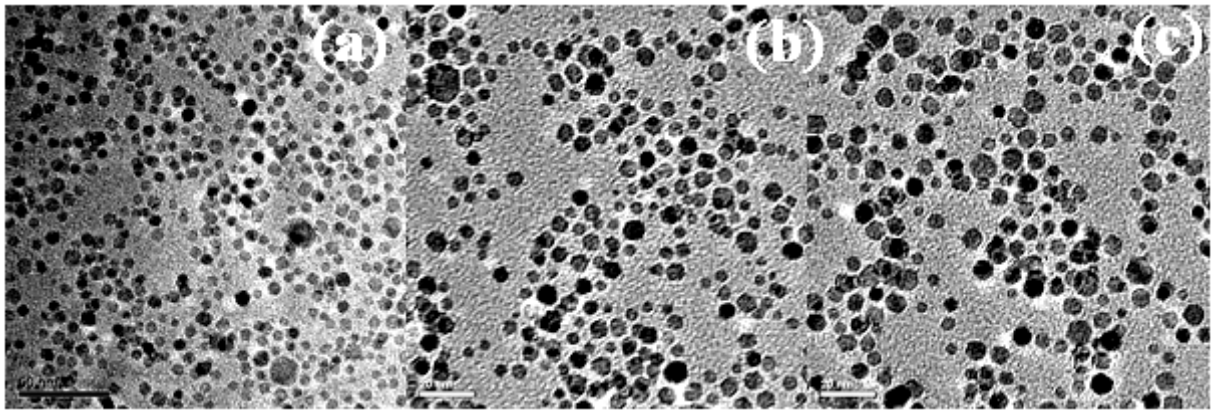

Figure 4.15. TEM images for the samples (a) D5, (b) D6 and (c) D7 (scale bar - 20 nm).

To confirm the solvent effect, we have prepared particles using single OM surfactant. Figure 4.16 (a), (b) and (c) show the TEM images for the samples D8, D9 and D10 which are prepared at 330ºC varying the reaction time interval (1/2 to 4h) removing the OA surfactant from the previous surfactants mixture (OA+OM) (Table 4.1). The particle size increase very slowly from 8 to 10 nm with increasing the reaction time from 1/2 to 4h which also indicating that growth of the particle is confined in the absence of the solvent.

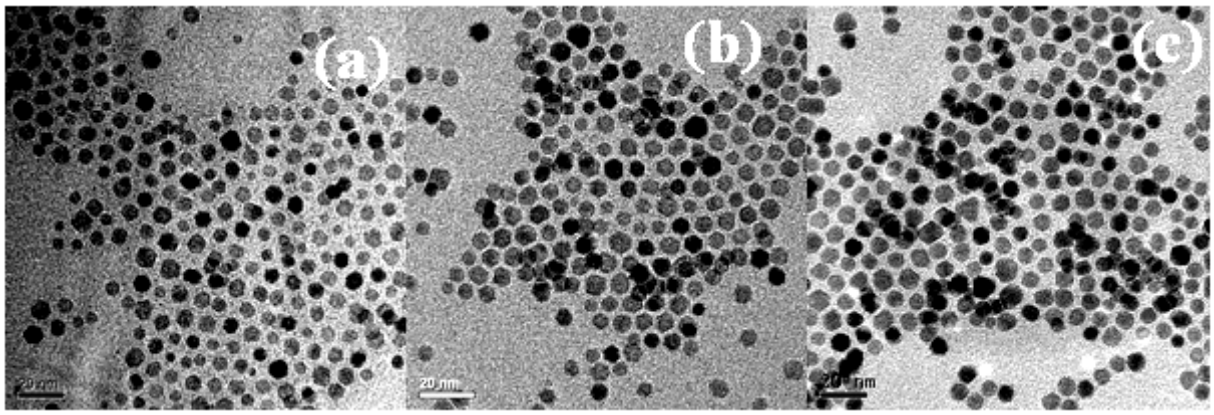

Figure 4.16. TEM images for the samples (a) D8, (b) D9 and (c) D10 (scale bar - 20 nm).

Figure 4.17 A and B show the high resolution TEM (HRTEM) and selected area electron diffraction (SAED) pattern of the D8 samples which was prepared in absence of solvent (in presence of only OM surfactant). It can be seen from the HRTEM image (Figure 4.17 A) that the magnetite nanoparticles prepared by the solvent-free thermal decomposition technique are highly monodispersed. Moreover, the clear lattice fringes and clear diffraction rings which are shown in HRTEM (Figure 4.17A) and SAED (Figure 4.17B) respectively indicate that the as-prepared magnetite nanoparticles are highly crystalline. Each ring represents a set of (hkl) planes which contributes to the electron diffraction. The diffraction rings are attributed to the (220), (311), (400), (422), (511) and (440) planes which further confirms that the as-prepared nanoparticles are of magnetite (Fe_3O_4) phase.

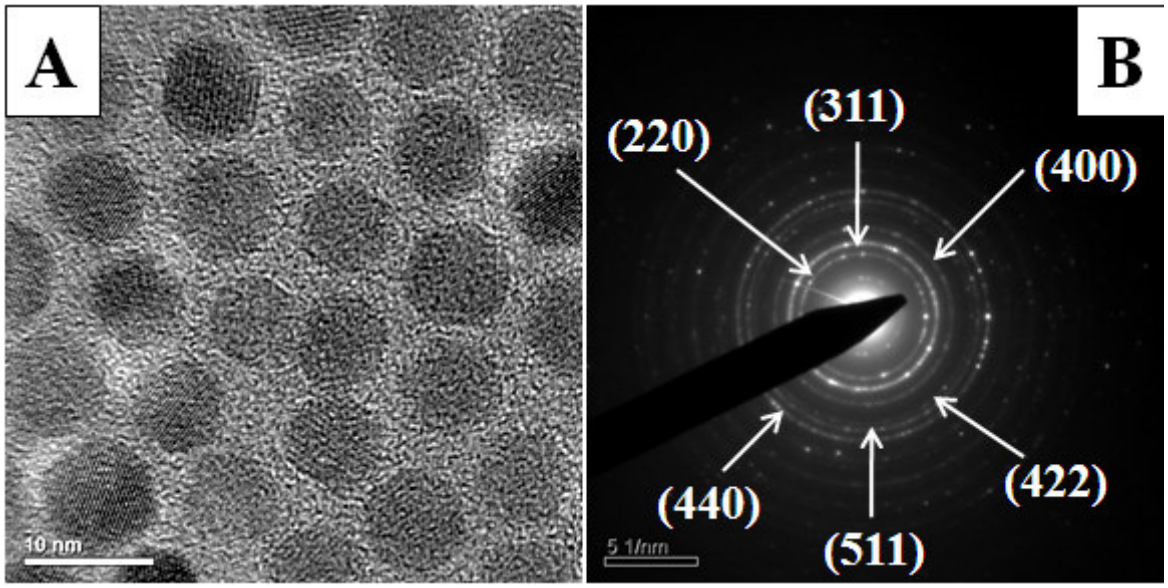

Figure 4.17. A. HRTEM image and **B.** SAED pattern of D8 samples prepared in presence of only OM surfactant.

Figure 4.18 (a), (b), (c), (d) and (e) show the magnetization (M-H) curves for the samples C3, D2, D4, D7 and D10, respectively. It can be seen that in absence of solvent, the M_S value significantly increases with the increase of the reaction temperature and reaction time although the change in particle size is not so significant (Table 4.1). The increase in M_S value could be due to the increase in crystallinity of the magnetite particles which increases with the reaction time and temperature. Zero coercivity (H_c) and zero remanance (M_r) on the M-H curves indicate that the samples prepared in absence of solvent are superparamagnetic (SPM) in nature at the room temperature [10].

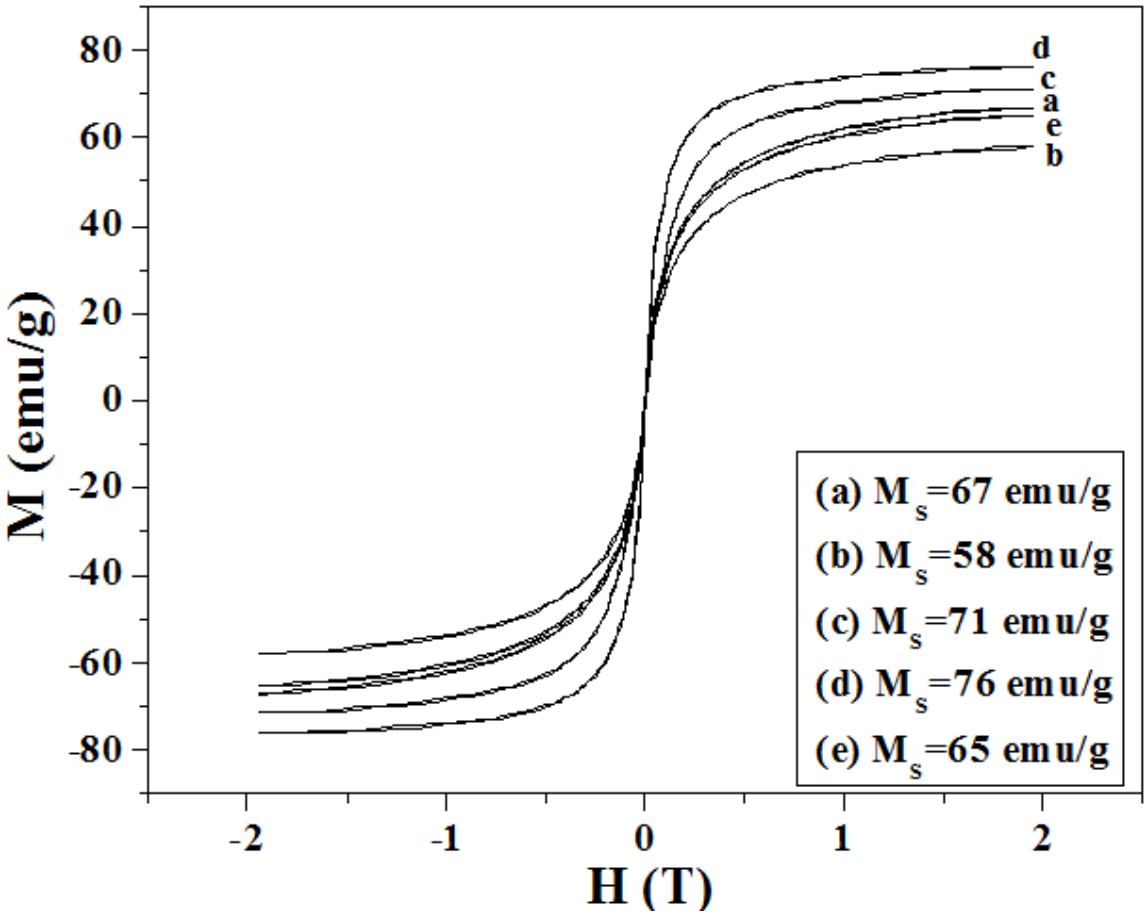

Figure 4.18. M-H curves for the samples (a) C3, (b) D2, (c) D4, (d) D7 and (e) D10.

In summary, the growth of particles is well controlled relatively at lower reaction temperature and for shorter reaction time which results in formation of the smaller size particles with narrow size distribution and lower value of M_S. The M_S of the particles is significantly improved with increasing the reaction time and temperature, however, size distribution of those particles is found to be very wide. The uniform size particles can be synthesized at higher reaction temperature using longer reaction time by adopting the surfactant or solvent effect. The growth of the particles is restricted if the reaction is carried out in absence of the solvent that that carried in presence of OA surfactant. Therefore, magnetite nanoparticles with enhanced M_S can be synthesized by solvent free thermal decomposition reaction using higher reaction temperature and longer reaction time while keeping size of the particles smaller with narrow distribution.

Temperature dependence of magnetization was measured using SQUID between 10 and 300 K in the applied field of 100 Oe. Figure 4.19 shows the zero field cooling (ZFC) and field cooling (FC) curves for the sample D7 with the size of 9nm. The similar feature of the ZFC and FC curves are observed for all the samples (D1 to D10) which also confirms that the particles prepared in absence of solvent are SPM in nature [11]. The ZFC curve reached the maximum at about 100 K, which corresponded to the blocking temperature (T_B) of the sample. Above T_B the sample is superparamagnetic and below is ferromagnetic. The M-H curves of the sample at 300 and 10 K are shown in Figure 4.20. Again, the Zero coercivity and zero remanence indicating that the particles are superparamagnetic at the room temperature (300 K) while the particles exhibit

ferromagnetic behavior at 10K and the observed values of the coercivity and saturation magnetization are about 600 Oe and 83 emu/g, respectively.

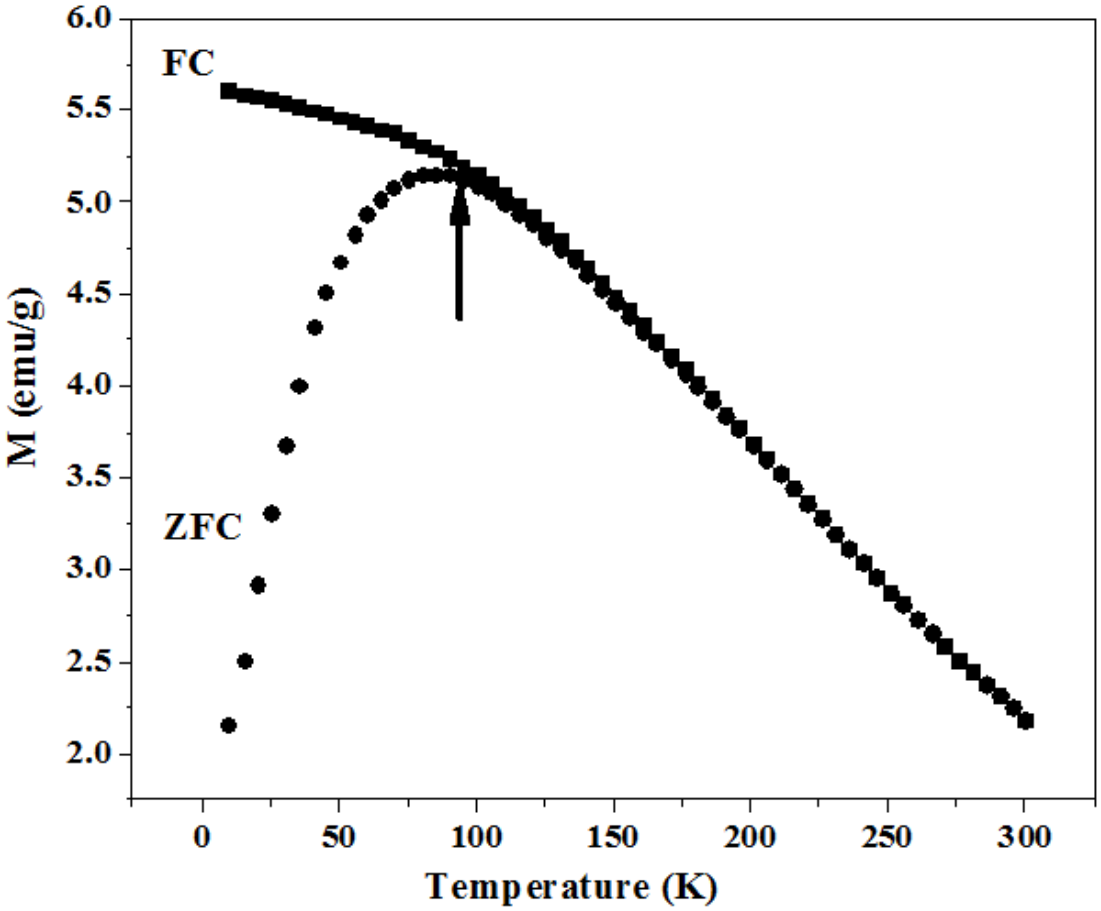

Figure 4.19. ZFC and FC magnetization curves for the sample D7 under an applied field of 100 Oe.

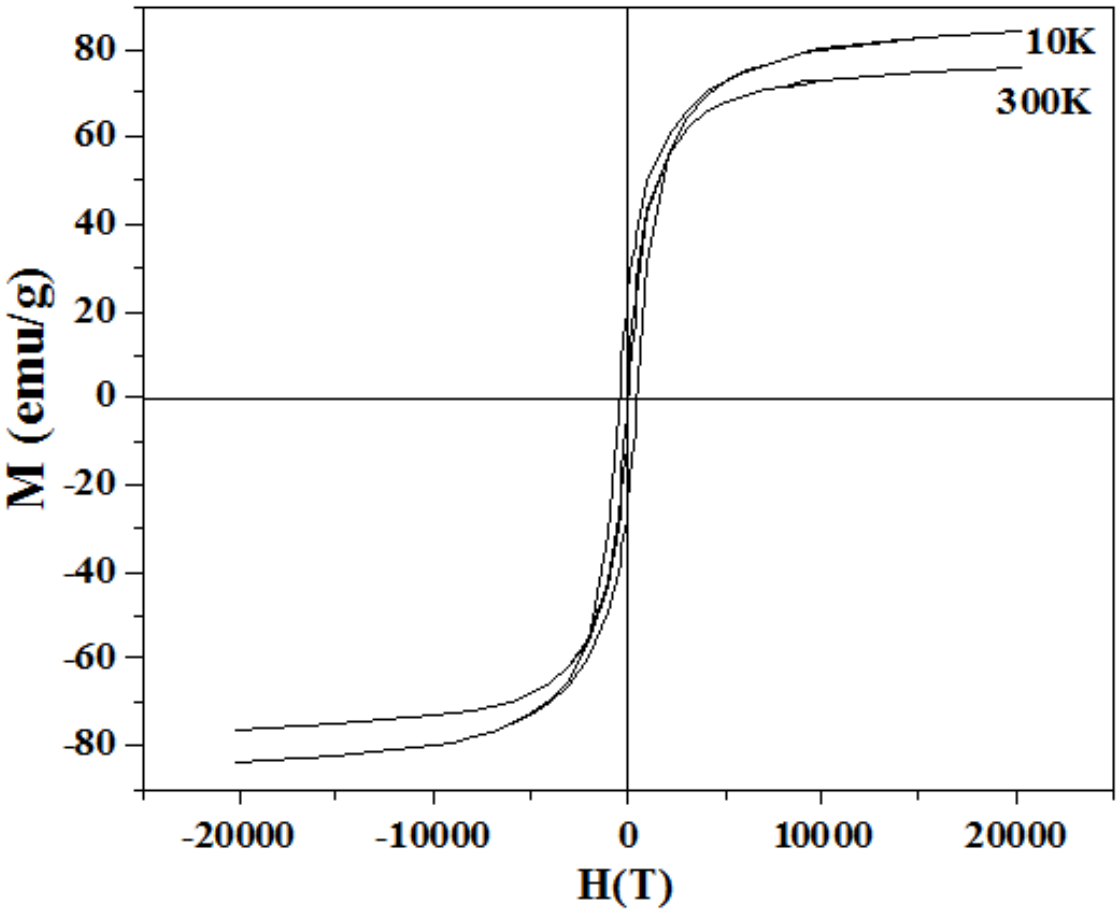

Figure 4.20. SQUID magnetization (M-H) curves measured at 10 and 300 K.

4.3.5. Identification of Organic Coating

The chemically adsorbed organic coating on the particle surfaces were recognized by FT-IR, XPS and TGA measurements. Figure 4.21 (a) and (b) show the FTIR spectra of the D10 and D7 samples which are prepared in OM and OA+OM surfactant media (Table 4.1). The similar FT-IR spectra are observed for the particles prepared in presence of OM and OA+OM surfactant(s) media. The peaks below 800 cm^{-1} belong to the Fe_3O_4 particles

while the peaks (with star marked) above 800 cm^{-1} are due to the OA and OM coating adsorbed to the particle surfaces (Table 4.2) [10, 12-13].

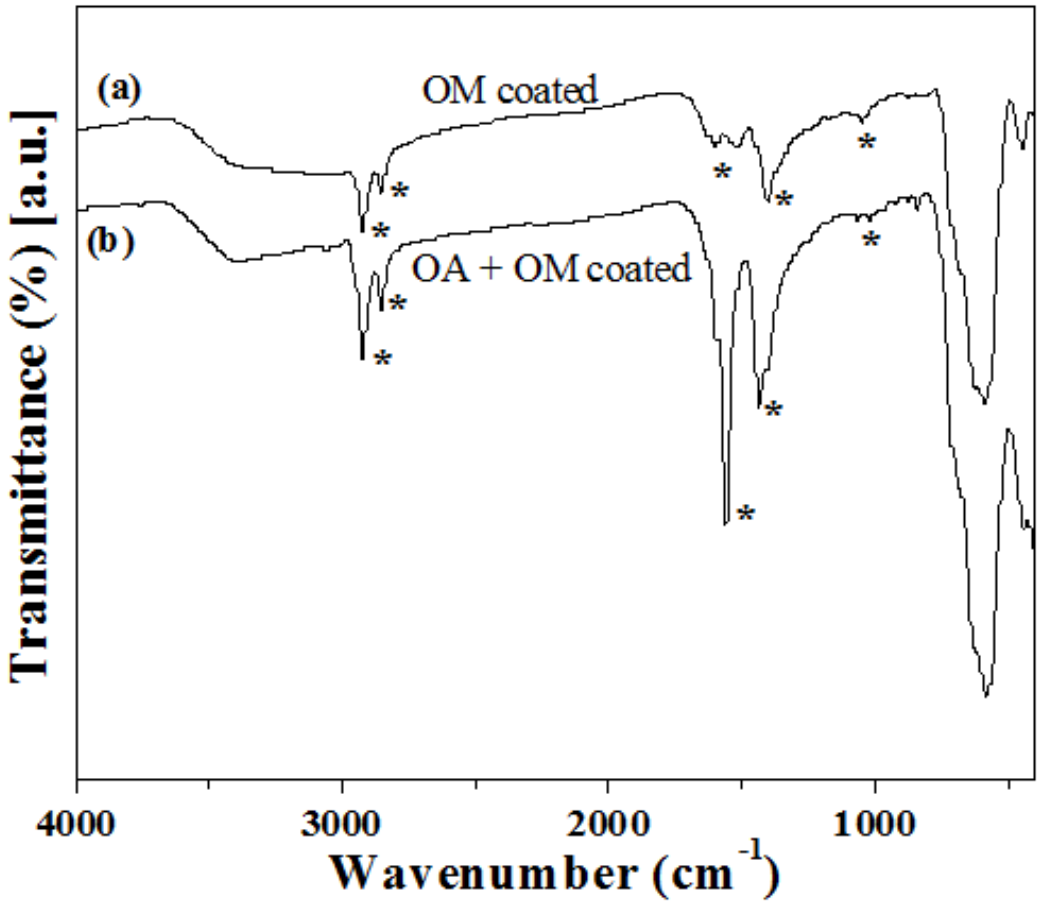

Figure 4.21. FT-IR spectra of (a) OM and (b) OA+OM coated magnetite particles.

The broad band between 3600 and 3000 cm^{-1} centered at 3400 cm^{-1} is assigned for the O–H stretching vibration arises due to the water which is physically adsorbed onto the particle surface. The peaks at about 2924; 2852 cm^{-1} are assigned to the C–H stretching vibration which arises from the particle surface adsorbed OA and/or OM coatings. The peaks at about 1599; 1500 and 1411; 1047 cm−1 are attributed for N–H bending and C–N stretching vibration due to the surface adsorbed OM coating while the peaks at 1562

and 1440 cm^{-1} are assigned to COO^- stretching vibration due to the surface adsorbed OA coating. In addition, the strong absorption peaks at about 585 cm^{-1} is due to the Fe–O stretching vibration of Fe_3O_4 nanoparticles.

Table 4.2. Analysis of FTIR absorption frequencies of the organic coated magnetite nanoparticles [10, 12-13].

Absorption frequencies (cm^{-1}) for		**Remarks** (υ: stretching vibration; δ: bending vibration)
OM coated	OM+OA coated	
3600-3000	3600-3000	υ(O-H) for H_2O
2924 and 2852	2924 and 2852	υ(C-H) for OM and OA
~1599 and ~1500	~1599	δ(N-H) for OM
---	1560 and ~1440	υ(COO^-) for OA
~1411 and ~1047	~1411 and ~1047	υ(C-N) for OM
881	843	δ(C=C) for OM and OA
585, 451	585, 451	υ(Fe–O) for Fe_3O_4

Figure 4.22 A (a) and (b) depict the wide scan XPS spectrum of the D10 and D7 samples which are prepared in OM and OA+OM surfactant media (Table 4.1). The corresponding deconvoluted O(1s) and C(1s) spectrum are shown in Figure 4.22 B and C, respectively. The position of the O(1s) and C(1s) peaks component are shown in Table 4.3. The O(1s) peak at about 531.4, 532.4 and 533.9 eV are assigned for the O–H, C=O and C–O bond, while the C(1s) peak components at about 285.3, 286.6, 288.9 and 289.4 eV are assigned for the C–C/C–H, C-N, C=O and C–O bond, respectively, arising from surface adsorbed OA and OM coatings and water [13-18]. In addition, the Fe($3p_{3/2}$), O(1s), Fe($2p_{3/2}$) and

Fe($2p_{1/2}$) peaks components at around 55.2, 530.2, 710.8 and 724.4 eV are attributed to the Fe-O bonds [13-14].

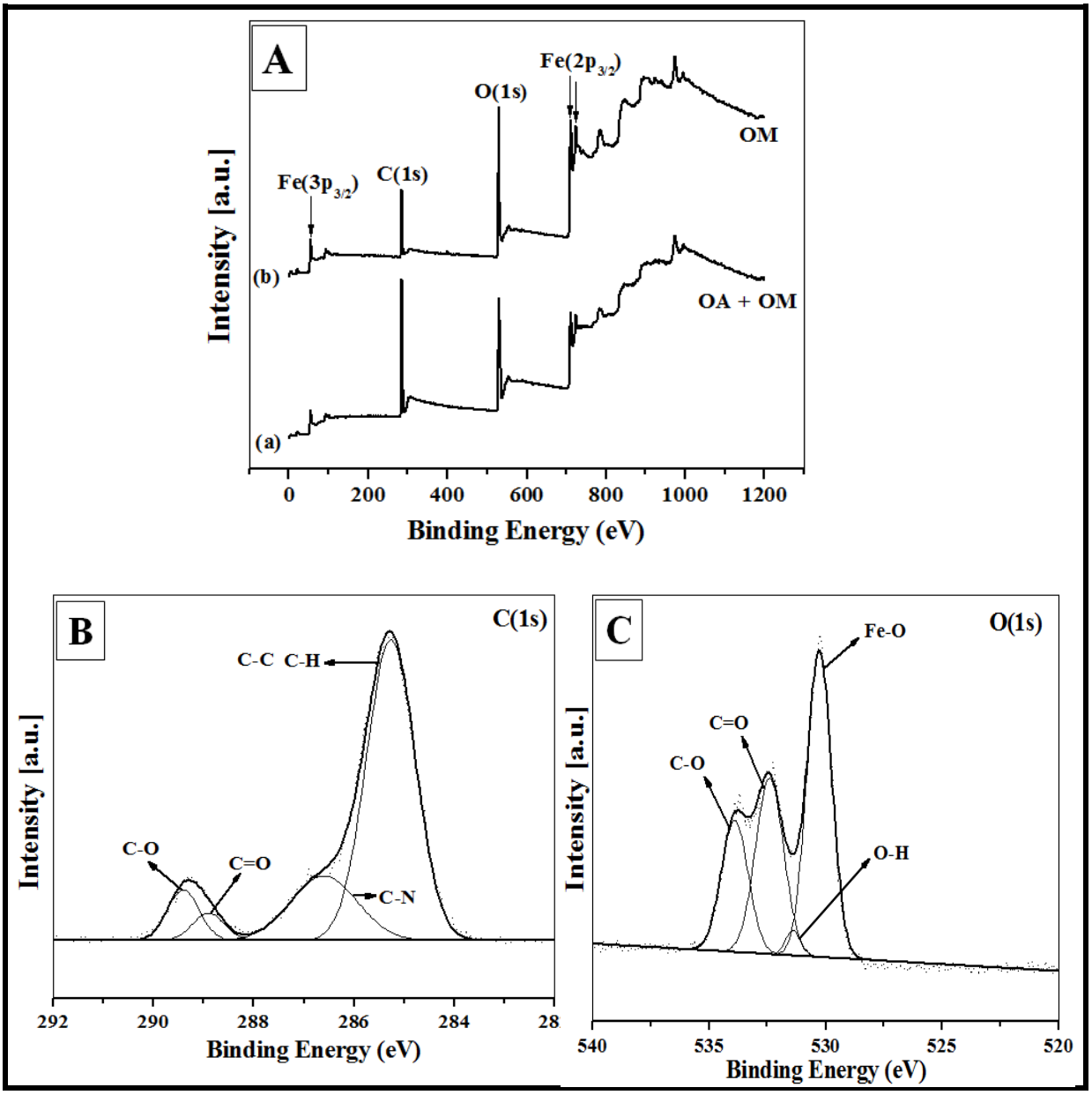

Figure 4.22. A. Wide scan XPS spectra of (a) OM and (b) OM+OA coated magnetite particles. **B.** convoluted O(1s) XPS spectra and **C.** convoluted C(1s) XPS spectra of D7 sample.

The similar XPS spectra are observed for all the particles prepared in presence of OM and OA+OM media. Thus, the XPS results further confirm the chemically adsorbed OA and OM coatings onto surface of the Fe_3O_4 nanoparticles.

Table 4.3. Analysis of O(1s) and C(1s) XPS spectra of the organic coated magnetite nanoparticles [13-18].

Peaks	**B.E. (eV)**	**Remarks**
O(1s)	530.2	Fe–O in Fe_3O_4
	531.4	O-H in physically adsorbed H_2O
	532.4	C=O from the (–COOH) of OA
	533.9	C–O from the (–COOH) of OA
C(1s)	285.3	C–C/C–H in OM and/or OA
	286.6	C–N in OM
	288.9	C=O from the (–COOH) of OA
	289.4	C–O from the (–COOH) of OA

The adsorbed organic coating on the particle surfaces can be furthered recognized by TGA measurements. Figure 4.23 (a) and (b) show the TGA curves of D10 and D7 samples which are prepared in OM and OA+OM surfactant media (Table 4.1). TGA curves represent a two-stage weight loss in the temperature ranges of 25 – 200ºC and 200–800ºC. The first slight amount of weight loss is due to the evaporation of physically adsorbed water and the second major weight loss is due to the decomposition of chemically adsorbed organic coating from the particle surface. It is estimated from the TGA result that the total amount of weight losses are 12 and 16 wt % for the OM and

OA+OM coated magnetite particles. The similar pattern of TGA curves are observed for the particles prepared in presence of OM and OA+OM media.

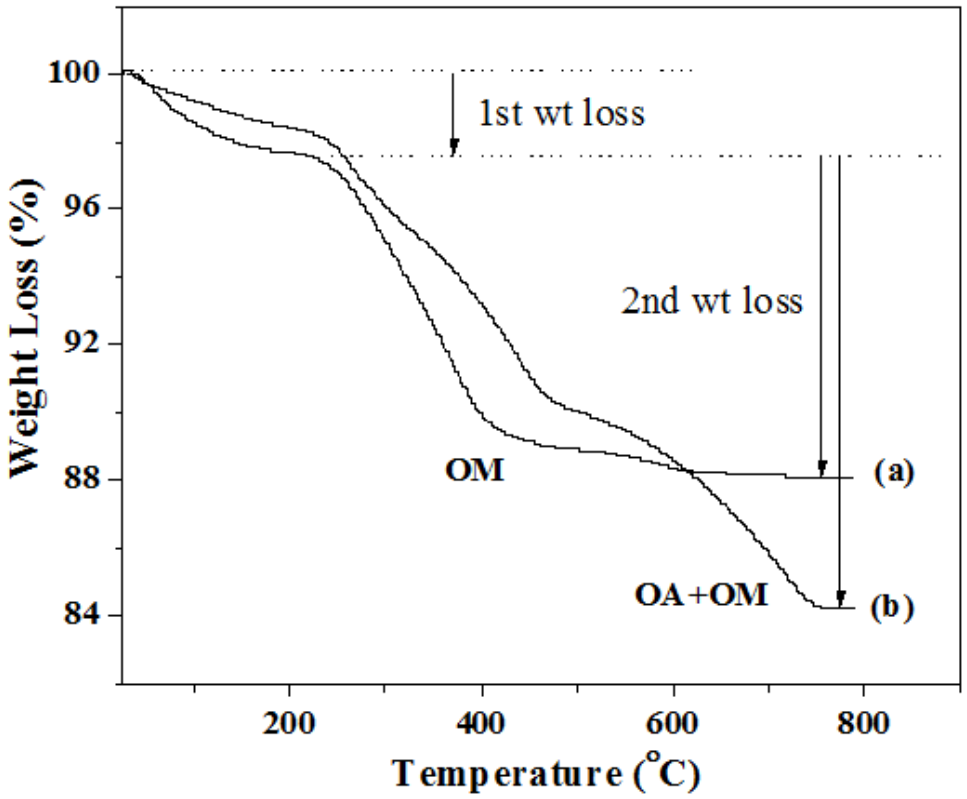

Figure 4.23. TGA curves of (a) OM and (b) OM+OA coated magnetite particles.

Thus the FTIR, XPS and TGA analysis indicate that OA and OM molecules are chemically adsorbed to the particle surface and taken part to control the growth of particles.

4.4. Conclusions

The growth of particles is well controlled relatively at lower reaction temperature and for shorter reaction time which results in formation of the smaller size particles with narrow size distribution and lower value of M_S. The M_S of the particles is significantly improved with increasing the reaction time and temperature, however, size distribution of those particles is found to be very wide. The uniform size particles can be synthesized at higher reaction temperature using longer reaction time by adopting the surfactant or solvent effect. The growth of the particles is slower if the reaction is carried out in absence of the solvent than that carried in presence of OA surfactant. Therefore, magnetite nanoparticles with enhanced M_S can be synthesized by solvent free thermal decomposition reaction using higher reaction temperature and longer reaction time while keeping size of the particles smaller with narrow distribution.

In summary, a novel solvent free thermal decomposition method has been developed to synthesize high quality magnetite nanoparticles. Reaction temperature of this method can be easily adjusted due to the absence of solvent. By using this method, the Ms value of the synthesized Fe_3O_4 nanoparticles can reach 76 emu/g, while the superparamagnetic property of the Fe_3O_4 nanoparticles is well retained. The obtained Fe_3O_4 nanoparticles can be well dispersed in organic solvent and form stable ferrofluid.

4.5. References

1. S. Sun, H. Zeng, D.B. Robinson, S. Raoux, P.M. Rice, S.X. Wang, G. Li, J. Am. Chem. Soc. 126 (2004) 273.
2. S. Sun, H. Zeng, J. Am. Chem. Soc. 124 (2002) 8204.
3. J. Xie, C. Xu, N. Kohler, Y. Hou, S. Sun, Adv. Mater. 19 (2007) 3163.
4. J. Park, K. An, Y. Hwang, J.-G. Park, H.-J. Noh, J.-Y. Kim, J.-H.Park, N.-M. Hwang, T. Hyeon, Nat. Mater. 3 (2004) 891.
5. T. Hyeon, S. Seong Lee, J. Park, Y. Chung, H.B. Na J. Am. Chem. Soc. 123 (2001) 12798.
6. D. Maity, J. Ding, J-M Xue, Func. Mater. Lett. 1 (2008) 189.
7. D. Maity, S-G Choo, J. Yi, J. Ding, J-M Xue, J. Magn. Magn. Mater. 321 (2009) 1256.
8. H.P. Klug, L.E. Alexander, X-Ray Diffraction Procedures, Wiley, New York, (1959).
9. R. Si, Y. W. Zhang, L.P. You, C.H. Yan, Angew. Chem. Int. Ed. 44 (2005) 3256.
10. D. Maity, D.C. Agrawal, J. Magn. Magn. Mater. 308 (2007) 46.
11. C. Liu, B. Zou, A.J. Rondinone, Z.J. Zhang, J. Am. Chem. Soc. 122 (2000) 6263.
12. Dyer J. R. Applications of Absorption Spectroscopy of Organic Compounds, Prentice-Hall, Inc. (1965).
13. R.M. Cornell, U. Schertmann, The iron oxides: structure, properties, reactions, occurrence and uses, VCH Publishers, Weinheim (2003).
14. C.D. Wagner, W.M. Riggs, L.E. Davis, J.F. Moulder, G.E. Muilenberg, Handbook of X-ray Photoelectron Spectroscopy, Perkin-Elmer Corporation, (1979).

15. Q.-L. Fan, K.-G. Neoh, E.-T. Kang, B. Shuter, S.-C. Wang, Biomaterials 28 (2007) 5426.

16. S. Gélinas, J.A. Finch, P. Böhme, Coll. Surf. A : Physicochem. Eng. Asp. 172 (2000) 103.

17. F.-Y. Cheng, C.-H. Su, Y.-S.g Yang, C.-S. Yeh, C.-Y. Tsai, C.-L. Wu, M.-T. Wu, D.-B. Shieh Biomaterials 26 (2005) 729.

18. Y. Zhang, J. Zhang, J. Coll. Inter. Sci. 283 (2005) 352.

CHAPTER 5

Conversion of Hydrophobic to Hydrophilic Nanoparticles

5.1. Introduction

The hydrophobic magnetite nanoparticles prepared from the thermal decomposition technique are coated with a layer of oleate and/or oleylamine and cannot immediately be used in biological applications because they are only soluble in hexane and other nonpolar or weakly polar organic solvents. For such particles to be useful in biology, they must be soluble in water in a pH range of about 5 to 9, at salt concentrations up to a few hundred mM, and temperatures up to 95 °C for various biological reactions [1]. To meet these biocompatibility requirements, the hydrophobic nanoparticles need to be modified. There are two general approaches in nanoparticle surface modifications: surface functionalization and encapsulation.

5.1.1. Surface Functionalization

Surface functionalization can be achieved by surfactant addition (i.e. bi-layer surfactant stabilization) and surface surfactant exchange (i.e. ligand exchange) [2-3]. The surfactant addition uses the hydrophobic interaction of the incoming long-chain hydrocarbon with that from the surfactant to form a cell-membrane-like double-layer structure, as shown in Figure 5.1 A [1]. In this approach, the nanoparticles are surrounded by the double-layer structure and the surface of the particles is functionalized with the functional group “F”. Depending on the chemical property of “F”, such modified nanoparticles can be dispersed in various liquid media, including water and PBS. Surface surfactant exchange, as shown in Figure 5.1 B, refers to the replacement of original surfactant on the surface of the particles by a bi-functional surfactant (single layer) with one functional group capable of binding to the particle surface via strong chemical bond and the other functional group

"F" having the polar character so that the particles can be dispersed in water or be further conjugated with bio-molecules like monoclonal antibody or folate receptor for *in vivo* site-specific targeting applications.

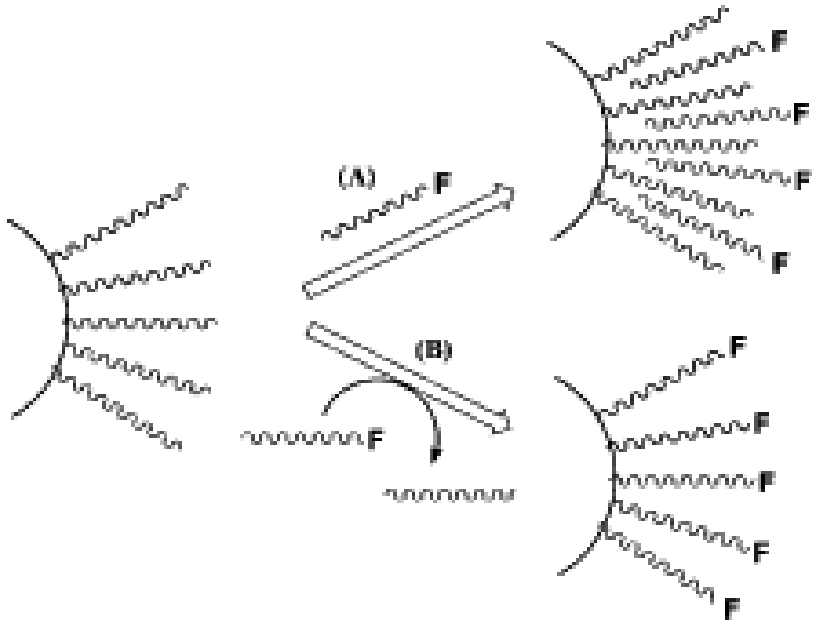

Figure 5.1. Schematic representation of surface functionalization of hydrophobic magnetite nanoparticles: **A.** double layer and **B.** single layer [1].

5.1.2. Encapsulation

Encapsulation can be achieved by entrapping the hydrophobic nanoparticles into a polymer matrix [4]. In this approach, the magnetite nanoparticles are confined (encapsulated) to a core surrounded by a hydrophilic polymeric membrane and thus obtain a biocompatible encapsulated polymeric nanoparticle, as shown in Figure 5.2. The polymeric nanoparticles can be freeze-dried for long-term storage and are more chemically and physically stable *in vivo.*

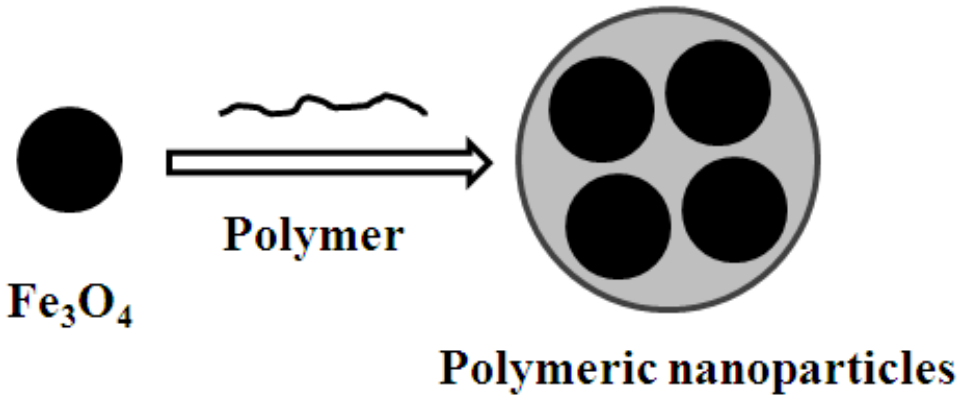

Figure 5.2. Schematic representation of surface encapsulation of hydrophobic magnetite nanoparticles.

A number of different polymers have been used in formulating polymeric nanoparticles, but those receiving the most attention are the biodegradable polymers because they have the advantage of not requiring surgical removal after they serve their intended purposes. Moreover, biodegradable matrices can provide a further control of release rates, by joining the typical diffusive mechanism with tunable polymer degradation. Therefore, biodegradable polymers especially poly(lactic acid) (PLA), poly(lactic-co-glycolic acid) (PLGA) and poly (ε-caprolactone) (PCL) have been commonly used over the past two decades for the development of polymeric nanoparticles in cancer and other biomedical applications [5-6]. However, these polymers are highly hydrophobic and there by the encapsulated nanoparticles made of these polymers are not water soluble. Moreover, nanoparticles composed of those polymers are difficult to conjugate directly hydrophilic molecular probes for targeting, for which amphiphilic linker molecules are needed, resulting in complications in the technology. To solve this problem, amphiphilic copolymers (with one hydrophobic and one hydrophilic end) have been developed inserting hydrophilic elements into the hydrophobic chains of the polymers. Recently,

Feng S-S groups have synthesized various biodegradable copolymers such as PLA-methoxy poly(ethylene glycol) (PLA-mPEG) [7-8] and PLA-d-α-tocopherol polyethylene glycol 1000 succinate (PLA-TPGS) [9-10]. Among these, they have significantly used PLA-TPGS copolymers for the formulation of the polymeric nanoparticle due to its controllable biodegradability, high encapsulation efficiency, high emulsification efficiency, high cellular uptake, excellent biocompatibility and non-toxicity. Polymeric nanoparticles can be prepared by several techniques such as emulsification-solvent evaporation method (single and double emulsion method) [11-12], solvent displacement method (nanoprecipitation method) [13-14], and the micelle formation [15-17]; depending on the nature of the polymeric material and the characteristics of the therapeutic agents to be loaded [18].

In this work, we have tried to covert functionalize the hydrophobic nanoparticles into hydrophilic by following three approaches:

1. Bi-Layer surfactant stabilization using lauric acid (LA).
2. Ligand exchange with the polyethylene glycol diacid (PEGDA), poly(acrylic acid) (PAA) and 3-aminopropyltriethoxysilane (APTES).
3. Encapsulation within a copolymer of poly(lactide) (PLA) and D-α-tocopherol polyethylene glycol 1000 succinate (TPGS).

The structure, morphology and properties of the converted nanoparticles are characterized to evaluate their potentiality in hyperthermia therapy and MRI imaging applications.

5.2. Experimental

Oleylamine (OM), lauric acid (LA), polyethylene glycol diacid (PEGDA, M_w = 600), dopamine (DPA) hydrochloride, sodium carbonate, *N*-hydroxysuccinimide (NHS), *N*,*N*′-dicyclohexylcarbodiimide (DCC), dimethylformamide (DMF), poly(acrylic acid) (PAA, M_w = 1800), diethylene glycol (DEG), 3-aminopropyltriethoxysilane (APTES), poly(lactide) (PLA), stannous octoate and organic solvents used in the syntheses were purchased from Sigma Aldrich. Vitamin E D-α-tocopherol polyethylene glycol 1000 succinate (TPGS) was from Eastman chemical company (USA), which was freeze dried for two days before use. Chemical structure of OM, LA, PEGDA, DPA, PAA, APTES, PLA and TPGS are shown in Figure 5.3.

The OM coated hydrophobic magnetite nanoparticles are synthesized using the solvent-free thermal decomposition technique as described in the previous chapter. Typically, 2 mmol of $Fe(acac)_3$ was dissolved in a 20 mL oleylamine and magnetically stirred under a flow of argon. The solution was dehydrated at 120 °C for 30 min, and then quickly heated to 320 °C and kept at this temperature for 1h. The black solution was cooled to room temperature by removing the heat source. 20 mL of ethanol was added into the solution and the precipitated particles were collected by centrifugation at 10000 rpm followed by three times washing with ethanol. The resulting OM coated hydrophobic nanoparticles are then converted into hydrophilic nanoparticles either by functionalization with hydrophilic molecules or encapsulation within hydrophilic polymeric matrix.

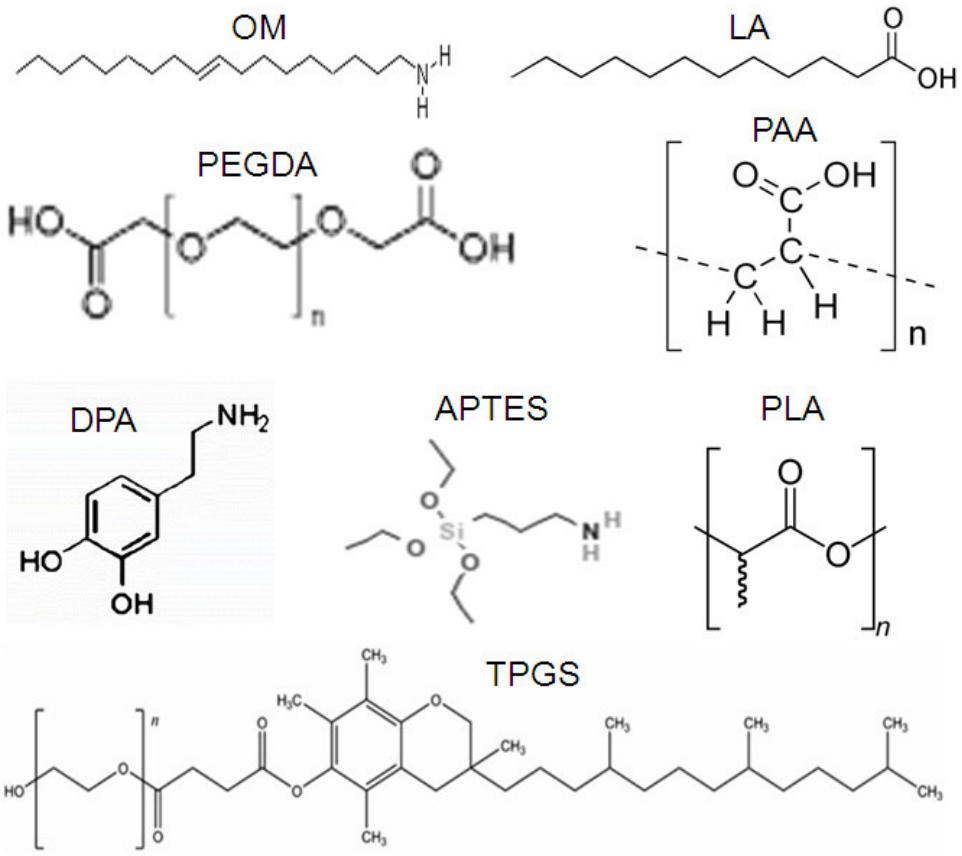

Figure 5.3. Chemical structure of oleylamine (OM), lauric acid (LA), polyethylene glycol diacid (PEGDA), dopamine (DPA), poly(acrylic acid) (PAA), 3-aminopropyltriethoxysilane (APTES), poly(lactide) (PLA) and D-α-tocopherol polyethylene glycol 1000 succinate (TPGS) molecules.

5.2.1. Synthesis of Bi-Layer Surfactant Stabilized Nanoparticles

Bi-layer stabilized hydrophilic Fe_3O_4 nanoparticles were prepared following the method reported in my previous paper [19], except that the lauric acid (dodecanoic acid) was used for the outer layer coating (Figure 5.4) of the Fe_3O_4 nanoparticles. Typically, ~1g of the washed OM coated Fe_3O_4 nanoparticles obtained by thermolysis (as described in

Chapter 4, Section 4.2.1) was combined with 20 ml deionized water and the slurry was heated to 60°C under vigorous stirring. A solution of 10% (w/v) ammonium salt of lauric acid (LA) was prepared separately by mixing 30 mL water, 3 g lauric acid and 30-40 drops of a solution of NH_4OH (pH = 10). This solution was added to the slurry dropwise using a 1 mL plastic syringe under constant stirring at 60°C until the slurry changed into a stable suspension. To confirm the stability of the aqueous suspension of the Fe_3O_4 nanoparticles was exposed to a permanent magnet for 10 min, and no phase separation was observed. Thus, the hydrophobic Fe_3O_4 nanoparticles was coated with double surfactant layers to stabilize them in water medium to obtain stable water-based magnetic fluid. The first inner layer of OM molecules are chemically adsorbed surfactant and the second layer of LA molecules are physically absorbed onto the surface of the Fe_3O_4 nanoparticles [20].

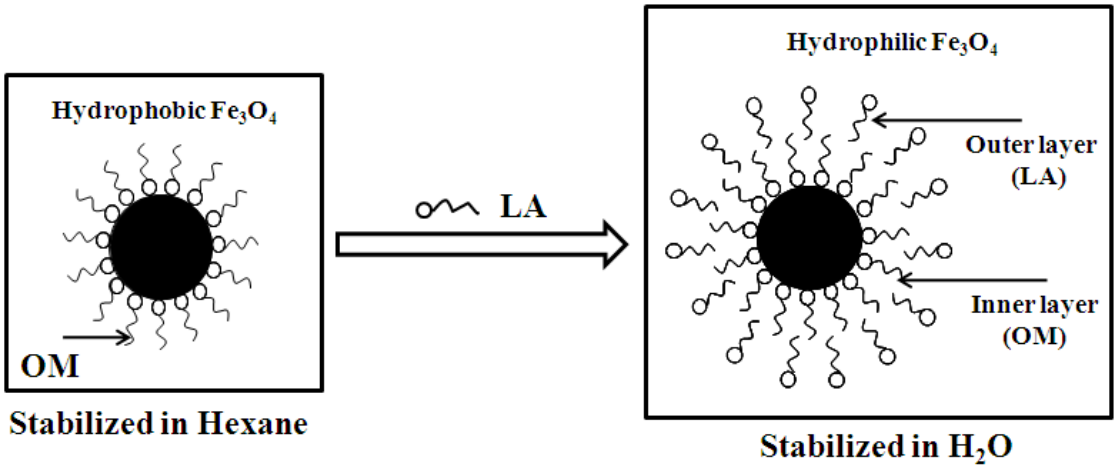

Figure 5.4. Schematic representation for the synthesis of bi-layer surfactant modified nanoparticles [19].

5.2.2. Synthesis by Ligand Exchange

5.2.2.1. Synthesis of PEGylated Nanoparticles

PEGylated hydrophilic magnetite nanoparticles were prepared using the method reported by Xie et al [21]. In this method, dopamine (DPA) was first linked with one of the carboxylic groups in the PEG diacid (PDA) via the EDC/NHS chemistry and then the resulting PEG-dopamine-acid (PDA) was covalently anchored on the surface of the particles through DPA replacing the oleylamine as shown in Figure 5.5.

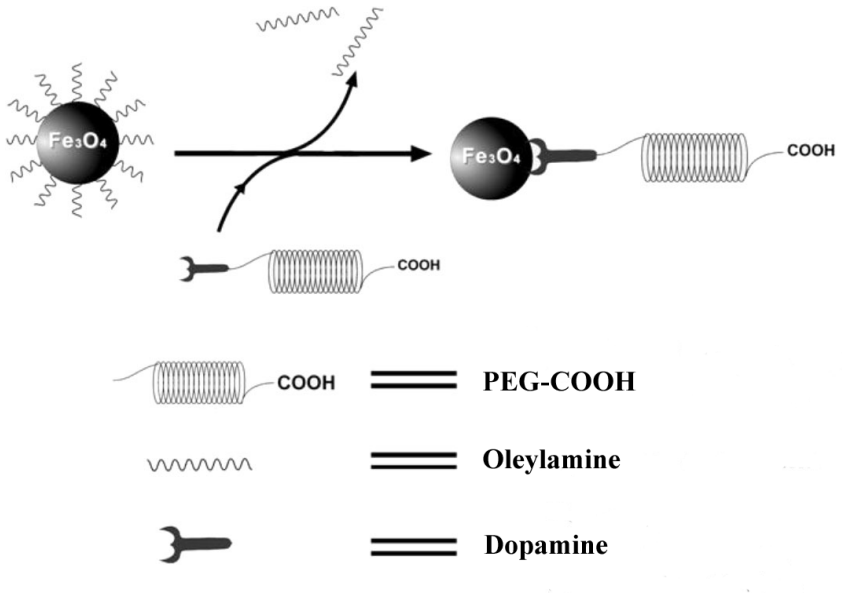

Figure 5.5. Schematic representation for the synthesis of PEG-dopamine-acid (PDA) modified nanoparticles [21].

Typically, 4 mL PEG diacid, 2 mg NHS (*N*-hydroxysuccinimide), 3 mg DCC (dicyclohexylcarbodiimide) and 1.27 mg dopamine hydrochloride were dissolved in a mixture solvent containing 2 mL $CHCl_3$, 1 mL DMF (dimethylformamide) and anhydrous 10 mg Na_2CO_3. The solution was stirred at room temperature for 2 h. Then 5 mg OM coated Fe_3O_4 nanoparticles were added, and the resulting solution was stirred

overnight at room temperature under Ar flow. The PDA modified Fe_3O_4 nanoparticles were precipitated by adding hexane, collected by a permanent magnet and dried overnight in oven. The particles were then dispersed in water.

5.2.2.2. Synthesis of PAA Modified Nanoparticles

Hydrophobic nanoparticles can be transferred into water medium by the ligand exchange approach using polyelectrolyte molecules such as poly(acrylic acid) (PAA) as reported by Zhang et al [22].

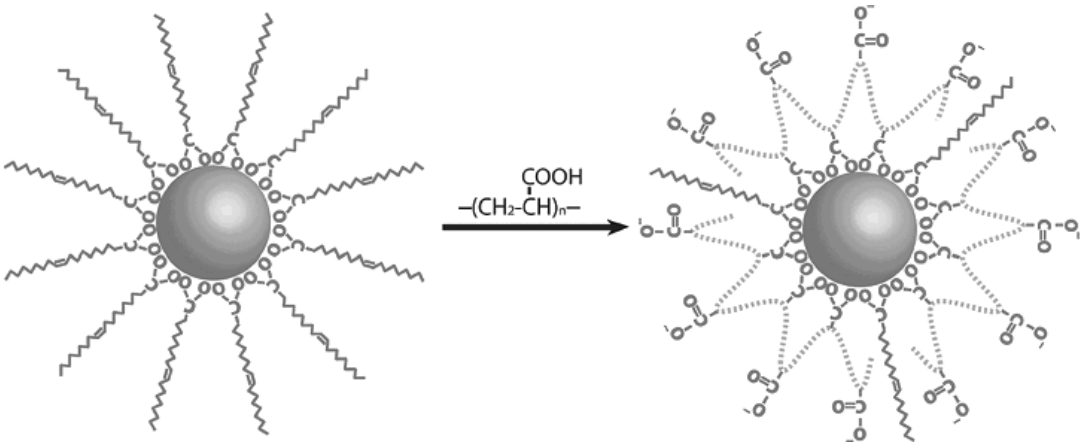

Figure 5.6. Schematic representation for the synthesis of PAA modified nanoparticles [22].

Typically, 8.0 mL DEG solution containing 0.5 g PAA was heated to 110°C with vigorous stirring under Ar flow. A toluene solution of OM coated Fe_3O_4 nanocrystals with 5 mg/mL Fe concentration was injected to the hot solution which became turbid immediately. The system was heated to 240°C and kept at this temperature for 1 h until the solution became clear. The hydrophobic OM coating was replaced by PAA molecules

due to the strong coordination of their functional groups to the nanocrystal surface as shown in Figure 5.6. After the solution was cooled down to room temperature, excess dilute hydrochloric aqueous solution was added, and a brown-black magnetic powder was obtained by centrifuging. The powder was washed three times with pure water. Finally, the washed powders are dispersed in water.

5.2.2.3. Synthesis of APTES Modified Nanoparticles

The 3-aminopropyltriethoxysilane (APTES) molecule consists of three alkoxy groups and amino (NH_2) group at two opposite ends of its chemical structure (Figure 5.3) and thus it can covalently bond to the nanoparticles through the alkoxy groups while keeping the NH_2 functional groups available for further bio-conjugation (Figure 5.7). Moreover, APTES can provide very good biocompatibility to the nanoparticles for their applications in biology [23]. Therefore, the method of surface functionalization with APTES could be promising for converting hydrophobic nanoparticles into hydrophilic nanoparticles to transfer them in an aqueous medium. Several groups have been tried to functionalize the magnetite nanoparticles with APTES [24-26]. However, the APTES functionalized nanoparticles have been found to be heavily agglomerated in all these previous results. Thus, here we have tried to synthesize non-agglomerated APTES functionalized magnetite nanoparticles using the modified aqueous/organic solvent deposition method [27]. Typically, OM coated magnetite nanoparticles were suspended in 30 ml 1:1 ethanol-water mixture (5% wt/v) and pH of the solution was adjusted to 5 by addition of acetic acid. Then, 10 ml of APTES was added to the solution and the resulting mixture solution was magnetically stirred at room temperature for 3 days under a flow of argon. Then, the

resulting APTES functionalized nanoparticles were precipitated from the supernatant by centrifugation at 8000 rpm for 15 min followed by three times washing with ethanol. Finally, one half of the functionalized nanoparticles were dispersed in water after washing and the other half was dried overnight in oven to obtain dry functionalized nanoparticles.

In the aqueous/organic solvent deposition method, the APTES molecules are adsorbed to the surface of the magnetite nanoparticles by two step reaction procedures (Figure 5.8). In the hydrolysis-condensation reaction (step 1), alkoxide groups ($–OC_2H_5$) of APTES molecules are replaced by hydroxyl groups (OH) to form reactive silanol groups, which condense with other silanol groups to form silane polymer producing siloxane bonds (Si–O–Si). In the second step, the silane polymers are chemically adsorbed to the magnetite nanoparticles forming covalent Fe–O–Si bonds through the silanization reaction.

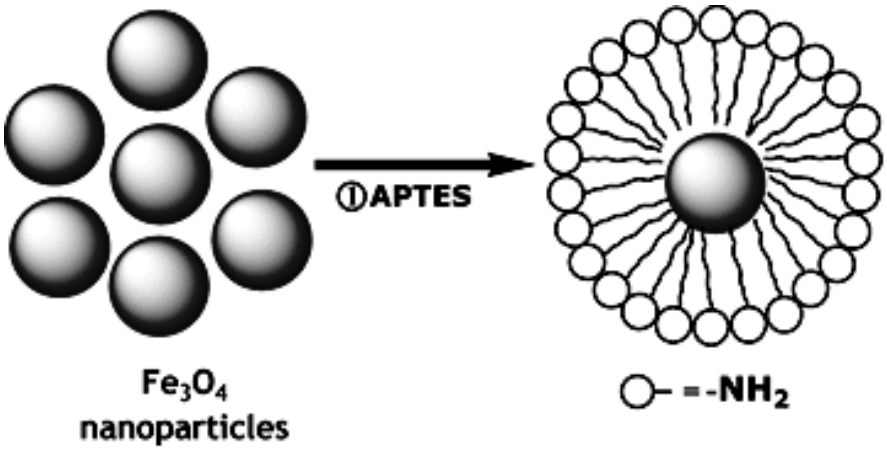

Figure 5.7. Schematic representation for the synthesis of APTES modified nanoparticles [23].

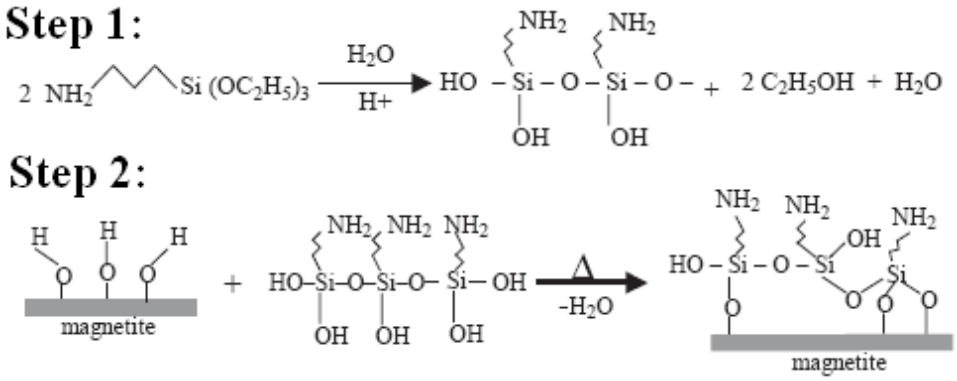

Figure 5.8. Deposition of APTES on the surface of the magnetite core through hydrolysis-condensation (Step 1) and silanization (Step 2) reactions [26].

5.2.3. Synthesis by Polymeric Encapsulation

5.2.3.1. Synthesis of PLA-TPGS Polymer

The PLA-TPGS copolymer (90:10 w/w ratio) was synthesized by the ring opening polymerization procedure reported elsewhere [9]. In brief, 9 g of PLA, 1 g of TPGS and 0.05 g stannous octate (in distilled toluene, 1%) were taken in an ampoule. The ampoule was evacuated in liquid nitrogen for 45 min. After that the ampoule was sealed by butane burner and reacted in silicone oil bath at 145^{o}C. After 12 h, the reaction product was dissolved in dichloromethane (DCM) and then precipitated in excess cold methanol to remove unreacted lactide monomers and TPGS. The final product was collected by filtration and vacuum dried at 45^{o}C for two days.

5.2.3.2. Preparation of Fe_3O_4 Encapsulated Polymeric Nanoparticles

Fe_3O_4 encapsulated PLA-TPGS nanoparticles (IO-PNPs) were prepared by both the single emulsion and nanoprecipitation method.

A. Single Emulsion Method

A schematic representation of formation of the encapsulated polymeric nanoparticles (PNPs) using the single emulsion method is shown in Figure 5.9. Typically, 100 mg of the polymer and 2 mg OM coated Fe_3O_4 were added to 8 ml of dichloromethane (DCM) and the resulting solution was vortexed till the polymer was completely dissolved in the organic solvent and a clear solution was obtained. The organic phase was then added into 120 ml of aqueous phase containing the emulsifier at a given concentration (15% w/v TPGS) and sonicated (at 25 W output) for 90 seconds to disperse the emulsion using a probe sonicator. The resulting emulsion was allowed to stir overnight to evaporate the organic solvent completely. Finally, the polymeric nanoparticles were obtained by centrifugation at 10,000 rpm for 30 minutes followed by removal of the emulsifier by several times washing with water.

In this preparation method, the organic phase consisting of water insoluble solvent (DCM), polymer (PLA-TPGS) and magnetic nanoparticles (MNPs) occupy the hydrophobic core of the micelle which is initially formed in the aqueous phase as shown in Figure 5.10. Due to immiscibility of solvent (DCM), the non-solvent (water) does not diffuse into the organic phase however, the solvent diffuse into the non-solvent (water) or evaporates due to its low boiling point. Thus, the solvent carry the MNPs and deposit them at the interface between the

solvent/non-solvent. Therefore, the MNPs are dispersed near the periphery of the polymeric nanoparticles as shown in Figure 5.9.

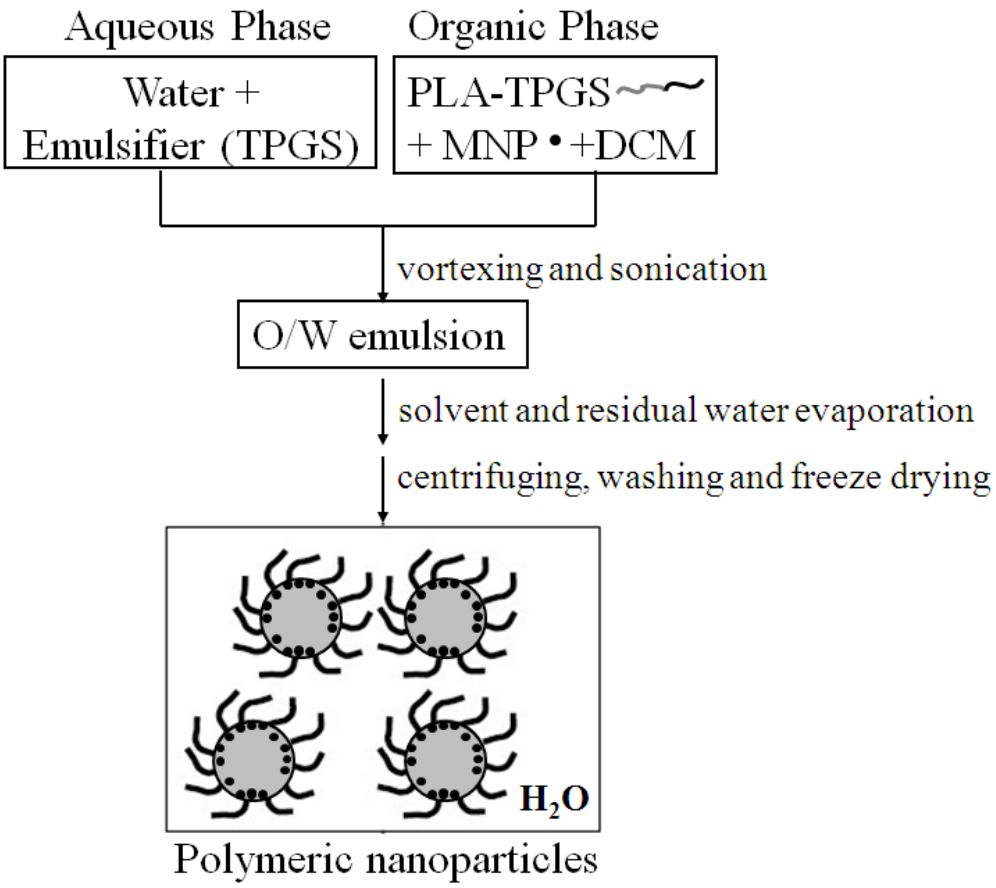

Figure 5.9. Schematic representation of synthesis of the polymeric nanoparticles by single emulsion method.

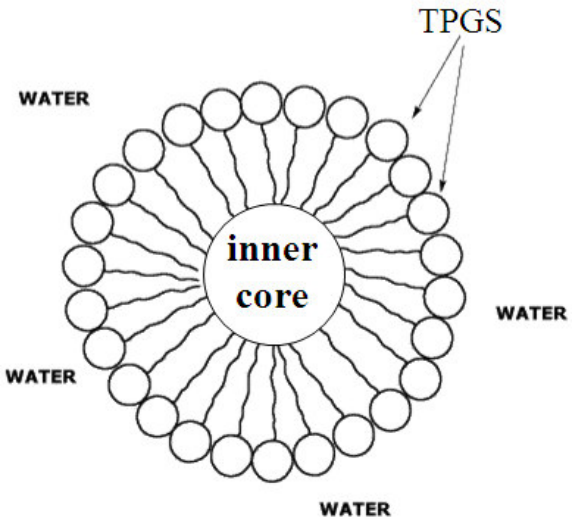

Figure 5.10. Structure of micelle formed by dissolving, an emulsifier (TPGS) in water. The inner hydrophobic core of the micelle can dissolve organic-soluble compounds.

B. Nanoprecipitation Method

A schematic representation of formation of the encapsulated polymeric nanoparticles (PNPs) using the nanoprecipitation method is shown in Figure 5.11. Typically, 100 mg of the polymer and 2 mg of OM coated Fe_3O_4 were added to 8 ml of tetrahydrofuran (THF) and the resulting solution was vortexed till the polymer was completely dissolved in the organic solvent and a clear solution was obtained. A 30 ml of aqueous phase containing a known concentration of the emulsifier (15% w/v TPGS) was well dispersed using a probe sonicator for 30 seconds. The organic phase was then added into the aqueous phase. The solution was vigorously stirred still uniformity and finally diluted with large volume of water.

The resulting solution was then allowed to be stirred overnight to eliminate the organic solvent. Finally, the polymeric nanoparticles were obtained by centrifugation at 10,000 rpm for 30 minutes followed by removal of the emulsifier by several times washing with water.

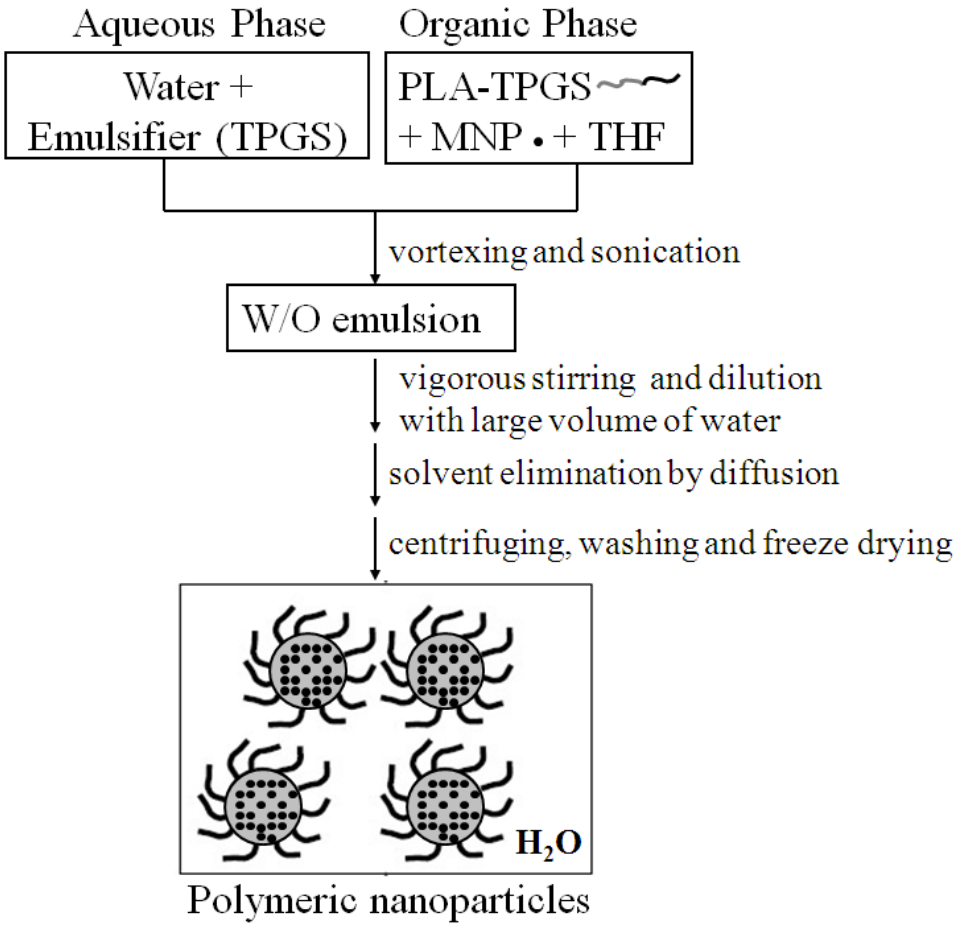

Figure 5.11. Schematic representation of synthesis of the polymeric nanoparticles (IO@PLA-TPGS) by nanoprecipitation method.

In this preparation method, the organic phase consisting of partially water soluble solvent (THF), polymer (PLA-TPGS) and magnetic nanoparticles (MNPs) occupy the

hydrophobic core of the micelle which is initially formed in the aqueous phase as shown in Figure 5.9. However due to the partial water miscibility of the solvent (THF), the non-solvent (water) diffuse into the core and co-exist with the organic phase bringing interaction of the emulsifier with the polymer. Thus, the emulsifier influences the distribution of the MNPs within the polymer matrix to develop uniformly MNP dispersed polymeric nanoparticles (IO@PLA-TPGS) as shown in Figure 5.11.

5.2.4. Characterization of Nanoparticles

The size and morphology of the functionalized magnetite nanoparticles were determined by transmission electron microscopy (TEM, JEOL 2010) while their structure was identified Fourier transform infrared spectroscopy (FTIR, Varian 3100) and thermogravimetric analysis (TGA, DMSE SDTQ600). Magnetic properties were measured using vibrating sample magnetometer (VSM, Lakeshore, Model 665). Iron (Fe) content within the polymeric nanoparticles (PNPs) was measured by ICP MS (Agilent ICP MS 7500 Series). For this, a known amount of PNPs were dissolved in 2 ml of concentrated nitric acid and the resulting solutions were analyzed using ICP-MS after sufficient dilution with milli-Q water. The analysis of sample was done in comparison with the ICP-MS standard (Sigma Aldrich).The encapsulation efficiency (EE %) and iron content (% Fe) of the PNPs were calculated using the following equations:

$$\text{EE\%} = \frac{\text{Amount of } Fe_3O_4 \text{ present in the polymeric nanoparticles}}{\text{Amount of } Fe_3O_4 \text{ used in the preparation of polymeric nanoparticles}} \times 100$$

$$\text{\% Fe content} = \frac{\text{Weight of Fe present in X g of polymeric nanoparticles}}{\text{X g of polymeric nanoparticles}} \times 100$$

Cell viability studies were performed by MTT assay using MCF-7 mammalian breast cancer cells. For this, the MCF-7 cancer cells were incubated for 24 h with media containing APTES coated (IO@APTES) and PLA-TPGS encapsulated (IO@PLA-TPGS) nanoparticles at concentrations ranging from 0.625 – 10 mg/ml Fe. AC magnetic field induced heating ability of the IO@APTES nanoparticles was determined from the time-dependent calorimetric measurements using a RF generator operating at 240 kHz. The T1, T2 and $T2^*$ relaxation times of aqueous suspensions of IO@APTES and IO@PLA-TPGS nanoparticles with the Fe concentration of 0.0066 – 0.4 mM was measured at 9.4T using a Varian MRI scanner. The IO@PLA-TPGS nanoparticles were injected into a Wistar rat body at a dosage of 0.8 mg [Fe]/kg body through tail vein and then *in vivo* MRI images of rats were obtained by using a fast spin echo sequence (TR/TE =1000/28.24 ms, flip angle = 90°, field of view = 8 cm, thickness = 2 mm, intersection gap = 0.3 mm, matrix = 256 x 192, under fat saturation and external trigger).

5.3. Results and Discussion

5.3.1. Structure Identification

Figure 5.12 A, B, C and D shows the FTIR spectra of the bi-layer surfactant, PDA, PAA and APTES modified nanoparticles, respectively. The peaks below 700 cm^{-1} are due to Fe–O stretching vibration for the iron oxide nanoparticles [29] while the peaks above 700 cm^{-1} are due to the organic coating adsorbed onto the surface of the nanoparticles. The broad band between 3600 and 3000 cm^{-1} are due to the O–H stretching vibration attributed for water molecules adsorbed to the particle surface [30].

The peaks in Figure 5.12 A at about ~3400, 3130-3030, 2962-2809, ~1670, 1501-1602 and ~1435 are due to N–H stretching, NH^{4+} bending, C–H stretching, O–H stretching, N–H bending and O-C=O stretching vibration respectively (Table 5.1), which are attributed to adsorbed OM (inner layer) and LA (outer layer) molecules onto the particle surface [19, 21, 30-31]. The band at 1100-1250 cm^{-1} are assigned due to the bridging between COOH groups of the outer layer lauric acid molecules and the excess (free) lauric acids molecules through H-bonding [33].

The peaks in Figure 5.12 B at about ~3400, 2962-2809, ~1670, ~1643, 1501-1602, ~1435 and 1100-1250 cm^{-1} are due to N–H stretching, C–H stretching, O–H stretching, C=O stretching, N–H bending, O-C=O stretching and C–O–C stretching vibration respectively (Table 5.1), which are attributed to adsorbed PDA molecules onto the particle surface [19, 21, 29-31].

The peaks in Figure 5.12 C at about 2962-2809, ~1710, ~1670, 1550-1610 and 1396, and ~1060 cm^{-1} are due to C–H stretching, C=O stretching, O–H stretching, COO^- stretching and O-H bending vibration respectively (Table 5.1), which are attributed to adsorbed PAA molecules onto the particle surface [19, 22, 29-31].

The peaks in Figure 5.12 D at about 3429, 2962-2809, 1625, 1385, 1120-1048 and ~ 935 cm^{-1} are due to N–H stretching, C–H stretching, N–H bending, C–N stretching, Si-O–Si stretching and Si–O–Et bending vibration respectively (Table 5.1), which are attributed to adsorbed APTES molecules onto the Fe_3O_4 nanoparticle surface [26, 33-34].

Table 5.1. FT-IR absorption frequencies (4000-400 cm^{-1}) of bi-layer surfactant, PDA, PAA and APTES modified nanoparticles [19, 21-22, 26-27, 30-34].

Samples	**Absorption frequencies (cm^{-1})**	**Remarks** (υ: stretching vibration; δ: bending vibration)
Bi-layer surfactant modified	3130-3030	δ(NH^{4+}) for ammonium salts of LA
	2962-2809	υ(C-H) for –CH_2 of OM and LA
	~1670	υ(O-H) for –CO_2H of LA
	~3400 and 1501-1602	υ(N-H) and δ(N-H) for -NH_2 of OM
	~1435	υ(O-C=O) for –CO_2H of LA
	1100-1250	The couple between –COOH of LA (outer layer) and –COOH of LA (free)
PDA modified	2962-2809	υ(C-H) for –CH_2 of PDA
	~1670	υ(O-H) for –CO_2H of PDA
	~1643	υ(C=O) for amide of PDA
	~3400 and 1501-1602	υ(N-H) and δ(N-H) for amide of PDA
	~1435	υ(O-C=O) for –CO_2H of PDA
	1100-1250	υ(C-O-C) of PDA
PAA modified	3600-3000	υ(O-H) for H_2O
	2962-2809	υ(C-H) for –CH_2 of PAA
	~1710	υ(C=O) for –CO_2H of PAA
	~1670	υ(O-H) for –CO_2H of PAA
	1550-1610 and 1396	υ(COO^-) for –CO_2H of PAA
	~1060	δ(O-H) for –CO_2H of PAA
APTES modified	3600-3000	υ(O-H) for H_2O
	2962-2809	υ(C-H) for propyl group of APTES
	~3400 and 1625	υ(N-H) and δ(N-H) for NH_2 group of APTES
	1385 cm^{-1}	υ(C-N) for CH_2-NH_2 of APTES
	1120-1048 and ~ 935	Si-O–Si and Si–O–Et bonds of silanized APTES

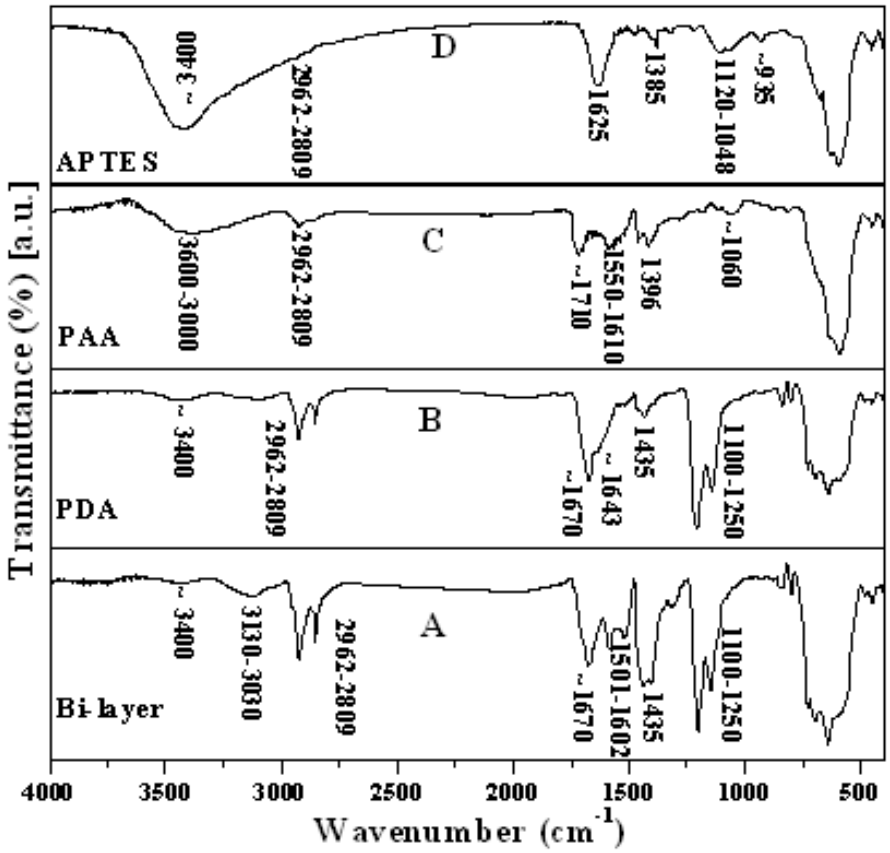

Figure 5.12. FTIR patterns of the **A.** bi-layer surfactant, **B.** PDA, **C.** PAA and **D.** APTES modified nanoparticles.

The surface adsorbed organic coatings were further identified by TGA analysis. Figure 5.13 A, B, C and D depict TGA curves the bi-layer surfactant, PDA, PAA and APTES modified nanoparticles, respectively. The minor weight loss in the temperature range of 25–200ºC is due to the evaporation of water while the major weight loss in the temperature range of 200–800ºC is due to the decomposition of the adsorbed organic coating from the particle surface. The total amount of weight losses were 32 wt%, 25 wt%, 11 wt% and 14 wt% for the bi-layer, PDA, PAA and APTES modified nanoparticles, respectively. Two different type of weight loss occurs between 200-800°C

for the bi-layer coated nanoparticles: the first weight loss occurs rapidly in the temperature range of 200-350°C due to thermal degradation of outer (secondary) layer which is physically adsorbed (reversibly and weakly bonded) onto the particle surface while the second weight loss occurs in the temperature range of 350-800°C due to the thermal degradation of inner (primary) layer which is chemically adsorbed (irreversibly and strongly bonded) onto the particle surface [19-20].

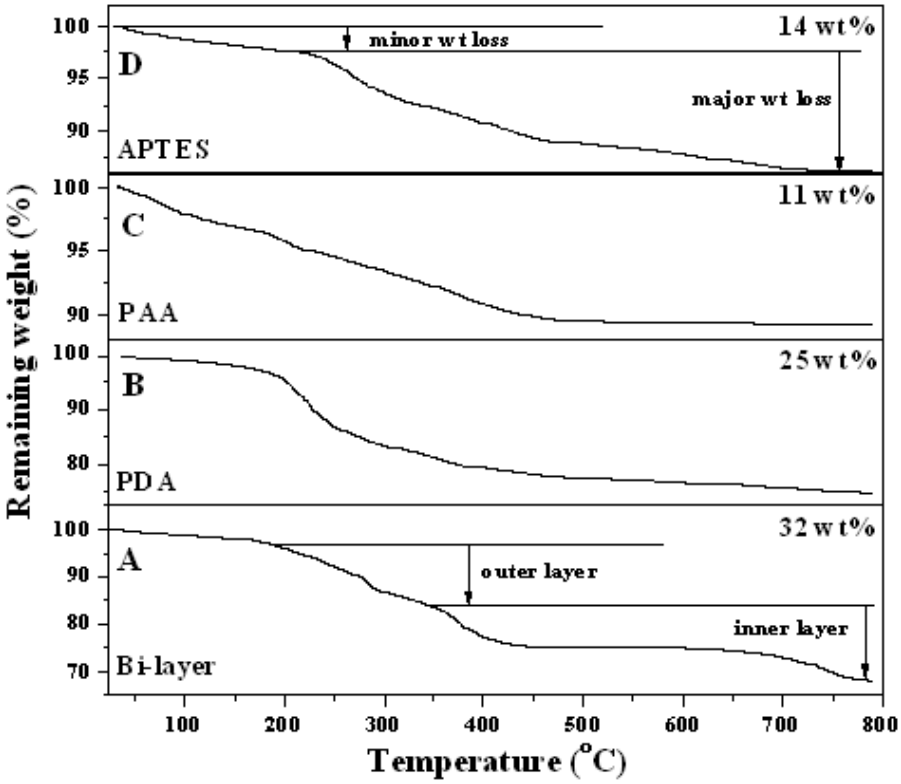

Figure 5.13. TGA curves of the **A.** bi-layer surfactant, **B.** PDA, **C.** PAA and **D.** APTES modified nanoparticles.

Thus, the FTIR and TGA results indicate that the LA molecules are physically adsorbed forming an outer layer of the bi-layer (inner OM layer) modified nanoparticles while the PDA, PAA and APTES molecules are chemically adsorbed on to surface of the magnetite

nanoparticles replacing the OM coating of the hydrophobic nanoparticles through the ligand exchange procedure. The free -CO_2H and NH_2 functional groups of the bi-layer surfactant, PDA, PAA and APTES modified nanoparticles are further required to be conjugated with the bio-molecules (antibody, folate receptor etc.) so that they can be used in the site-specific targeting applications.

Figure 5.14 A and B show the FTIR spectra of the encapsulated PLA-TPGS (IOs-PNPs) nanoparticles prepared by single emulsion and nanoprecipitation method, respectively. The peaks at about 2962-2809, ~1755, 1501-1602, ~1435 and 1100-1250 cm^{-1} are due to C–H stretching, C=O stretching and C–O–C stretching vibration respectively, which are attributed to encapsulating PLA-TPGS polymer molecules onto the Fe_3O_4 particle surface [19, 21, 29-31]. The peaks in Figure 5.14 B are broader than the peaks in 5.14 A indicating that the size of the PNPs prepared by nanoprecipitation method is smaller than those prepared by the single emulsion method [29-31].

Figure 5.15 shows the TGA curve the IOs-PNPs nanoparticles. The major weight loss in the temperature range of 200–500ºC is due to the evaporation the complete decomposition of the PLA-TPGS matrix of IOs-PNPs nanoparticles. After 500ºC, the straight line portion of the graph is due to the remaining IO only which is less than 1 wt%.

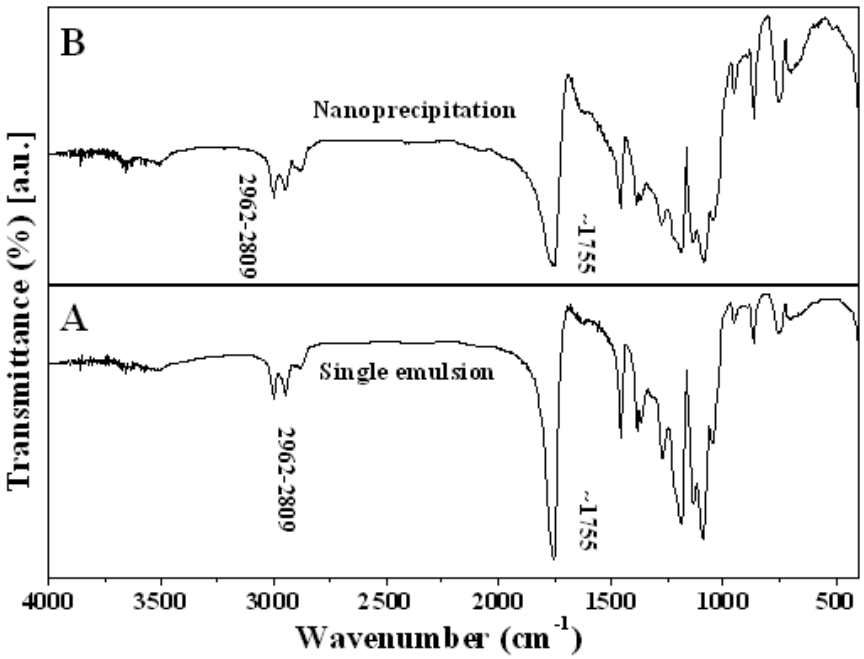

Figure 5.14. FTIR spectra of the encapsulated PLA-TPGS nanoparticles (IOs-PNPs) prepared by **A.** single emulsion and **B.** nanoprecipitation method, respectively**.**

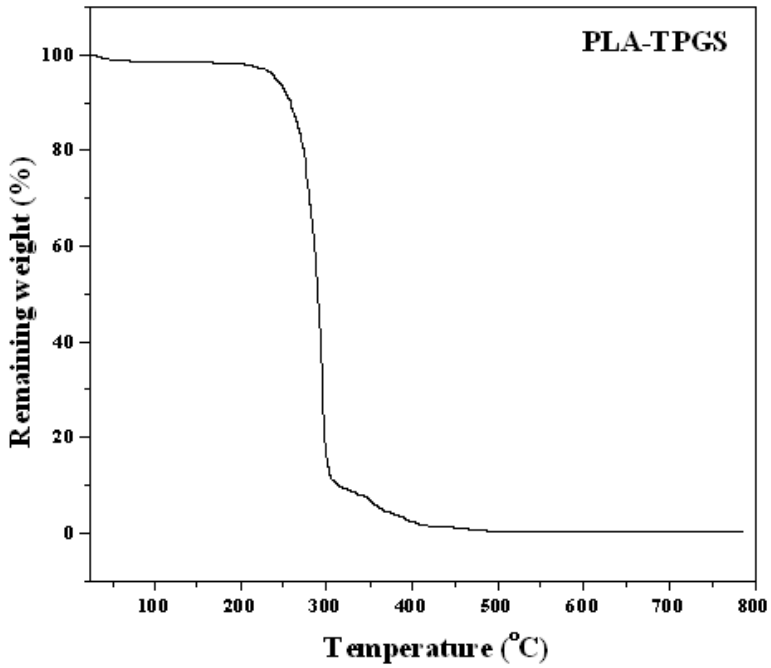

Figure 5.15. TGA curve of the encapsulated PLA-TPGS (IOs-PNPs) nanoparticles.

5.3.2. Morphology

Figure 5.16 A, B, C and D shows the TEM images of the bi-layer surfactant, PDA, PAA and APTES modified nanoparticles suspended in an aqueous medium, respectively. It can be seen that the bi-layer surfactant and PAA modified nanoparticles are are very much agglomerated in an aqueous medium while, the PDA and APTES modified nanoparticles are very well dispersed in aqueous media.

The TEM results indicate that the procedure of converting the hydrophobic nanoparticles either by adding a second layer of LA onto them or replacing the OM layer with PAA are not as effective to prevent the agglomeration in their aqueous suspension. However, the ligand exchange via PEGylation or APTES functionalization is very effective to transfer the nanoparticles in aqueous media without any agglomeration. The clear lattice fringes and electron diffraction rings of HRTEM and SADP image which are shown in the Figure 5.16 E and F respectively indicate that the nanoparticles are still consisting of highly crystalline magnetite phase even after their surface functionalization.

Figure 5.17 A and B show the TEM images of Fe_3O_4 encapsulated polymeric (PLA-TPGS) nanoparticles (IOs-PNPs) prepared by the single emulsion and nanoprecipitation method, respectively. It can be seen that the magnetite nanoparticles distributed more towards the periphery (PDI = 0.153) of the PNPs prepared using the single emulsion method while the magnetite nanoparticles are distributed homogeneously (PDI = 0.093) within the matrix of the PNPs prepared using the nanoprecipitation method. Moreover, size of the PNPs prepared by single emulsion method (D = 282 nm) is larger than those prepared by nanoprecipitation method (D = 249 nm).

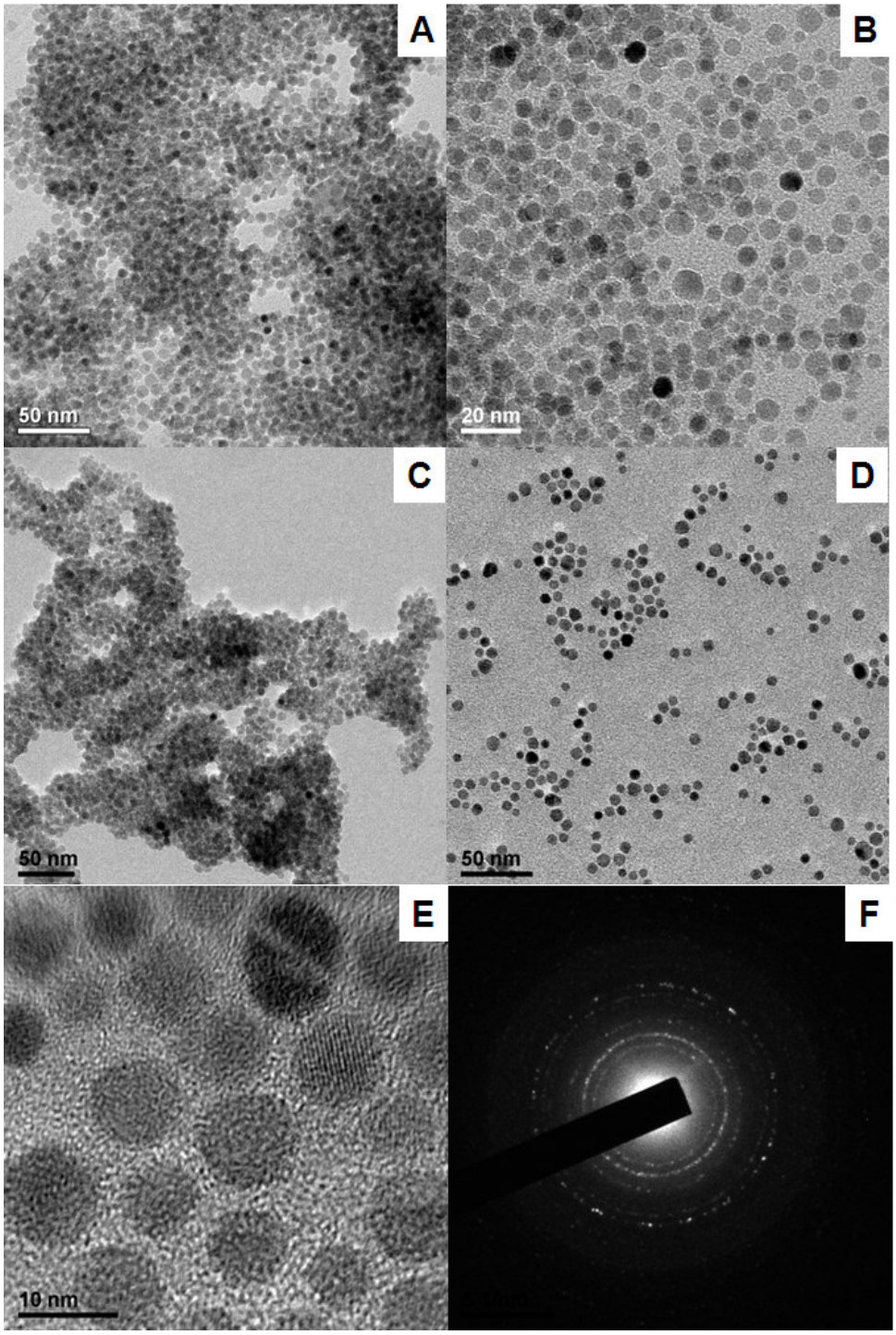

Figure 5.16. TEM images of the **A.** bi-layer surfactant, **B.** PDA, **C.** PAA and **D.** APTES modified nanoparticles. **E.** HRTEM and **F.** SADP of APTES modified nanoparticles.

Hence, the encapsulation efficiency of the PNPs prepared by single emulsion method is lower than those prepared by nanoprecipitation method (Table 5.2). Polydispersity index of size distribution (as determined by the Zetasizer Nano-ZS) of the NPs are 0.153 and 0.093 respectively. We can thus conclude that the preparation of the PNPs by the nanoprecipitation method is more efficient to control the particle size and the distribution of magnetic nanoparticle within the polymeric matrix.

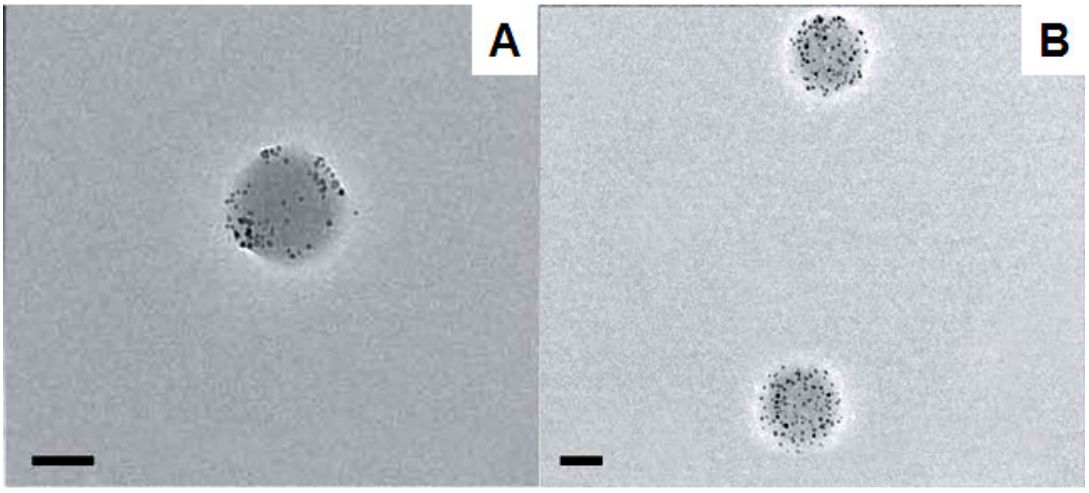

Figure 5.17. TEM images of Fe_3O_4 encapsulated PLA-TPGS (IOs-PNPs) nanoparticles prepared by **A.** single emulsion and **B.** nanoprecipitation method, respectively (scale bar = 100 nm).

Table 5.2. Characteristics of PLA-TPGS encapsulated polymeric nanoparticles.

Preparation Method	Loading of MNP (wt %)	Encapsulation Efficiency (EE %)	Size (nm)	Polydispersity Index (PDI)
Single emulsion	2	16.03 ± 3.31	282	0.153
Nanoprecipitation	2	64.17 ± 2.32	249	0.093

5.3.3. Magnetic properties

Figure 5.18 A, B, C and D show the magnetization (M-H) curves (measured at 2 T) of the bi-layer surfactant, PDA, PAA and APTES modified nanoparticles suspended in an aqueous medium, respectively. Their saturation magnetization (M_S) values were estimated as 54, 60, 65 and 63 emu/g respectively. The M_S values are different because of the different amount of nonmagnetic (surfactant or polymer) coating on to the Fe_3O_4 nanoparticle surface. The zero coercivity and zero remanance on all of the M-H curves indicate that the surface modified magnetite nanoparticles are superparamagnetic in nature at the room temperature.

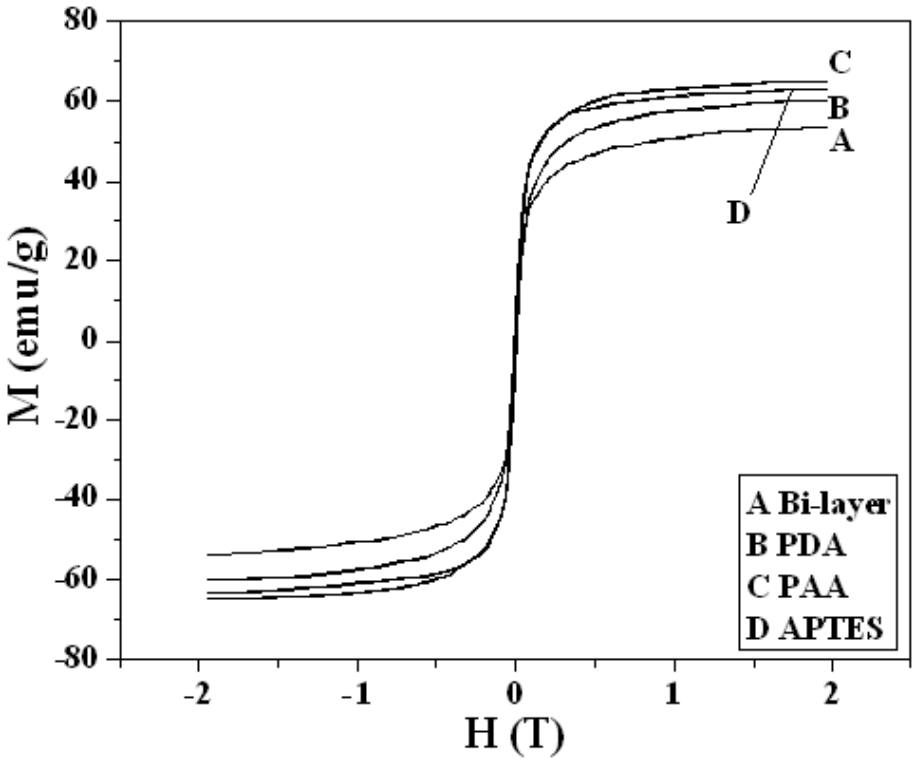

Figure 5.18. Room temperature M-H curves of the **A.** bi-layer surfactant, **B.** PDA, **C.** PAA and **D.** APTES modified magnetite nanoparticles.

Figure 5.19 shows the temperature dependence of the zero-field cooled/field cooled (ZFC-FC) magnetization of the APTES functionalized nanoparticles measured by SQUID under an applied field of 50 Oe. The ZFC curve reached the maximum at about 129 K, which corresponded to the blocking temperature (T_B) of the nanoparticles. The similar feature of ZFC-FC curves are observed for all the surface functionalized magnetite nanoparticles which also confirms that the functionalized nanoparticles are superparamagnetic in nature [30].

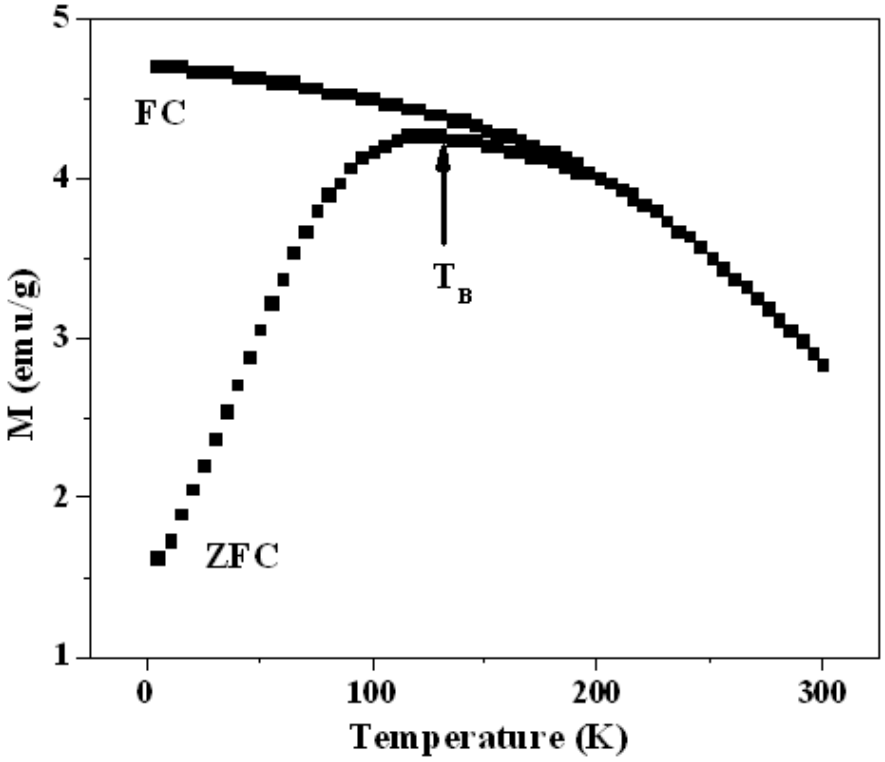

Figure 5.19. ZFC and FC magnetization curves of the APTES functionalized magnetite nanoparticles under an applied field of 50 Oe.

Figure 5.20 A and B depict the M-H curves (measured at 0.5 T) of the IOs-PNPs prepared by single emulsion and nanoprecipitation method, respectively. The M_S values were

estimated as 5 and 25 emu/g indicating that the M_S value of the former IOs-PNPs is lower than latter IOs-PNPs. The higher M_S value of the IOs-PNPs prepared by nanoprecipitation is due to their higher encapsulation efficiency (64.17%) and smaller size (249 nm).

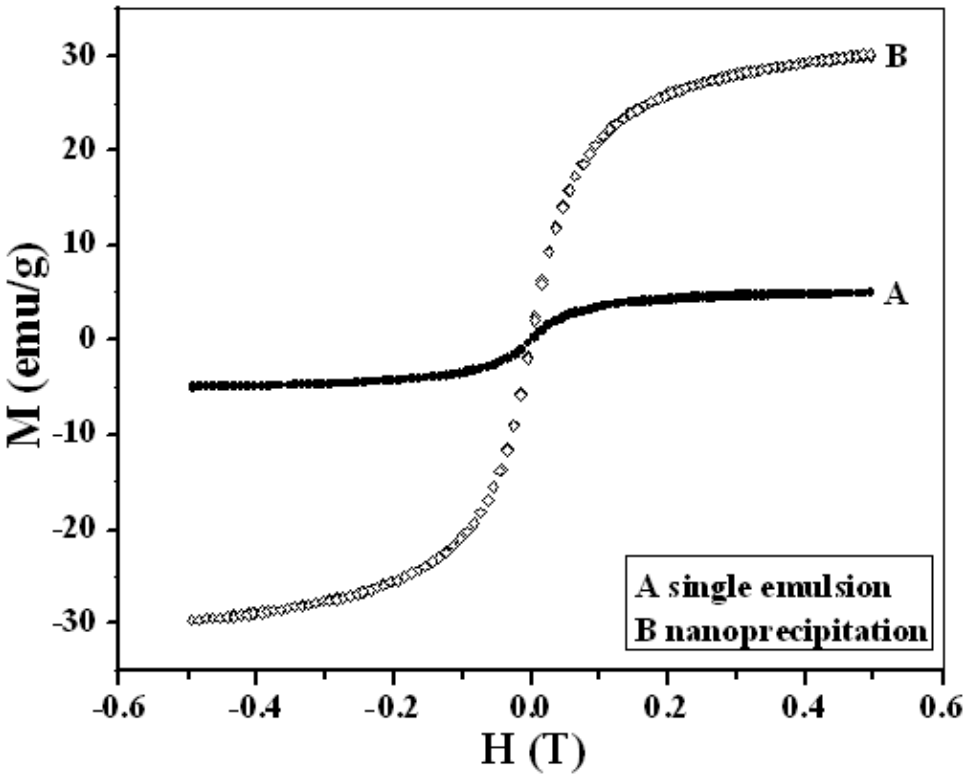

Figure 5.20. Room temperature M-H curves of the Fe_3O_4 encapsulated PLA-TPGS nanoparticles (IOs-PNPs) prepared by **A.** single emulsion and **B.** nanoprecipitation method, respectively**.**

5.3.4. In vitro Cytotoxicity Studies

Figure 5.21 shows the cytotoxicity profile of the APTES coated (IO@APTES) and PLA-TPGS encapsulated (IO@PLA-TPGS) nanoparticles using the MCF-7 breast cancer cells. It can be seen that MCF-7 cells do not show any cytotoxicity with the magnetite

nanoparticles in the range of 0.625 – 10 mg Fe/ml concentrations. Thus, both the APTES coated and PLA-TPGS encapsulated magnetite nanoparticles are biocompatible up to the iron concentration of 10 mg/ml with MCF-7 breast cancer cells.

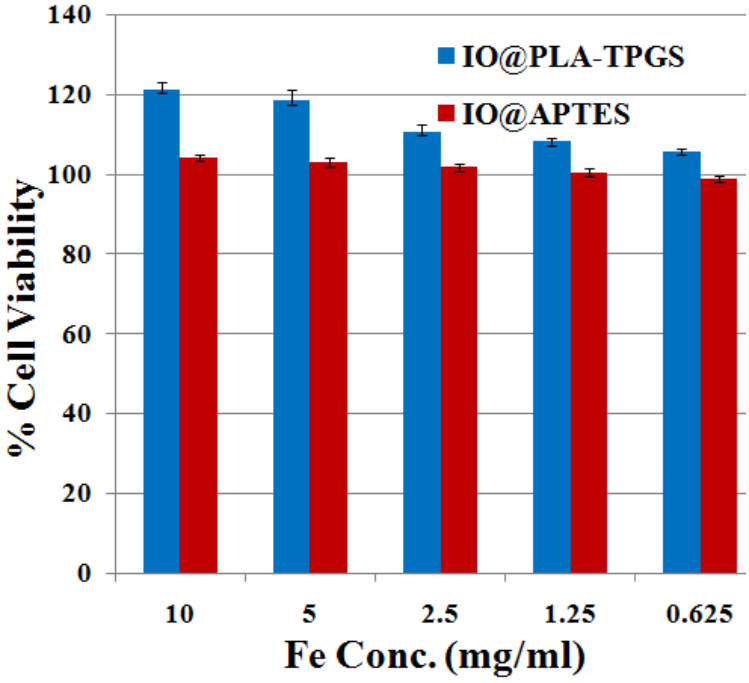

Figure 5.21. Cytotoxicity profile of the APTES coated (IO@APTES) and PLA-TPGS encapsulated (IO@PLA-TPGS) nanoparticles on MCF-7 breast cancer cells.

5.3.5. Magnetic Hyperthermia Studies

Figure 5.22 shows the time dependent temperature rise of 1 ml aqueous suspension of the APTES coated magnetite nanoparticles (IO@APTES) with the iron concentrations of 0.5, 1, 2.5, 5 and 10 mg/ml upon exposure to 89 kA/m AC magnetic field at 240 kHz frequency. The time required to raise the temperature up to 42ºC for the IO@APTES

nanoparticles with different iron concentration (0.5-10 mg/ml) are given in Table 5.3. The results indicate that the rate of temperature rise systematically increases with the iron concentration of both the IO@APTES nanoparticles (Figure 5.33). The heating of the IO@APTES nanoparticles under AC magnetic field could be due to Neel and Brownian loss which arise from rotation of the magnetization vector and the nanoparticles itself, respectively [35]. Inset of Figure 5.22 depicts the AC magnetic field (H) dependent SAR (specific absorption rate) values of the IO@APTES nanoparticles with 1 mg/ml iron concentration at 240 kHz frequency, indicating that the SAR values varies nearly with H^2 as reported in literature [36-37].

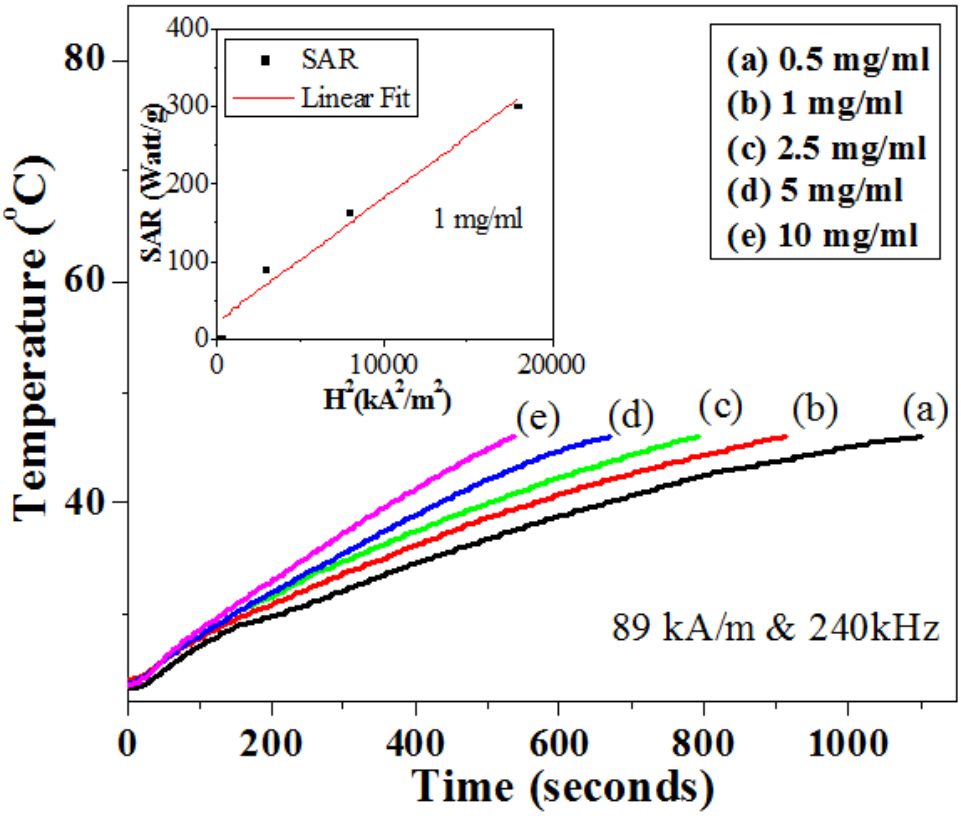

Figure 5.22. Time dependent temperature rise of 1 ml IO@APTES sample with different iron concentration. Inset shows field dependent SAR values of 1 ml IO@APTES sample.

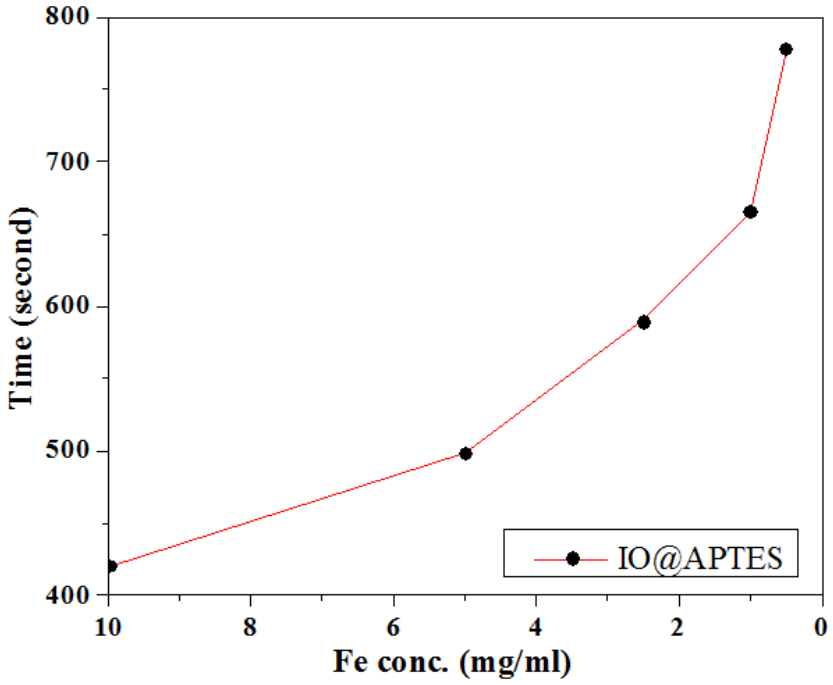

Figure 5.23. The time required time to raise the temperature up to 42 ℃ for the IO@250 and IO@APTES nanoparticles with different Fe concentrations.

Table 5.3. The time required to raise the temperature up to 42 ℃ for the IO@APTES nanoparticles with different Fe concentrations.

Sample	Fe Concentration (mg/ml)	Time required (second)	Magnetic field (kA/m)	Frequency (kHz)
IO@APTES	10	420	89	240
	5	498		
	2.5	589		
	1	665		
	0.5	778		

5.3.6. MRI Relaxivity Studies

Figure 5.24 A and B show the transverse relaxation rates (1/T2 and 1/T2* at 9.4 T) of the IO@APTES and IO@PLA-TPGS nanoparticles with different Fe concentration. The corresponding relaxivities ($r1$, $r2$, and $r2^*$) values of the IO@APTES are estimated as 0.4543, 168.3 and 275.2 $mM^{-1}s^{-1}$ and those values for the IO@PLA-TPGS nanoparticles are estimated as 0.3772, 104.9 and 224.4 $mM^{-1}s^{-1}$respectively which indicates both the IO@APTES and IO@PLA-TPGS nanoparticles could be used as a T2 MRI contrast agent. Moreover, the $r2$, and $r2^*$ relaxivity values of the IO@APTES nanoparticles are relatively greater than that of the IO@PLA-TPGS nanoparticles due to the greater magnetization of IO@APTES nanoparticles (Ms = 63 emu/g) than that of IO@PLA-TPGS (Ms = 25 emu/g).

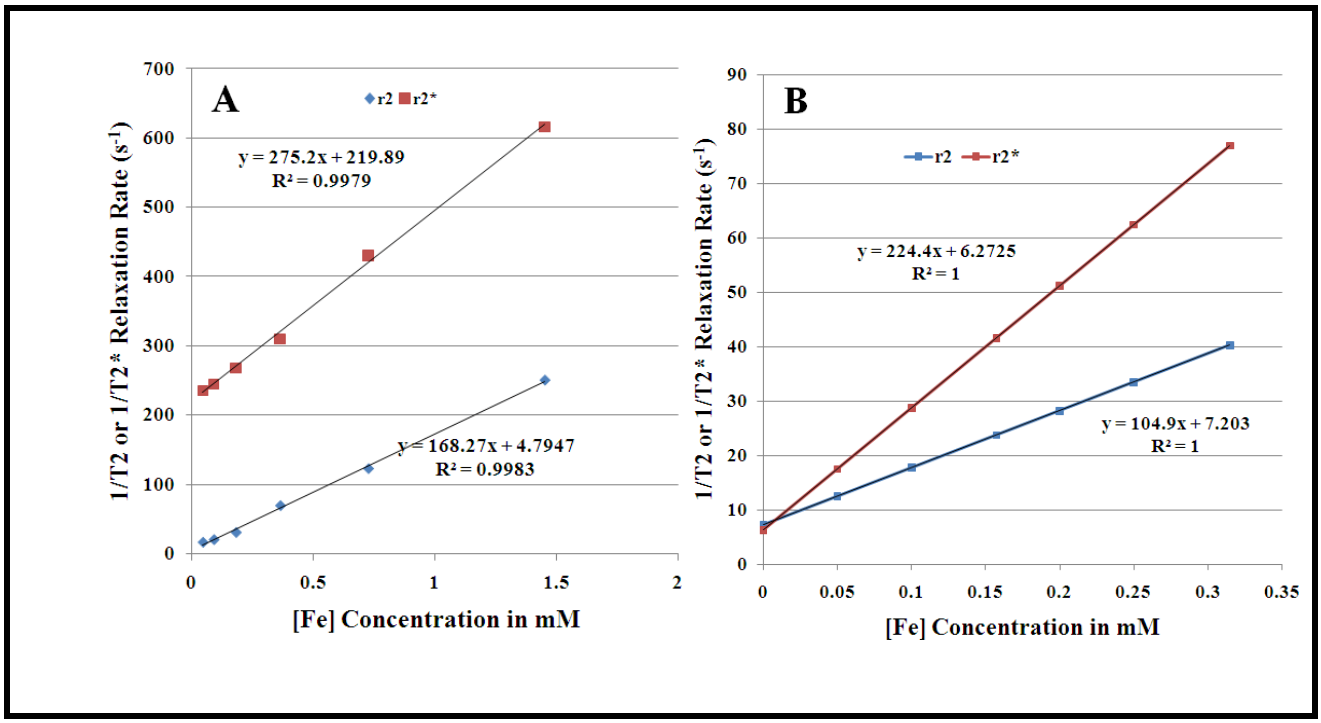

Figure 5.24. Transverse relaxation rates (1/T2 and 1/T2*) vs Fe concentration of **A.** IO@APTES and **B.** IO@PLA-TPGS nanoparticles measured at 9.4 T.

5.3.7. In vivo MRI Imaging

Figure 5.25 show the coronol image of the rat liver before injection (A) and after injection (B) of the IO@PLA-TPGS nanoparticles. The postcontrast image (Figure 5.25 B) shows a darker liver image compared to the precontrast image (Figure 5.25 A) indicating accumulation of the IO@PLA-TPGS nanoparticles in the liver. Hence, signal reduction is occurred due to the change of brightness i.e. darkness in MRI image due to accumulation of IO@PLA-TPGS nanoparticles in the liver. This signal reduction after administration of the IO@PLA-TPGS nanoparticles indicating that the IO@PLA-TPGS nanoparticles could be used as a good MRI contrast agent.

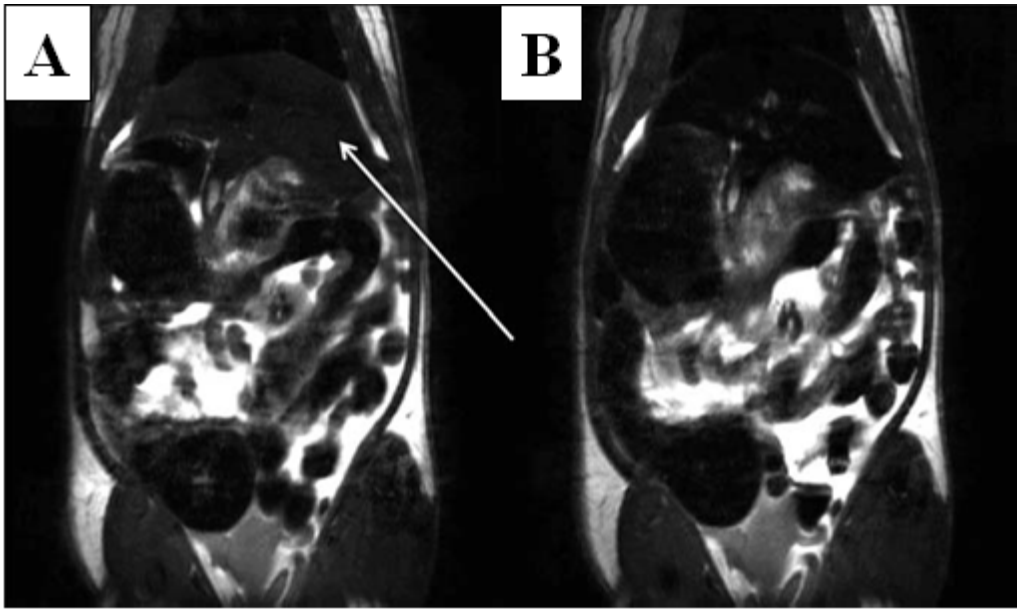

Figure 5.25. Shows the coronol image of the rat liver before injection (**A**) and after injection (**B**) of the IO@PLA-TPGS nanoparticles. Arrows indicate liver of the rat.

5.4. Conclusions

The hydrophobic nanoparticles are successfully converted into the hydrophilic nanoparticles either by functionalization or polymeric encapsulation. The M_S values of the PDA, PAA and APTES modified nanoparticles are found to be different (54, 60, 65 and 63 emu/g respectively) because of the different amount of nonmagnetic (surfactant or polymer) coating on to the Fe_3O_4 nanoparticle surface. The surface modified magnetite nanoparticles are superparamagnetic in nature at the room temperature. The preparation of the encapsulated PLA-TPGS nanoparticles by the nanoprecipitation method is more efficient over the single emulsion method with respect to higher encapsulation efficiency, controlled particle size, higher Ms and the uniformity of the distribution of magnetic nanoparticle within the polymeric matrix.

In vitro cell viability studies indicate that both the IO@APTES and IO@PLA-TPGS nanoparticles are cytocompatible up to the iron concentration of 10 mg/ml. The significant temperature rise of the IO@APTES nanoparticles upon exposure of AC magnetic field upto 89 kA/m at 240 kHz frequency confirm their potential applicability for magnetic hyperthermia applications. The $r2^*$ relaxivity values of the IO@APTES nanoparticles ($r2^*$= 275.2 $mM^{-1}s^{-1}$) are found to be relatively greater than that of the IO@PLA-TPGS nanoparticles ($r2^*$= 224.4 $mM^{-1}s^{-1}$) due to the greater magnetization of IO@APTES nanoparticles (Ms = 63 emu/g) than that of IO@PLA-TPGS (Ms = 25 emu/g). Thus, both the IO@APTES and IO@PLA-TPGS nanoparticles could be used as a MRI T2 contrast agent and the IO@PLA-TPGS nanoparticles demonstrated promising contrast *in vivo* MR imaging.

5.5. References

1. J. Xie, S. Peng, N. Brower, N. Pourmand, S. X.Wang, S. Sun, Pure Appl. Chem. 78 (2006) 1003.

2. X. Michalet, F.F. Pinaud, L.A. Bentolila, J.M. Tsay, S. Doose, J.J. Li, G. Sundaresan, A.M. Wu, S.S. Gambhir, S. Weiss. Science 307 (2005) 538.

3. I. L. Medintz, H.T. Uyeda, E.R. Goldman, H. Mattoussi. Nat. Mater. 4 (2005) 435.

4. R. Gref, A. Domb, P. Quelled, T. Blunk, R.H. Miillerd, J.M. Verbavatz, R. Langer, Adv. Drug Del. Rev. 16 (1995) 215.

5. J.M. Anderson, M.S. Shive, Adv. Drug Del. Rev. 28 (1997) 5.

6. S-S. Feng Nanomedicine 1(2006) 297.

7. Y.C. Dong, S.-S. Feng, Biomaterials 25 (2004) 2843.

8. Y.C. Dong, S.-S. Feng, J. Biomed. Mater. Res. A 78A (2006) 12.

9. Z.P. Zhang, S.-S. Feng, Biomaterials 27 (2006) 262.

10. Z.P. Zhang, S.-S. Feng, Biomaterials 27 (2006) 4025.

11. S.-J. Lee, J.-R. Jeong, S.-C. Shin, J.-C. Kim, Y.-H. Chang, K.-H. Lee, J.-D. Kim, Colloids Surf, A 255 (2005) 19.

12. Y. Wang, Y.W. Ng, Y. Chen, B. Shuter, J. Yi, J. Ding, S.-c. Wang, S. -S. Feng, Adv. Funct. Mater. 18 (2008) 308.

13. S. Staunmesse, A.M. Orechioni, E. Nakache, F. Puisieux, H. Fessi. Colloid Polym. Sci. 273 (1995) 505.

14. J. Cheng, B.A. Teply, I. Sherifi, J. Sung, G. Luther, F.X. Gu, E. Levy-Nissenbaum, A.F. Radovic-Moreno, R. Langer, O.C. Farokhzad, Biomaterials 28 (2007) 869.

15. B.-S. Kim, J.-M. Qiu, J.-P. Wang, T.A. Taton, Nano Lett. 10 (2005) 1987.

16. J. Lu, S. Ma, J. Sun, C. Xia, C. Liu, Z. Wang, X. Zhao, F. Gao, Q. Gong, B. Song, X. Shuai, H. Ai, Z. Gu Biomaterials 30 (2009) 2919.

17. M. Talelli, C.J.F. Rijcken, T. Lammers, P.R. Seevinck, G. Storm, C.F.v. Nostrum, W.E. Hennink, Langmuir 25 (2009) 2060.

18. R. Solaro, China-EU Forum on Nano Technology, Beijing, P R China (2002).

19. D. Maity, D.C. Agrawal, J. Magn. Magn. Mater. 308 (2007) 46.

20. L. Shen, P.E. Laibinis, T.A. Hatton, Langmuir 15 (1999) 447.

21. J. Xie, C. Xu, N. Kohler, Y. Hou, S. Sun, Adv. Mater., 19 (2007) 3163

22. T. Zhang, J. Ge, Y. Hu, Y. Yin, Nano Lett. 7 (2007) 3203.

23. S.F. Farah U.S. Patent 5217743 (2003).

24. A.d. Campo,T. Sen, J-P. Lellouche, I.J. Bruce, J. Magn. Magn. Mater. 293 (2005) 33.

25. D. Caruntu, B.L. Cushing, G. Caruntu, C.J. O'Connor, Chem. Mater. 17 (2005) 3398.

26. M. Yamaura, R.L. Camilo, L.C. Sampaio, M.A. Macêdo, M. Nakamurad, H.E. Tomad J. Magn. Magn. Mater. 279 (2004) 210

27. A.P. Herrera, C. Barrera C. Rinaldi, J. Mater. Chem. 18 (2008) 3650.

28. G.T. Hermanson, Bioconjugate Techniques, second ed., Elsevier, (2008) p.566.

29. R.M. Cornell, U. Schwertmann, The Iron Oxides: Structure, Properties,Reactions, Occurrence and Uses, second ed., Wiley–VCH, Weinheim, (2003).

30. J.R. Dyer, Applications of Absorption Spectroscopy of Organic Compounds, Prentice-Hall, Inc., (1965).

31. D. Maity, S-G. Choo, Ji. Yi, J. Ding, J-M. Xue, J. Magn. Magn. Mater. 321 (2009) 1256.

32. D. Maity, S.N. Kale, R.K. Ghanekar, J-M Xue, J. Ding, J. Magn. Magn. Mater. 321 (2009) 3093.

33. X.Q. Xu, H. Shen, J.R. Xu, X.J. Li, Appl. Surf. Sci. 221 (2004) 430.

34. X-C. Shen, X-Z. Fang, Y-H. Zhou, H. Liang, Chem. Lett. 33 (2004) 1468.

35. S. Mornet, S. Vasseur, F. Grasset, E. Duguet, J. Mater. Chem. 14 (2004) 2161.

36. R. Hergt, R. Hiergeist, M. Zeisberger, G. Gl.ockl, W. Weitschies, L.P. Ramirezc, I. Hilgerd, W.A. Kaiser, J. Magn. Magn. Mater. 280 (2004) 358.

37. L.L. Lao, R.V. Ramanujan, J. Mater. Sci.: Mater. Med. 15 (2004) 1061.

CHAPTER 6

One Step Synthesis of Hydrophilic Magnetite Nanoparticles

6.1. Introduction

Magnetite (Fe_3O_4) nanoparticles have been extensively used in magnetic separation [1-3], targeted drug delivery [4-8], as contrast agents magnetic resonance imaging (MRI) [9-14], and hyperthermia for cancer treatment [14-20] due to their superparamagnetic behavior, relatively high saturation magnetization (M_S), low toxicity, good chemical stability and excellent biocompatibility [1,11, 20-23]. The superparamagnetic behavior of the magnetite nanoparticles is highly dependent on their size, shape and crystallinity. Besides the superparamagnetic behaviors and biocompatibility, water suspensibility of the magnetite nanoparticles is another key factor for their successful use in biomedical applications [22-23]. The magnetite nanoparticles synthesized from the co-precipitation method are usually polydisperse in size and heavily aggregated, leading to a poor suspensibility in water. Moreover, due to the limitation of the reaction temperature (<90 ^oC), the magnetite nanoparticle obtained by this method are semi-crystalline (or semi-amorphous) and weekly bonded with the surface capping agents and hence easily oxidized into maghemite structure resulting significant reduction of their M_S value. Therefore, we have demonstrated (in Chapter 3) the synthesis of high quality (i.e. high crystallinity, monodispersed, high Ms and phase pure) magnetite nanoparticles by the high temperature (>200 ^oC) thermal decomposition of iron (III) acetylacetonate, $Fe(acac)_3$ in presence of oleic acid and/or oleylamine [24-27]. However, the obtained magnetite nanoparticles are hydrophobic in nature i.e. they are only suspendable in non-polar (organic) solvent which makes them inappropriate for biomedical applications. Therefore, further surface modifications on these hydrophobic nanoparticles are necessary to optimize their water suspensibility and biocompatibility for *in vivo*

applications. Various surface coating materials such as lipids [28-30], surfactants [31-33], polymers [34-37], silica [38-40] and Au [41-43] have been attempted to convert the hydrophobic magnetite nanoparticles to be hydrophilic.

However, it has been noted that these surface modification procedures are usually very complicated, tedious and time consuming. Moreover, the surface modified magnetite nanoparticles are not preferred for long term applications due to the risk of dissociation of the coating layers, which leads to agglomeration of the nanoparticles. In addition, the use of toxic solvents and chemicals during the surface modifications may reduce the biocompatibility of the surface modified nanoparticles, although iron oxide itself is considered a biocompatible material.

Thus, direct one pot synthesis of hydrophilic magnetite nanoparticles is extremely important to realize the full potential of these materials in biomedicine. Thus, several groups have further modified the thermal decomposition technique to synthesize hydrophilic magnetite nanoparticles by a single step method [44-47]. Thermolysis of $Fe(acac)_3$ in liquid polyol is a very facile technique for synthesizing hydrophilic magnetite nanoparticles. An obvious advantage of this approach is that the polyol acts for a triple role as high-boiling solvent, reducing agent, and stabilizer to efficiently control the particle growth and prevent interparticle aggregation. Thus, no further reducing agent and surfactants are required, which made this process easy to scale-up for mass. In addition, the decomposition in a bio-friendly polyol solvent reduces the chance of lowering the biocompatibility of the magnetite nanoparticles during the organic synthesis.

In this work, we have selected four different liquid polyols (diethylene glycol (bp 245ºC), tri ethylene glycol (bp 280ºC), tetra ethylene glycol (bp 300ºC) and poly ethylene glycol (bp 330ºC) and tried to optimize the reaction parameter to synthesize the high quality hydrophilic magnetite (Fe_3O_4) nanoparticles directly by the thermolysis of iron (III) acetylacetonate in these polyol media. The structure and properties of the as-prepared nanoparticles are characterized to explore their surface structure, morphology and colloidal stability. The hydrophilic nanoparticles are further investigated to evaluate their potentialities for the magnetic hyperthermia therapy and MRI imaging applications.

6.2. Experimental

Absolute ethanol and ethylacetate were used without purification. Di(ethylene glycol) (DEG, 99%), Tri(ethylene glycol), (TEG, 99%), Tetra(ethylene glycol) (TTEG, 99%) poly(ethylene glycol) (PEG, 99%) and Iron(III) acetylacetonate ($Fe(acac)_3$, 97%) were purchased from Sigma-Aldrich.

6.2.1. Synthesis of Hydrophilic Magnetite Nanoparticles

Hydrophilic magnetite nanoparticles were prepared by a modified thermal decomposition method [26]. The reaction temperature was kept above 200ºC because the decomposition temperature of $Fe(acac)_3$ is 200ºC. The flow chart for the above synthesis procedure is shown in Figure 6.1.

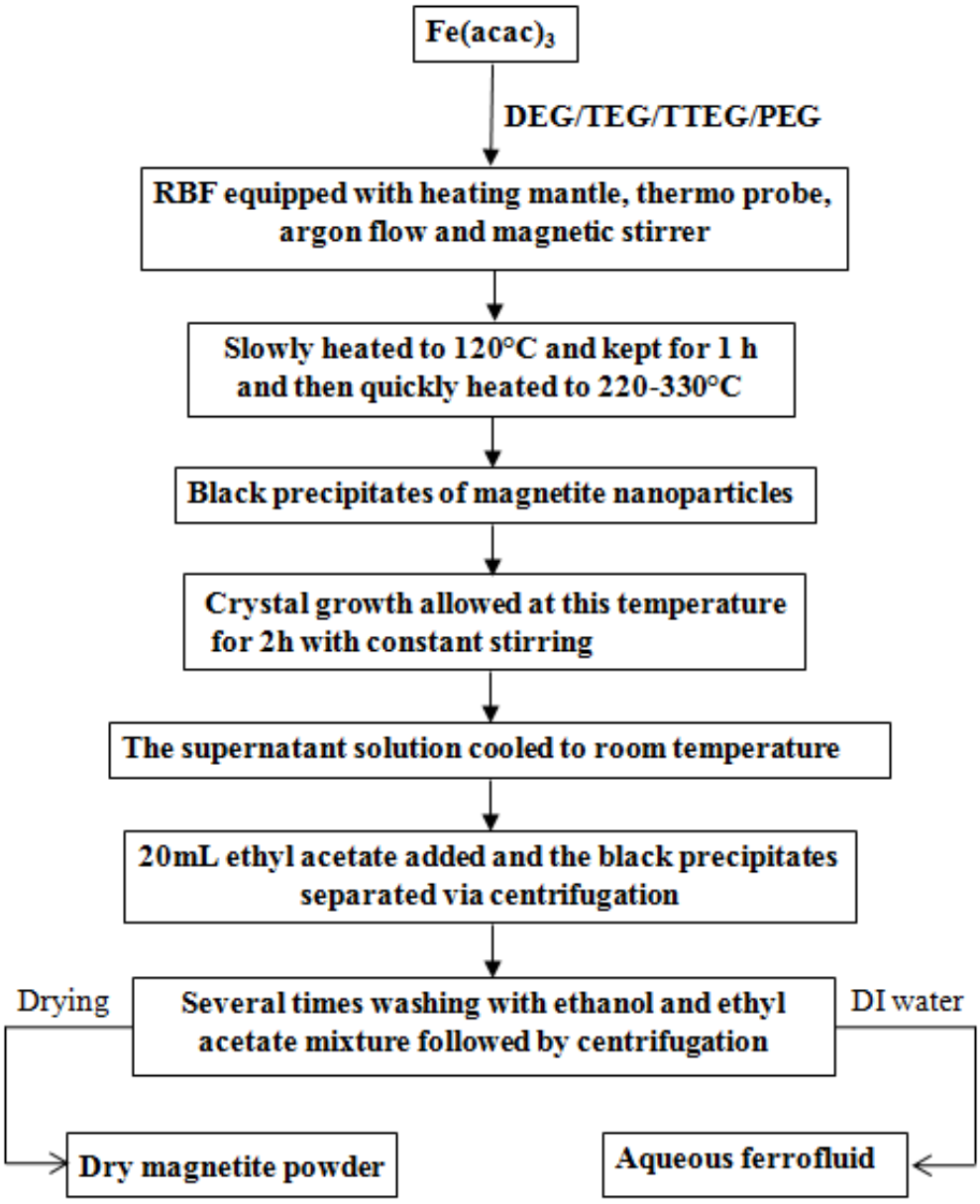

Figure 6.1. Flow chart for synthesis of hydrophilic magnetite nanoparticles by thermal decomposition.

Typically, 2 mmol of $Fe(acac)_3$ was dissolved in a 20 ml of polyol (DEG, TEG, TTEG or PEG) medium into a three necked round bottom flask (RBF) and magnetically stirred under a flow of argon. The resulting solution was dehydrated at 120°C for 1 h, and then

quickly heated to a certain temperature (up to refluxing temperature) and kept at this temperature for 2 h reaction time. The resulting black supernatant solution was cooled to room temperature by removing the heat source. A 20 mL of ethyl acetate was added into the supernatant solution and the precipitated particles were collected by centrifugation at 10000 rpm. The precipitated particles were washed several times using 1:2 (v/v) ethanol and ethyl acetate mixture followed by centrifugation. Finally, one half of the washed particles were dispersed in deionized (DI) water to get a stable aqueous ferrofluid suspension and the other half were dried overnight (at 40°C) in oven to obtain dry magnetite nanoparticles for characterizations. Thus, all the samples prepared using different reaction temperature is given in Table 6.1.

Table 6.1. Hydrophilic magnetite nanoparticles samples and corresponding results.

Sample code	**Preparation condition**		**Zeta Potential (mV)**	**TEM Particle Size (nm)**	**M_S (emu/g)**	**Water solubility**
	Polyols	**Temp. (°C)**				
P1		245 (reflux)	+35	7	59	good
P2	DEG	220	+40	---	50	good
P3 (IO@280)		280 (reflux)	+40	11	65	good
P4 (IO@250)	TEG	250	+42	9	60	good
P5 (IO@220)		220	+45	5	52	good
P6		310 (reflux)	+17	14	70	not good
P7	TTEG	250	+26	---	61	not good
P8		220	+36	---	52	good
P9		330 (reflux)	+6	13	68	not good
P10	PEG	250	+16	8	60	not good
P11		220	+30	4	48	good

6.2.2. Characterization of Nanoparticles

Size and morphology of the as-prepared nanoparticles were determined using transmission electron microscopy (TEM, JEOL 2010) while their crystal structure was identified by X-ray diffraction (XRD, Bruker D8 Advance). Surface charge and surface coating of the nanoparticles were recognized by Fourier transform infrared spectroscopy (FTIR, Varian 3100), X-ray photoelectron spectra (XPS, Kratos AXIS Ultra DLD), thermogravimetric analysis (TGA, DMSE SDTQ600) and Laser Doppler anemometry (Zetasizer Nano-ZS, Malvern Instruments). Magnetic properties of the nanoparticles were studied by the superconducting quantum interference device (SQUID, Quantum Design, MPMS XL) and vibrating sample magnetometer (VSM, Lakeshore, Model 665).

Cell viability studies were performed by MTT assay using MCF-7 mammalian breast cancer cells and NIH-3T3 mouse fibroblast cell lines. In one experiment, the MCF-7 cancer cells were incubated for 24 h with media containing polyol (DEG, TEG, TTEG and PEG) coated nanoparticles at concentrations ranging from 0.625 – 10 mg/ml Fe. In another experiment, the both NIH-3T3 and MCF-7 cells were incubated for 24 h with media containing TEG coated (IO@250, prepared at 250 ºC) and Resovist® nanoparticles (Schering AG, BERLIN, Table 6.2) at concentrations ranging from 7 to 57 µg of Fe/well. The cellular uptake studies were performed by both qualitatively and quantitatively on the MCF-7 cancer cells using the IO@250 and Resovist® nanoparticles. AC magnetic field induced heating ability of the as prepared magnetite nanoparticles was determined from the time-dependent calorimetric measurements while *in vitro* cellular hyperthermia measurements were performed on MCF-7 cancer cells using a RF generator operating at 240 kHz. The T1, T2 and $T2^*$ relaxation times of aqueous suspensions of IO@250 and

Resovist® containing various Fe concentrations of 0.0066 – 0.4 mM were measured using 1.5T MRI scanner and 9.4T MRI scanner. I*n vivo* MRI studies were carried out on Wistar rats and tumor-bearing SCID mice using a Bruker 7T Clinscan MRI.

Table 6.2. Physical Properties of commercial Resovist®

Component	Water based ferrofluid consisting carboxydextran-coated superparamagnetic iron oxide (SPIO) particles
Hydrodynamic diameter (nm)	between 45 and 60
Viscosity at 37 °C (mPa x s)	1.03
Density at 37° C (g/ml)	1.057
PH	5.5 - 7.0

6.3. Results and Discussion

The boiling point (i.e. refluxing temp) of DEG, TEG, TTEG and PEG are 245, 280, 310 and 330ºC respectively. The Fe_3O_4 nanoparticles are prepared at maximum reaction temperature i.e. at the corresponding refluxing temperature of DEG, TEG, TTEG and PEG and then prepared lowering the reaction temperature to compare their properties with those prepared at the refluxing temperature.

6.3.1. Crystal structure

Figure 6.2 (a), (b), (c) and (d) are the XRD patterns of the P1, P3, P6 and P9 samples prepared in DEG, TEG, TTEG and PEG at their refluxing temperature at 2h reaction interval. Position of the diffraction peaks match well with the standard XRD data for bulk magnetite (JCPDS file No. 19-0629) which indicating the formation of Fe_3O_4 phase.

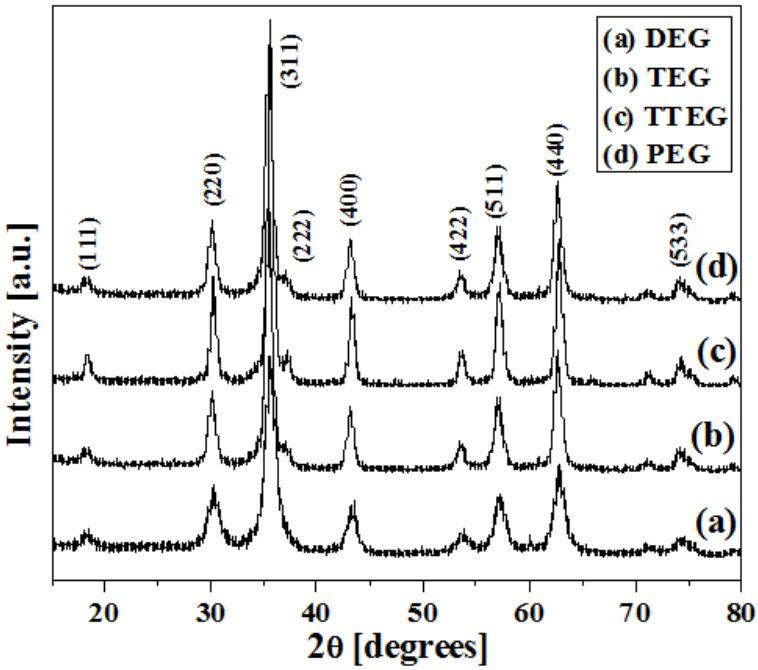

Figure 6.2. XRD patterns of the magnetite nanoparticles prepared in different polyols at their refluxing temperature: (a) DEG (245ºC), (b) TEG (280ºC), (c) TTEG (310ºC) and (d) PEG (330ºC).

6.3.2. Size and Morphology

Figure 6.3 shows the TEM images of the P1, P3, P6 and P9 samples prepared in DEG, TEG, TTEG and PEG at their refluxing temperature at 2h reaction interval. The average sizes of the particles are about 7, 11 and 14 and 13 nm respectively. TEM images (Figure 6.3) indicate that the particles prepared in DEG and TEG are very well dispersed however, those prepared in TTEG and PEG are very much agglomerated in an aqueous medium. It is to note that the refluxing temperature of PEG (330 ºC) and TTEG (300 ºC) are quite higher than that of DEG (245 ºC) and TEG (280 ºC). The reason for the agglomeration of the magnetite nanoparticles which are prepared in TTEG and PEG

could be due to the degradation of these polyols at very high refluxing temperature. Thus, interests arise to synthesize magnetite nanoparticles without any agglomeration lowering the reaction temperature below refluxing temperature.

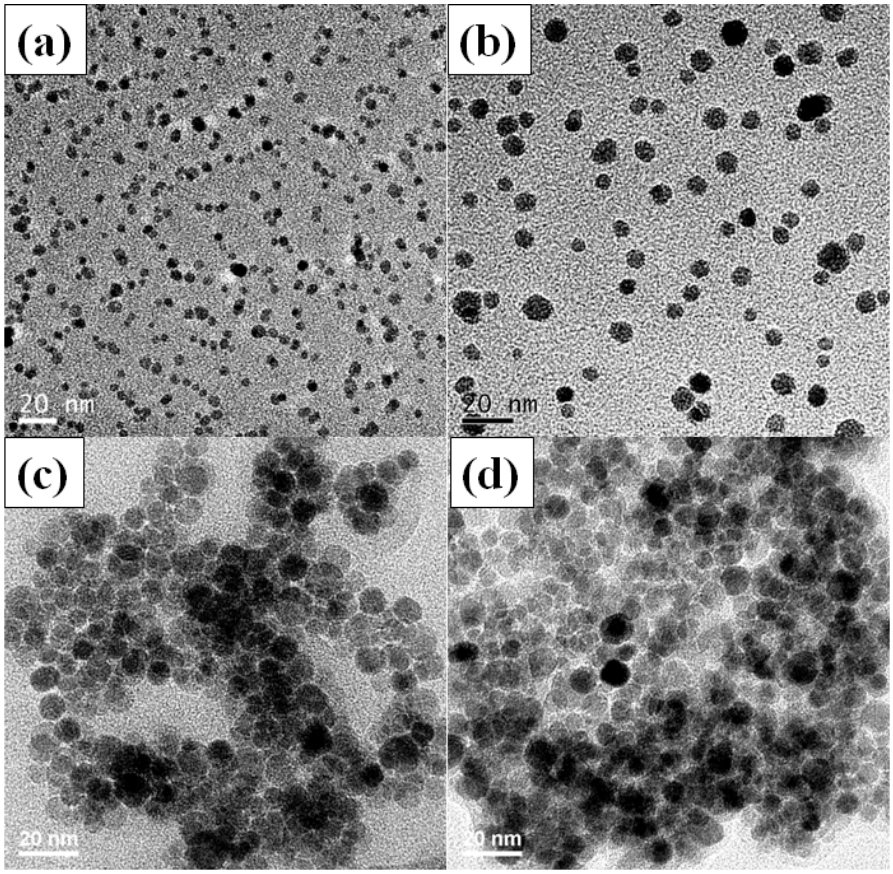

Figure 6.3. TEM images of the magnetite nanoparticles prepared in different polyols at their refluxing temperature: (a) DEG (245ºC), (b) TEG (280ºC), (c) TTEG (310ºC) and (d) PEG (330ºC).

Figure 6.4 shows the TEM images of the P10 and P11 samples prepared in PEG lowering the reaction temperature to 250 and 220 ºC respectively. It can be seen that particle size has been reduced from 13 to 4 nm while decreasing the reaction temperature from 330 to220 ºC (Table 6.1) however, the TEM images (Figure 6.4) indicate that the particles

prepared in PEG medium below the refluxing temperature particularly at 220 ºC (Figure 6.4 B) are very well dispersed without any agglomeration. In a similar way, well dispersed magnetite nanoparticles are obtained by lowering the reaction temperature to 220 ºC.

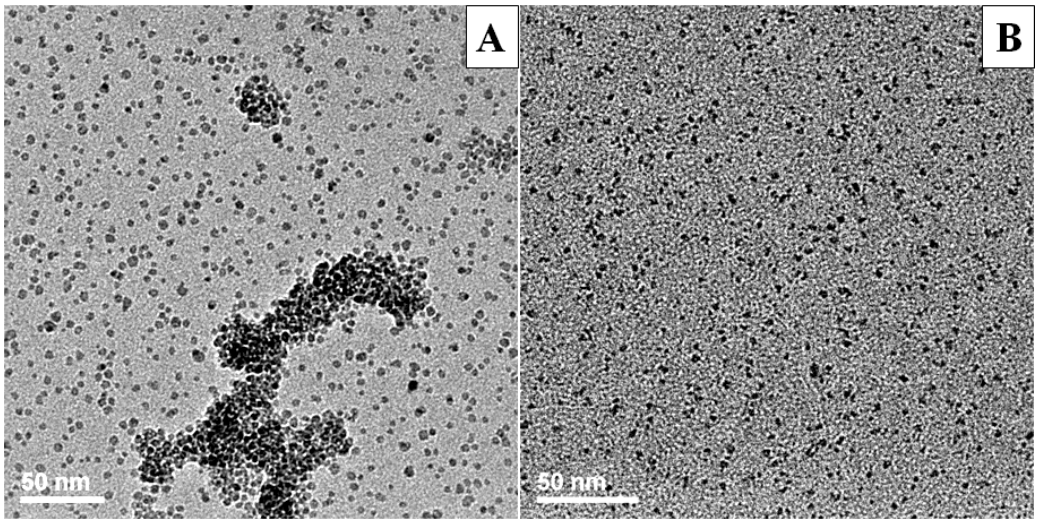

Figure 6.4. TEM images of the magnetite nanoparticles prepared in PEG medium using reaction temperature **A.** 250 and **B.** 220^{o}C.

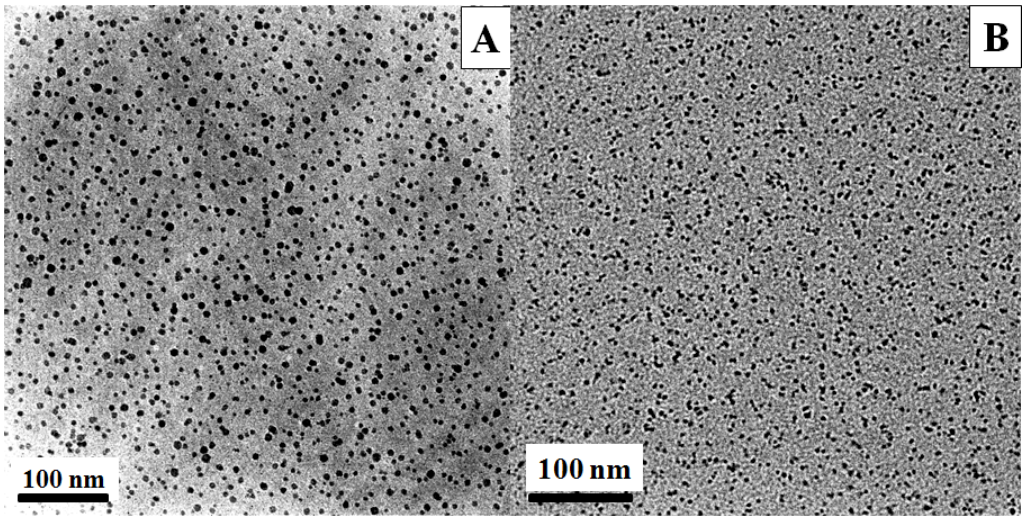

Figure 6.5. TEM images of the magnetite nanoparticles prepared in TEG medium using reaction temperature **A.** 250 and **B.** 220^{o}C.

The magnetite nanoparticles prepared in TEG at refluxing temperature (330°C) are well dispersed as shown in Figure 6.3 (b). However, to explore the temperature effect on the particle size and distribution, the magnetite nanoparticles have also been synthesized in TEG medium at lower reaction temperature 250°C and 220°C. Figure 6.5 shows the TEM images of the P4 and P5 samples prepared in TEG using the reaction temperature 250 and 220 ºC respectively. The average size of the magnetite particles are found to be reduced from 11 to 5 nm when the reaction temperature reduced from 280°C to 220°C (Table 6.1).

Figure 6.6 shows the particle size distribution histogram based on the TEM images of the magnetite nanoparticles prepared using different reaction temperatures. The Gaussian size distributions (Figure 6.6) which are 9-14 nm, 7-11 and 3-7 nm corresponding to the reaction temperature 280°C, 250°C and 220°C, respectively, indicates that size distribution of the particles prepared at 250°C and 220°C are narrower than those fabricated at 280°C.

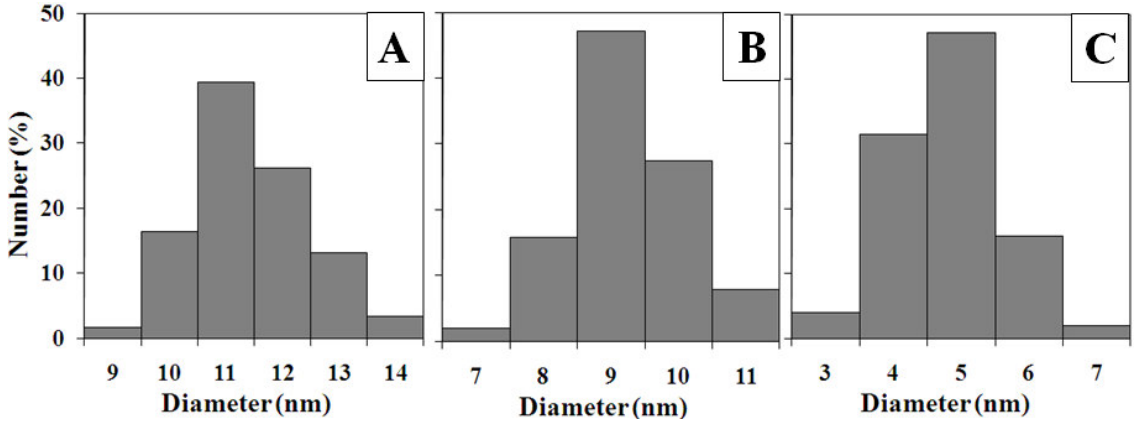

Figure 6.6. Particle size distribution histogram of the magnetite nanoparticles prepared in TEG using reaction temperature **A.** 280, **B.** 250 and **C.** 220°C.

In summary, magnetite nanoparticles prepared in DEG and TEG are well dispersed while those prepared in TTEG and PEG are agglomerated in aqueous suspension. Well dispersed particles are obtained in TTEG and PEG by lowering the reaction temperature below the refluxing temperature. The size of the particles reduces with the lowering of reaction temperature while the size distribution of particles is significantly improved by lowering the reaction temperature below the refluxing temperature.

Figure 6.7 shows the photo of aqueous suspension of magnetite nanoparticles prepared in TEG at 280^{o}C. No phase separation of particles was observed when the aqueous suspension was exposed to a permanent magnet. The flow like liquid (Figure 6.7) in presence of magnet confirms the formation of stable aqueous ferrofluid suspension.

Figure 6.7. Photo of aqueous ferrofluid (in presence of a permanent magnet) consisting of magnetite nanoparticles prepared in TEG at 280^{o}C.

Figure 6.8 A shows the selected area electron diffraction (SAED) of magnetite nanoparticles prepared in TEG at 250^{o}C (P4 samples). Similar SAED pattern were observed for all the samples (Table 6.1) prepared in polyol medium. The clear diffraction rings attributed to the (220), (311), (400), (422), (511) and (440) planes also indicates the magnetite (Fe_3O_4) phase of the nanoparticles prepared in polyol medium. Figure 6.8 B shows the HRTEM image of a single magnetite nanoparticle, in which the lattice fringes are clearly observed, indicating that the resultant magnetite nanoparticles are well crystallized. The lattice spacing of 2.53 A˚, which is the spacing between two (311) planes, also corroborate the magnetite (Fe_3O_4) phase of the nanoparticles.

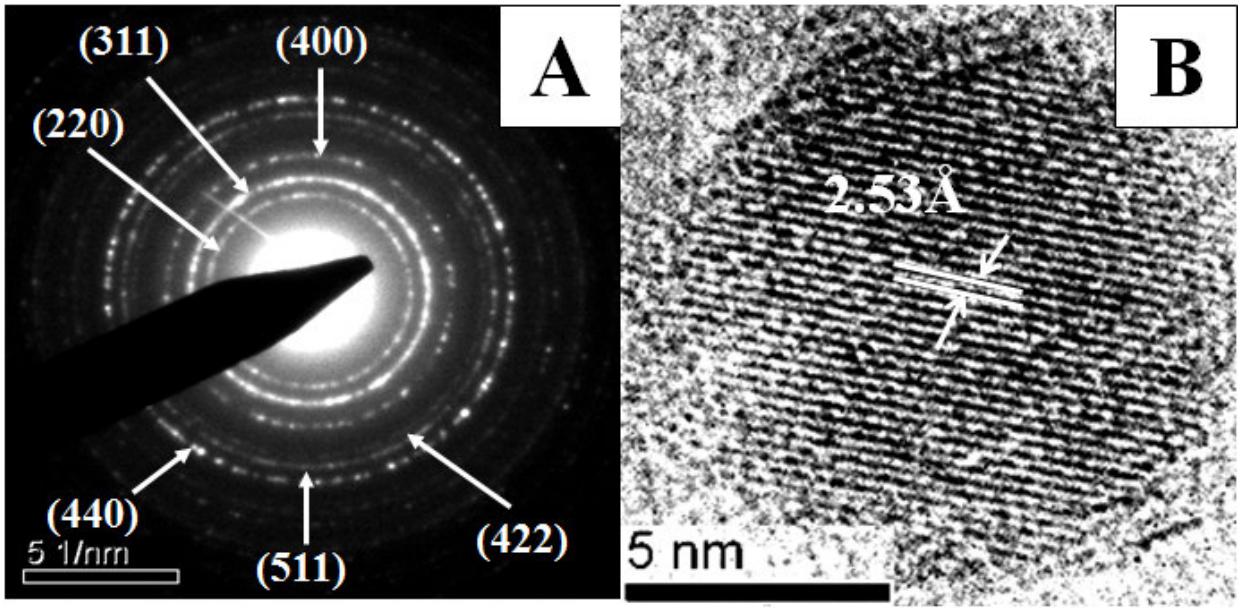

Figure 6.8. A. Selected area electron diffraction (SAED) pattern of P4 samples **B.** HRTEM of a single magnetite nanoparticle.

6.3.3. Identification of Surface Charge and Surface Coating

Figure 6.9 shows FTIR spectra of the P1, P3, P6 and P9 samples prepared in different polyols (DEG, TEG, TTEG and PEG) at the refluxing temperature of corresponding polyols. Similar FTIR peaks are observed for all of the particles prepared in different polyols. The peaks at about 2962-2809, 1632, 1455, 1350; 1251 and 1063 cm^{-1} are due to C–H stretching, O–H stretching, C–H bending, C–O bending and O–H bending vibration respectively, which are attributed to adsorbed polyol molecules onto the particle surface [47]. The broad band between 3600 and 3000 cm^{-1} centered at about 3400 cm^{-1} are due to the O–H stretching vibration attributed for water and polyol molecules adsorbed to the particle surface. In addition, the absorption bands at about 585 cm^{-1} are due to Fe–O stretching vibration for the Fe_3O_4 nanoparticles. Thus, the FTIR spectra (Figure 6.9) indicate that surface of the as-prepared magnetite nanoparticles are adsorbed with polyol coating.

The similar trend of FTIR spectra (Figure 6.10 and Figure 6.11) are observed for the particles prepared in TEG and PEG medium using different reaction temperature. The intensity of the FTIR peaks increases with the decrease of the reaction temperature which indicates that the amount of polyol coating increases while lowering the reaction temperature.

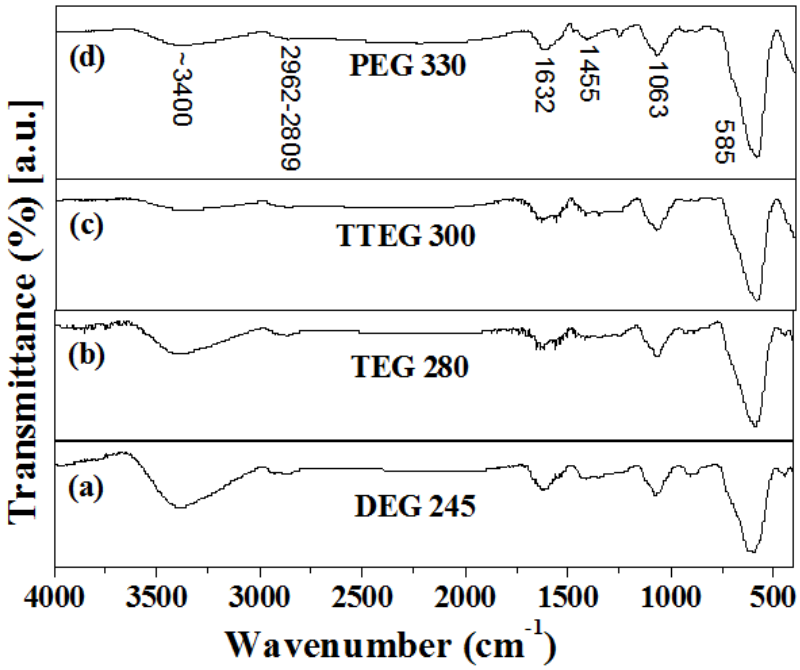

Figure 6.9. FTIR spectra of the magnetite nanoparticles prepared in different polyols: (a) DEG, (b) TEG, (c) TTEG and (d) PEG at their refluxing temperature.

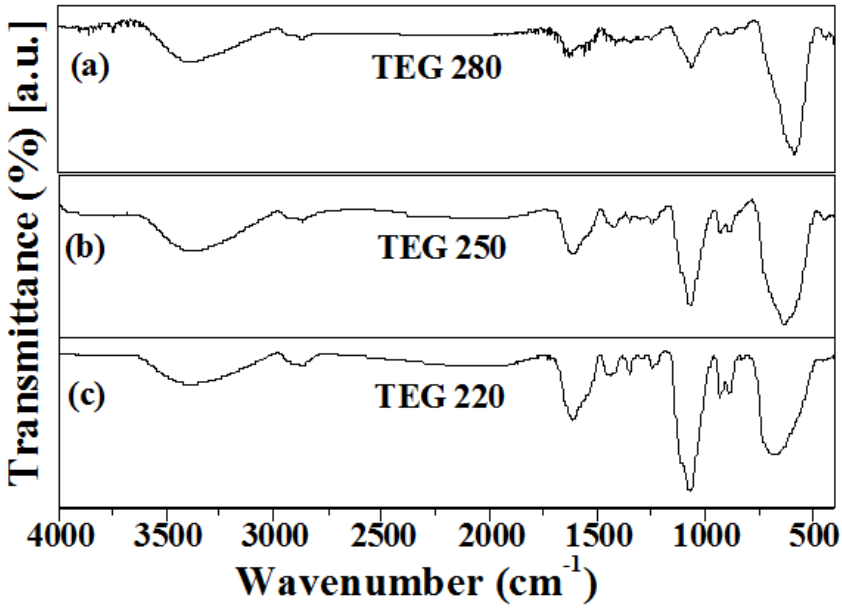

Figure 6.10. FTIR spectra of the magnetite nanoparticles prepared in TEG medium at **(a)** 280 (i.e. refluxing temperature), **(b)** 250 and **(c)** 220^{o}C.

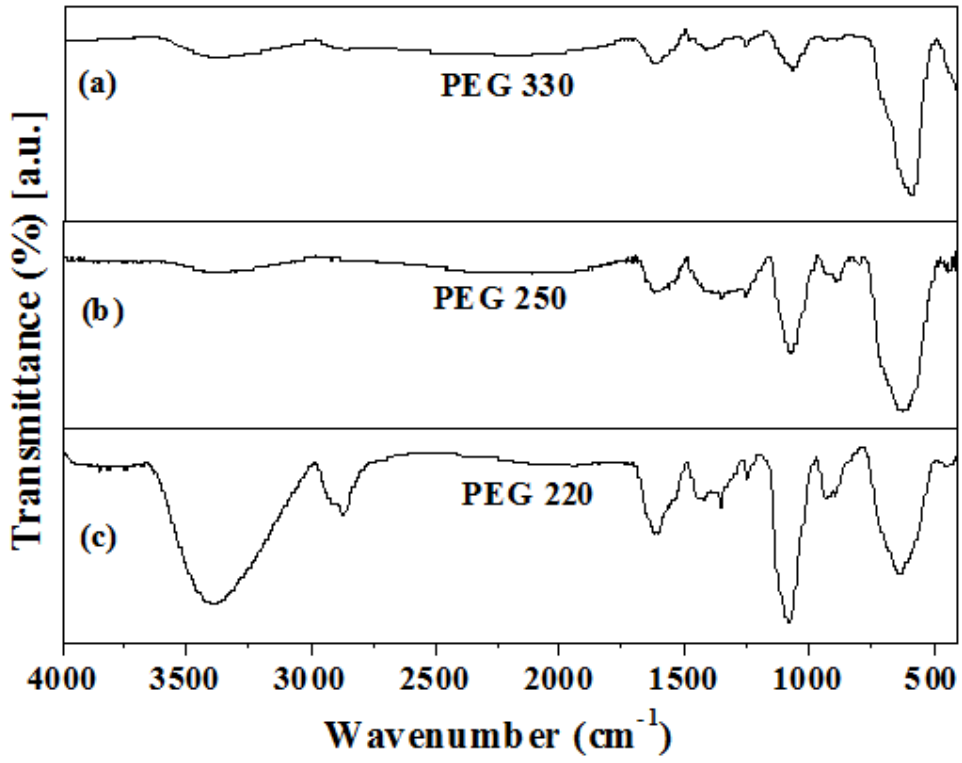

Figure 6.11. FTIR spectra of the magnetite nanoparticles prepared in PEG medium at **(a)** 330 (i.e. refluxing temperature), **(b)** 250 and **(c)** 220^{o}C.

The adsorbed polyols coating on the particle surfaces are furthered recognized by TGA measurements. Figure 6.12 depicts TGA curves of the P1, P3, P6 and P9 samples prepared in different polyols medium (DEG, TEG, TTEG and PEG) at the refluxing temperature of corresponding polyol. TGA curves reveal a two-stage weight loss in the temperature ranges of 25 – 200ºC and 200–800ºC. The first slight amount of weight loss is due to the evaporation of physically adsorbed water and the second major weight loss is due to the decomposition of surface adsorbed polyol coating from the particle.

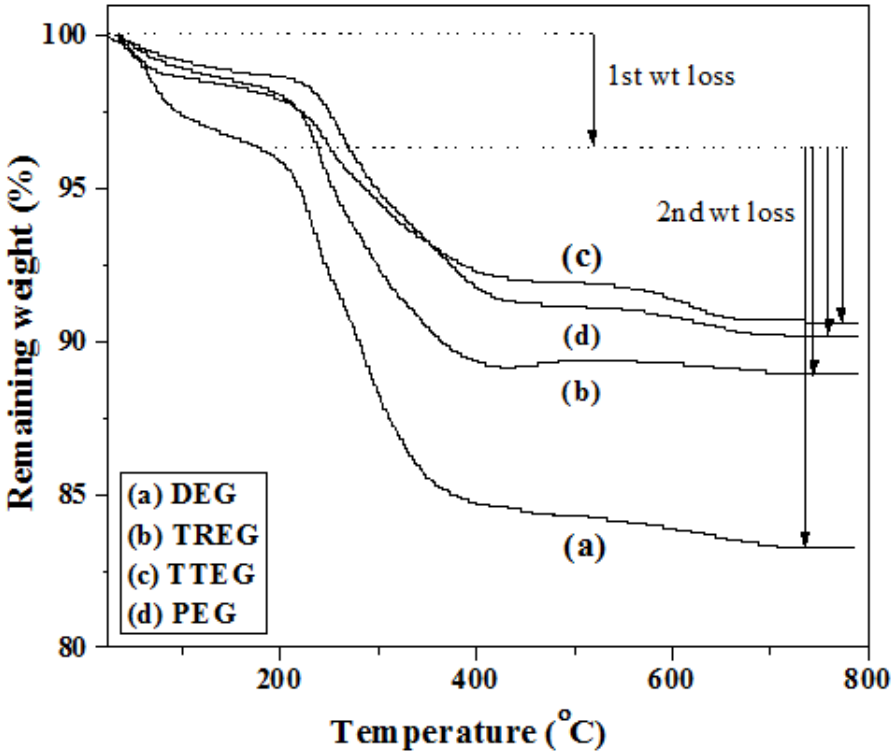

Figure 6.12. TGA curves of the magnetite nanoparticles prepared in different polyols: (a) DEG, (b) TEG, (c) TTEG and (d) PEG at their refluxing temperature.

The total amount of weight losses are estimated as 16.7, 11, 9.3 and 9.8 wt% for the particles prepared in DEG, TEG and TTEG medium respectively. It can be seen that the amount of surface adsorbed polyol coating for the particles prepared in DEG and TEG media is higher than those prepared in TTEG and PEG media which could be due to the degradation of TTEG and PEG molecules at very high refluxing temperature. The similar pattern of TGA curves (Figure 6.13 and Figure 6.14) are observed for the particles prepared in TEG and PEG medium using different reaction temperature. The amount of polyol coating increases with the lowering of the reaction temperature and this trend are found to same for all the polyol coated particles.

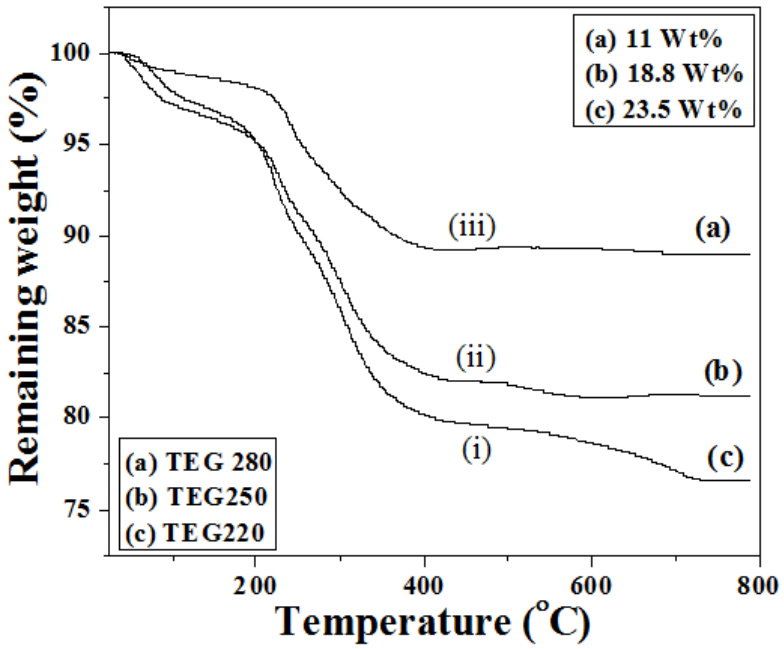

Figure 6.13. TGA curves of the magnetite nanoparticles prepared in TEG medium at **(a)** 280 (i.e. refluxing temperature), **(b)** 250 and **(c)** 220°C.

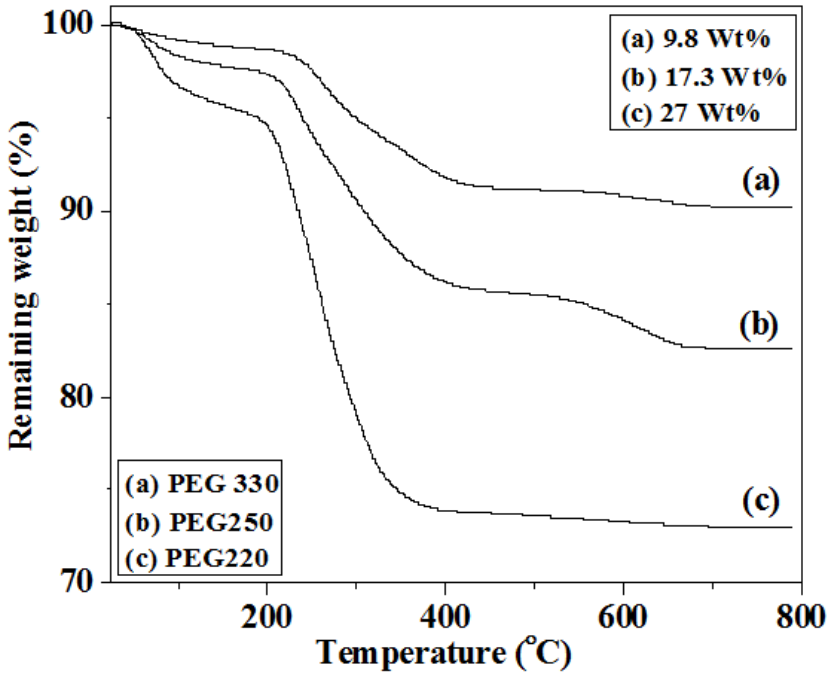

Figure 6.14. TGA curves of the magnetite nanoparticles prepared in PEG medium at (a) 220, (b) 250 and (c) 330°C (i.e. refluxing temperature).

Thus, the FTIR and TGA analysis indicate that surface of the as-prepared magnetite nanoparticles are adsorbed with polyol coating and hence, they are suspendable in an aqueous medium due to the steric repulsions of the surface adsorbed polyol molecules.

Figure 6.15 shows the zeta potential distribution plots of the P1, P3, P6 and P9 samples prepared in DEG, TEG, TTEG and PEG at their refluxing temperature.

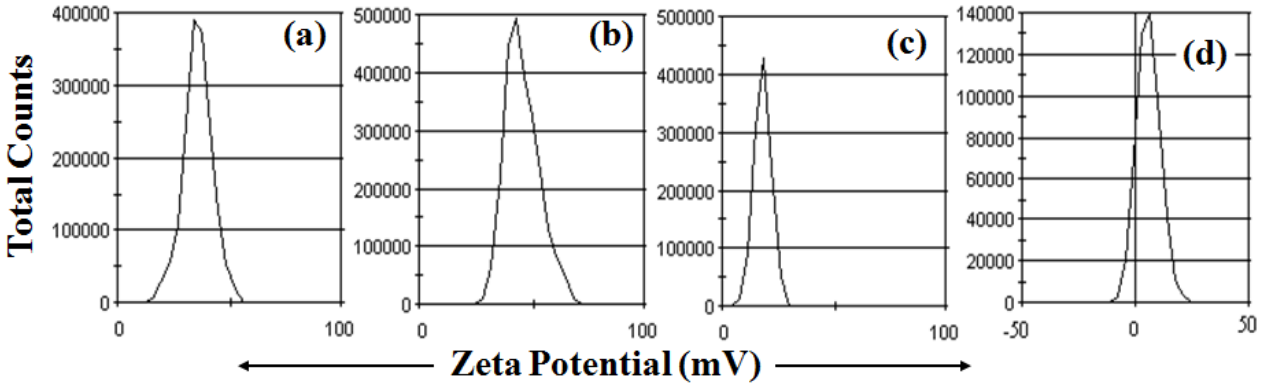

Figure 6.15. Zeta potential distribution plots of the magnetite nanoparticles prepared in different polyols: (a) DEG, (b) TEG, (c) TTEG and (d) PEG at their refluxing temperature.

The positive zeta potential values indicate that surfaces of the polyol coated magnetite nanoparticles are adsorbed with positively charged ions which could be H^+ ions produced due to the polarization of the polyol molecules ($R\text{-}OH \Leftrightarrow R\text{-}O^- + H^+$, where $R \equiv (CH_2\text{-}CH_2\text{-}O)_x\text{-}H$) at elevated reaction temperature [26]. The $R\text{-}O^-$ part of polyol molecules coordinates with Fe^{2+}/Fe^{3+} of the Fe_3O_4 nanoparticle (which is confirmed by FTIR, XPS and TGA) while the H^+ ions associates with the particles along with the $R\text{-}O^-$ and as a consequence surface of the nanoparticles become positively charged. Thus, adsorbed R-

O^- the is responsible for the steric repulsion of the particles while the associated positively charged H^+ ions provide strong electrostatic repulsion between the particles to suspend them in an aqueous media (Figure 6.16) [47].

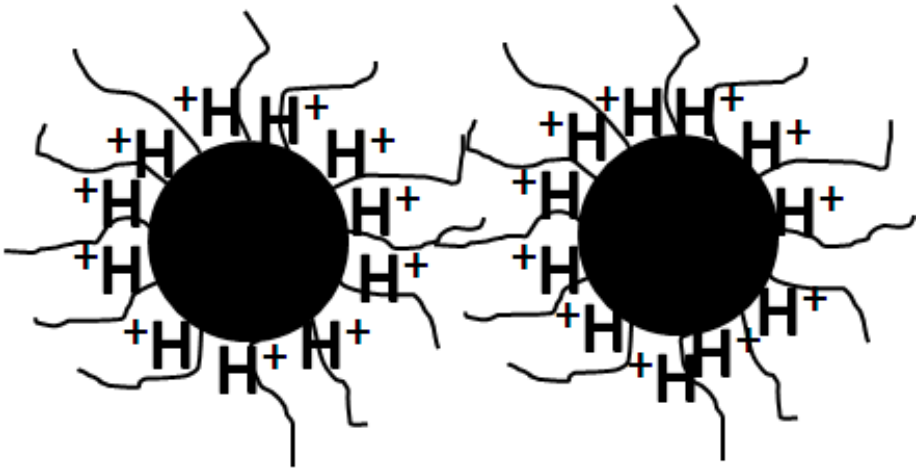

Figure 6.16. Steric and electrostatic interactions between the magnetite nanoparticles in an aqueous suspension.

Zeta potential values of all the samples prepared in different polyol medium using different reaction temperature are given in Table 6.1. Particles with zeta potentials more positive than +30 mV or more negative than -30 mV are normally considered stable. It can be seen that the zeta values of the particles prepared in DEG and TEG are above +30 mV always however, the zeta values are +6 and + 17 mV for the TTEG and PEG coated particles prepared at their refluxing temperature. Thus, the measured zeta potential values indicate that colloidal stability of DEG and TEG coated magnetite particles are very good compare to the TTEG and PEG coated magnetite particles which corroborate with the previous TEM results. The zeta values are found to be increased with the decrease of the reaction temperature for all the polyol coated particles. This could be due to the increase

of the amount of adsorbed polyol coating with the decreasing of reaction temperature as confirmed by FTIR and TGA measurements. Thus, the colloidal stability of the TTEG and PEG coated particles are significantly improved (to +36 and 30 mV respectively) by reducing the reaction temperature to 220 °C.

Figure 6.17 shows wide scan XPS spectra of the P4 samples which are prepared in TEG at 250°C (leveled as IO@250). Inset (i) and (ii) of Figure 6.17 are the corresponding deconvoluted O(1s) and C(1s) spectra. The O(1s) peaks at 531.6 and 533.3 eV are due to O-H and C-O bond which arise from the adsorbed water and TEG coating, respectively [47]. The C(1s) peaks at 285.5 and 288 eV are due to C–C/C–H and C–O–C bond, respectively arise from the chemically adsorbed TEG coating to the particle surface. In addition, the Fe($3p_{3/2}$), O(1s), Fe($2p_{3/2}$) and Fe($2p_{1/2}$) peaks at about 55, 530.3, 710 and 724 eV are due to Fe–O bond of the Fe_3O_4 nanoparticles. The ratio of the Fe^{2+} : Fe^{3+} is estimated as 1:2 from the intensity of the Fe($2p_{3/2}$) and Fe($2p_{1/2}$) peaks indicating that the particles consists of pure Fe_3O_4 phase which also corroborate XRD results (Figure 6.2).

Figure 6.18 shows the zeta potential vs pH plot for the P4 samples which are prepared in TEG at 250°C (leveled as IO@250) suggesting that the isoelectric point (IEP) of the IO@250 nanoparticle is approximately pH 5.9. The colloid stability studies of the nanoparticles were also performed using dynamic light scattering measurements (DLS). Hydrodynamic diameter of the IO@250 nanoparticles suspended in water and cell culture media were initially (at 0 h) measured as 80 and 110 nm respectively. The hydrodynamic diameter was remained around 80 nm in water up to 30 hours, indicating the good

colloidal stability of the IO@250 nanoparticles in water. On the other hand, the hydrodynamic diameter was increased to 180 nm in cell culture media after 30 hours. This could be due to the replacement of TEG coating with ionic groups [48] and the subsequent particle aggregation may be one of the reasons for this size increase in the cell culture media. Although the hydrodynamic size of the particles in the cell culture medium was increased, however good colloidal suspension of the IO@250 nanoparticles was observed even after 30 hours.

In summary, the aqueous stability of as-prepared hydrophilic magnetite nanoparticles fully depends on inter-particle steric and electrostatic interactions arising from the surface adsorbed polyol coating and positively charged H^+ ions. The particles prepared in DEG and TEG are quite stable in an aqueous medium due to large amount of surface adsorbed polyol coating and positive charges. However, the particles prepared in TTEG and PEG are not stable in aqueous suspension due to less amount of polyol coating and charges and thereby less inter-particle interactions. The stability of the aqueous suspension of TTEG and PEG coated particles can be improved by reducing the reaction temperature to 220 ºC. Thus, the aqueous suspension of the PEG coated particles prepared at the refluxing temperature is not good. However, the aqueous stability of the PEG coated particles prepared at 220ºC are good due to the increase of amount of surface-adsorbed polyol coating (27 wt%) and associated positive charges (+30 mV). The aqueous suspension of the TEG coated IO@250 nanoparticles are highly stable at the biological pH = 7.4 (- 43mV).

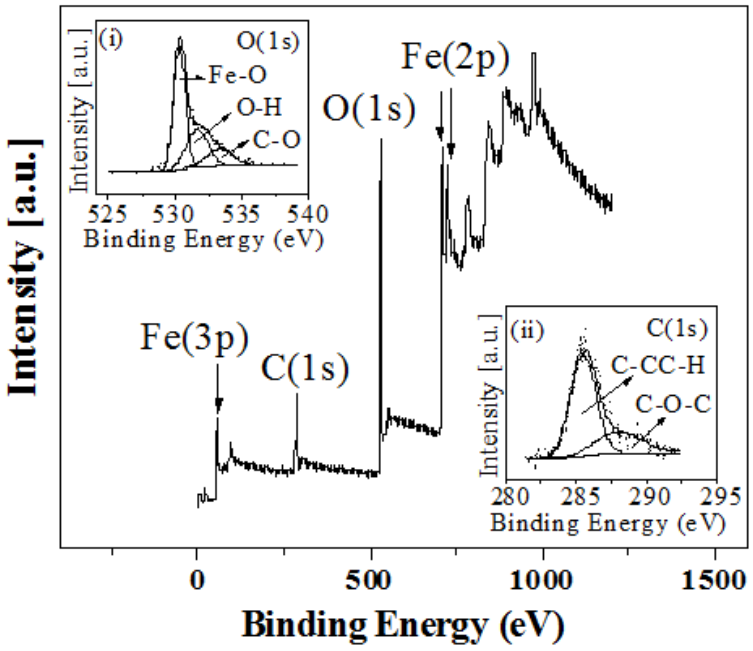

Figure 6.12. Wide scan XPS spectra of the of the p4 samples prepared in TEG at 250°C. Inset (i) and (ii) are deconvoluted O(1s) and C(1s) spectra, respectively.

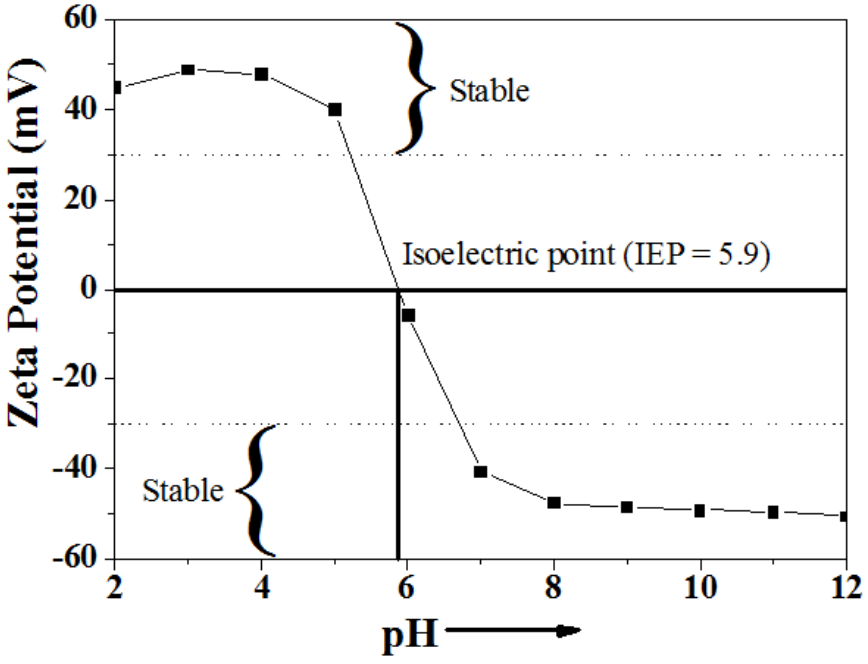

Figure 6.18. Zeta potential vs pH plot of the p4 samples prepared in TEG at 250°C.

6.3.4. Magnetic Properties

Figure 6.19 shows the magnetization (M-H) curves of the P1, P3, P6 and P9 samples prepared in DEG, TEG, TTEG and PEG at their refluxing temperature. Figure 6.20 depict the M-H curves of the PEG coated particles prepared using different reaction temperature. The M_S values of all the samples prepared under different reaction conditions are given in Table 6.1. The saturation magnetizations (Ms) of the TEG coated of magnetite nanoparticles i.e. IO@220, IO@250 and IO@280 nanoparticles (prepared at reaction temperature 220, 250 and 280°C respectively) were measured as 47, 57 and 65 emu/g, respectively. TGA results showed the total amount of weight loss of IO@220, IO@250 and IO@280 nanoparticles as 23.5, 18.8, and 11 wt% (Figure 6.14), suggesting that the amount of magnetite (Fe_3O_4) core content of the corresponding TEG coated IO@220, IO@250 and IO@280 nanoparticles were 76.5, 81.2 and 89 wt% respectively. The M_S values of IO@220, IO@250 and IO@280 nanoparticles were estimated as 62, 70 and 73 emu/g considering only the magnetic core of the nanoparticles (Table 6.1). It can be seen that the M_S value decreases with decrease of the reaction temperature which could be due to the decrease of the particle size (Table 6.1) or the crystallinity while reducing the reaction temperature. The zero coercivity and zero remanance on the M-H curves indicate that the polyol coated hydrophilic magnetite nanoparticles are superparamagnetic (SPM) at the room temperature.

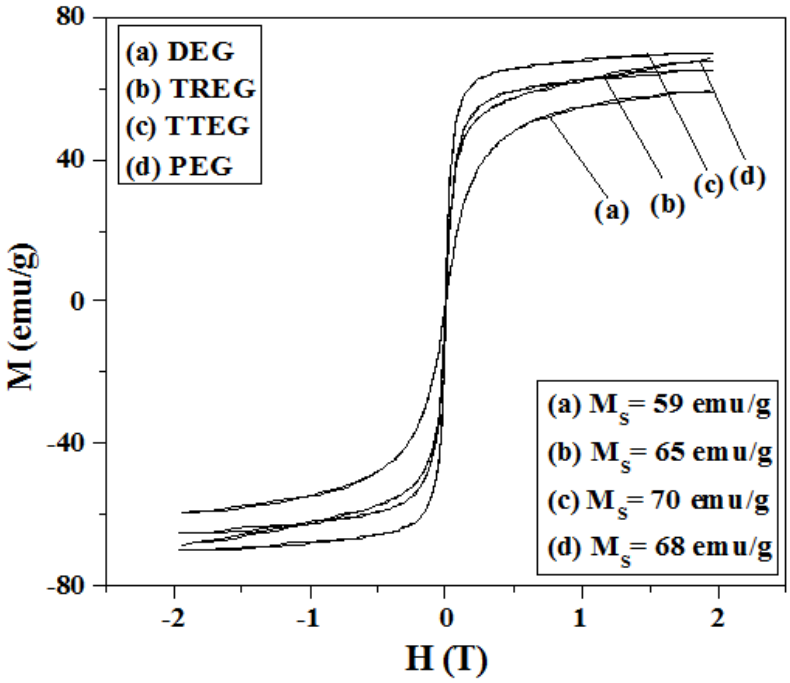

Figure 6.19. M-H curves of the magnetite nanoparticles prepared in different polyols: (a) DEG, (b) TEG, (c) TTEG and (d) PEG at their refluxing temperature.

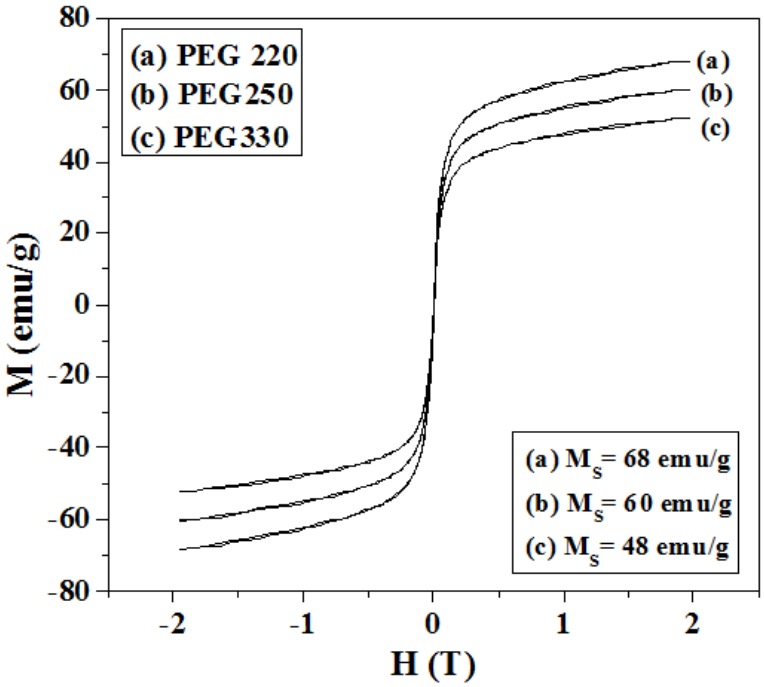

Figure 6.20. M-H curves of the magnetite nanoparticles prepared in PEG medium at **(a)** 330 (i.e. refluxing temperature), **(b)** 250 and **(c)** 220^{o}C.

The zero-field cooled/field cooled (ZFC-FC) magnetization of the polyol coated magnetite nanoparticles was by SQUID under an applied field of 100 Oe. Figure 6.21 shows the temperature dependence of the ZFC-FC magnetization of the magnetite nanoparticles prepared in TEG at 250^{o}C (P4 samples). The similar feature of ZFC-FC curves were observed for all the samples prepared in different polyol medium (Table 6.1). The feature of the ZFC-FC curves indicates that the polyol coated magnetite nanoparticles are of SPM in nature [47]. Inset of figure 6.21 shows the M-H curves of the P4 samples measure by SQUIS at 300 and 10 K. The feature of the M-H curves indicate that the particles are superparamagnetic at the room temperature but ferromagnetic at 10 K with the saturation magnetization (M_S) 70 emu/g.

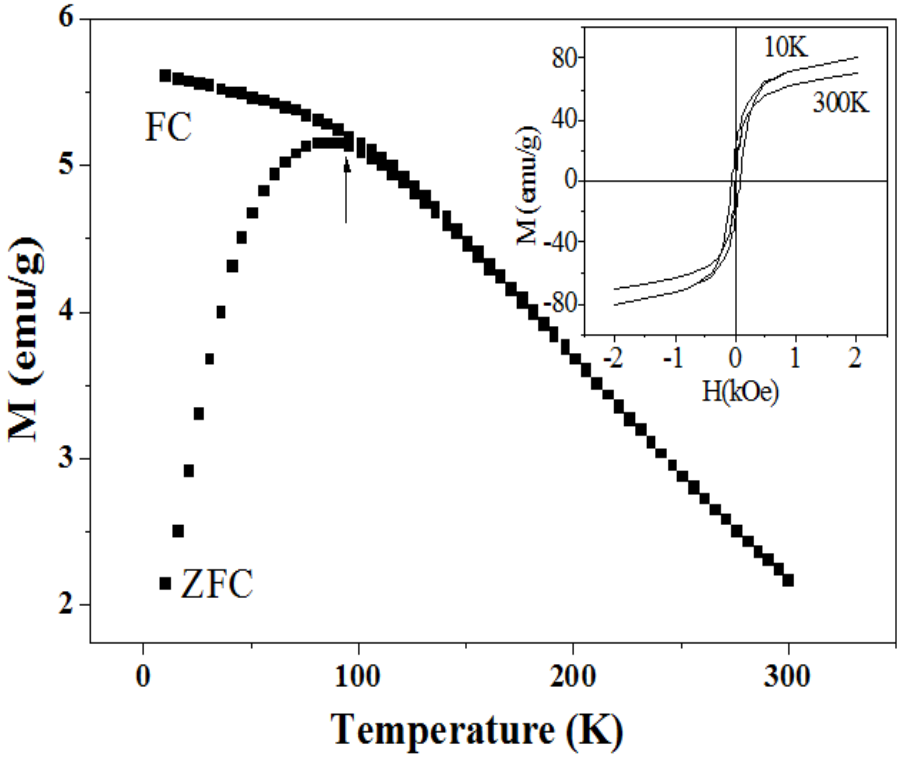

Figure 6.21. ZFC–FC magnetization curves of the magnetite nanoparticles prepared in TEG at 250 ºC. Inset is M-H curves at 10 and 300K.

6.3.5. In Vitro Cytotoxicity Studies

Figure 6.22 shows the cytotoxicity profile of the different polyol (DEG, TEG, TTEG and PEG) coated magnetite nanoparticles using the MCF-7 breast cancer cells. It can be seen that MCF-7 cells do not show any cytotoxicity with the magnetite nanoparticles in the range of 0.625 – 10 mg Fe/ml concentrations. Thus, the polyol coated magnetite nanoparticles are biocompatible up to the iron concentration of 10 mg/ml with MCF-7 breast cancer cells.

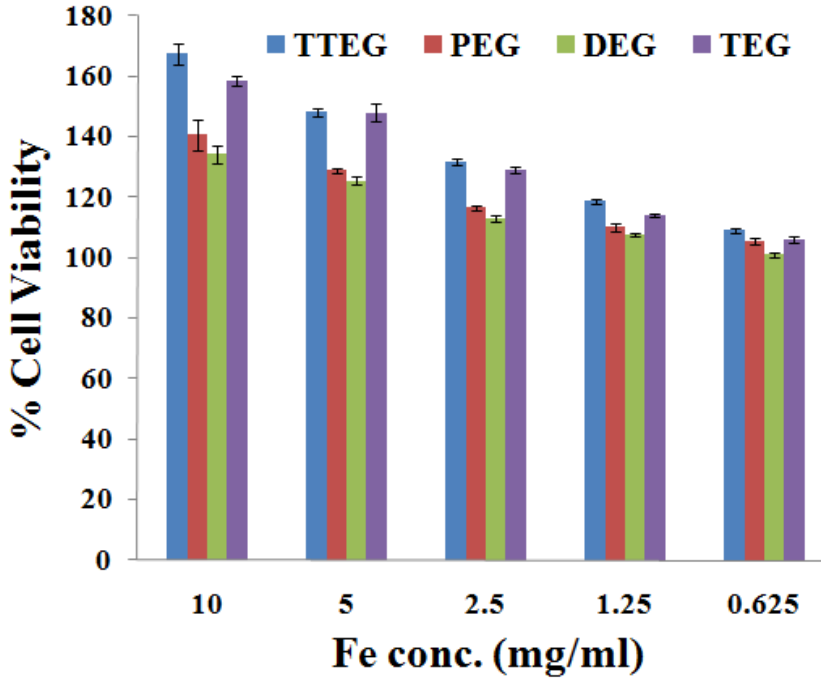

Figure 6.22. Cytotoxicity profile of the polyol (DEG, TEG, TTEG and PEG) coated nanoparticles on MCF-7 breast cancer cells.

Figure 6.23 A and B represent the percentage cell viability of the IO@250 nanoparticles in comparison with Resovist® for NIH-3T3 fibroblast cells and MCF-7 breast cancer cell line respectively. It can be seen from the graph that the IO@250 nanoparticles showed

comparable cytotoxity with the commercial Resovist® nanoparticles at respective concentration of 7-57 µg Fe/well. From the cell viability studies, differences between the two samples were not significant as seen from their respective standard deviation. The samples did not show significant change of viability as compared to the control cells (untreated cell), where the cell viability was considered as 100%. Therefore, it can be inferred from the data that both the samples are cyto-compatible up to the concentration of 57µg of Fe/well, the highest concentration tested in this work.

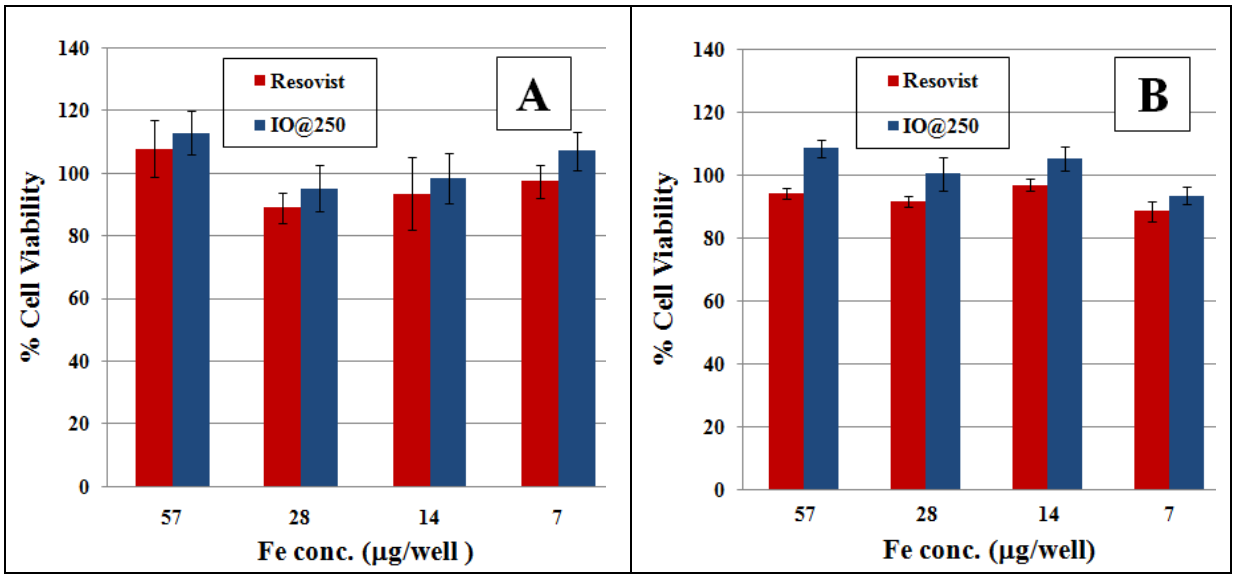

Figure 6.23. Cell toxicity study of IO@250 and Resovist® nanoparticles using **A.** NIH-3T3 fibroblast cells **B.** MCF-7 breast cancer cell line.

6.3.6. In Vitro Cellular Uptake Studies

Cellular uptake study was performed by incubating IO@250 nanoparticles with MCF-7 breast cancer cell line. Figure 6.24 A shows the TEM image of the MCF-7 cell uptaken

IO@250 nanoparticles and Figure 6.24 B depicts the cross sectional view of the IO@250 uptaken MCF-7 cell.

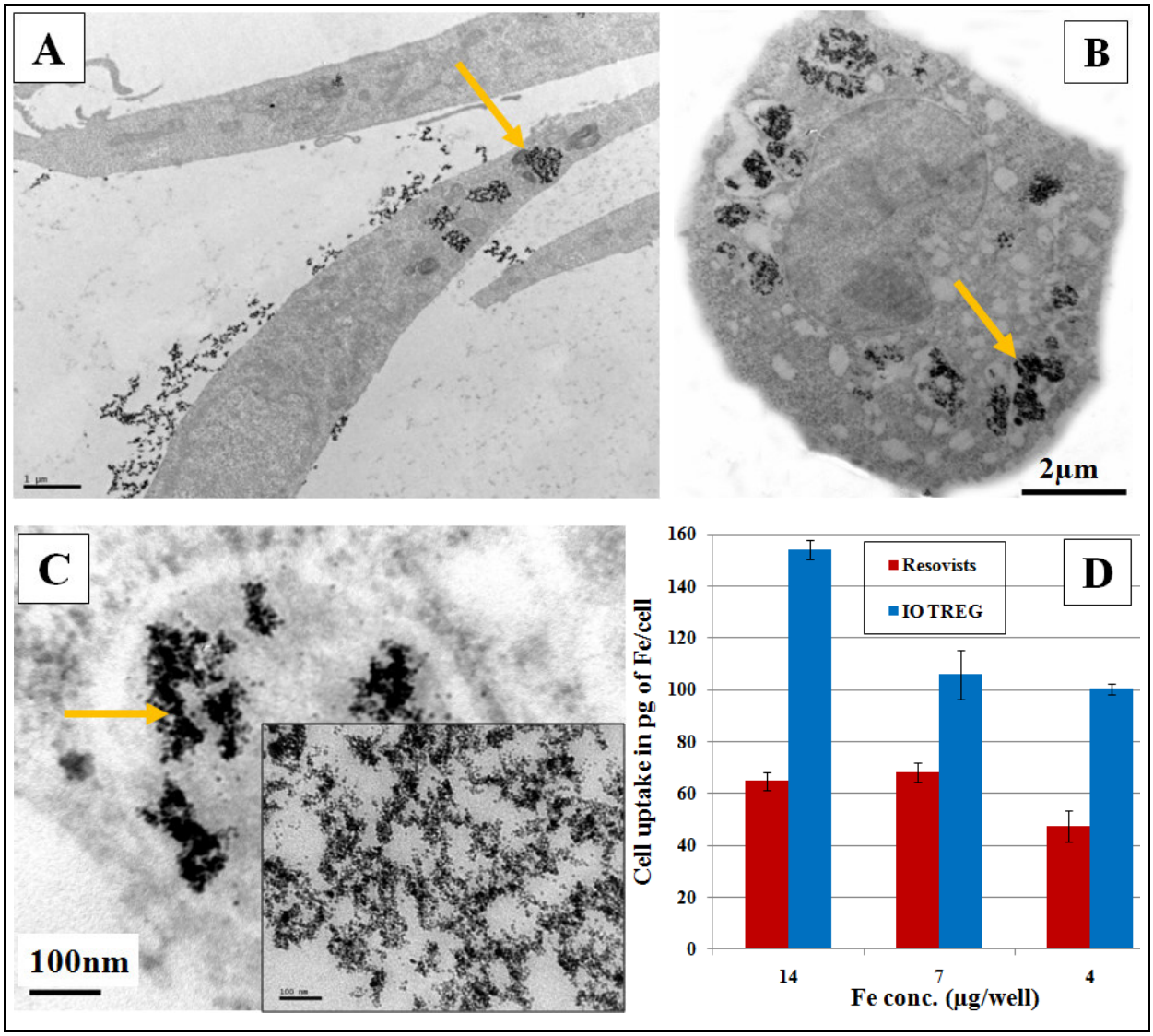

Figure 6.24 A. TEM image of the IO@250 uptaken MCF-7 breast cancer cell. **B.** Cross sectional view of the IO@250 uptaken MCF-7 cell. **C.** Magnified view of the vesicle consisting IO@250 nanoparticles inside. Inset shows the IO@250 nanoparticles confined in the vesicles. **D.** Quantitative cellular uptake results using the MCF-7 cancer cell line.

It can be seen that the IO@250 nanoparticles get attached to the cell surface and then trapped into the cell by endocytosis and finally appeared within the cytoplasm. Figure 6.24 C shows that a large amount of IO@250 nanoparticles were confined in the vesicles. Since the particles are positively charged (confirmed by zeta potential measurements in acidic condition) and the cell membrane are negatively charged, thus the IO nanoparticles are strongly attracted to the cell membrane and there by large amount of nanoparticles are adhered to cell surface which could possibly be a reason for higher cell uptake. Figure 6.24 D depicts the quantitative cell uptake results of the IO@250 nanoparticles in comparison with the Resovist® nanoparticles. It can be seen that the cell uptake efficiency of the IO@250 nanoparticles are several folds higher than that for Resovist® nanoparticles at the incubation concentrations of 4-14 µg/well Fe.

6.3.7. Magnetic Hyperthermia Studies

Figure 6.25 shows the time dependent temperature rise of 1 ml aqueous suspension of the TEG coated magnetite nanoparticles (IO@250) with the iron concentrations of 0.5, 1, 2.5, 5 and 10 mg/ml upon exposure to 89 kA/m AC magnetic field at 240 kHz frequency. The time required to raise the temperature up to 42ºC for the IO@250 nanoparticles with different iron concentration (0.5-10 mg/ml) are given in Table 6.3. The results indicate that the rate of temperature rise systematically increases with the iron concentration of the IO@250 nanoparticles (Figure 6.26). The heating of the superparamagnetic IO@250 nanoparticles under AC magnetic field could be due to Neel and Brownian loss which arise from rotation of the magnetization vector and the nanoparticles itself, respectively [17]. Inset of Figure 6.25 depicts the field dependent SAR values of the IO@250

nanoparticles with 1 mg/ml iron concentration at 240 kHz frequency, indicating that the SAR values varies nearly with H^2 as reported in literature [49-50].

The time dependent temperature rise for the nanoparticles prepared in different polyol media at the refluxing temperature are also performed at 240 kHz frequency using 89 kA/m AC magnetic field. Figure 6.27 shows the time dependent temperature rise of 1 ml aqueous suspension of different polyol (DEG, TEG, TTEG and PEG) coated nanoparticles with the iron (Fe) concentration of 1 mg/ml. It can be seen that the required time to raise the temperature to 42 ºC is 12.3, 10.1, 8.9 and 9.6 minutes for the DEG (7nm), TEG (11nm), TETEG (14nm) and PEG (13nm) coated particles respectively which indicates that heating rate of the bigger size particles are faster than that of the smaller size particles. This could be due to the higher magnetization of the bigger size particles.

Table 6.3. The time required to raise the temperature up to 42 ºC for the IO@250 and IO@APTES nanoparticles with different Fe concentrations.

Sample	**Fe Concentration (mg/ml)**	**Time required (second)**	**Magnetic field (kA/m)**	**Frequency (kHz)**
IO@250	10	423	89	240
	5	540		
	2.5	575		
	1	608		
	0.5	707		

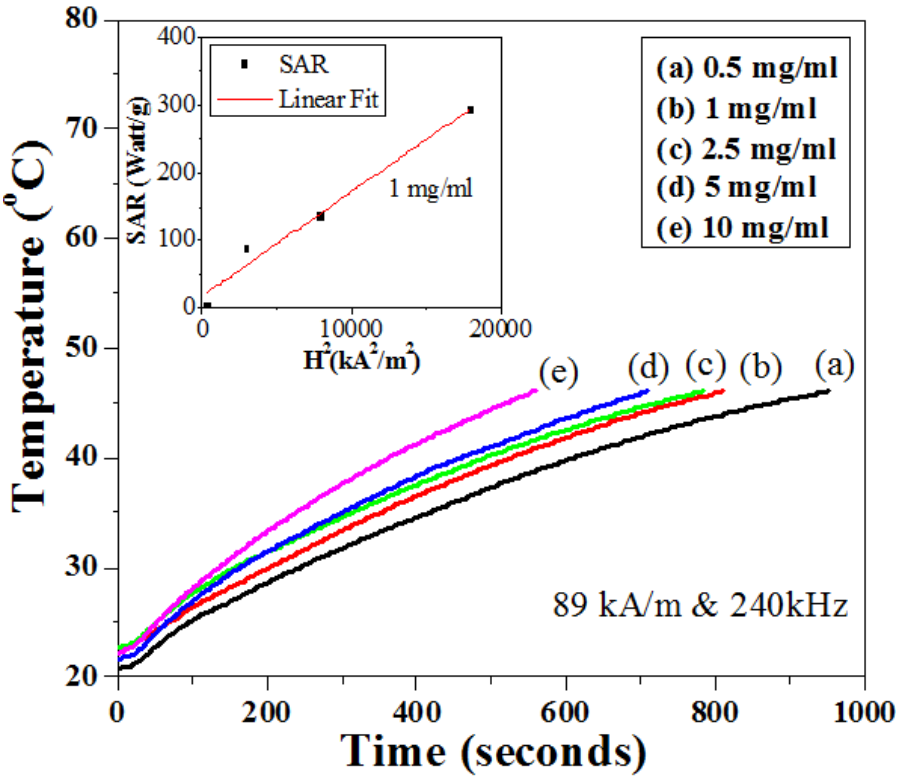

Figure 6.25. Time dependent temperature rise of 1 ml IO@250 sample with different iron concentration. Inset shows field dependent SAR values of 1 ml IO@250 sample.

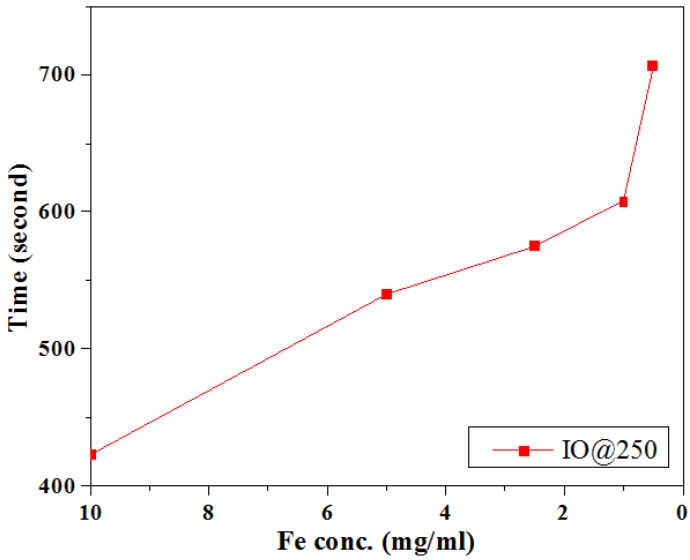

Figure 6.26. The time required time to raise the temperature up to 42 ºC for the IO@250 nanoparticles with different Fe concentrations.

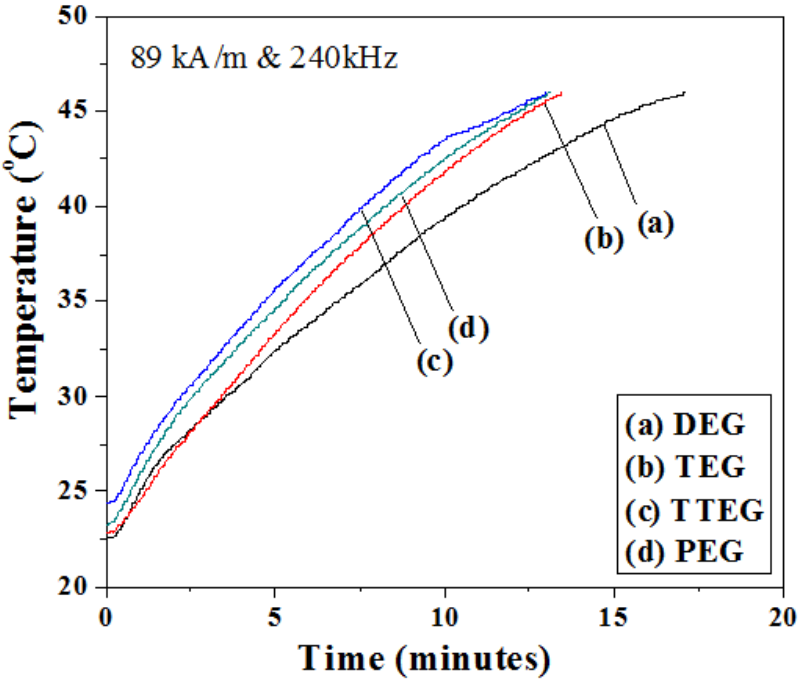

Figure 6.27. Time dependent temperature rise of 1 ml aqueous suspension of the nanoparticles prepared in different polyols: (a) DEG, (b) TEG, (c) TTEG and (d) PEG.

6.3.8. In vitro Hyperthermia

Figure 6.28 A shows the *in vitro* cytotoxic effect on MCF-7 breast cancer cells treated with magnetic hyperthermia using the IO@250 nanoparticles (1 mg/ml of Fe concentration) upon exposure to 89 kA/m AC field at 240 kHZ frequency. As a comparison, the cancer cells were also exposed to only magnetic field i.e. 89 kA/m AC (without adding any IO@250 nanoparticles) and only IO@250 nanoparticles (without exposing to the magnetic field) with 1mg/ml of Fe concentration.

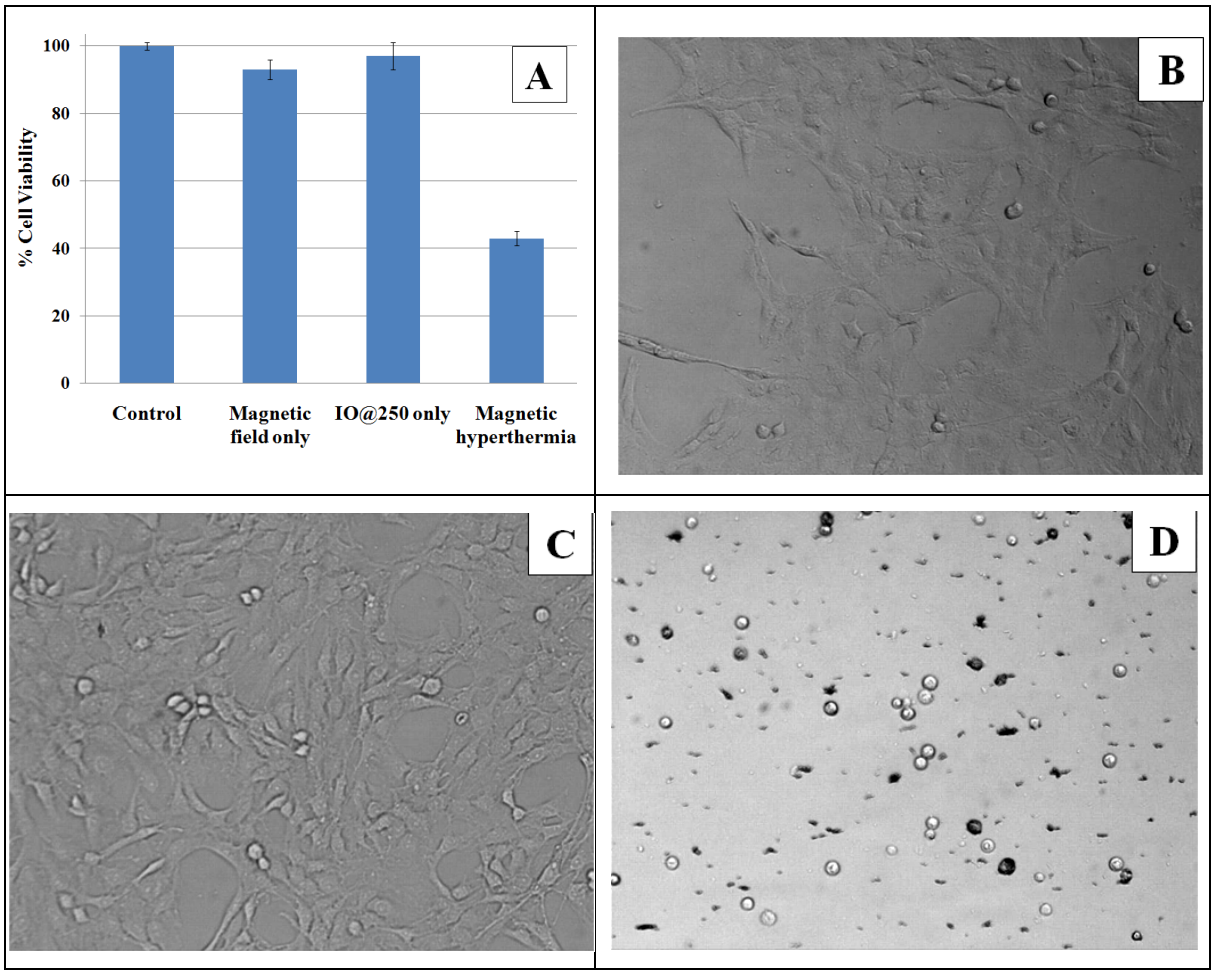

Figure 6.28 A. Cell viability plot shows the cytotoxic effect on MCF-7 breast cancer cells treated with magnetic hyperthermia (~ 45ºC), treated with IO@250 only, and treated with magnetic field only in comparison with the control cells. **B., C.** and **D** are optical microscope images of MCF-7 breast cancer cells treated with IO@250 only, magnetic field only and treated with magnetic hyperthermia.

Results (Figure 6.28 A) show that the magnetic hyperthermia at 45°C caused 60% cell death, while cell viability in the case of exposure to only the magnetic field or only IO@250 nanoparticles were comparable to that of the control. Thus, it was confirmed that about 60% loss of MCF-7 cancer cell viability was due to the magnetic hyperthermia

treatment. Figure 6.28 B, C and D show optical microscope images of MCF-7 breast cancer cells treated with only IO@250 (without magnetic field), only AC magnetic field (without IO@250), and with magnetic hyperthermia (using both IO@250 and magnetic field). It was observed that the cells treated with magnetic hyperthermia, lost their ability to attach to the surface and fail to grow (as shown in Figure 6.28 D) while the cells treated with only IO@250 (as shown in Figure 6.28 B) and the cells treated with only magnetic field (as shown in Figure 6.28 C) are attached to the surface which clearly indicates that the losses of cell viability (also as shown by the MTT assay) are due to the magnetic hyperthermia treatment using the IO@250 nanoparticles.

Although our *in vitro* hyperthermia results show promising results, the issues which need to be taken care for successful *in vivo* magnetic hyperthermia applications using the magnetic (IO@250 and IO@14) nanoparticles are as follows:

1) Direct injection of magnetic nanoparticles (MNPs) locally in tumor to have sufficient amount (~ 1-2 mg) of MNPs in the tumor area which would enable heating of tumor substantially up to 42-46^{o}C under AC magnetic field.
2) Another option could be administration of MNPs in the tumor feeding blood vessel or intravenously where accumulation of MNPs in the tumor area can be enhanced by an external permanent magnet using principle of magnetic drug targeting (MDT) concept [51]. Further, surface functionalization of MNPs with a biological targeting ligand such as folate receptor or monoclonal antibodies could be helpful for accumulation of MNPs with substantially higher amount in tumor area under the influence of permanent magnet [52].

Also, localized exposure of AC magnetic field needs to be done to avoid heating of the undesired organs such as liver, lung, spleen, where the MNPs may be extravassated following intravenous administration and thus an optimized design of coil with AC magnetic field generator is required for successful application of magnetic hyperthermia in vivo, particularly in human patient [53].

6.3.9. MRI Relaxivity Studies

Figure 6.29 shows the transverse relaxation rates (1/T2 and 1/T2* at 1.5 T) vs Fe concentration of IO@250 and Resovist® nanoparticles. The corresponding relaxivities ($r1$, $r2$, and $r2^*$ at 1.5 T) were calculated (Table 6.4). It is clear that the r2 and r2* relaxivities of IO@250 are greater than those of Resovist®. In particular, the $r2^*$ relaxivities of IO@250 reached 617.5$s^{-1}mM^{-1}$, which is much higher than that of Resovist®, suggesting IO@250 nanoparticles are very promising for $T2$ contrast agent application. The higher r2* of IO@250 nanoparticles could be due to their fine size and the presence of TEG coating onto the nanoparticle surface. Thus the MRI relaxivities of the nanoparticles depend on the coating materials and size of the nanoparticles. Figure 6.30 shows the transverse relaxation rates (1/T2 and 1/T2*) of the IO@250 nanoparticles at 9.4 T. The corresponding relaxivities ($r1$, $r2$, and $r2^*$) values are estimated as 0.589, 205.6 and 309.2, respectively which further indicates that the IO@250 nanoparticles are very promising for T2 MRI contrast agent.

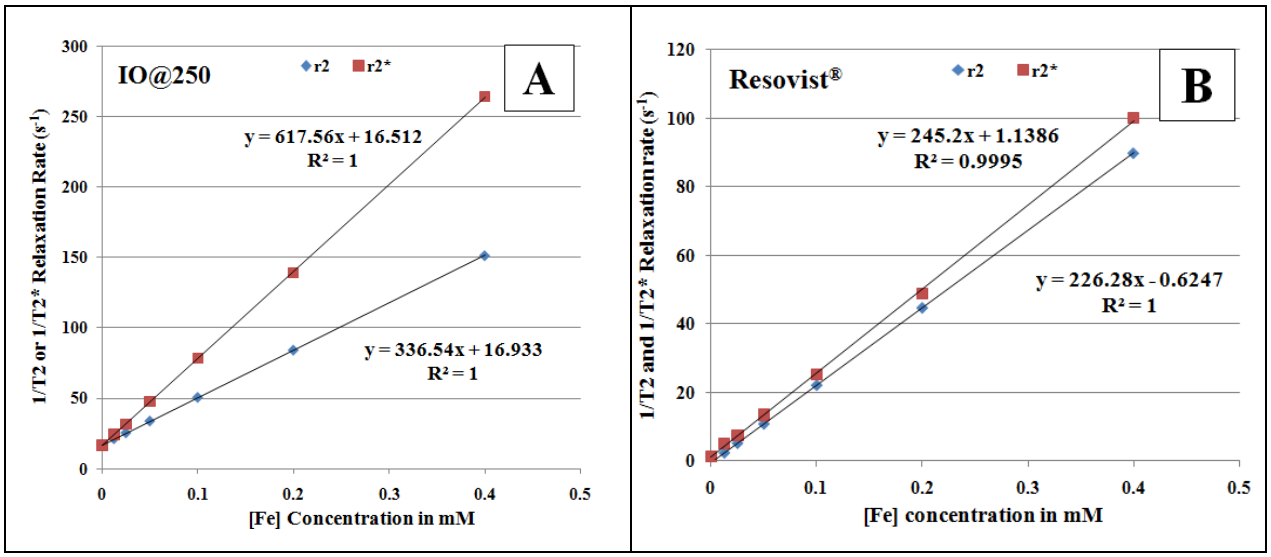

Figure 6.29. Transverse relaxation rates (1/T2 and 1/T2*) vs Fe concentration of **A.** IO@250 and **B.** Resovist® nanoparticles measured at 1.5 T.

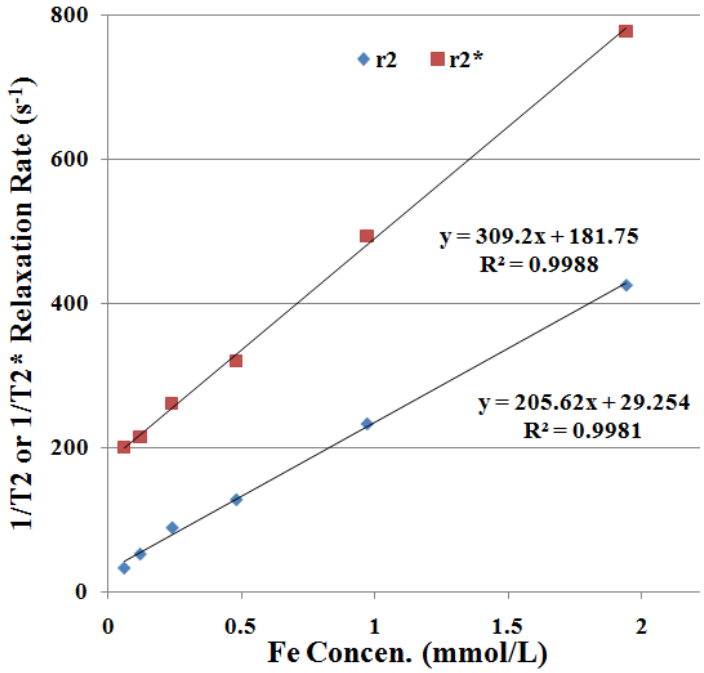

Figure 6.30. Transverse relaxation rates (1/T2 and 1/T2*) vs Fe concentration of IO@250 nanoparticles measured at 9.4 T.

Table 6.4. Relaxivity of IO@250 and Resovist® nanoparticles.

Samples	**Relaxivity** ($mM^{-1}s^{-1}$)		
	r1	**r2**	**r2***
Resovist® (at 1.5 T)	11.3	226.3	245.2
IO@250 (at 1.5 T)	9.5	336.5	617.5
IO@250 (at 9.4 T)	0.589	205.6	309.2

8.3.10. In Vivo MRI Imaging

Figure 6.31 A, B, C and D show the coronal images of the rat liver and kidney before injection (A and B) and after injection of the IO@250 nanoparticles (C and D). Figure 6.31 E, F, G and H show the coronal images of the rat liver and kidney before injection (E and F) and after injection of the Resovist® nanoparticles (G and H). Signal reduction was observed in liver and kidney for both the nanoparticles.

Signal change from the MRI over the first half an hour after administration of the nanoparticles was studied to understand the kinetics of the contrast agent. Figure 6.32 shows the % normalized contrast from the liver and kidney. The % normalized contrast of IO@250 nanoparticles in the liver was smaller than that of the Resovist® nanoparticles. It can be seen that the Resovist® nanoparticles accumulated rapidly in liver and saturated there soon within a few minutes after the injection while IO@250 nanoparticles accumulated slowly within about 15 min. In the kidney, there was a transient increase of Resovist® nanoparticles but did not accumulate there. On the contrary, IO@250 nanoparticles started to accumulate in the kidney about 10 min after injection, suggesting

that part of them might have been excreted through the kidney. These also indicated that IO@250 nanoparticles had different biodistribution behavior than Resovist® nanoparticles, which could be due to their relatively smaller size and surface chemistry of the coating. The slower accumulation of IO@250 nanoparticles in the liver and kidney also implied potentially longer blood circulation time and slower excretion by the reticuloendothelial system (RES). It has already been reported that the polyol coated IOs (Clariscan™, PEG-IO, NC100150) could be used as blood pool contrast agent due to their long circulation time [54]. The long circulation time could be used to facilitate the delivery of the nanoparticles to the site of interest using a localized magnetic field gradient.

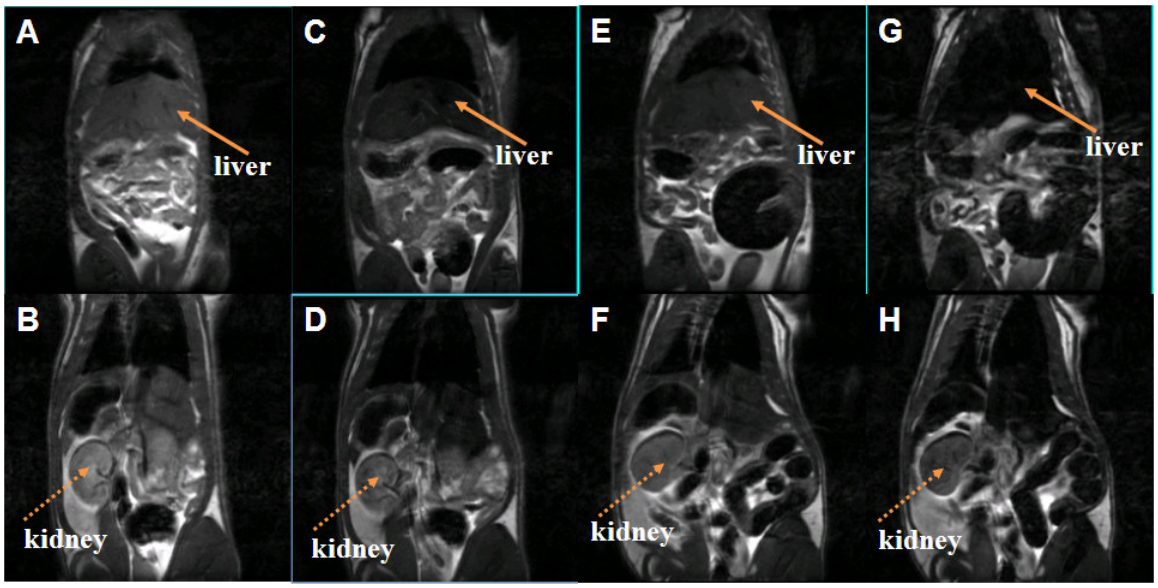

Figure 6.31. Top (A and C) and bottom (B and D) shows the coronal image of the rat liver and kidney before (left) and after (right) injection the IO@250 nanoparticles respectively. Top (E and G) and bottom (F and H) shows the coronal image of the rat

liver and kidney before (left) and after (right) injection of the Resovist® nanoparticles respectively. Arrows indicate liver and kidney of the animal.

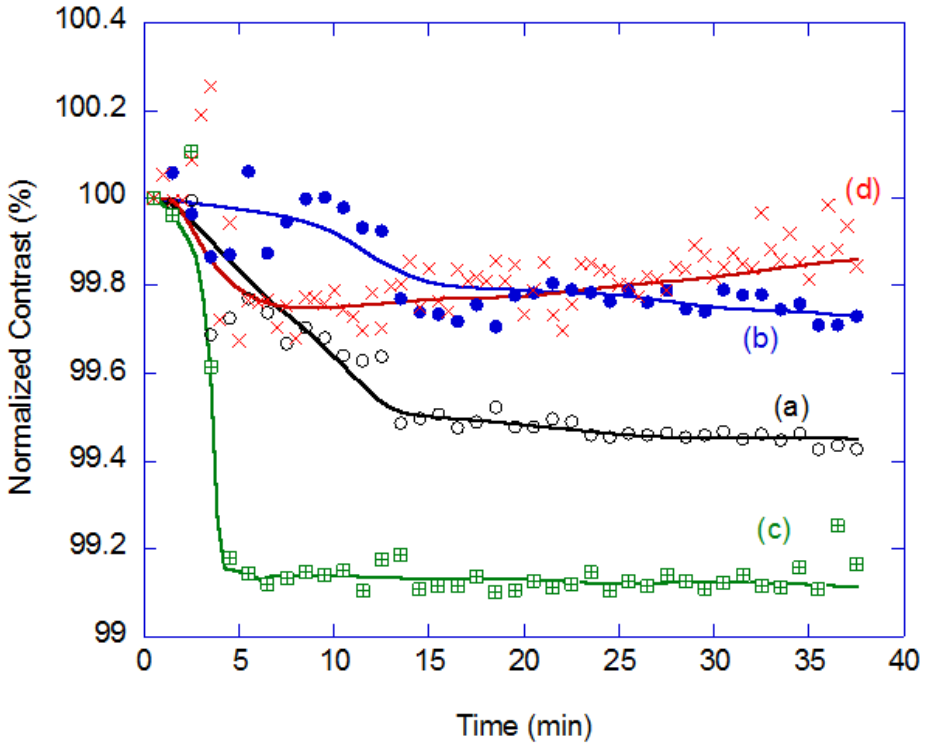

Figure 6.32. The % SNR change time courses for (a) IO@250 in liver; (b) IO@250 in kidney; (c) Resovist® in liver; (d) Resovist® in kidney (the solid-lines as a guide to eyes).

We further exploited the IO@250 for the application for *in vivo* tumor imaging. Figure 6.33 shows the signal intensity normalized by the signal in the saline phantom at different time points in tumor (red line), muscles (blue line) and liver (green line). It can be seen that the signal reduction for the liver and tumor is higher as compared to that for the muscles. Figure 6.34 shows the axial image of tumor before and after 10.5 hours of injection of IO@250 nanoparticles in tumor induced on the right flank of the SCID mice. IO@250 nanoparticles have the tendencies to accumulate at tumor sites by a means of

passive targeting called enhanced permeation and retention (EPR), as a result of leaky vasculature of the tumor site due to ill formed blood vessels (angiogenesis). From the signal trend and from the heterogeneity which was developed in the tumor site after 10.5 hours, it can be concluded that IO@250 nanoparticles accumulate at the tumor site through passive targeting. The long retention in the tumor indicates that the IO@250 nanoparticles have high affinity towards tumor and thus could be applicable as tumor sensitive contrast agent as well as for hyperthermia therapy.

In the present study, the IO@250 nanoparticles have been demonstrated to be useful for in vitro magnetic hyperthermia as well as in vitro and in vivo magnetic resonance imaging applications. Thus simultaneous applications of magnetic hyperthermia and magnetic resonance imaging of tumor using the IO@250 nanoparticles may be realized. However, the major difficulty which may be confronted is to achieve substantial amount of IO@250 nanoparticles (in mg) in the tumor area. In this regard, efficacy of magnetic field guided targeting of IO@250 nanoparticles equipped with targeting ligands in vivo remains to be seen.

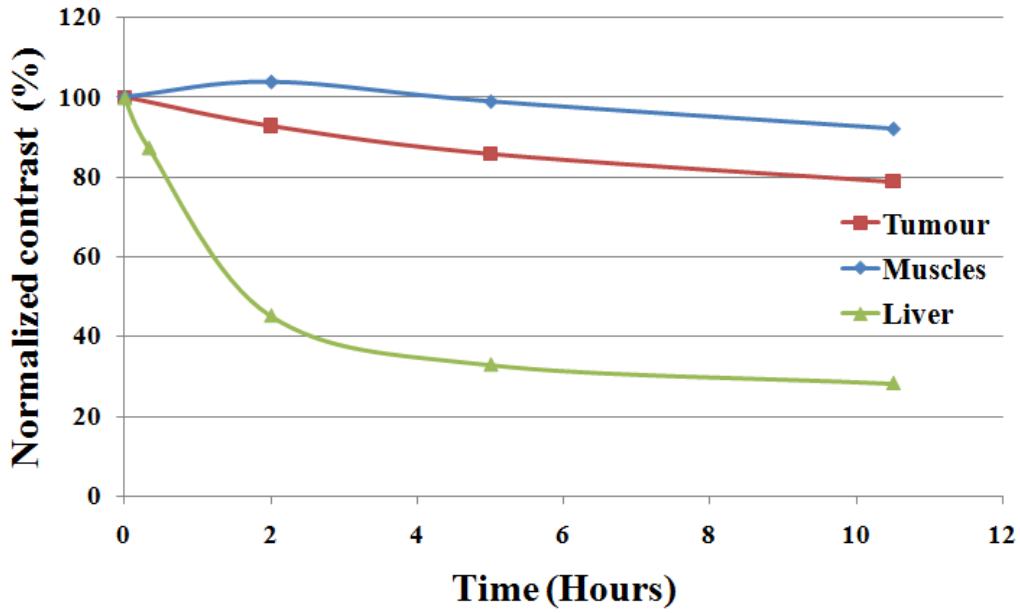

Figure 6.33. The normalized signal change at different time points in tumor tissue (red line), muscles (blue line) and in liver (green line).

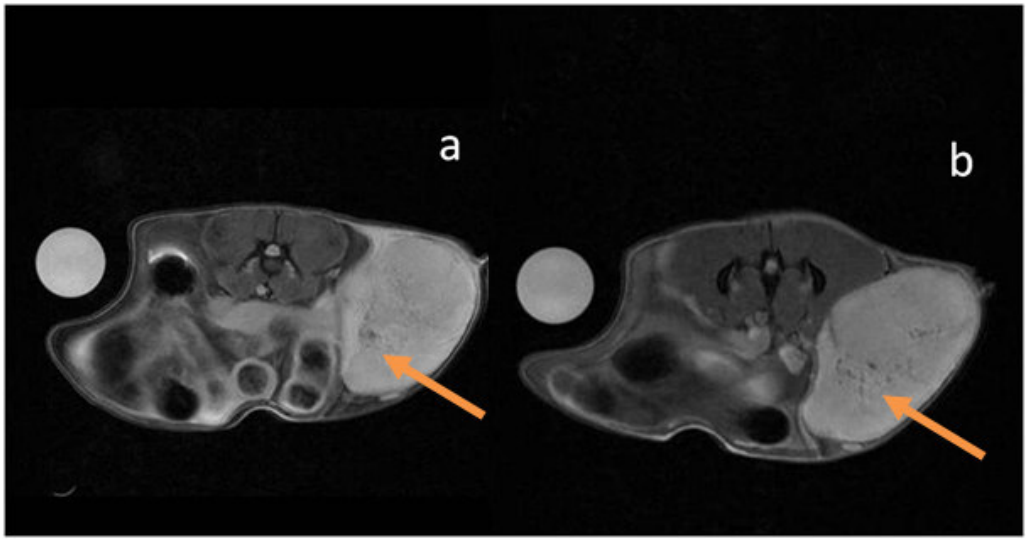

Figure 6.34. Axial image of tumor (pointed by solid arrow) before (a) and after 10.5 hours (b) of the injection of IO@250 nanoparticles in the tumor mouse.

6.4. Conclusions

The stability of the aqueous suspension of the magnetite nanoparticles prepared in polyol medium depends on the the amount of polyol coating attached on to their surface. The PEG and TTEG coated particles prepared at the refluxing temperature (300 and 330 °C respectively) are agglomerated as compared to the DEG and TEG coated particles which are well dispersed in an aqueous medium. However, the water solubility of the PEG and TTEG coated particles can be significantly improved by reducing the reaction temperature.

The reaction temperature has been optimized to 250 °C to synthesize highly water soluble well dispersed superparamagnetic IO@250 nanoparticles. *In vitro* studies demonstrated that the IO@250 nanoparticles have high cellular uptake and low cytotoxicity to the biological cells. The IO@250 nanoparticles demonstrated high r_2^* relaxivity value (617.5$s^{-1}mM^{-1}$ Fe) as compared to commercial Resovist® nanoparticles (245.2 $s^{-1}mM^{-1}$) which could be ascribed to their fine size and surface charge due to polyol coating onto their surface. *In vivo* MRI imaging studies of the IO@250 nanoparticles have demonstrated very promising contrast i*n vivo* tumor imaging. *In vitro* hyperthermia studies have confirmed that the IO@250 nanoparticles are able to produce significant temperature rise upon exposure to AC magnetic field (SAR~135 Watt/g) and thus, 60% loss of cancer cell viability was observed due to the magnetic hyperthermia treatment. It can thus be concluded that the IO@250 particles are very promising candidate for clinical MRI imaging as well as for cancer hyperthermia therapy.

6.5. References

1. A.K. Gupta, M. Gupta, Biomaterials 26 (2005) 3995.

2. S.J. Son, J. Reichel, B. He, M. Schuchman S.B. Lee, J. Am. Chem. Soc. 127 (2005) 7316.

3. H.H. Weetall, M. Lee, J. Appl. Biochem. Biotechnol. 22 (1989) 311.

4. S. Guo, D. Li, L. Zhang, J. Li, E. Wang, Biomaterials 30 (2009) 1881.

5. S. Dandamudi, R.B. Campbell, Biomaterials 28 (2007) 4673.

6. L.E. van Vlerken, M.M. Amiji, Expert. Opin. Drug. Deliv. 3 (2006) 205.

7. S. Chen, Y. Li, C. Guo, J. Wang, J. Ma, X. Liang, Langmuir 23 (2007) 12669.

8. U. Hafeli, W. Schutt, J. Teller, M. Zborowski, Scientific and clinical applications of magnetic carriers, Plenum Press, New York, (1997).

9. M. Bra1hler, R. Georgieva, N. Buske, A. Mu1ller, S. Mu1ller, J. Pinkernelle, U. Teichgra1ber, A. Voigt, H. Ba1umler, Nano Lett. 6 (2006) 2505.

10. H. Pardoe, W. Chua-anusom, T. G. St Pierre J. Dobson, Phys. Med. Biol. 48 (2003) N89.

11. P. Majewski, B. Thierry, Critic. Rev. Solid State Mater. Sci. 32 (2007) 203.

12. Y-w. Jun, Y-M. Huh, J-s. Choi, J-H. Lee, H-T. Song, S. Kim, S. Yoon, K-S. Kim, J-S. Shin, J-S. Suh, J. Cheon, J. Am. Chem. Soc. 127 (2005) 5732.

13. A.G. Roca, S. Veintemillas-Verdaguer, M. Port, C. Robic, C.J. Serna, M.P. Morales, J. Phys. Chem. B 113 (2009) 7033.

14. J. Qin, S. Laurent, Y.S. Jo, A. Roch, M. Mikhaylova, Z.M. Bhujwalla, R.N. Muller, M. Muhammed, Adv. Mater. 19 (2007) 1874.

15. P. Pradhan, J. Giri, G. Samanta, H.D. Sarma, K.P. Mishra, J. Bellare, R. Banerjee, D. Bahadur, J. Biomed. Mater. Res. Part B: Appl. Biomater. 81B (2007) 12.

16. M. Kawashita, M. Tanaka, T. Kokubo, Y. Inoue, T. Yao, S. Hamada, T. Shinjo, Biomaterials 26 (2005) 2231.

17. S. Mornet, S. Vasseur, F. Grasset, E. Duguet, J. Mater. Chem. 14 (2004) 2161.

18. M. Andrés Vergés, R. Costo, A.G. Roca, J.F. Marco, G.F. Goya, C.J. Serna, M.P. Morales, J. Phys. D: Appl. Phys. 41 (2008) 134003.

19. R. Hertg, W. Andrä, C.G. d'Ambly, I. Hilger, W.A. Kaiser, U. Richter, H.G. Schmidt, IEEE Trans. Magn. 34 (1998) 3745.

20. A. Jordan, R. Scholz, P. Wust, H. Fahling, R. Felix, J Magn. Magn. Mater. 201 (1999) 413.

21. A-H. Lu, E. L. Salabas, F. Schüth, Angew. Chem. Int. Ed. 46 (2007) 1222.

22. R Gref., Y. Minamitake, M.T. Peracchia, V. Trubetskoy, V. Torchilin, R. Langer, Science 263 (1994) 1600.

23. T.K. Jain, M.K. Reddy, M.A. Morales, D.L. Leslie-Pelecky, V. Labhasetwar, Mol. Pharm. 5 (2008) 316.

24. S. Sun, H. Zeng, J. Am. Chem. Soc. 124 (2002) 8204

25. S. Sun, H. Zeng, D.B. Robinson, S. Raoux, P.M. Rice, S.X. Wang, G. Li, J. Am. Chem. Soc. 126 (2004) 273.

26. D. Maity, S.-G. Choo, J. Yi, J. Ding, J.-M. Xue, J. Magn. Magn. Mater. 321 (2009) 1256.

27. D. Maity, J. Ding, J.-M. Xue, Func. Mater. Lett. 1 (2008) 189.

28. A. Wijaya, K. Hamad-Schifferli, Langmuir 23 (2007) 9546.

29. J. Xie, S. Peng, N. Brower, N. Pourmand, S.X. Wang, S. Sun, Pure Appl .Chem. 78 (2006) 1003.

30. H.-C. Huang, P.-Y. Chang, K. Chang, C.-Y. Chen, C.-W. Lin, J.-H. Chen, C.-Y. Mou, Z.-F. Chang, F.-H. Chang, J. Biomed. Sci. 16 (2009) 86.

31. X. Michalet, F.F. Pinaud, L.A. Bentolila, J.M. Tsay, S. Doose, J.J. Li, G. Sundaresan, A.M. Wu, S. S. Gambhir, S. Weiss, Science 307 (2005) 538.

32. I.L. Medintz, H.T. Uyeda, E.R. Goldman, H. Mattoussi, Nat. Mater. 4 (2005) 435.

33. H-T. Song, J-s. Choi, Y-M. Huh, S. Kim, Y-w Jun, J-S Suh, J. Cheon, J. Am. Chem. Soc. 127 (2005) 9992.

34. J. Xie, C. Xu, N. Kohler, Y. Hou, S. Sun, Adv. Mater. 19 (2007) 3163.

35. T. Zhang, J. Ge, Y. Hu, Y. Yin, Nano. Lett. 7 (2007) 3203.

36. Y. Zhang, N. Kohler, M. Zhang, Biomaterials 23 (2002) 1553.

37. J.-J. Yuan and S. P. Armes, Y. Takabayashi, K. Prassides, C.A.P. Leite, F. Galembeck, A.L. Lewis Langmuir 22 (2006) 10989.

38. Y. Lu, Y. Yin, B.T. Mayers, Y. Xia, Nano. Lett. 2 (2002) 183.

39. A.P. Herrera, C. Barrera, C. Rinaldi, J. Mater. Chem. 18 (2008) 3650.

40. J. Kim, J.E. Lee, J. Lee, J.H. Yu, B.C. Kim, K. An, Y. Hwang, C-H. Shin, J.-G. Park, J. Kim, T. Hyeon, J. Am. Chem. Soc. 128 (2006) 688.

41. J.L. Lyon, D.A. Fleming, M.B. Stone, P. Schiffer, M.E. Williams, Nano. Lett. 4 (2004) 719.

42. I.Y. Goon, L.M.H. Lai, M. Lim, P. Munroe, J.J. Gooding, R. Amal, Chem. Mater. 21 (2009) 673.

43. M. Mikhaylova, D.K. Kim, N. Bobrysheva, M. Osmolowsky, V. Semenov, T. Tsakalakos, Langmuir 20 (2004) 2472.

44. N. Pinna, S. Grancharov, P. Beato, P. Bonville, M. Antonietti, M. Niederberger, Chem. Mater. 17 (2005) 3044.

45. Z. Li, H. Chen, H. Bao, M. Gao, Chem. Mater.16 (2004) 1391.

46. J. Wan, W. Cai, X. Meng, E. Liu, Chem. Commun. 47 (2007) 5004.

47. D. Maity, S.N. Kale, R. Kaul-Ghanekar, J.-M. Xue, J. Ding, J. Magn. Magn. Mater. 321 (2009) 3093.

48. W.C. Miles, J.D. Goff, P.P. Huffstetler, C.M. Reinholz, N. Pothayee, B.L. Caba, J.S. Boyd, R.M. Davis, J.S. Riffle, Langmuir 25 (2009) 803.

49. R. Hergt, R. Hiergeist, M. Zeisberger, G. Gl.ockl, W. Weitschies, L.P. Ramirezc, I. Hilgerd, W.A. Kaiser, J. Magn. Magn. Mater. 280 (2004) 358.

50. L.L. Lao, R.V. Ramanujan, J. Mater. Sci.: Mater. Med. 15 (2004)1061.

51. C. Alexiou, W. Arnold, R.J. Klein, F.G. Parak, P. Hulin, C. Bergemann, W. Erhardt, S. Wagenpfeil and A.S. Lubbe, Cancer Res. 60 (2000) 6641.

52. P. Pradhan, J. Giri, F. Rieken, C. Koch, O. Mykhaylyk, M. Döblinger, R. Banerjee, D. Bahadur, C. Plank, J. Control. Rel. 142 (2010) 108.

53. M. Johannsen, U. Gneveckow, B. Thiesen, K. Taymoorian, C.H. Cho, N. Waldofner, R. Scholz, A. Jordan, S.A. Loening and P. Wust, Eur. Urol. 52 (2007) 1653.

54. M. Saeed, M.F. Wendland, M. Engelbrecht, H. Sakuma, C.B. Higgins, Eur. Radiol. 8 (1998) 1047.

CHAPTER 7

One Step Synthesis of Hydrophilic Magnetite Nanoclusters

7.1. Introduction

Superparamagnetic iron oxide (particularly magnetite (Fe_3O_4) and maghemite (γ-Fe_2O_3) nanoparticles have been studied extensively for the biomedical applications such as magnetic separation [1-3], drug delivery [4-6], hyperthermia treatment for tumors [7-9] and contrast agents in magnetic resonance imaging (MRI) [10-12]. Recently, many groups have also found that the superparamagnetic iron oxide nanoclusters are very promising in biological applications [13-16]. In all these studies, the iron oxide nanoclusters have been synthesized using the traditional approach which relied on the aqueous coprecipitation of ferrous and ferric salts using a base such as ammonium hydroxide or sodium hydroxide and then stabilized them with polymer [13], oleic acid [14] and citrate ligands [15-16]. The main problem in this approach is the uncontrolled aggregation of particles which eventually leads to polydisperse size of the nanoclusters and secondly, the obtained nanoclusters are semi-amorphous in nature due to the lower reaction temperature (below 80ºC) which eventually leads to very low saturation magnetization (Ms) (below 40 emu/g) of the nanoclusters. Thus, the synthesis of stable colloidal magnetic nanoclusters with high magnetization is very challenging. To date, the thermal decomposition method is very promising technique to fabricate high-quality monodisperse superparamagnetic iron oxide nanoparticles with high Ms (above 60 emu/g) [17–20]. Typically, this method involves decomposition of Iron (III) acetylacetonate, $Fe(acac)_3$ in a high-boiling temperature solvent in presence of stabilizing surfactants and reducing agent such as oleic acid and oleylamine. However, the obtained magnetite nanoparticles are organic soluble which makes them inappropriate for bio-medical applications. Therefore, many groups have further developed the thermal

decomposition method to directly synthesize water-soluble magnetic nanoparticles [21-23]. We have also studied (Chapter 6) and reported the synthesis of water stable superparamagnetic magnetite nanoparticles by the high temperature decomposition of Fe $(acac)_3$ in TEG medium in which the TEG has been used for a triple role as high-boiling solvent, reducing agent and stabilizer to efficiently control the particle growth and prevent interparticle aggregation [24-25]. Here, we have tried to fabricate magnetite nanoclusters by the thermolysis of Fe $(acac)_3$ either completely replacing TEG with other more polar solvent or adding more polar solvent with TEG. The ratios and reaction time interval have been systematically varied to optimize for obtaining well dispersed magnetite nanoclusters. The idea behind the replacing with or addition of more solvent with the TEG is to reduce the stabilizing effect of the TEG so that clustering of nanoparticles happens either to reduce their surface energy or due to the strong inter particle attractive magnetic force. The structure, morphology, magnetic properties, MRI imaging and magnetic hyperthermia studies of the as-prepared nanoparticles have been investigated to evaluate their potentiality in magnetic hyperthermia and MRI imaging applications. We hypothesize that due to clustering of multiple magnetic nanoparticles into single magnetic nanocluster, saturation magnetization (Ms) would be increased and thereby their heating efficiency under alternating current (AC) magnetic field and contrasting effect in MRI would be maximized and thus the magnetic nanoclusters would be better candidate for both magnetic hyperthermia and MRI applications as compared to their individual magnetic nanoparticles form.

7.2. Experimental

Ethanol amine (EA), diethanol amine (DEA), triethanol amine (TEA), DEG, TEG) and $Fe(acac)_3$ were purchased from Sigma-Aldrich.

7.2.1. Synthesis of cluster particles

Magnetite nanoparticles were prepared by thermolysis of $Fe(acac)_3$ either in a pure solvent or in a solvent mixture. Typically, 2 mmol of $Fe(acac)_3$ was dissolved in a 20 ml of solvent or in a solvent mixture (Table 7.1). The resulting mixture solution was magnetically stirred under a continuous flow of argon. The solution was dehydrated at 120°C for 1 h, and then quickly heated to reflux and maintained at the refluxing temperature under the argon flow for different time intervals (Table 6.1). Thereafter, the black solution was cooled to room temperature and the nanoparticles were precipitated by addition of ethyl acetate. Finally, the obtained magnetite nanoparticles were washed several times with the ethanol and ethyl acetate (1:2 v/v) mixture followed by centrifugation. All the samples prepared using different reaction conditions are given in Table 7.1.

7.2.2. Characterization of Nanoparticles

Structure of the as-prepared magnetite nanoparticles was identified by XRD, FTIR, XPS and TGA. Morphology of the particles was determined using TEM. Magnetic properties of the particles were determined using VSM and SQUID measurements.

Table 7.1. List of samples prepared under different reaction conditions

Sample	Reaction Temperature	Reaction time	Pure Solvent / Solvent Mixture (v/v ratio)
A	reflux (180ºC)	1/2 and 16h	EA
B	reflux (220ºC)	1/2, 1, and 2h	DEA
C	reflux (245ºC)	1/2, 1, and 2h	TEA (0:1 TEG:TEA)
D	reflux (245ºC)	1/2 and 2h	2:1 and 1:1 DEG:DEA
E	reflux (270ºC)	1/2, 1, 2 and 4h	4:1 TEG:TEA
F	reflux (250ºC)	1/2, 1, 2 and 4h	2:1 TEG:TEA
G	reflux (250ºC)	1/2, 1, 2 and 4h	1:1 TEG:TEA
H	reflux (250ºC)	1/2, 1, 2 and 4h	1:2 TEG:TEA
I	reflux (245ºC)	1/2, 1, 2 and 4h	1:4 TEG:TEA

Cell viability studies were performed by MTT assay using MCF-7 mammalian breast cancer cells. For this, the MCF-7 cancer cells were incubated for 24 h with media containing TEA coated magnetite nanoclusters (IO@14 which is prepared at 1h using 1:4 TEG:TEA ratio) at concentrations ranging from 0.625 – 10 mg/ml Fe. AC magnetic field induced heating ability of the magnetite nanoclusters was determined from the time-dependent calorimetric measurements using a RF generator operating at 240 and ~400 kHz. *In vitro* cellular hyperthermia measurements were performed on MCF-7 cancer cells using a RF generator operating at 240 kHz. The T1, T2 and $T2^*$ relaxation times of aqueous suspensions of IO@14 nanoclusters containing various Fe concentrations of 0.0066 – 0.15 mM were measured using 9.4T MRI scanner. I*n vivo* MRI studies were carried out on tumor-bearing SCID mice using a Bruker 7T Clinscan MRI.

7.3. Results and Discussion

7.3.1. Morphology

Figure 7.1, 7.2 and 7.3 show the TEM images of the nanoparticles prepared in EA, DEA and TEA respectively using different reaction time intervals. It can be seen that the magnetite nanoparticles prepared in ethanol amine (EA) are isolated single particle even after 16 hours of reaction time interval (Figure 7.1 A2). However, the particles prepared in diethanol amine (DEA) and triethanol amine (TEA) are aggregated with each other to form dumbbell and flower shaped magnetite nanoclusters at shorter reaction time (as shown in Figure 7.2 B1 and Figure 7.3 C1). These dumbbell and flower shaped magnetite nanoclusters are gradually liked with each other to form chain like structures while prolonging the reaction time (as shown in Figure 7.2 B3 and Figure 7.3 C3). Figure 7.4 show the chemical structure of EA, DEA and TEA molecules.

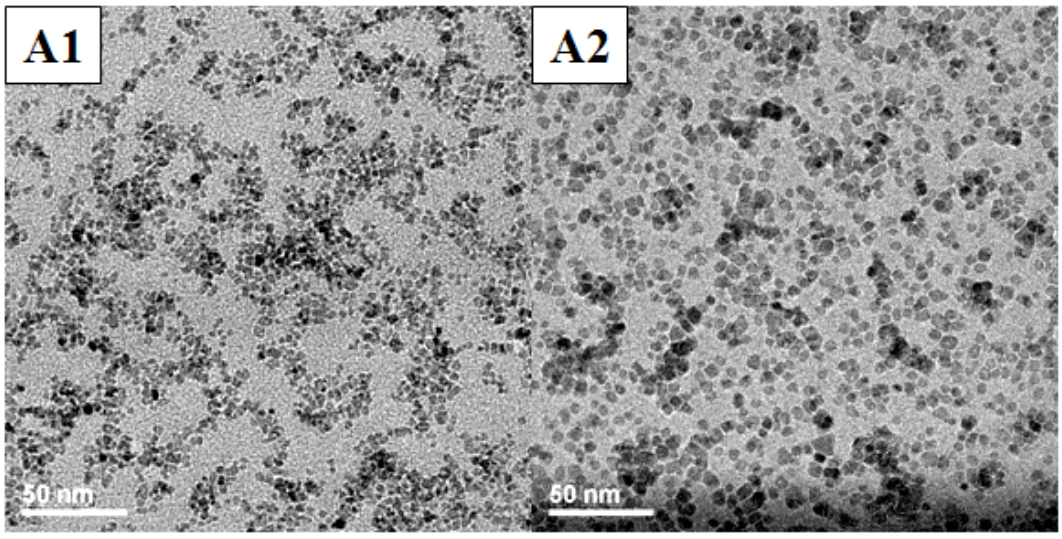

Figure 7.1. TEM images of the magnetite nanoparticles prepared in EA using the reaction time of **A1.** 30 min and **A2.** 16h.

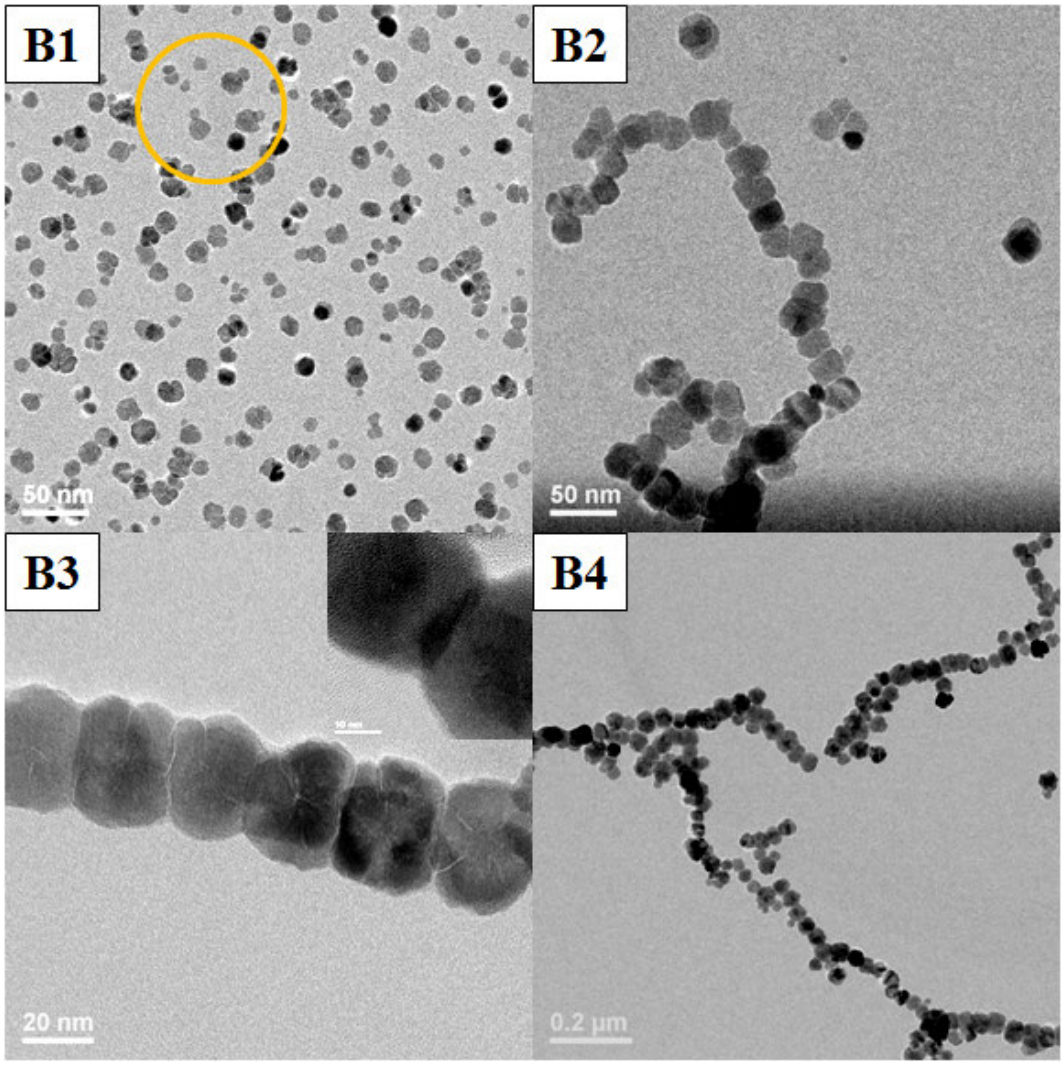

Figure 7.2. TEM images of the magnetite nanoparticles prepared in DEA using the reaction time of **B1.** 30 min, **B2.** 1h, and **B3** ; **B4.** 2h. Inset of **B3** shows the HRTEM of dumbbell shaped magnetite particle.

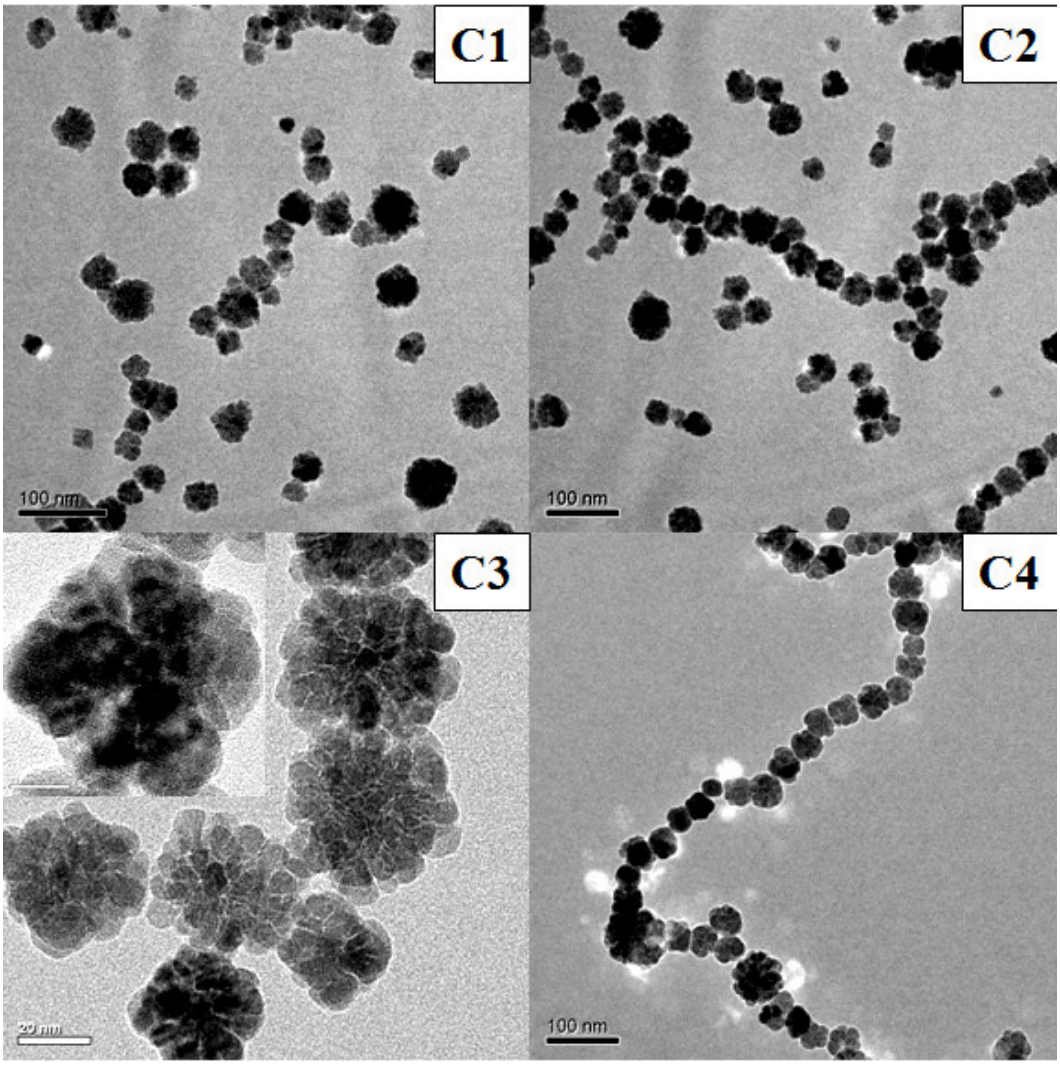

Figure 7.3. TEM images of the magnetite nanoparticles prepared in TEA using the reaction time of **C1.** 30 min, **C2.** 1h, and **C3** ; **C4.** 2h. Inset of **C4** shows the HRTEM of flower shaped magnetite particle.

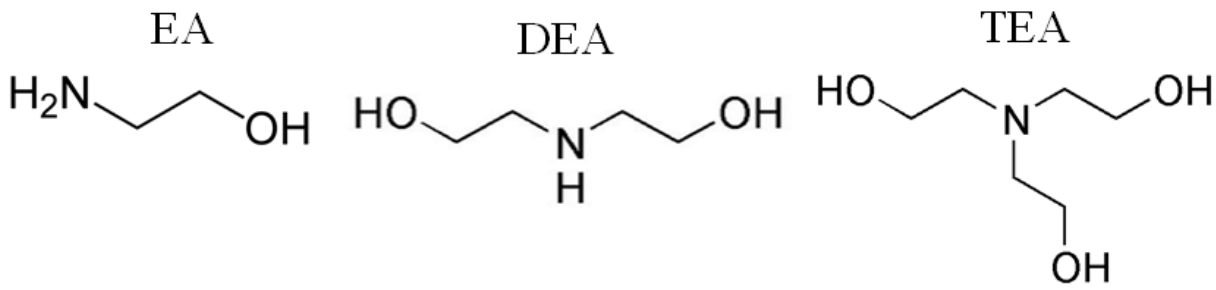

Figure 7.4. Chemical structure of ethanol amine (EA), diethanolamine (DEA) and triethanol amine (TEA) molecules.

The magnetite (Fe_3O_4) nanoparticles formed by thermal decomposition of $Fe(acac)_3$ are immediately coated with EA or DEA or TEA molecules through the reactive OH groups (Figure 7.5). For this, OH group(s) of EA/DEA/TEA molecules easily donates two lone pairs to coordinate with the Fe ions of the Fe_3O_4 nanoparticles. The DEA and TEA coated particles are further interconnected with each other through the other end OH groups to develop dumbbell shaped and flower shaped particles. Here, the DEA and TEA molecules play the key role to interconnect the magnetite nanoparticles into dumbbell (Figure 7.6) and flower structure respectively (Figure 7.7). The magnetite nanoparticles which are initially nucleated by the decomposition of $Fe(acac)_3$ (Figure 7.5) comes close to each other due to magnetic dipole-dipole interactions and thus favor the interaction of the multiple hydroxyl (-OH) groups of the surface adsorbed DEA or TEA molecules leading to condensation of the nanoparticles into a dumbbell (Figure 7.6) or flower (Figure 7.7) like structure followed by removal of water.

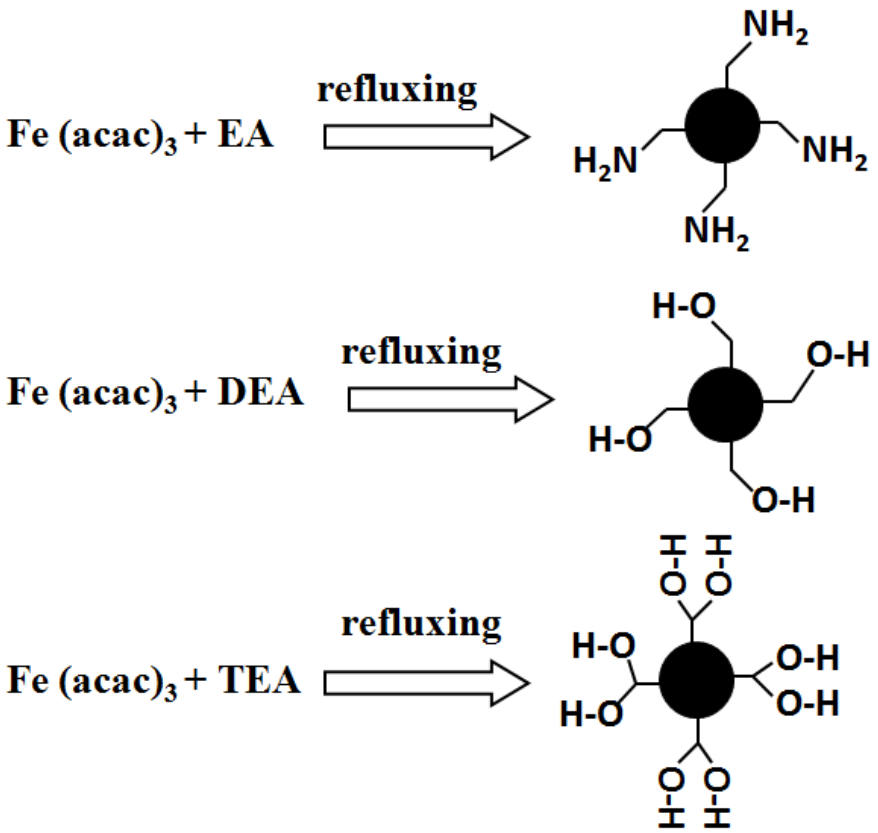

Figure 7.5. Schematic representations of EA, DEA and TEA coated Fe_3O_4 nanoparticles which are formed by thermal decomposition of $Fe(acac)_3$ in EA, DEA and TEA at the corresponding refluxing temperature.

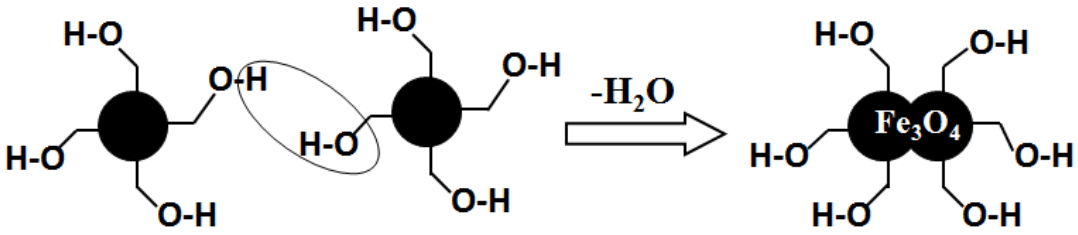

Figure 7.6. Mechanism of formation of dumbbell shaped magnetite particles through condensation of hydroxyl groups of DEA molecules adsorbed to surface of the spherical nanoparticles which are initially formed by thermal decomposition of $Fe(acac)_3$ in DEA.

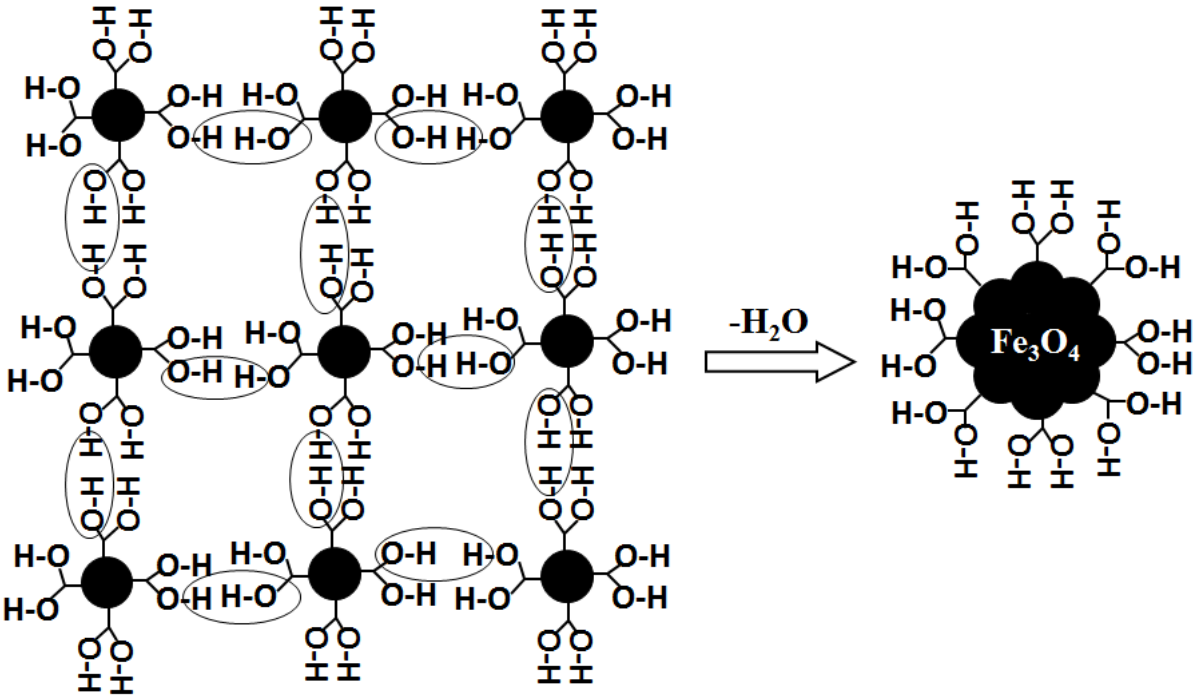

Figure 7.7. Mechanism of formation of MNF particles through condensation of hydroxyl (OH) groups of TEA molecules adsorbed to surface of the spherical nanoparticles which are initially formed by thermal decomposition of $Fe(acac)_3$ in TEA.

The dumbbell and flower shaped nanoparticles are rapidly interconnected with each other to form long chain structure (as shown in Figure 7.2 B3 and Figure 7.3 C3). Therefore, we have added DEG and TEG with the DEA and TEA separately to develop uniformly dispersed dumbbell or flower shaped magnetite nanoparticles. Figure 7.8 show the TEM images of the nanoparticles prepared using different ratio of DEG:DEA (v/v) at different reaction time intervals. It can be seen that uniformly dispersed nanoparticles can be prepared in the mixture solvent of DEG and DEA even at prolonged reaction time of 2h (Figure 7.8 D4).

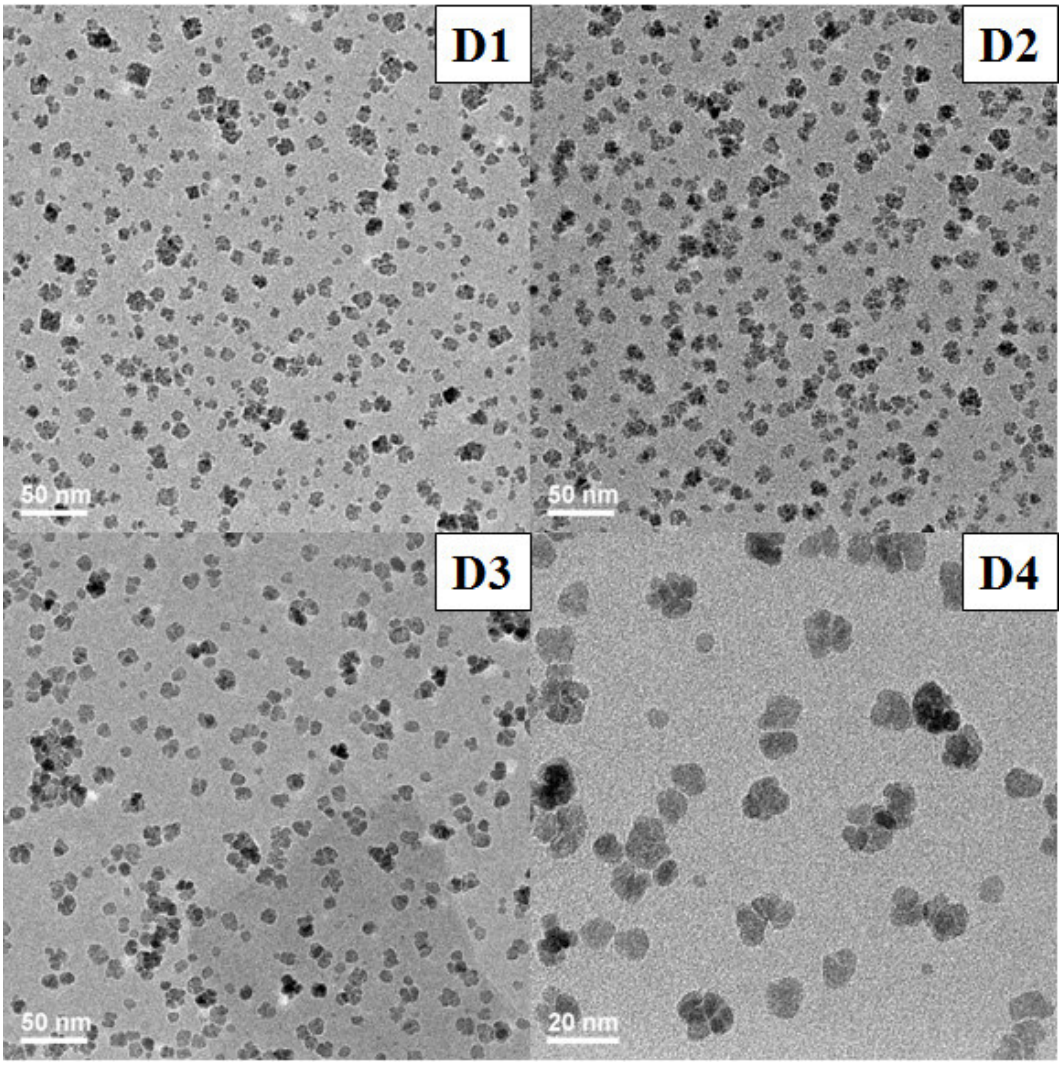

Figure 7.8. TEM images of the nanoparticles prepared using different (v/v) ratio of DEG: DEA at the reaction time intervals: **D1.** 2:1; 2h, **D2.** 1:1; 1/2 h, **D3 & D4.** 1:1; 2h.

Figure 7.9 to Figure 7.13 show the TEM images of the nanoparticles prepared using different ratio of TEG:TEA (4:1 to 1:4 v/v) at different reaction time intervals (1/2 to 4 h). It can be seen that as usual isolated spherical shaped nanoparticles are formed when the concentration of TEA is low (TEG:TEA $\geq$ 2:1). However, with increasing the TEA concentration (TEG:TEA <2:1), the flower shaped nanoparticles gradually developed. Figure 7.11 show that about 4-5 spherical particles are interconnected with each other to

develop flower like structure. Thus, the flower structure starts to develop with the ratio of TEG:TEA = 1:1. Figure 7.12 and Figure 7.13 indicate that more number of spherical particles are gradually linked into the flower structure while increasing the TEA concentration (TEG:TEA = 1:2 and 1:4). Moreover, the flower particles are prepared using shorter react time interval (up to 1h) are dispersed separately while they are gradually self-assembled into chain like structures with prolonging the reaction time (>1h).

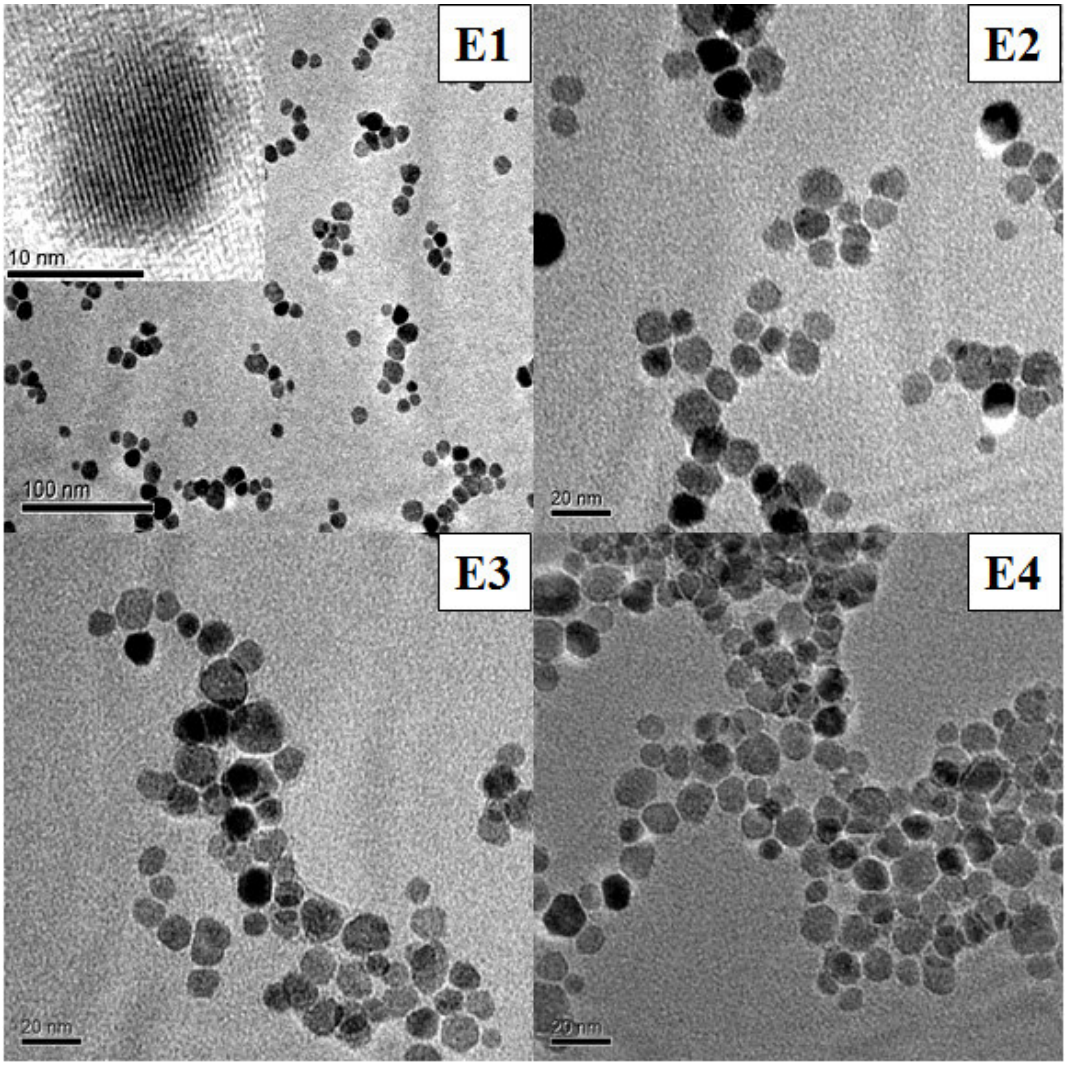

Figure 7.9. TEM images of the nanoparticles prepared using 4:1 (v/v) ratio of TEG: TEA at the reaction time of **E1.** 30 min, **E2.** 1h, **E3.** 2h and **E4.** 4h. All scale bars are 20 nm.

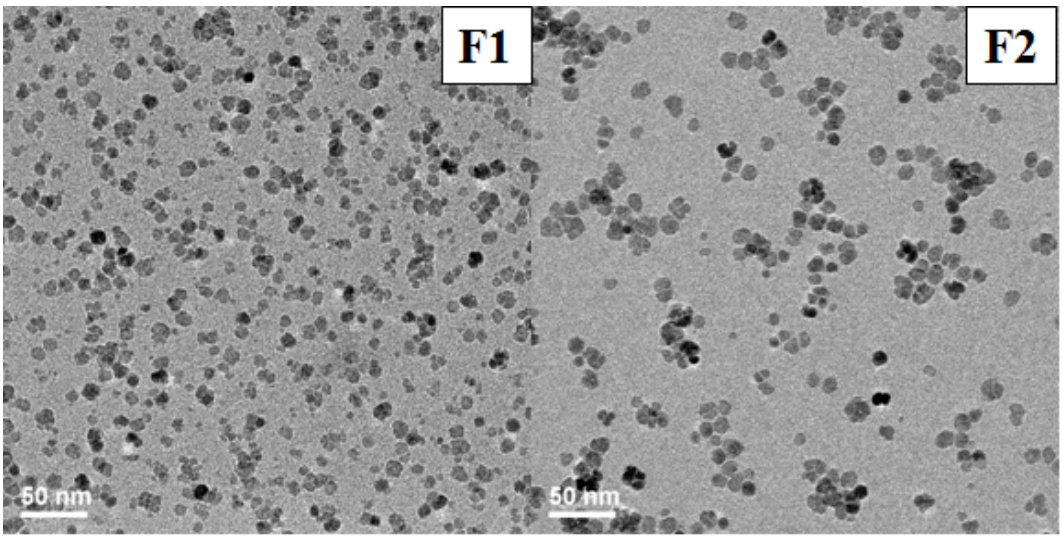

Figure 7.10. TEM images of the nanoparticles prepared using 2:1 (v/v) ratio of TEG: TEA at the reaction time of **F1.** 30 min, **F2.** 2h.

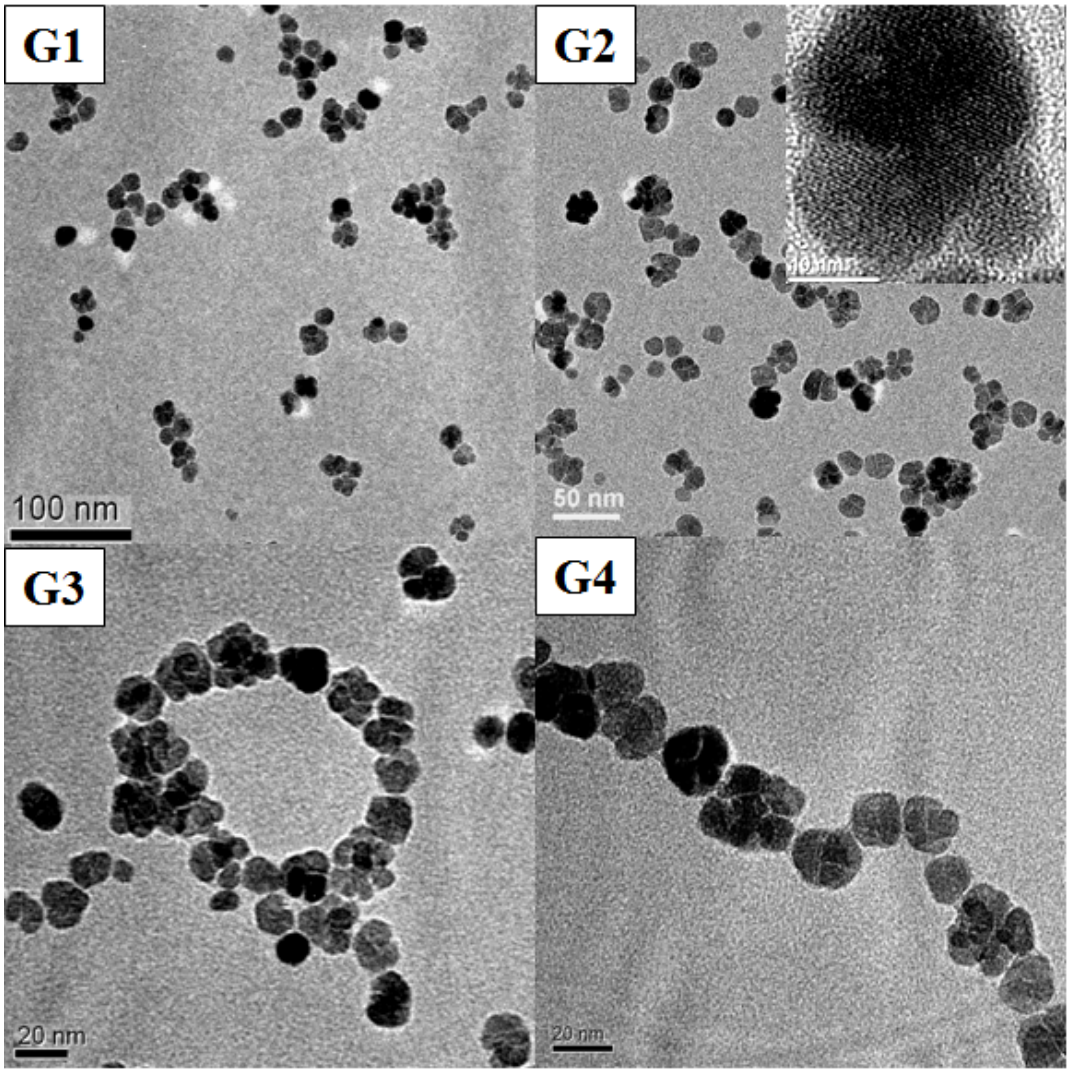

Figure 7.11. TEM images of the nanoparticles prepared using 1:1 (v/v) ratio of TEG: TEA at the reaction time of **G1.** 1/2 h, **G2.** 1h, **G3.** 2h and **G4.** 4h.

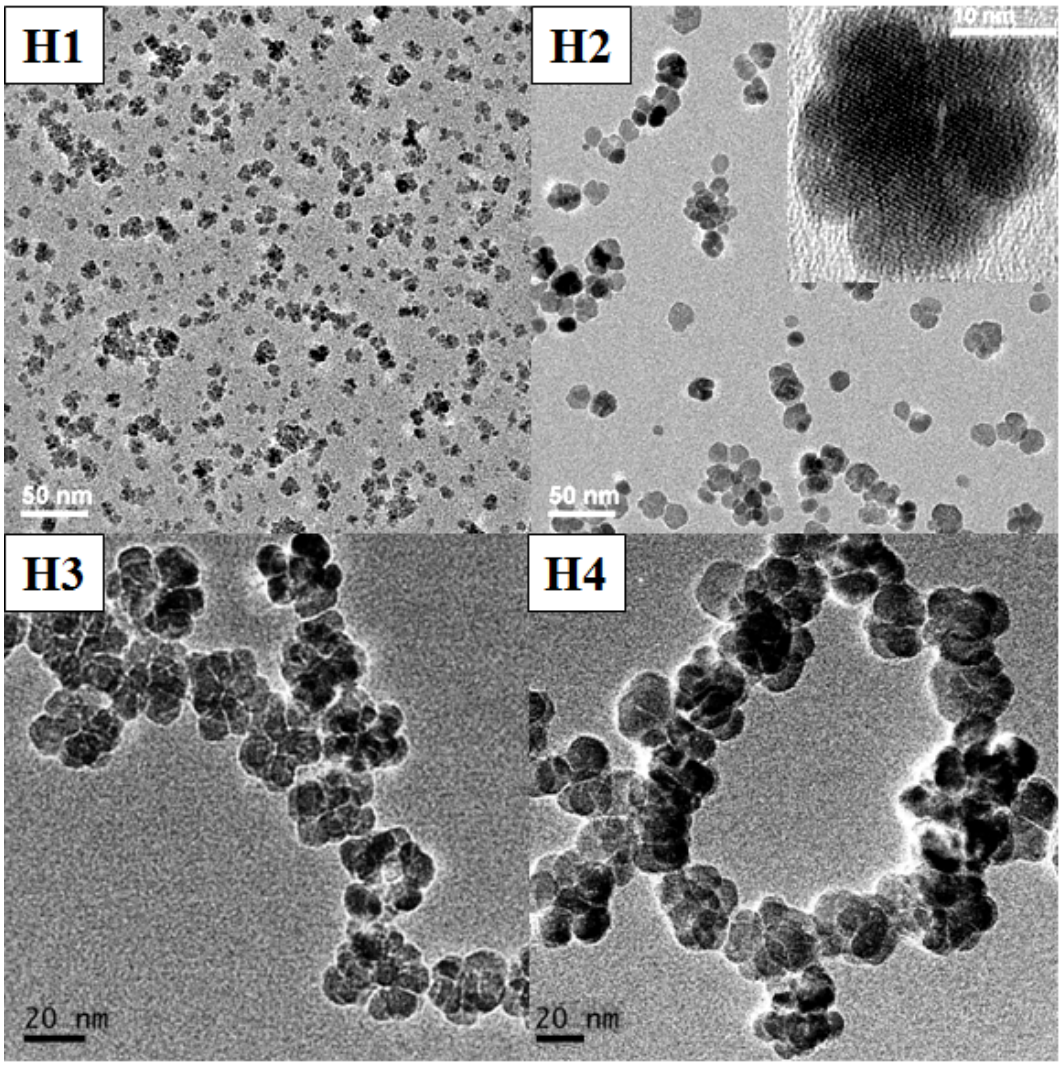

Figure 7.12. TEM images of the nanoparticles prepared using 1:2 (v/v) ratio of TEG: TEA at the reaction time of **H1.** 1/2 h, **H2.** 1h, **H3.** 2h and **H4.** 4h.

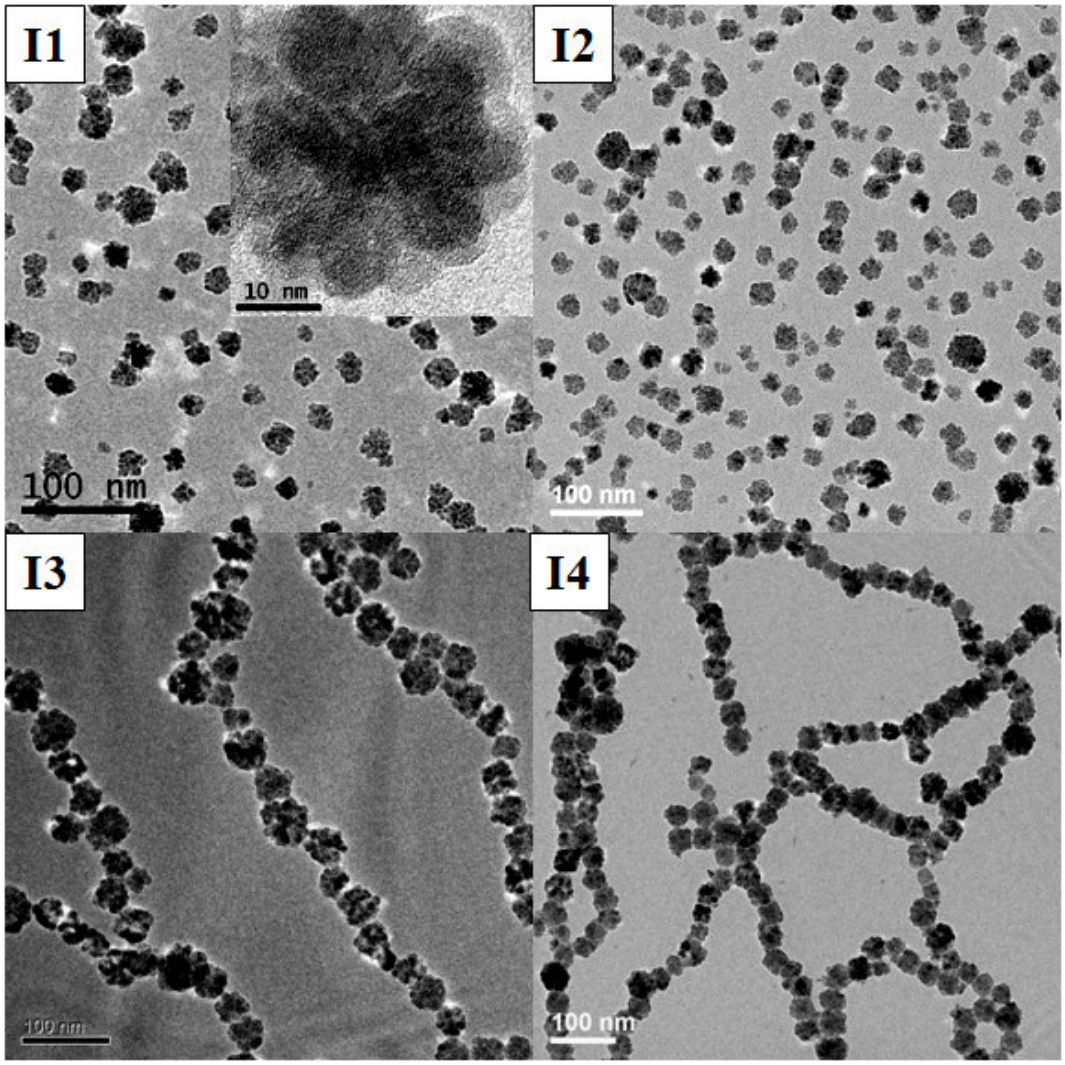

Figure 7.13. TEM images of the nanoparticles prepared using 1:4 (v/v) ratio of TEG: TEA at the reaction time of **I1.** 1/2 h, **I2.** 1h, **I3.** 2h and **I4.** 4h.

In summary, the spherical shaped nanoparticles are formed up to the 2:1 ratio and thereafter (i.e. <2:1); the shape of the particles is gradually transformed into the flower like structure. The MNF particles prepared using the shorter reaction time (≤1h) are very well dispersed but, they are progressively self-assembled into chain like patterns while prolonging the reaction time (>1h).

Figure 7.14 I5 shows the HR-TEM image of a single IO@14 nano-cluster particle which clearly indicates that each of the flower particles consists of inter-connected many small (~ 10 nm) spherical nanoparticles. Figure 7.14 I6 indicates that IO@14 nano-clusters are self-assembled into the chains which could be due to the increased magnetic interactions between the flower particles prepared at a prolonged reaction time (>2h).

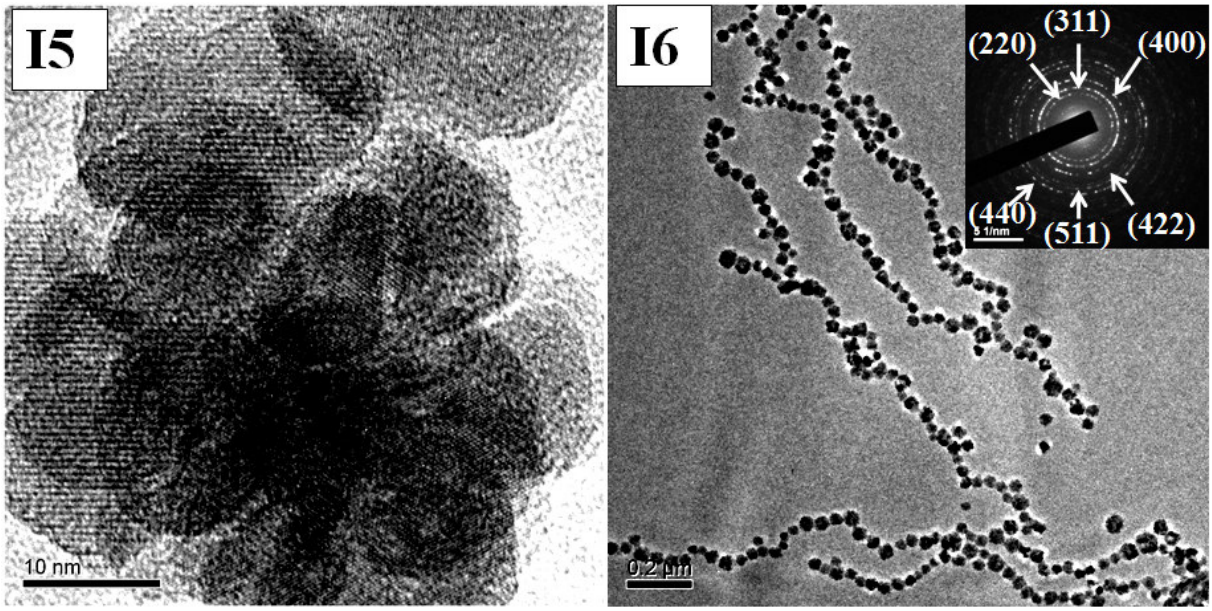

Figure 7.14. I5. HRTEM images of a single IO@14 nano-cluster particle **I6.** Self-assembled magnetite nano-cluster particles. Inset is SAED patterns of the nano-flower particles.

7.3.2. Structural Characterization

Figure 7.15 shows XRD patterns of the nanoparticles prepared using different TEG: TEA ratio at 1h reaction time interval. Positions of the diffraction peaks match well with the

standard XRD patterns for bulk magnetite (JCPDS file No. 19-0629) indicating that the particles consist of pure magnetite phase.

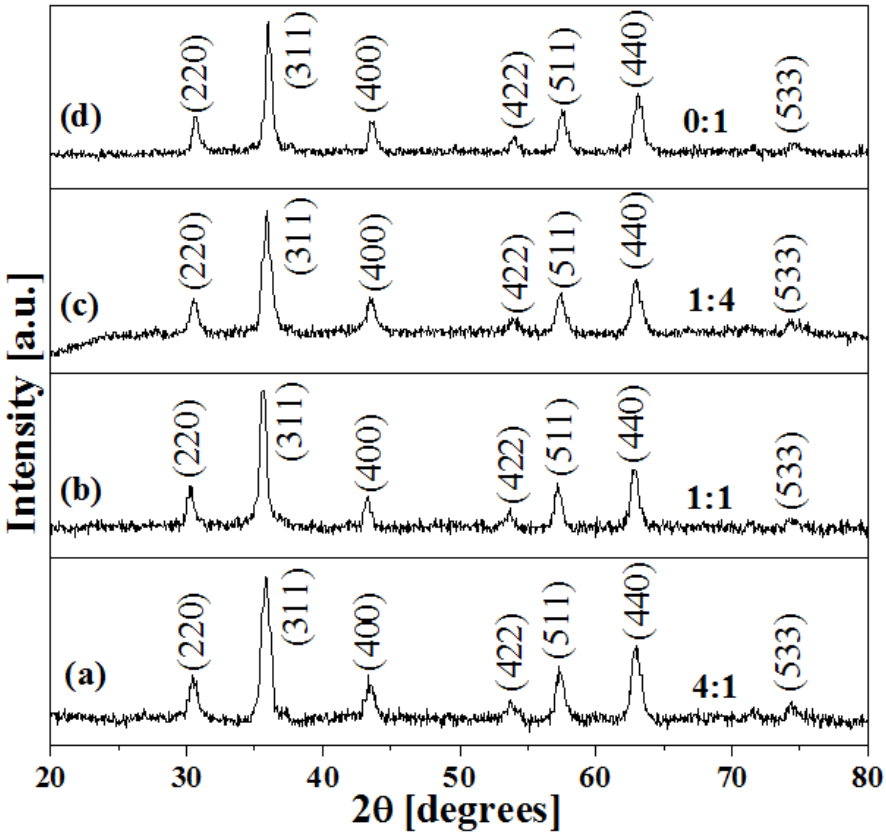

Figure 7.15. XRD patterns of the nanoparticles prepared using different TEG: TEA ratio: (a) 4:1, (b) 1:1, (c) 1:4 and (d) 0:1 at 1h reaction time interval.

Figure 7.16 depicts FTIR spectra of the nanoparticles prepared using different TEG: TEA ratio at 1h reaction time interval. The peaks at about 2962–2809, 1681-1534, 1485-1340, 1084, 910 cm^{-1} are due to C–H stretching, O–H stretching, C–H bending, C–O stretching and O–H bending vibrations respectively [25-27], which are attributed to the TEG and TEA molecules adsorbed on to the particle surface. The broad band between 3600 and 3000 cm^{-1} centered at about 3400cm^{-1} is assigned to O–H stretching vibration which

arises due to the adsorbed water molecules. In addition, the strong absorption band at about 585 cm^{-1} is due to Fe–O stretching vibration of the Fe_3O_4 particles [28].

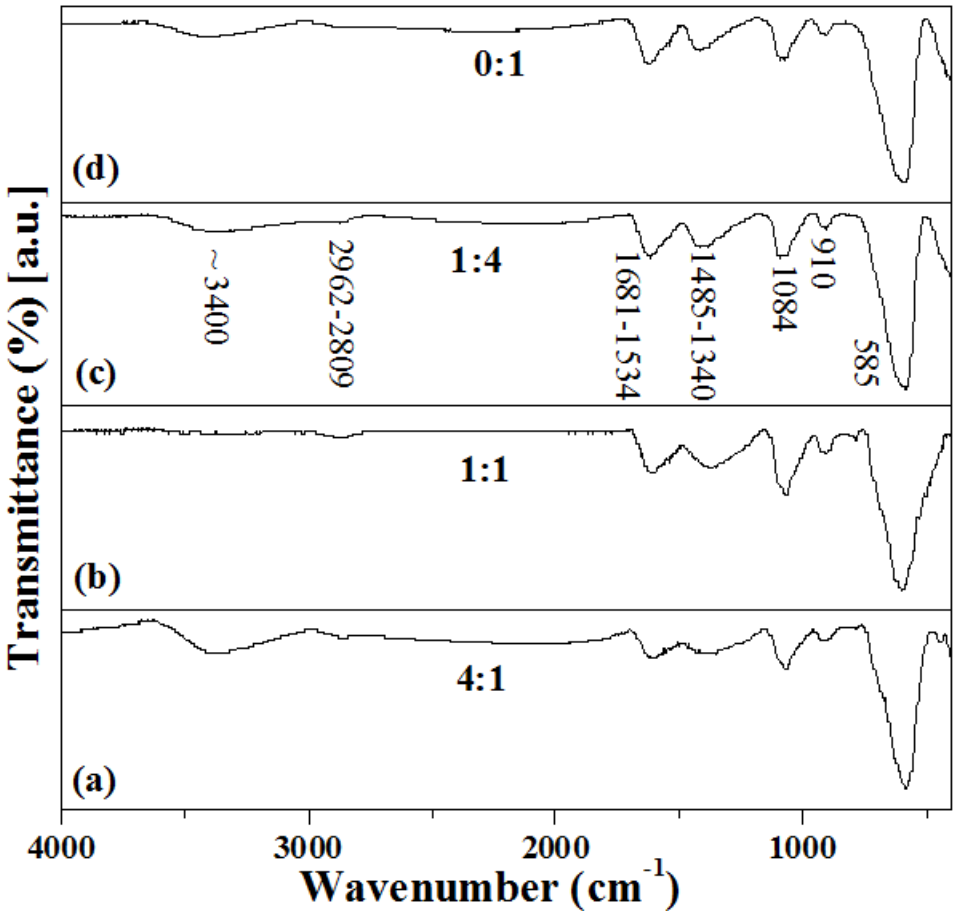

Figure 7.16. FTIR spectra of the nanoparticles prepared using different TEG: TEA ratio: (a) 4:1, (b) 1:1, (c) 1:4 and (d) 0:1 at 1h reaction time interval.

Figure 7.17 (b) and (c) show the wide scan XPS spectra of the nanoparticles prepared using the 1:4 and 0:1 TEG: TEA ratio at 1h reaction time interval. The nanoparticles prepared using the 1:1 and 4:1 ratio show the similar XPS spectra. It can be seen that the peaks except the N(1s) peak are very similar to that of the nanoparticles prepared using the 1:0 TEG:TEA ratio (Figure 7.17 (a)). The deconvoluted N(1s) spectra is shown in the

inset of Figure 7.17 while the deconvoluted O(1s) and C(1s) spectra are similar to that of the 1:0 nanoparticles as shown in the insets of Figure 6.12 (Chapter 6). The O(1s) peaks at 533.3; 531.6 eV and the C(1s) peak at 285.5 eV, which are assigned to C-O; O-H and C–C/C–H bond respectively [25, 29], are due to the adsorbed TEG/TEA molecules. The peaks at about 288 eV (C(1s)) and 399.5 eV (N(1s)) are due to C–O–C and C-N bond of the adsorbed TEG and TEA molecules, respectively [25,30]. In addition, the Fe($3p_{3/2}$), O(1s), Fe($2p_{3/2}$) and Fe($2p_{1/2}$) peaks at about 55, 530.3, 710 and 724 eV are due to Fe–O bond of the Fe_3O_4 particles [25, 29].

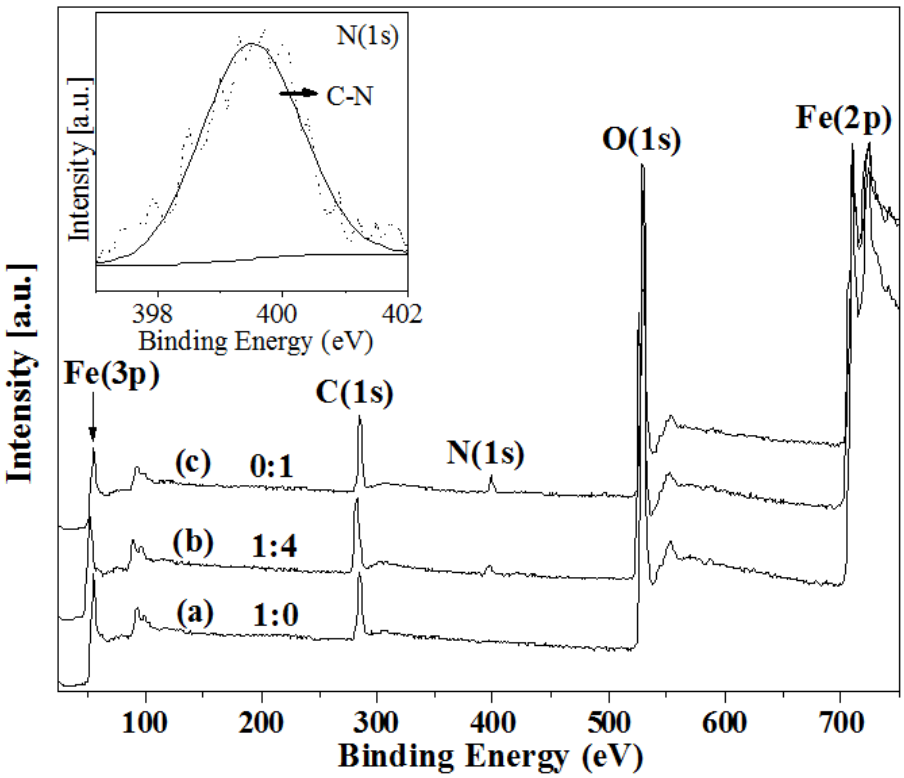

Figure 7.17. XPS spectra of the nanoparticles prepared using different TEG: TEA ratio: (a) 1:0, (b) 1:4 and (c) 0:1 at 1h reaction time interval. Inset of **C s**hows the deconvoulted N(1s) spectra.

Figure 7.18 shows the TGA curves of the nanoparticles prepared using different TEG: TEA ratio at 1h reaction time interval. The TGA curves represent two-stage weight loss: the first weight loss (between 25–200ºC) is due to the evaporation of water and the second weight loss (between 250–800ºC) is due to the decomposition of surface adsorbed chemically adsorbed organic coating from the particle surface. It is estimated from the TGA result that the amount of the adsorbed TEG and TEA coating on the surface of the MNF particles is 6 to 9 wt%.

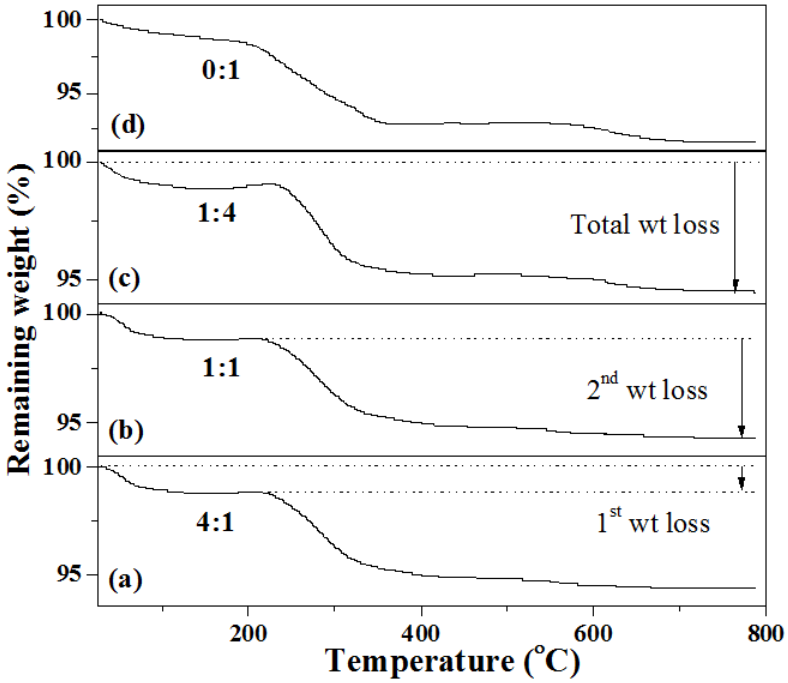

Figure 7.18. TGA curves of the nanoparticles prepared using different TEG: TEA ratio: (a) 4:1, (b) 1:1, (c) 1:4 and (d) 0:1 at 1h reaction time interval.

Thus, the XRD, FTIR, XPS and TGA studies confirm that the as-prepared nanoparticles are consisting of pure magnetite phase and their surfaces are coated with TEG and/or TEA molecules.

7.3.3. Magnetic Properties

Figure 7.19 A shows the VSM magnetization (M-H) curves of the particles prepared using different TEG: TEA ratio at 1h reaction time interval and Figure 7.19 B shows the M-H curves of the particles prepared using the 1:4 ratio at different reaction time intervals. It can be seen that the saturation magnetization (Ms) value of the particles increases from 67 to 80 emu/g with decreasing TEG:TEA ratio from 4:1 to 0:1 and increases from 75 to 86 emu/g with increasing reaction time from 1 to 4h for the samples prepared using the 1:4 TEG:TEA ratio. This increase of Ms value could be either due to the clustering of more and more number of magnetic nanoparticles into single a structure or due to self-assembly of the nanoclusters into the chain like structures while prolonging the reaction time as shown by above TEM studies (Section 7.2.1).

Figure 7.20 A and B shows the temperature dependence of the zero-field cooled/field cooled (ZFC-FC) SQUID magnetization curves of the magnetite nanoclusters prepared using at 1h and 2h reaction time intervals. It can be seen that the nanoclusters prepared at 1h reaction time are superparamagnetic in nature with the blocking temperature (T_B) at around 270 K (Figure 7.20 A). However, the nanoclusters prepared at 2h reaction time are no more superparamagnetic at the room temperature, which could be due to the self-assembly of the magnetite nanoclusters into a chain like structures as shown by the above TEM studies (Section 7.2.1). Thus, we have optimized the TEG: TEA ratio to 1:4 and reaction time at 1h for the preparation of well dispersed superparamagnetic IO@14 nanoclusters with high M_S (75 emu/g) and their potentialities for the magnetic hyperthermia and MRI applications were further investigated.

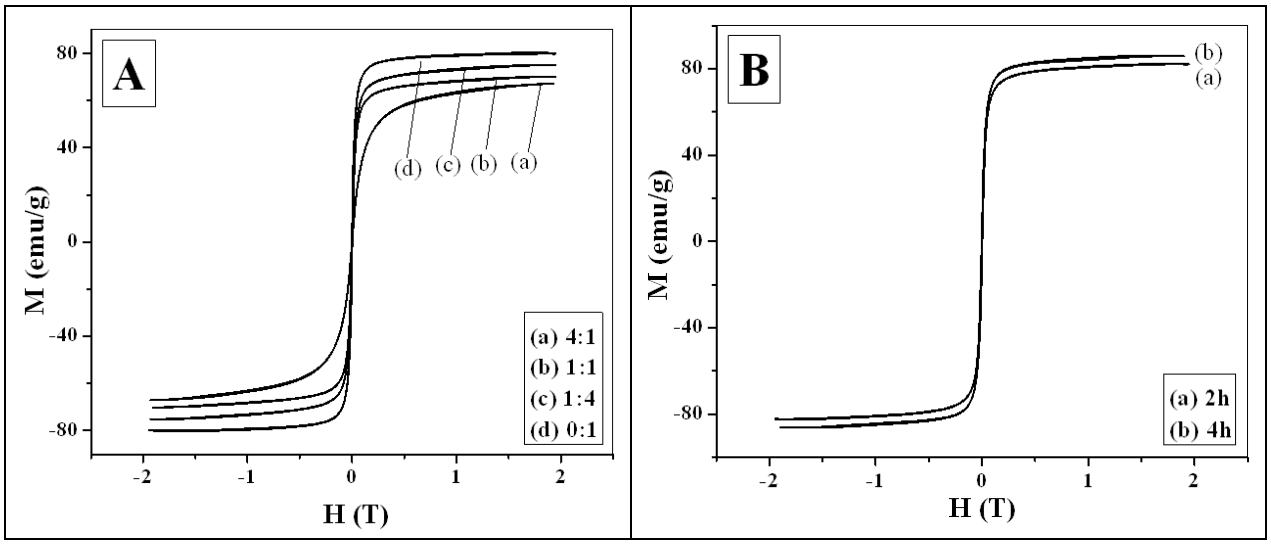

Figure 7.19. M-H curves the nanoparticles prepared **A.** using (a) 4:1, (b) 1:1, 1:4 (c) and (d) 1:4 TEG:TEA ratio at 1h reaction time interval. **B.** at (a) 2h and (b) 4h reaction time intervals using 1:4 TEG:TEA ratio.

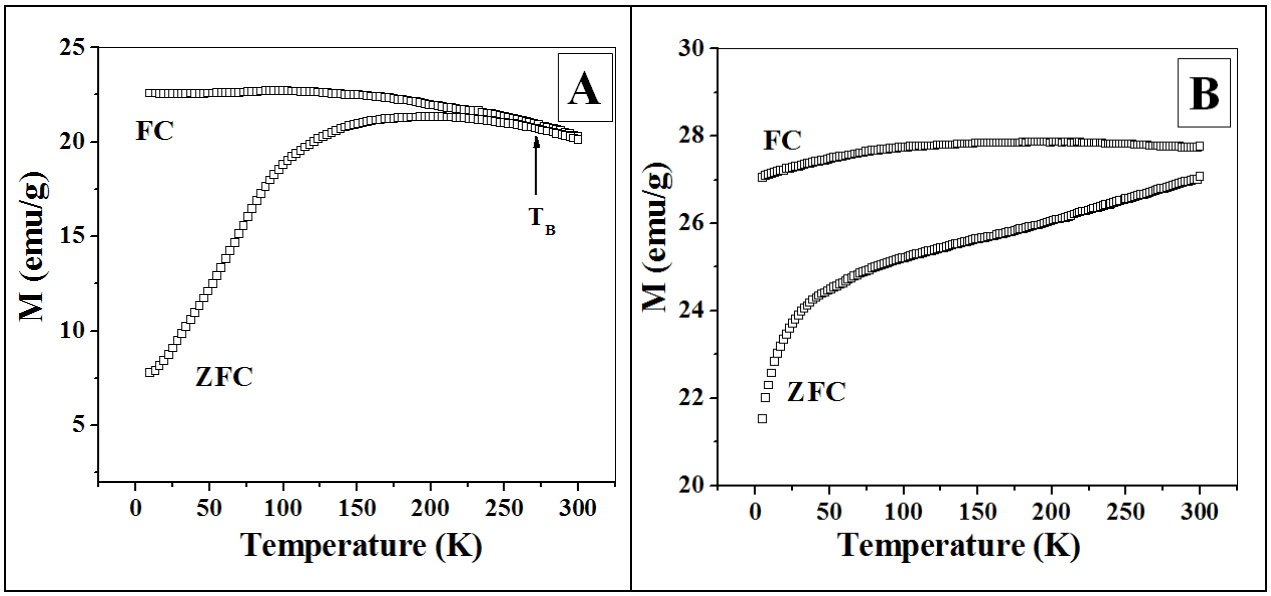

Figure 7.20. Zero-field cooled/field cooled (ZFC/FC) magnetization of **A.** I2 and **B.** I3 samples prepared at 1h and 2h respectively, under an applied field of 50 Oe.

7.3.4. In vitro Cytotoxicity Studies

Figure 7.21 shows the cytotoxicity profile of the TEA coated (IO@14) magnetite nanoparticles using the MCF-7 breast cancer cells. It can be seen that the IO@14 nanoparticles do not show any cytotoxicity in MCF-7 cells. Thus, the TEA coated magnetite nanoparticles are biocompatible up to the iron concentration of 10 mg/ml with MCF-7 breast cancer cells. Cell viability found to be increased at 10 mg Fe/ml as compared to 0.625 mg Fe/ml which could be due to increased cell mitochondria metabolic activity with more nanoparticle loading.

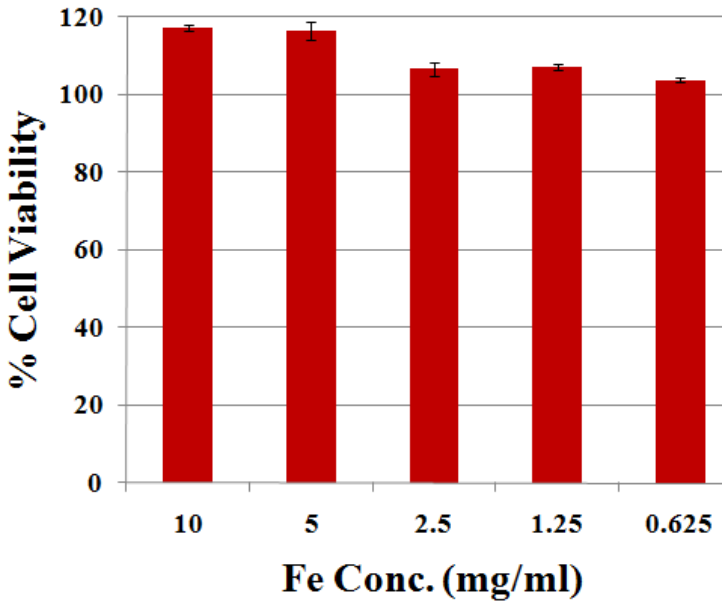

Figure 7.21. Cytotoxicity profile of the TEA coated (IO@14) nanoparticles on MCF-7 breast cancer cells.

7.3.5. Magnetic Hyperthermia Studies

Figure 7.22 show the time dependent temperature rise of 1 ml aqueous suspension of the TEA (1:4 TEG:TEA) coated (IO@14) nanoparticles with the iron concentrations of 0.5, 1, 2, 4 and 8 mg/ml upon exposure to 89 kA/m AC magnetic field at 240 kHz frequency. Inset of Figure 7.22 depicts the field dependent SAR values of the IO@250 nanoparticles with 1 mg/ml iron concentration at 240 kHz frequency, indicating that the SAR values varies nearly with H^2 as reported in literature [49-50]. The SAR values under 89 kA/m AC magnetic field at 240 kHz frequency is about 500 Watt/g for the IO@14 nanoclusters with the 0.5 mg/ml iron concentration.

The time required to raise the temperature up to 42ºC for the IO@14 nanoparticles with different iron concentration (0.5- 8 mg/ml) using different frequency (240 and ~ 400 kHz) are given in Table 8.2 and Table 8.3 respectively. The results indicate that the rate of temperature rise systematically increases with the iron concentration of IO@14 nanoparticles. Moreover, the rate of temperature rise depends on the applied frequency and AC magnetic field. The heating of the IO@14 nanoparticles could be due to Neel/Brownian relaxation or hysteretic loss when they are exposed to an alternating (AC) magnetic field [17].

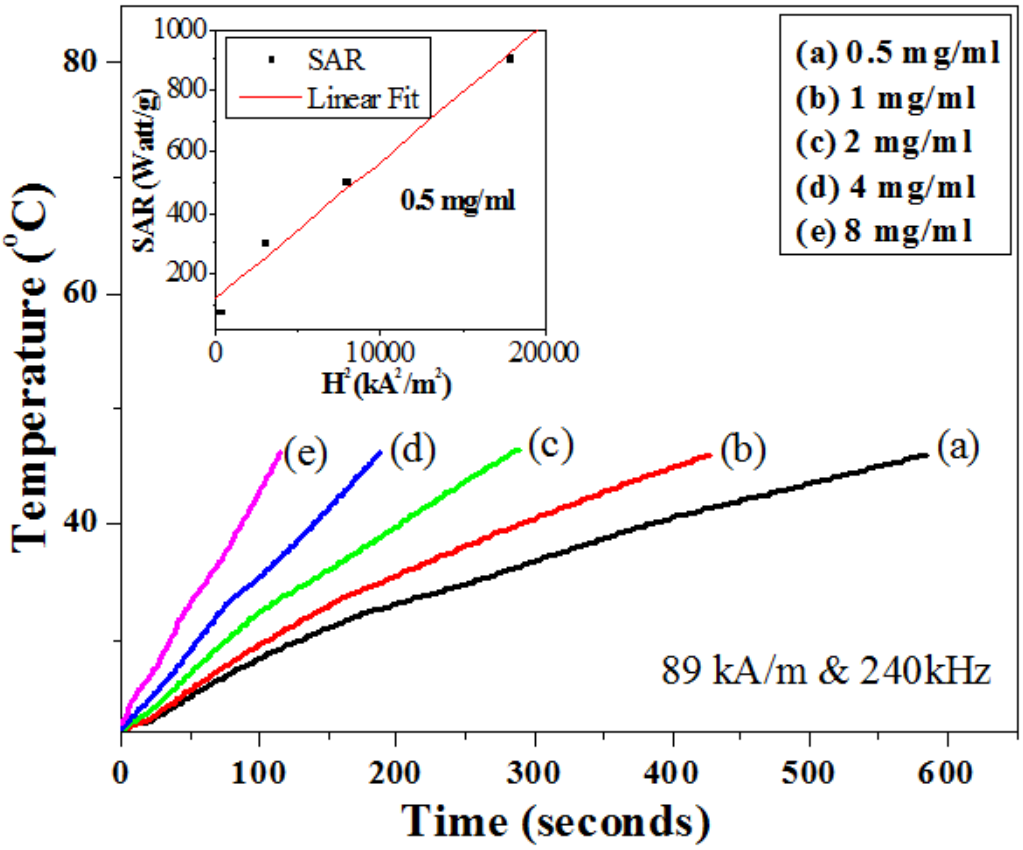

Figure 7.22. Time dependent temperature rise of 1 ml IO@14 sample with different iron concentration. Inset shows field dependent SAR values of 1 ml IO@14 sample.

Table 7.2. The time required (within 600 second of experiment) to raise up to 42 ºC for the IO@14 nanoparticles with different Fe concentrations at ~ 240 kHz frequency.

Sample	Fe Concentration (mg/ml)	Time required to raise at 42 ºC (second)	Magnetic field, H (kA/m)	Frequency, f (kHz)	H×f ($Am^{-1}S^{-1}$)
IO@14	8	134	18 (100A)	240	0.4×10^{10}
	4	283			
	2	462			
	1	Not reached (32 ºC)			
	0.5	Not reached (27 ºC)			
	8	116	54 (300A)	240	1.3×10^{10}
	4	206			
	2	314			
	1	569			
	0.5	Not reached (36 ºC)			
	8	96	89 (500A)	240	2.1×10^{10}
	4	156			
	2	228			
	1	335			
	0.5	449			
	8	81	134 (max limit of 750A)	240	3.2×10^{10}
	4	127			
	2	175			
	1	234			
	0.5	274			

Table 7.3. The time required (within 600 second of experiment) to raise up to 42 ºC for the IO@14 nanoparticles with different Fe concentrations at ~ 400 kHz frequency.

Sample	Fe Concentration (mg/ml)	Time required to raise at 42 ºC (Seconds)	Magnetic field, H (kA/m)	Frequency, f (kHz)	H×f ($Am^{-1}S^{-1}$)
IO@14	8	250	17 (50 A)	~400	0.7×10^{10}
	4	419			
	2	Not reached (32 ºC)			
	1	Not reached (29 ºC)			
	0.5	Not reached (27 ºC)			
	8	112	35 (100A)	~400	1.4×10^{10}
	4	167			
	2	491			
	1	Not reached (35 ºC)			
	0.5	Not reached (30 ºC)			
	8	61	69 (200A)	~400	2.8×10^{10}
	4	124			
	2	308			
	1	Not reached (41 ºC)			
	0.5	Not reached (33 ºC)			
	8	55	104 (300A)	~400	4.2×10^{10}
	4	118			
	2	255			
	1	498			
	0.5	Not reached (37 ºC)			

7.3.6. In vitro Hyperthermia

Figure 7.23 A shows the *in vitro* cytotoxic effect on MCF-7 breast cancer cells treated with magnetic hyperthermia using the IO@14 nanoparticles (0.5 mg/ml of Fe concentration) upon exposure to 89 kA/m AC field at 240 kHZ frequency. As a comparison, the cancer cells were also exposed to only magnetic field (89 kA/m AC, without adding any IO@14 nanoparticles) and only IO@14 nanoparticles with 0.5 mg/ml of Fe concentration (without exposing to the magnetic field). Results (Figure 7.23 A) show that the magnetic hyperthermia at 45°C caused 74% of cell death, while cell viability in the case of exposure to only the magnetic field or only IO nanoparticles were comparable to that of the control. Thus, it was confirmed that about 74 % loss of MCF-7 cancer cell viability was due to the magnetic hyperthermia treatment. Figure 7.23 B, C and D show optical microscope images of MCF-7 breast cancer cells without any treatment (i.e. control) and the cells treated with only AC magnetic field (without IO@14), and with magnetic hyperthermia (using both IO@14 and magnetic field). It was observed that the cells treated by magnetic hyperthermia, lost their ability to attach to the surface and fail to grow (as shown in Figure 7.23 D) while the control cells (as shown in Figure 7.23 B) and the cells treated with only magnetic field (as shown in Figure 7.23 C) are attached to the surface, which clearly indicates that the losses of cell viability (also as shown by the MTT assay) are due to the magnetic hyperthermia treatment using the IO@14 nanoparticles.

The percentage loss of MCF-7 cancer cell viability due to the IO@14 nanoparticles as well as the IO@250 nanoparticles (which are prepared by refluxing $Fe(acac)_3$ in TEG)

are compared in Table 8.4. It can be seen that the percentage cell death is greater for the IO@14 nanoparticles (74%) than IO@250 nanoparticles (60%). This could be due to the clustering of magnetite nanoparticles which leads to greater Ms (75 emu/g) and higher SAR value (500 Watt/g) and thereby faster heating rate of IO@14 nanoparticles under the AC magnetic field as compared to unclustered IO@250 nanoparticles (60 emu/g, 135 Watt/g). Thus, the IO@14 nanoparticles are much better for magnetic hyperthermia applications than the IO@250 nanoparticles as the amount of magnetic materials required for the treatment would be less and undesired toxicity which may arise due to high dose in vivo can be avoided.

Table 7.3. Average particle size, saturation magnetization (Ms), SAR and percentage cell death for IO@250 nanoparticles and IO@14 nanoclusters.

Samples	**Average particle size (nm)**	**Ms (emu/g)**	**SAR (Watt/g)**	**Cell death (%)**
IO@10	10	60	135	60
IO@14	44	75	500	74

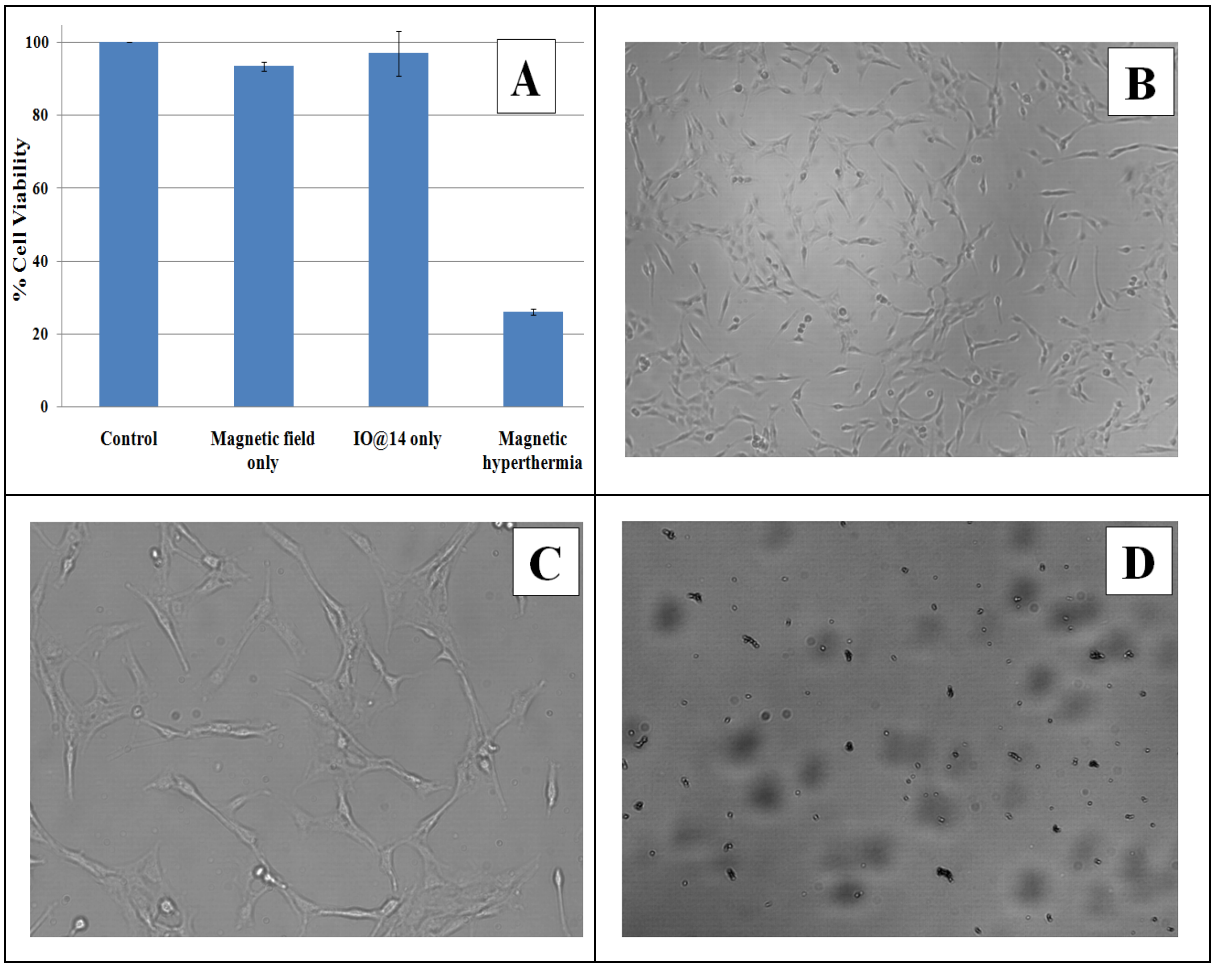

Figure 7.23. A. Cell viability plot shows the cytotoxic effect on MCF-7 breast cancer cells treated with magnetic hyperthermia (~ 45ºC), treated with IO@14 only, and treated with magnetic field only in comparison with the control cells. **B.** is optical microscope images of control MCF-7 breast cancer cells **C.** and **D.** are optical microscope images of control MCF-7 breast cancer cells treated with only magnetic field and magnetic hyperthermia.

7.3.7. MRI Relaxivity Studies

Figure 7.24 show the transverse relaxation rates (1/T2 and 1/T2*) various Fe concentration of IO@14 nanoclusters measured at 9.4 T. The corresponding relaxivities ($r2$, and $r2^*$) were estimated as 294.99 and 450.05 $s^{-1}mM^{-1}$ suggesting that IO@14 nanoclusters can also be used as a MRI T_2 contrast agent.

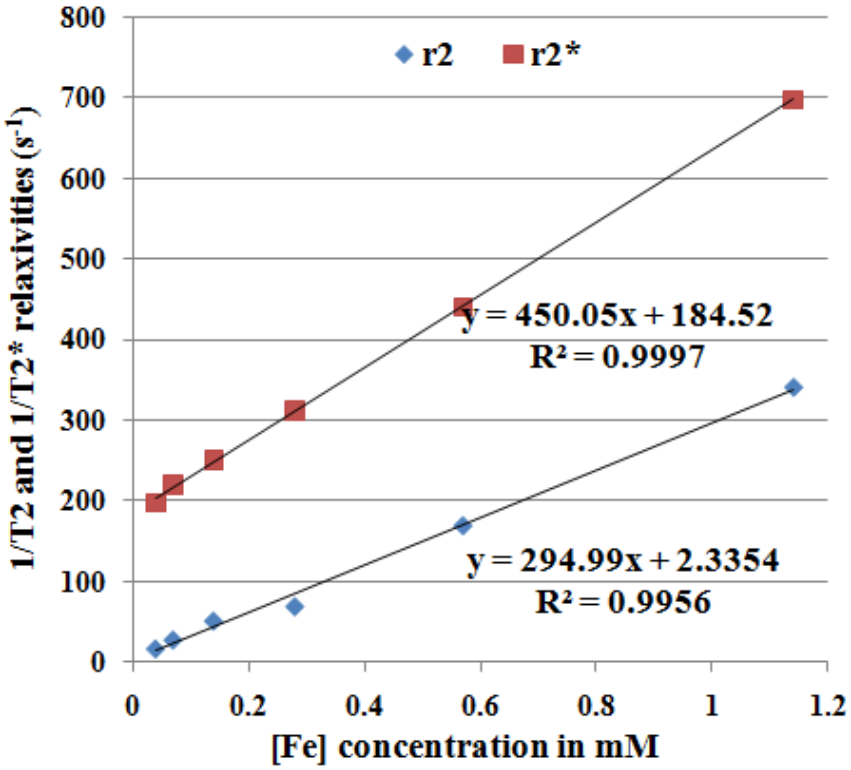

Figure 7.24. Transverse relaxation rates (1/T2 and 1/T2*) vs Fe concentration of IO@14 nanoparticles measured at 9.4 T.

7.3.8. In vivo MRI Imaging

We further evaluated the efficacy of the IO@14 nanoclusters for *in vivo* MRI imaging application. The IO@14 nanoclusters were injected in SCID mice having subcutaneous xenograft tumor of MCF-7 cancer cells. Figure 7.25 shows the signal intensity normalized by the signal in the background at different time points in tumor (blue line), liver (red line) and kidney (green line). Left images in Figure 7.26 show the corresponding axial image of tumor (top left) and liver & kidney (bottom left) before injection while right images in Figure 8 show the axial image of tumor (top right) and liver & kidney (bottom right) after 6 hours injection of the IO@14 nanoclusters. It can be seen that the percentage of signal reduction for the liver is higher as compared to kidney and tumor (Figure 7.25) and this is also obvious from the large signal intensity reduction in post contrast image of liver (Figure 7.26) which is due to massive accumulation of the IO@14 nanoclusters in the liver. The contrast change in kidney suggests that the IO@14 nanoclusters are accumulated in kidney however they are excreted quickly. It can also be observed that there is some contrast changes in tumor which is relatively less as compared to that of liver (Figure 7.25). However, there is a significant reduction of signal intensity in post contrast tumor image which is obvious from the colored intensity scale (Figure 7.26) also indicating the accumulation of the IO@14 nanoclusters in the tumor region and thereby reduces the T2 of the tumor tissue. Thus it can be concluded that the IO@14 nanoclusters could be used as a potential MRI contrast agent and have the tendencies to accumulate at tumor sites by a means of passive targeting in which the nanoparticles penetrate through the leaky vasculature of the tumor site by enhanced permeation and retention (EPR) mechanism. However, tumor accumulation of the

IO@14 nanoclusters can be further increased by using permanent magnetic field gradient near tumor area following the principle of magnetic drug targeting (MDT) [33].

Taken together, the IO@14 nanoclusters are able to heat up efficiently under AC under magnetic field and can be detected by MRI due to their high T2 contrast enhancement properties. Thus, IO@14 nanoclusters are very promising for both cancer diagnostic and therapeutic (theranostic) purposes. However, further in vivo investigations are warranted before their clinical use.

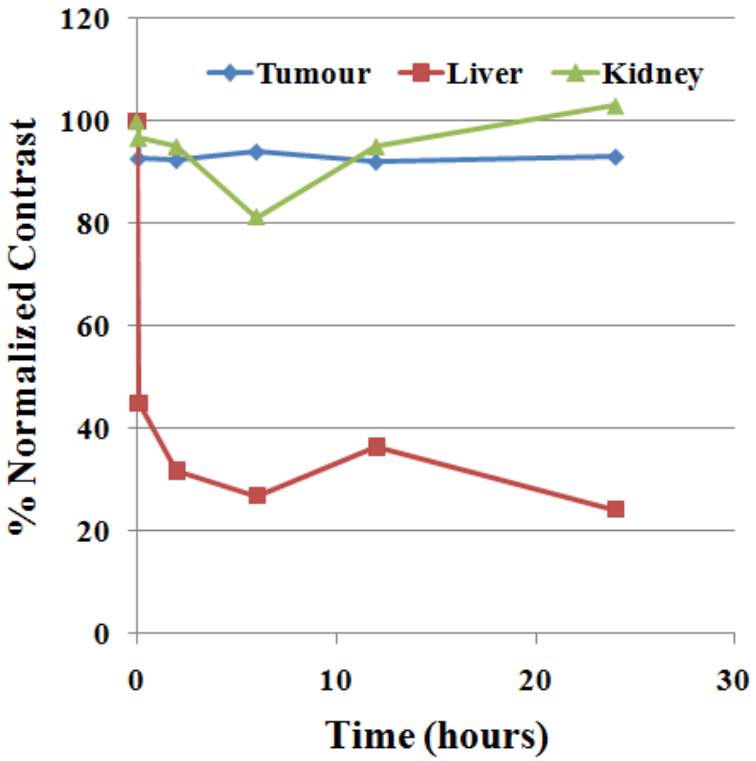

Figure 7.25. The normalized signal change at different time points in tumor (blue line), liver (red line) and kidney (green line).

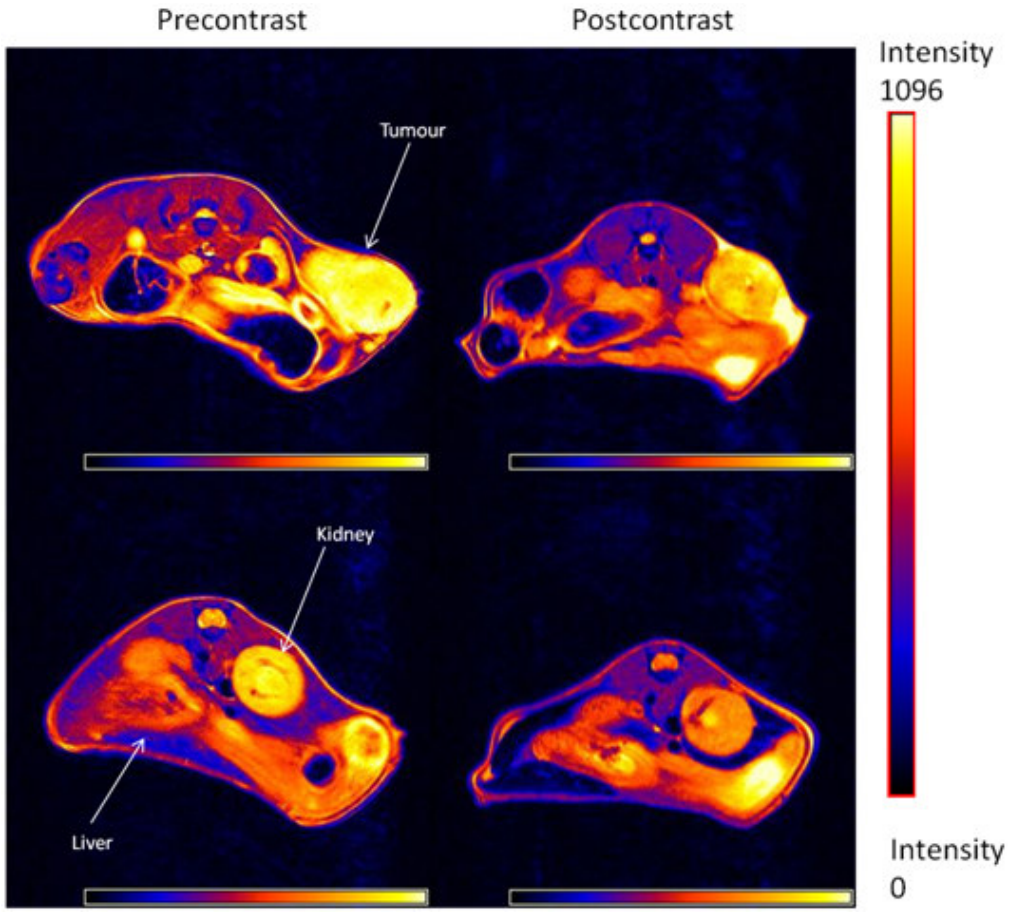

Figure 7.26. Top images show the axial image of tumor (marked by arrow) and bottom images show the axial image of liver & kidney (marked by arrow) before injection (left) and after 6 hours of injection (right) of the IO@14 nanoparticles. The change in signal intensity can be noticeable and can be compared to the scale given.

7.4. Conclusions

Magnetite nanoclusters have been successfully synthesized by a facile one-step thermal decomposition of $Fe(acac)_3$ in a liquid mixture of TEG and TEA. To the best of our knowledge, this is the first report on the single-step facile synthesis of magnetite nanoclusters using a thermal decomposition method. The well dispersed superparamagnetic IO@14 nanoclusters obtained at an optimized 1:4 TEG:TEA (v/v) ratio resulted higher Ms (75 emu/g) than similar unclustered magnetic nanoparticles (65 emu/g). The IO@14 nanoclusters are found to be cytocompatible. *In vitro* hyperthermia studies have confirmed that the Fe_3O_4 nanoclusters are able to produce significant temperature rise upon exposure to AC magnetic field and yielded high specific absorption rate (SAR~500 Watt/g) values. The heating rate of IO@14 nanoclusters under AC magnetic field are faster and thus cause more percentage loss of MCF-7 cancer cell viability (74%) than that for the Fe_3O_4 nanoparticles (60%). Moreover, IO@14 nanoclusters showed significant r2 and r2* relaxivities (294.99 and 450.05 $s^{-1}mM^{-1}$) and promising contrast i*n vivo* MRI imaging too. Thus, the novel IO@14 nanoclusters are very promising candidate for for magnetic hyperthermia treatment of cancer and they could be used for clinical MRI imaging

7.5. References

1. A.K. Gupta and M. Gupta, Biomaterials 26 (2005) 3995.

2. S.J. Son, J. Reichel, B. He, M. Schuchman, S.B. Lee, J. Am. Chem. Soc. 127 (2005) 7316.

3. H.H. Weetall, M.J. Lee Appl Biochem Biotechnol 22 (1989) 311.

4. S. Guo, D. Li, L. Zhang, J. Li, E. Wang, Biomaterials 30 (2009) 1881.

5. S. Dandamudi, R.B. Campbell, Biomaterials 28 (2007) 4673.

6. S. Chen, Y. Li, C. Guo, J. Wang, J. Ma, X. Liang Langmuir 23 (2007) 12669.

7. P. Pradhan, J. Giri, G. Samanta, H.D. Sarma, K.P. Mishra, J. Bellare, R. Banerjee, D. Bahadur, J. Biomed. Mater. Res. Part B: Appl. Biomaterials 81B (2007) 12.

8. M. Kawashita, M. Tanaka, T. Kokubo, Y. Inoue, Y. Yao, S. Hamada, T. Shinjo, Biomaterials 26 (2005) 2231.

9. S. Mornet, S. Vasseur, F. Grasset, E. Duguet, J. Mater. Chem. 14 (2004) 2161.

10. M. Bra1hler, R. Georgieva, N. Buske, A. Mu1ller, S. Mu1ller, J. Pinkernelle, U. Teichgra1ber, A. Voigt, H. Ba1umler Nano Lett. 6 (2006) 2505.

11. H. Pardoe, W. Chua-anusom, T.G. St Pierre, J. Dobson Phys. Med. Biol. 48 (2003) N89.

12. P. Majewski, B. Thierry, Critic. Rev. Solid State Mater. Sci. 32 (2007) 203.

13. L.L. Ma et al ACS Nano 3 (2009) 2686.

14. D.R. Ingram, C. Kotsmar, K.Y. Yoon, S. Shao, C. Huh, S.L. Bryant, T.E. Milner, K.P. Johnston, J. Colloid Interface Sci. 351 (2010) 225.

15. C. Kotsmar, K.Y. Yoon, H. Yu, S.Y. Ryoo, J. Barthd, S. Shao, T.E. Milner, S.L. Bryant, C. Huh, K.P. Johnston Indust. Eng. Chem. Res. 49 (2010) 12435.

16. M. Mehrmohammadi, K.Y. Yoon, M. Qu, K.P. Johnston, S.Y. Emelianov, Nanotechnology 22 (2011) 045502.

17. S. Sun, H. Zeng, J. Am. Chem. Soc. 124 (2002) 8204.

18. S. Sun, H. Zeng, D.B. Robinson, S. Raoux, P.M. Rice, S.X. Wang, G.X. Li J. Am. Chem. Soc. 126 (2004) 273.

19. J. Park, K. An, Y. Hwang, J.G. Park, H.J. Noh, J.Y. Kim, J.H. Park, N.M. Hwang, T. Hyeon, Nat. Mater. 3 (2004) 891.

20. D. Maity, S.G. Choo, J. Yi, J. Ding, J.M. Xue, J. Magn. Magn. Mater. 321 (2009) 1256.

21. Z. Li, H. Chen, H. Bao, M. Gao, Chem. Mater. 16 (2004)1391.

22. W. Cai, J. Wan, J. Coll. Inter. Sci. 305 (2007) 366.

23. J. Wan, W. Cai, X. Meng, E. Liu, Chem. Commun. 47 (2007) 5004.

24. D. Maity, S.N. Kale, R.K. Ghanekar, J.M. Xue, J. Ding J. Magn. Magn. Mater. 321 (2009) 3093.

25. D. Maity, P. Chandrasekharan, C.T. Yang, K.H. Chuang, B. Shuter, S.S. Feng, J.M. Xue, J. Ding, Nanomedicine 5 (2010) 1571.

26. D. Maity, D.C. Agrawal, J. Magn. Magn. Mater. 308 (2007) 46.

27. J.R. Dyer, Applications of Absorption Spectroscopy of Organic Compounds, Prentice-Hall, Inc., (1965).

28. R.M. Cornell, U. Schwertmann, The Iron Oxides: Structure, Properties,Reactions, Occurrence and Uses, second ed., Wiley–VCH, Weinheim, (2003).

29. C.D. Wagner, W.M. Riggs, L.E. Davis, J.F. Moulder, G.E. Muilenberg, Handbook of X-ray Photoelectron Spectroscopy, Perkin-Elmer Corporation, (1979).

30. Z. Li, H. Chen, H. Bao, M. Gao, Chem. Mater. 16 (2004) 1391.

31. R. Hergt, R. Hiergeist, M. Zeisberger, G. Gl.ockl, W. Weitschies, L.P. Ramirezc, I. Hilgerd, W.A. Kaiser, J. Magn. Magn. Mater. 280 (2004) 358.

32. L.L. Lao, R.V. Ramanujan, J. Mater. Sci.: Mater. Med. 15 (2004)1061.

33. C. Alexiou, W. Arnold, R. J. Klein, F. G. Parak, P. Hulin, C. Bergemann, W. Erhardt, S. Wagenpfeil and A. S. Lubbe, Cancer Res., 60 (2000) 6641.

CHAPTER 8

Summary and Future Work

8.1. Summary

- Monodispersed & superparamagnetic hydrophobic Fe_3O_4 nanoparticles with improved Ms (74 emu/g) are synthesized by solvent free thermal decomposition (SFTD) method.
- The hydrophobic Fe_3O_4 nanoparticles are converted into hydrophilic (i.e. water soluble) by functionalization and polymeric encapsulation to make them useful for biomedical applications.
- Other metal oxide and luminescence NPs like CoO, ZnO, Y_2O_3:Eu, $NaYF_4$:Yb,Er NPs have also been synthesized using the TD method.
- Hydrophilic superparamagnetic Fe_3O_4 nanoparticles have been synthesized directly by one-step polyol synthesis method.
- Hydrophilic superparamagnetic Fe_3O_4 nanoclusters with high saturation magnetization (Ms ~ 86 emu/g) have been synthesized by one-step synthesis method.
- *In vitro* cell viability studies have demonstrated high cellular uptake and low cytotoxicity of the Fe_3O_4 nanoparticles and nanoclusters.
- MRI relaxivity measurements have confirmed higher r_2* relaxivity (617.5 $s^{-1}mM^{-1}$) of the Fe_3O_4 nanoparticles as compared to commercial resovist nanoparticles (245.2 $s^{-1}mM^{-1}$).
- *In vivo* MRI imaging studies of the Fe_3O_4 nanoparticles and nanoclusters have demonstrated very promising contrast i*n vivo* tumor imaging.
- *In vitro* hyperthermia studies have confirmed that the Fe_3O_4 nanoparticles and nanoclusters are able to produce significant temperature rise upon exposure to AC magnetic field (SAR~ 135 Watt/g for the nanoparticles and ~500 Watt/g for

nanoclusters) and thus, 60-74% loss of cancer cell viability was observed due to the magnetic hyperthermia treatment.

It can thus be concluded that the Fe_3O_4 nanoparticles and nanoclusters are very promising candidate for clinical MRI imaging as well as for magnetic hyperthermia treatment of cancer.

8.2. Future Work

The magnetic nanoparticles (MNPs) could be combined with the anticancer drugs (chemotherapeutic agents) to develop the multifunctional nanoparticles which are very efficient to target MNPs and chemotherapeutic agent to a specific tumor site and thereby to produce combined magnetic hyperthermia and chemotherapeutic effect for cancer treatment. With this combined therapy, various side effects of chemotherapy could be avoided as lower chemotherapeutic dose is required and it could be possible to selectively heat up tumors by applying AC magnetic field to the targeted nanoparticles. However, improvements of combined therapeutic modality are still needed for more successful treatment of cancer. In this context, there is a need of efficient drug delivery systems to selectively deliver MNPs and chemotherapeutic agents to tumor cells and then apply localized hyperthermia to tumor site. There are three general directions to deliver chemotherapeutic agent and MNPS into specific cancer tissue avoiding the side effects: (i) Magnetic drug targeting, (ii) Site-specific active targeting and (iii) Site-specific triggering.

8.2.1. Magnetic Drug Targeting

Magnetic drug targeting (MDT) is the site specific delivery of chemotherapeutic agents to their target using magnetic nanoparticles (ferrofluids) bound to these agents, with an external magnetic field generated at the tumor site [1]. In this approach, magnetic particles along with the drug are formulated into a pharmaceutically stable formulation which can be held in position at the target site (or tumor) using an external magnetic field [1-3]. This approach helps in localizing the drug to the desired site, thereby minimizing the potential for accumulation of the drug in healthy tissues. A combination of improved target selectivity and enhanced duration of drug exposure to the target also reduces the overall amount of drug taken up by the RES. MDT uses much smaller doses of drug leading to several fold increased drug efficacy and reduced drug toxicity [1, 3-7]. In addition to some of the key advantages of MDT already mentioned above, the magnetic nanoparticles used in MDT also offer distinct advantages. They are:

a) The magnetic nanoparticles are biocompatible, non-immunogenic and injectable.

b) They are non-toxic, even if injected in larger quantities. They are metabolized by the hepato-renal system and used in the synthesis of hemoglobin.

c) They have controllable sizes (from a few nanometers to tens of nanometers).

d) They have high magnetic susceptibility and show high accumulation in the desired target tissue or organ.

e) They can be made to respond resonantly to an alternating magnetic field, with advantageous results related to the transfer of energy from the exciting field to the nanoparticle, as in case of hyperthermia.

f) They are superparamagnetic; hence they preferentially deliver the ferrofluid bound drug at the desired site under the influence of an external magnet. This reduces the amount of drug required and thus the side-effects owing to the drug [7-9].

Magnetic liposomes or magnetoliposomes are magnetic derivatives of liposomes and can be prepared by entrapment of ferrofluids within the liposomal core. In other words, they consist of magnetic nanoparticles wrapped in a phospholipid bilayer [2, 8]. Magnetoliposomes offer a promising tool for passive targeting with regard to the drug delivery of magnetic nanoparticles [8]. An advantage in formulating magnetic particles within liposomes is the enhanced protection against aggregation and oxidation when incorporated in liposomes [9]. Magnetic liposomes like conventional liposomes have biokinetic and structural advantages, like their ability to spontaneously encapsulate drugs or genes along with magnetite [8, 10-11]. Furthermore, their surface can be modified chemically to target specific tissues [8].

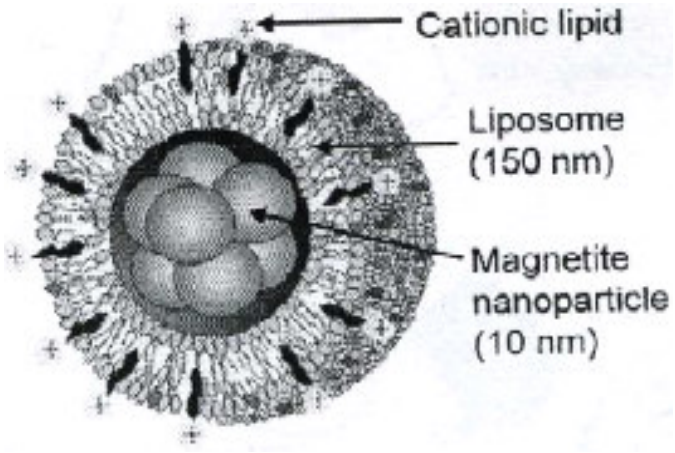

Figure 8.1. Magnetic cationic liposomes (MCLs) relatively biocompatible lipids [8].

Magnetic cationic liposomes (MCLs) are made of positively charged (cationic) and relatively biocompatible lipids (Figure 8.1). They have a positive charge on their surface, which is useful in the interaction of these liposomes with the negatively charged tumor vascular surface. Liposomes containing fluid MAG-C (magnetite) can maintain a positive charge potential and hence they have potential to target the tumor vasculature in the presence of the magnetic material. The liposomes have been shown to be taken up by the tumor endothelial cells and cancer cells as well. The application of an external magnet can thus enhance the vascular accumulation in tumors. It has also been shown that MCLs show superparamagnetic behavior and with an increase in the MAG-C content the saturation magnetization values of the MCLs significantly increase [6, 10].

For MDT, it is important to know if the ferrofluid micro-circulation and diffuses freely into interstitial space, or whether the complex remains within the vascular space [6,12]. Other important aspects to be considered for MDT are: 1) The type and concentration of the ferrofluid employed, 2) the magnetic strength of the external magnetic field, 3) the time duration for which the target tissue is exposed to the external magnet, 4) bioavailability of ferrofluid as well as the *in vivo* desorption time of the drug [6,12].

The application of hyperthermia is favored if phospholipids with transition temperature slightly above the physiological temperature are incorporated into liposomes. For drug loaded MCLs, the magnetic nanoparticles embedded within the lipid bilayer get heated by means of an AC field. The thermal energy is then transferred to the liposome bilayer which gets heated to its phase transition temperature. The bilayer then melts and results in efficient release of the incorporated drug substance [9, 13].

8.2.2. Site-specific Active Targeting

For the site-specific active targeting, first the drugs are immobilized on carrier particle and then surface of the particle is labelled with ligands or antibodies that target over expressed receptors in the tumor tissue [7, 14-15]. Liposomes [16-18], polymeric nanoparticles [19-22], micelles [23] and dendrimers [24-25] have been extensively used as a carrier for the delivery of drugs to tumors. Among these, the polymeric nanoparticles have been received most attention due to their high chemical stability [26-27]. A number of different polymers have been utilized as drug carriers, but PLA-PEG [14, 28.30] and PLGA-PEG [14, 30-33] diblock copolymers have been the focus of intense research on drug delivery over the past two decades because of their following characteristics:

1. biodegradability
2. excellent biocompatibility
3. "stealthy," i.e., not recognizable by the reticulo-endothelial (RES) system and thus reduce RES clearance and facilitates extravascular uptake
4. longer blood circulation due to hydrophilicity, flexibility and charge neutrality of PEG chains
5. consisting of both hydrophobic (PLA/PLGA) and hydrophilic (PEG) part and thus capable of encapsulating both the hydrophobic and hydrophilic materials
6. able to control drug release rate through tunable degradation
7. availability of functional groups to the distal end of a few PEG molecules for the conjugation with cell-specific ligands (folic acid, monoclonal antibodies etc.).

Polymeric nanoparticles can be prepared by several techniques (emulsification-solvent evaporation methods, solvent displacement methods, salting out methods.), depending on

the nature of the polymeric material and the characteristics of the drug to be loaded. Emulsification-solvent evaporation method is widely used for the preparation of nanoparticles made of PLA-PEG, PLGA-PEG block copolymers [28-31]. Thus, MNP and the drugs are encapsulated within PLA/PLGA-PEG and the obtained nanoparticles are called as pegylated nanoparticles (PNs). For increasing the probability of redirecting long-circulating PNs to the desired target, their surfaces are labeled with either the specific antibodies or the ligands targeting proteins expressed on cancer cell membranes or endothelial cells lining the newly generated blood vessels in the tumor. Antibody labelled PNs (pegylated immune-nanoparticles, PINs) consist of monoclonal antibodies (MAb) or antibody fragments, $F(ab)_2$ coupled to their surface, which causes the PINs to bind selectively to antigens or receptors that are either uniquely expressed or over-expressed on cancer cells, leading to increased drug delivery to the target cells. PNs conjugated with MAb not only selectively target cancer cells, but they could also improve the internalization of the encapsulated drugs into the targeted cancer cells. Several studies have dealt with PNs targeting through the attachment of the antibody directly to the tip of the PEG strands [26, 34-35]. For effective targeting, PINs should bear optimum number of antibody molecules to facilitate binding to target molecule as well as to escape RES uptake which needs fine tuning and optimization for different targeting molecules. PINs can be targeted to surface molecules expressed either in the vascular system or in the extra vascular system on tumor cell membranes. The most readily accessible target sites for PINs are the vascular endothelial surface of growing tumors and circulating cells related to the immune system. In this regard, different antibody molecules like anti-CD19, anti–CD20, anti-ICAM-1 antibody and anti-HER-2 can be attached to PNs and

hence targeting to specific cancers expressing corresponding antigens could be achieved. Another approach for PNs based targeting is folic acid mediated targeting. Folic acid is a vitamin that is essential for the biosynthesis of nucleotides. PNs conjugated with folic acid appeared to localize in the cell cytoplasm as a consequence of folate receptor-mediated endocytosis taking advantage of the frequent overexpression of folate receptors (FR) onto the surface of human cancer cells [34]. FR targeted PNs have proven effective in delivering doxorubicin *in vivo* [36] and have been found to bypass multidrug resistance in cultured tumor cells [37]. Thus, PNs labelled with MAb or FR are the potential candidates for the cancer-specific active drug targeting.

8.2.3. Site-specific Triggering

For the site-specific triggering, the drugs are immobilized on stimuli-resposive polymers. Various polymer matrices like gelatine [38], poly(vinylalcohol) [39], hydroxypropyl cellulose [40], poly(*N*-isopropylacrylamide) [41] or poly(*N*-isopropylmethacrylamide), [42] etc. have been explored. Their heat sensitive behaviour offers enormous possibilities for temperature triggered drug release at the pathological sites such as cancer. Amongst all, much attention has been paid on poly (N-isopropylacrylamide) (PNIPAAm) as a promising thermosensitive drug delivery system as its transition temperature (which is defined as lower critical solution temperature, LCST ~32-34 ºC) is very close to human body temperature. Its aqueous solubility has been well-studied by many researchers and they found that it exhibits inverse solubility with temperature [43]. Below this critical temperature (CT), the polymer chains are excessively hydrated (swollen) and form expanded structures (coil form). Above the CT (Lower Critical Solution Temperature,

LCST), the chains rapidly dehydrate (collapse) and aggregate to form compact structures (globule form). It contains hydrophilic moiety acryl amide and relatively hydrophobic isopropyl group which results in hydrophobic-hydrophilic interaction with aqueous medium that ultimately determines its solubility in water at a given temperature. The conformational change in a single chain segment upon heating is also well observed in PNIPAAm based macroscopic bulk hydrogels, crosslinked copolymers, microgels, latexes, interpenetrating networks (IPNs) and colloidal particles as well [44-45].

Redox polymerization of aqueous PNIPAAm in presence of sulphate initiators at some elevated temperature promotes the growing polymer chains to form highly monodisperse colloidal particles [46]. The polymer gels containing particles rather than interpenetrating network have their own advantages for *in vivo* biomedical studies like internalization into body cells. Being in particle form, these offer easy surface tailoring to attach desired drugs, enzyme etc. and release them by certain physical/chemical triggering mechanisms. Their higher electrophoretic mobility and submicron to nano size range (200-300 nm) can also be advantageous as a matrix for drug delivery systems to carry drug as well as magnetic nanoparticles in case of magnetic hyperthermia and DNA diagnosis [47]. Here magnetic nanoparticles could be used to generate heat under AC magnetic field and temperature triggered release of drug can occur through thermoresponsive polymeric colloidal system. In addition, these polymeric colloidal nanogel particles because of their higher mechanical strength and durability over other drug carriers like liposomal and bulk hydrogels have been proved to provide prolonged circulation and effectively release drug in controlled manner by diffusion from the carrier-polymer or by decomposition of the carrier itself. PNIPAAm colloidal gel particle surfaces need to be modified or to be

conjugated with some other biodegradable polymers in order to achieve an ideal biocompatible and biodegradable drug delivery system [48]. Chitosan, being a natural carbohydrate polymer is an excellent alternative of which the biocompatibility and biodegradability is well studied [49]. It is pH sensitive and association with PNIPAAm can formulate pH as well as thermoresponsive drug delivery systems [50]. One of the key challenges with the use of thermoresponsive PNIPAAm based gels has been to modulate its LCST above body temperature and favourably up to 42-43^{o}C, which is a desired temperature for hyperthermia treatment of cancer. Recently, an attempt has been made by Misra *et al*. [51], wherein, they reported the change in LCST by hydrophilic modification of PNIPAAm. Copolymerizing PNIPAAm with *N,N'*-dimethylacrylamide (DMAAm) caused a shift in LCST from 32^{o}C to 38^{o}C. However, the field is still in infancy stage and much research is needed to develop a PNIPAAm based drug delivery systems, which will contain both the drugs and magnetic nanoparticles and thus could be used for triggered drug delivery and cancer therapy by magnetic hyperthermia and chemotherapy. Moreover, photodynamic therapy (PDT) based on the upconverting luminescence nanoparticles has been recognized as a promising therapy for cancer treatment which involves killing of diseased cells by excitation of photosensitizer chemicals with high-energy light to produce cytotoxic oxygen species from surrounding dissolved oxygen [52-53]. Thus, the development of the multifunctional nanoparticles encapsulating the MNP combined with the photosensitizer and anticancer drugs will be a very good breakthrough in cancer treatment due to the effective killing of the cancer cells using the combined magnetic hyperthermia, photodynamic therapy and chemotherapeutic effect.

The approaches of future plan of work will be as follows-

A. Development and characterization of the multifunctional nanoparticles (MFNs).
B. Optimization of the MFNs in terms of their stability, encapsulation efficiency, release study, temperature sensitivity, luminescence efficiency, relaxivity and specific absorption rate (SAR).
C. *in vitro* biocompatibility study of the MFNs.
D. *in vitro* internalization study of the MFNs.
E. Conjugation of cancer specific folate ligand/monoclonal antibody to the MFNs.
F. Evaluation of folate receptor/monoclonal antibody mediated active targeting to the tumor site using a mice model.
G. Evaluation of external magnetic field guided magnetic targeting.
H. Evaluation of localization, retention and bioavailability of MFNs *in vivo*.
I. Evaluation of bio-imaging and MRI imaging efficacy
    i. *In vitro* imaging using different cancer cell lines.
    ii. *In vivo* imaging in animal surface tumor models.
J. Evaluation of therapeutic efficacy (chemotherapy and hyperthermia)
    i. *In vitro* using different cancer cell lines.
    ii. *In vivo* using animal tumor models.

8.2.4. Significance and novelty of the proposed future work

Controlled drug delivery technology represents one of the most rapidly advancing areas in biomedical research field. Delivery systems offer many advantages over conventional dosage forms, including improved efficacy, reduced toxicity, improved patient compliance, and cost effective therapeutic treatment. In particular, controlled and site specific release is strongly required for chemotherapeutic drugs to be efficiently used for

cancer therapy. As most of the chemotherapeutic drugs are equally toxic to normal cells, controlled targeted release of the drug will help to minimize the dose and undesirable toxic effects and to achieve the therapeutic outcome. There is number of chemotherapeutic drugs which is not being used to its full potential due to lack of efficient delivery system. Though the research has been going on since long, only a few have reached to the clinical trials. However, with the advent of nanotechnology, recently there is a lot of interest on the development of multifunctional smart (controlled and targeted) drug delivery system (Figure 8.2).

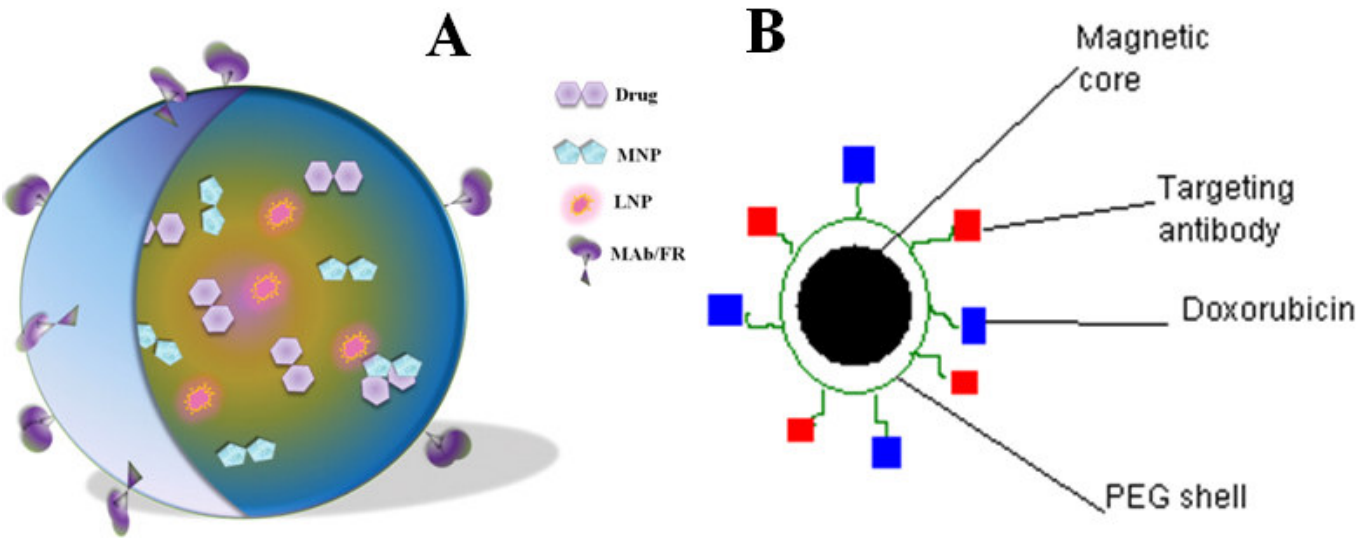

Figure 8.2. A. Encapsulated and **B.** Core-shell type multifunctional nanoparticle (MFNs) has the capability to simultaneously carry therapeutic agents, targeting ligand such as conjugated antibodies or folate receptor, and imaging probes.

Though there is a lot of research on the development of different polymers and phospholipids based nanoparticles for drug delivery on the last decade, research on the

designing of smart drug delivery system which releases its content specifically at the pathological site is at its infant stage. Thus, main focus of this project is the development of smart polymeric nanoparticles for drug delivery to cancers. Different polymers (biodegradable and thermosensitive) will be used to encapsulate drug, magnetic nanoparticles (MNP) and luminescence nanoparticles (LNP). The polymeric nanoparticles encapsulating drugs, PS, MNP and LNP will be concentrated in the tumor cells actively by ligand (folic acid or antibody) attached to the surface of the nanoparticles and passively by permanent magnet and release of the drugs will controlled by hyperthermia created by applying AC magnetic field.

Cancer is an international cause of concern in the medical science. Hyperthermia at 42 to 46 ºC is a promising therapy for cancer treatment. Heat may help to shrink tumors by damaging cells or depriving them of substances they need to live. Hyperthermia is also used with other forms of therapy (radiation therapy, chemotherapy, and biological therapy) to increase their effectiveness. In this proposal, hyperthermia based treatment of solid tumors is discussed in view of intracellular delivery of magnetic nanoparticles (with the help of a suitable delivery system). In the presence of AC magnetic field these intracellular localized magnetic particles will act as heat sources providing sufficient heat to build up necessary temperature to destroy the affected tissue. In the proposed therapy selective destruction of tumor cells will be tried out *in vitro* and *in vivo* on animal tumor models.

Photodynamic therapy (PDT) based on the upconverting luminescence nanoparticles has also been recognized as a promising therapy for cancer treatment. Thus, the development of the multifunctional nanoparticles encapsulating the MNP combined with the

photosensitizer and anticancer drugs will be a breakthrough in cancer treatment due to the effective killing of the cancer cells using the combined magnetic hyperthermia, photodynamic therapy and chemotherapy. It is also very crucial to continuously monitor the state of tumor during therapy to determine the therapy parameters. Because of the encapsulation of luminescence nanoparticles, the polymeric nanoparticles have the capability to provide a fast and non-invasive visible light imaging of tumor tissue and thus, the multifunctional nanoparticles (as shown in Figure 8.2) may be promising for the cancer therapy and imaging.

8.3. References

1. C. Alexiou, R. Jurgons, R.J. Schmid, C. Bergemann, J. Henke, W. Erhardt, E. Huenges, F. Parak, J Drug Target 11 (2003) 139.

2. I. Šafařík, M. Šafaříková, Monatshefte für Chemie 133 (2002) 737.

3. A.S. Lubbe, C. Alexiou, C.Bergemann, J. Surg. Res. 95 (2001) 200.

4. Z. Saiyed, S. Telang, C. Ramchand, Biomagn. Res. Technol. 1 (2003) 2.

5. C. Alexiou, W. Arnold, R.J. Klein, F.G. Parak, P. Hulin, C. Bergemann, W. Erhardt, S. Wagenpfeil, A.S. Lubbe, Cancer. Res. 60 (2000) 6641.

6. S. Dandamudi, R.B. Campbell, Biochim. Biophys. Acta. 1768 (2007) 427.

7. Q.A. Pankhurst, J. Connolly, S.K. Jones, J.Dobson, J. Phys. D:Appl. Phys. 36 (2003) R167.

8. A. Ito, M. Shinkai, H. Honda, T. Kobayashi, J. Biosci. Bioeng. 100 (2005) 1.

9. A.K. Silva, E.L. Silva, A.S. Carrico, E.S. Egito, Curr. Pharm. Des. 13 (2007) 1179.

10. S. Dandamudi, R.B. Campbell, Biomaterials 28 (2007) 4673.

11. T. Kubo, T. Sugita, S. Shimose, Y. Nitta, Y. Ikuta, T.Murakami, Int. J. Oncol. 18 (2001) 121.

12. A.S. Lübbe, C. Bergemann, J. Brock, D.G. McClure, J. Magn. Magn. Mater. 194 (1999) 149.

13. M. Babincova, P. Cicmanec, V.Altanerova, C. Altaner, P. Babinec, Bioelectro. 55 (2002) 17.

14. C.C. Berry, A.S.G. Curtis, J. Phys. D: Appl. Phys. 36 (2003) R198.

15. P. Tartaj, M.P. Morales, S. Veintemillas-Verdaguer, T. Gonzalez-Carreno, C.J. Serna, J. Phys. D: Appl. Phys. 36 (2003) R182.

16. S.M. Moghimi, A.C. Hunter, J.C. Murray, Pharm. Rev. 53 (2001) 283.

17. G. Gregoriadis, Ed.,Lyposome Tech., CRC Press, Boca Raton, Vol I-III (1984).

18. P. Pradhan, J. Giri, F. Rieken, C. Koch, O. Mykhaylyk, M. Döblinger, R. Banerjee, D. Bahadur, C. Plank, J. Control. Rel. 142 (2010) 108.

19. C. Perez , A. Sanchez , D. Putnam , D. Ting , R. Langer , M.J. Alonso, J. Contro. Rel. 75 (2001) 211.

20. A. Beletsi, L. Leontiadis, P. Klepetsanis, D.S. Ithakissios and K. Avgoustakis, Int. J. Pharm. 182 (1999) 187.

21. M.T. Peracchia, R. Gref, Y. Minamitake, A. Domb, N. Lotan R. Langer, J. Control. Rel. 46 (1997) 223.

22. R. Gref, Y Minamitake, M.T. Peracchia, V. Trubetskoy, V. Torchilin, R. Langer, Science 263 (1994) 1600.

23. V.P. Torchilin, Euro. J. Pharm. Sci. 11 (2000) S81.

24. D.A. Tomalia, A.M. Naylor, W.A. Goddard, Angew. Chem. Int. Ed. Engl. 29 (1990) 138.

25. A.E. Beezer, A.S.H. King, I.K. Martin, J.C. Mitchel, L.J. Twyman, C.F. Wain, Tetrahedron, 59 (2003) 3873.

26. J.C. Olivier, R. Huertas, H.J. Lee, F. Calon, W.M. Pardridge, Pharm. Res. 19 (2002) 1137.

27. Y. Li, M. Ogris, E. Wagner, J. Pelisek, M. Rüffer, Int. J. Pharm. 259 (2003) 93.

28. R. Gref, A. Domb, P. Quelled, T. Blunk, R.H. Miillerd, J.M. Verbavatz, R. Langer, Adv. Drug Del. Rev. 16 (1995) 215.

29. B. Denizot, G. Tanguy, F. Hindre, E. Rump, J.J.L. Jeune, P. Jallet, J. Coll. Inter. Sci. 209 (1999) 66.

30. V. Weissing, K.R. Whiteman, V.P. Torchilin, Pharm. Res. 15 (1998) 1552.

31. A.A. Gabizon, Cancer Res. 52 (1992) 891.

32. U.O. Hafeli, Int. J. Pharm. 277 (2004) 19.

33. K.M. Huh, Y.W. Cho, K. Park, Drug Del. Tech. 3 (2003) 5.

34. B. Stella, S. Arpicco, M.T. Peracchia, D. Desmaële, J. Hoebeke, M. Renoir, J. D'Angelo, L. Cattel, P. Couvreur, J. Pharm. Sci. 89 (2000) 1452.

35. W. Lu, Y. Zhang, Y.Z. Tan, K.-L. Hu, X.-G. Jiang, S.-K. Fu. J. Control. Rel. 107 (2005) 428.

36. X.Q. Pan, X. Zheng, G.F. Shi, H.Q. Wang, M. Ratnam, R.J. Lee, Blood, 100 (2002) 594.

37. D. Goren, A.T. Horowitz, D. Tzemach, M. Tarshish, S. Zalipsky, A. Gabizon, Clin Cancer Res. 6 (2000) 1949.

38. S.-H. Hu, T.-Y. Liu, D.-M. Liu, S.-Y. Chen, Macromolecules, 40 (2007) 6786.

39. T.-Y. Liu, S.-H. Hu, T.-Y. Liu, D.-M. Liu, S.-Y. Chen, Langmuir, 22 (2006) 5974.

40. D.C. Harsh, S.H. Gehrke, J. Contro. Rel. 17 (1991) 175.

41. S.S. Gil, E.M. Hudson, Prog. Polym. Sci. 29 (2004) 1173.

42. D. Duracher, A. Elaïssari, C. Pichot, Colloid Polym. Sci. 277 (1999) 905.

43. J.E. Wong, W. Richtering, Curr. Opin. Coll. Inter. Sci. 13 (2008) 403.

44. H.G. Schild, Prog. Polym. Sci. 17 (1992) 163.

45. M. Wang, Y. Fang, D. Hu, Reactive & Funct. Polym. 48 (2001) 215.

46. R. Pelton, Adv. Coll. Inter. Sci. 85 (2000) 1.

47. H. Kawaguchi, Prog. Polym. Sci. 25 (2000) 1171.

48. J.E. Wong, A.K. Gaharwar, D. Müller-Schulte, D. Bahadur, W. Richtering, J. Coll. Inter. Sci. 324 (2008) 47.

49. H. Onishi, Y. Machida, Biomaterials, 20 (1999) 175.

50. Q. Yuan, R Venkatasubramanian, S Hein, R.D.K Misra, Acta Biomaterialia, 4 (2008) 1024.

51. J. Zhang, R.D.K Misra, Acta Biomaterialia, 3 (2007) 838.

52. D. K. Chatterjee, Zhang Yong, Nanomedicine, 3 (2008) 73.

53. H.S. Qian, H.C. Guo, P. C.-L. Ho, R. Mahendran, Y. Zhang, Small, 5 (2009) 2285.

APPENDIX

Synthesis of Various Nanoparticles using Solvent-free Thermal Decomposition (STD) Method

A1. Experimental

Absolute ethanol (EtOH), ethyl acetate (EtAc) and acetylacetone (Hacac) were used without purification. Oleylamine (OM), tri(ethylene glycol), (TREG), iron(II) acetate ($Fe(ac)_2$), iron(III) citrate ($Fe(cit)_3$), iron(III) hydroxide oxide (Fe(hyd)), zinc acetylacetonate hydrate ($Zn(acac)_2.xH_2O$), cobalt (III) acetylacetonate ($Co(acac)_3$), yttrium(III) oxide (Y_2O_3) and europium(III) oxide (Eu_2O_3) were purchased from Sigma-Aldrich. Yttrium acetylacetonate ($Y(acac)_3$) and europium acetylacetonate ($Eu(acac)_3$) were prepared according to the procedure reported by Si et al. [1].

Synthesis of ZnO nanoparticles

ZnO nanoparticles were prepared using the STD method. Typically, 2 mmol of $Zn(acac)_2.xH_2O$ precursor was dissolved in a 20 mL of stabilizing media (OM or TEG) and magnetically stirred under a flow of argon. The solution is dehydrated at 120°C for 1 h, and then quickly heated to 320°C (for OM) or 260°C (for TEG) and kept at this temperature for 1 h. The white solution was cooled to room temperature (RT) by removing the heat source. Then, 20 mL of ETOH (for OM) or ETOH/ETAc (1:2 v/v) mixture (for TEG) was added into the solution and the precipitated particles were collected by centrifugation at 8000 rpm followed by three times washing with ETOH or the ETOH/ETAc mixture. Finally, the washed particles were dried overnight in oven to obtain dry ZnO nanoparticles.

Synthesis of Fe_3O_4 nanoparticles

Fe_3O_4 nanoparticles were prepared using the above mentioned STD procedure in presence of OM and TEG using different organometallic precursors like $Fe(ac)_2$, $Fe(cit)_3$ and Fe(hyd).

Synthesis of CoO nanoparticles

CoO nanoparticles were prepared using the above mentioned STD procedure in presence of OM using $Co(acac)_3$ precursor.

Synthesis of Y_2O_3:Eu nanoparticles

Y_2O_3:15%Eu nanoparticles were prepared using the above mentioned STD procedure in presence of OM using stoichiometric amount of $Y(acac)_3$ (1.81 mmol) and $Eu(acac)_3$ (0.19 mmol) precursors.

Synthesis of $NaYF_4$:20%Yb,2%Er nanoparticles

$NaYF_4$:20%Yb,2%Er nanoparticles were prepared using a modified procedure [2]. Typically, 1.56 mmol of Y_2O_3, 0.4 mmol of Yb_2O_3 and 0.04 mmol of Er_2O_3 were dissolved in 20 mL of 50% aqueous CF_3COOH at 80ºC. The residual water and acid were slowly evaporated to dryness at 80ºC. Then 4 mmol of CF_3COONa and 20 mL of OM were added to the reaction vessel. The resulting solution was magnetically stirred and dehydrated at 120°C for 1 h under a flow of argon. The solution was then quickly heated to 310°C and kept at this temperature for 1 h. The resulting yellow colloidal solution was cooled to RT and 20 mL of ETOH was added into the solution. The precipitated nanoparticles were collected by centrifugation at 8000 rpm followed by three times washing with ETOH. Finally, the washed particles were dried overnight in oven to obtain dry $NaYF_4$:Yb,Er nanoparticles.

Structure of the as-prepared nanoparticles was recognized by XRD, FTIR and TGA while their morphology was determined using TEM. Magnetic properties of the Fe_3O_4 and ZnO nanoparticles were measured VSM. Fluorescence spectra of the Y_2O_3:Eu and $NaYF_4$:Yb,Er nanoparticles were recorded on a LS-55 luminescence spectrometer using the excitation wavelength of 260 nm and 980 nm, respectively.

A2. Results and Discussion

A2.1. Structural characterization

Figure A1 shows the XRD patterns of as-prepared nanoparticles. Position of the diffraction peaks in Figure 1 A, B, C, D and E identifies the corresponding ZnO (JCPDS

file No. 80-0075), Fe_3O_4 (JCPDS file No. 19-0629), CoO [3], Y_2O_3:Eu (JCPDS file No. 25-1011) and $NaYF_4$:Yb,Er (JCPDS file No. 28-1192) phase of the nanoparticles, respectively.

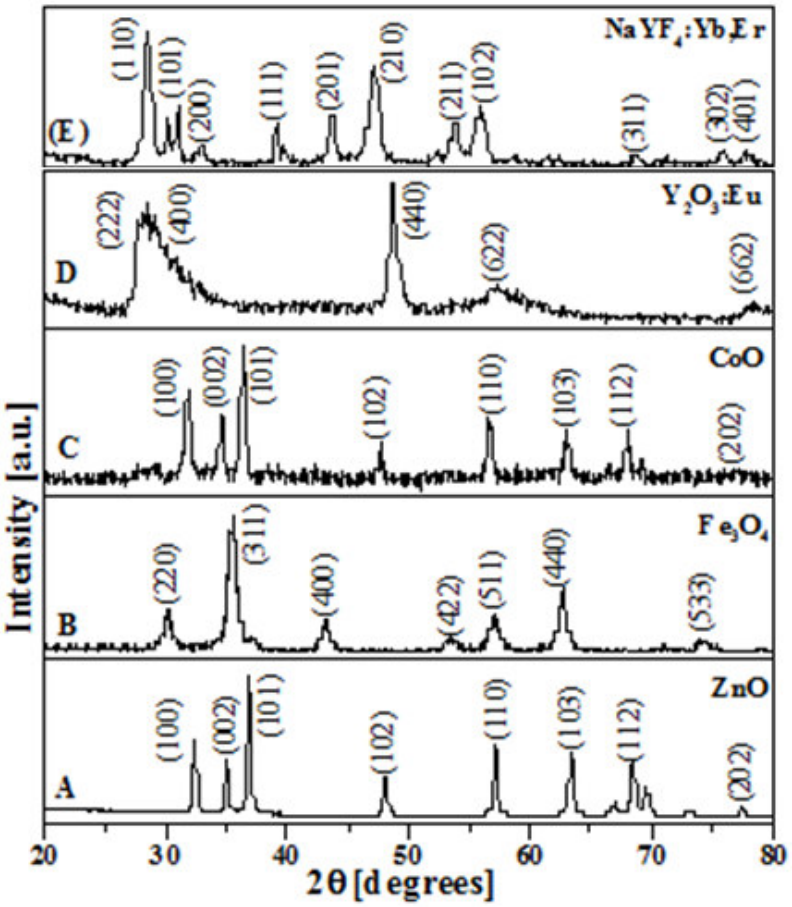

Figure A1. XRD patterns of **A.** ZnO, **B.** Fe_3O_4, **C.** CoO, **D.** Y_2O_3:Eu and **E.** $NaYF_4$:Yb,Er nanoparticles.

Figure A2 A and B show the FTIR spectra of the ZnO nanoparticles prepared in OM and TEG respectively. The peaks in Figure A2.A at about 2926; 2854, 1591-1501 and 1473-1402 cm^{-1} are due to C–H stretching, N–H bending and C–N stretching vibration, respectively attributed for chemically adsorbed OM coating to the hydrophobic ZnO nanoparticle surface [4-6]. On the other hand, the peaks in Figure A2.B at about 2962-2809, 1681-1534, 1409, 1143-1051 and 949-842 cm^{-1} are due to C–H stretching, O–H

stretching, C–H bending, C–O stretching and O–H bending vibration, respectively attributed for chemically adsorbed TEG coating to the hydrophilic ZnO nanoparticle surface [4-6]. The broad band between 3000-3600 cm^{-1} centered at ~ 3400 cm^{-1} is due to the O–H stretching vibration arising from the water adsorbed to the particle surface. The similar FTIR patterns were observed for the other OM / TEG coated Fe_3O_4, CoO, Y_2O_3:Eu and $NaYF_4$:Yb,Er nanoparticles.

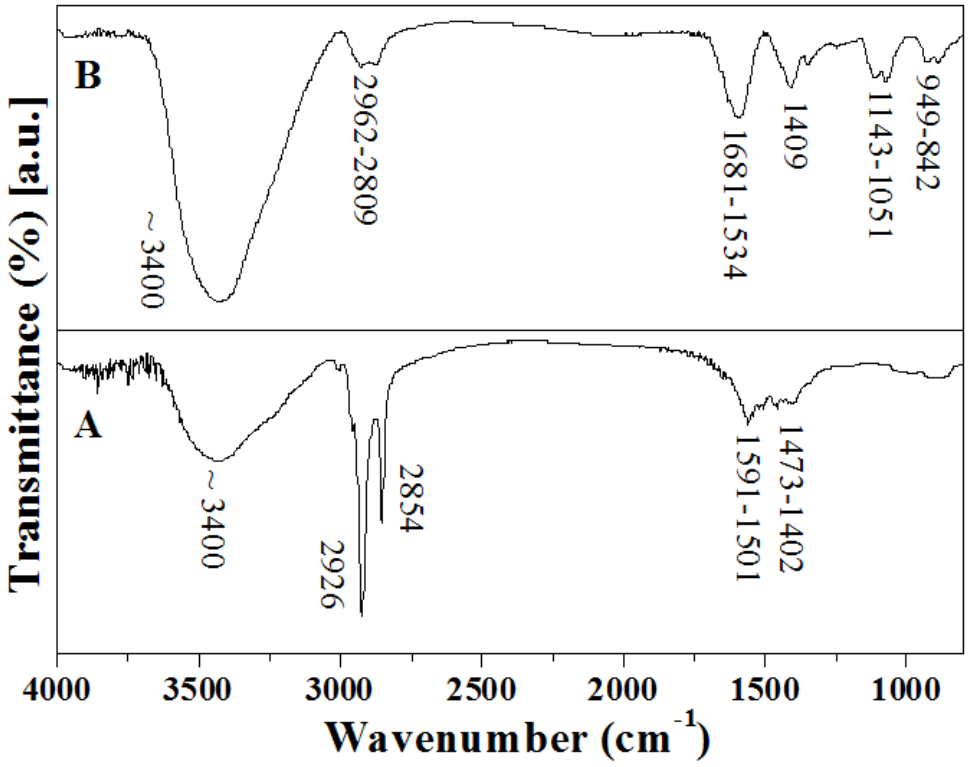

Figure A2. FT-IR spectra of **A.** OM coated and **B.** TEG coated ZnO nanoparticles, respectively.

The organic coating was further confirmed by TGA analysis. Figure A3.A and B show the TGA curves of the ZnO nanoparticles prepared in OM and TREG, respectively. TGA curves represent two-stage weight loss on heating of the samples from room temperature to 800°C. The first weight loss up to 200°C is due to the evaporation of the surface adsorbed water and the second major weight loss between 200 - 800°C is due to the decomposition of the organic (OM/TEG) coating. The similar trend in TGA plots were

also observed for the OM and TREG coated Fe_3O_4, CoO, Y_2O_3:Eu and $NaYF_4$:Yb,Er nanoparticles.

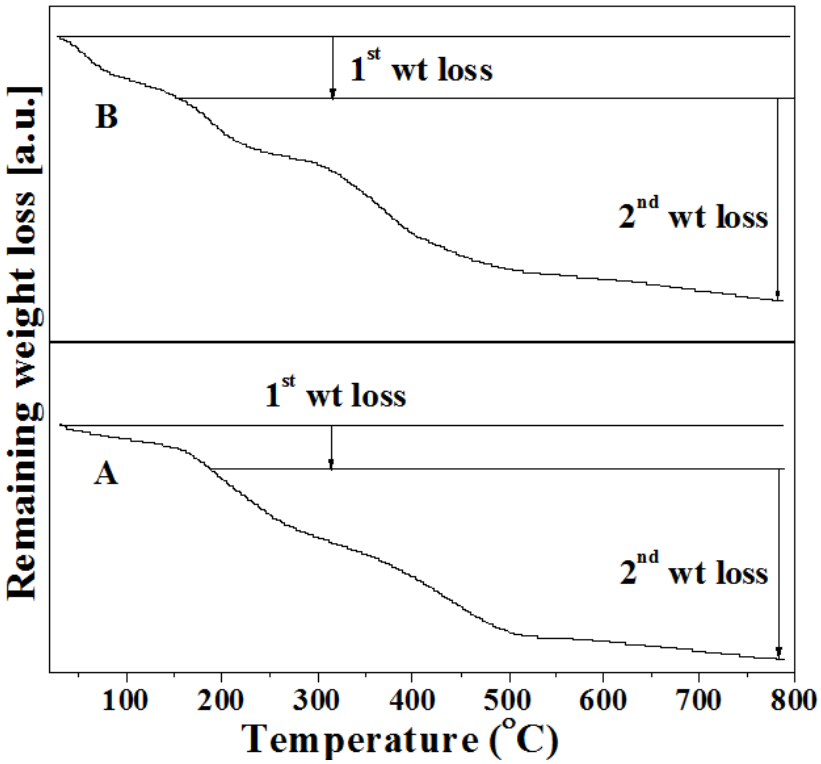

Figure A3. TGA curves of **A.** OM coated and **B.** TEG coated ZnO nanoparticles, respectively.

A2.2. Morphology

The resulting nanoparticles were highly dispersed without any agglomeration. Figure A4.A and B show the TEM images of the ZnO nanoparticles prepared in OM and TEG using the $Zn(acac)_2$ precursor. Figure A4.C and D show the TEM images of the Fe_3O_4 nanoparticles prepared in OM and TEG using the $Fe(ac)_2$ precursor. Figure A4.E and F show the TEM images of the Fe_3O_4 nanoparticles prepared in OM using $Fe(cit)_3$ and Fe(hyd) precursor, respectively. Figure A4.G, H and I show the TEM images of the CoO, Y_2O_3:Eu and $NaYF_4$:Yb,Er nanoparticles prepared in OM using $Co(acac)_3$ and $Y/Eu(acac)_3$ precursor, respectively. It can be seen that the highly dispersed different nanoparticles are obtained using the solvent-free thermolysis technique except those

agglomerated Fe_3O_4 nanoparticles which are prepared in OM using the $Fe(cit)_3$ and Fe(hyd) precursors. Thus, the TEM results indicate that highly dispersible hydrophobic or hydrophilic nanoparticles with diverse morphology can be synthesized by thermolysis of appropriate organometallic precursors in OM or TEG meidum, respectively.

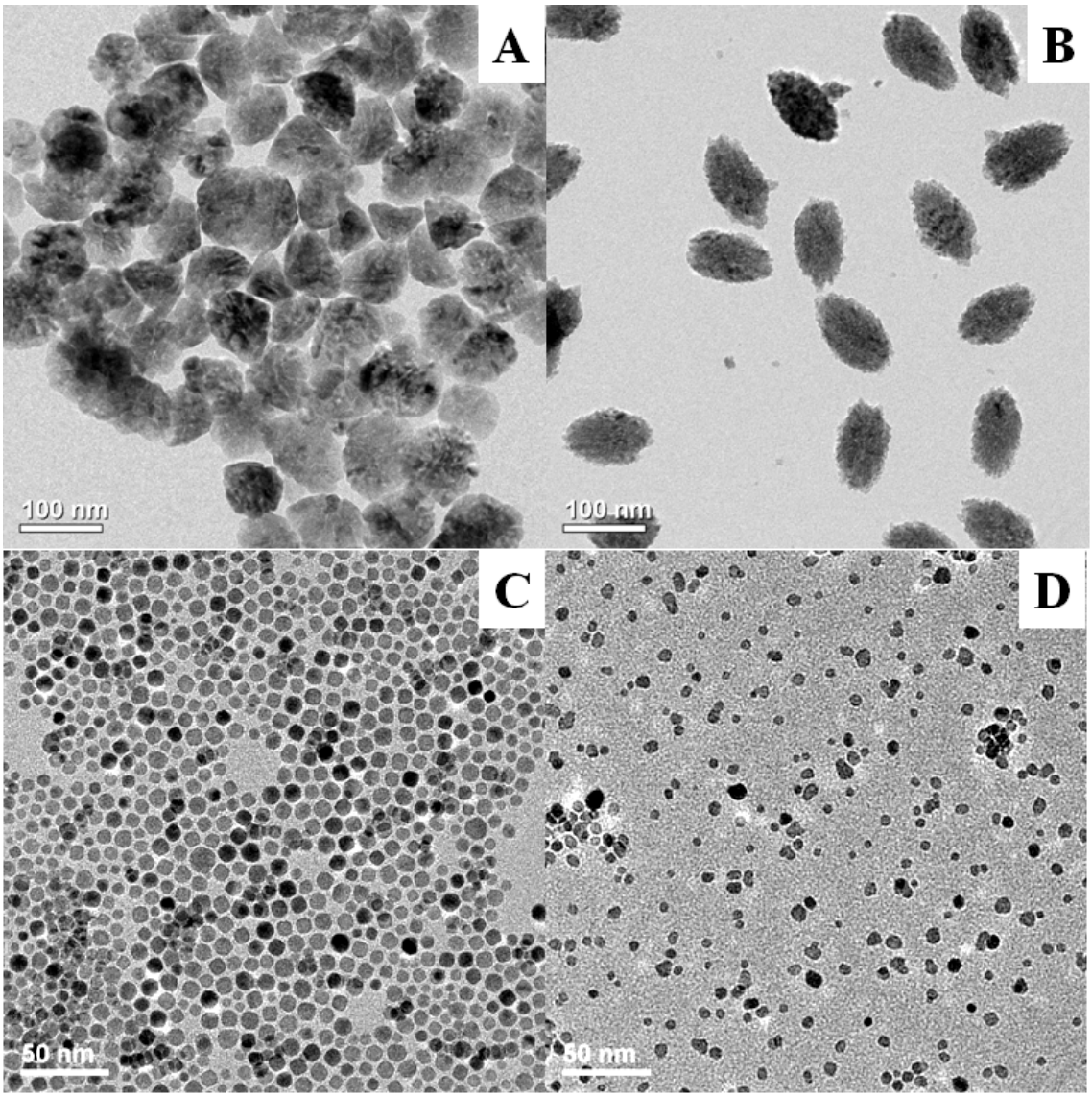

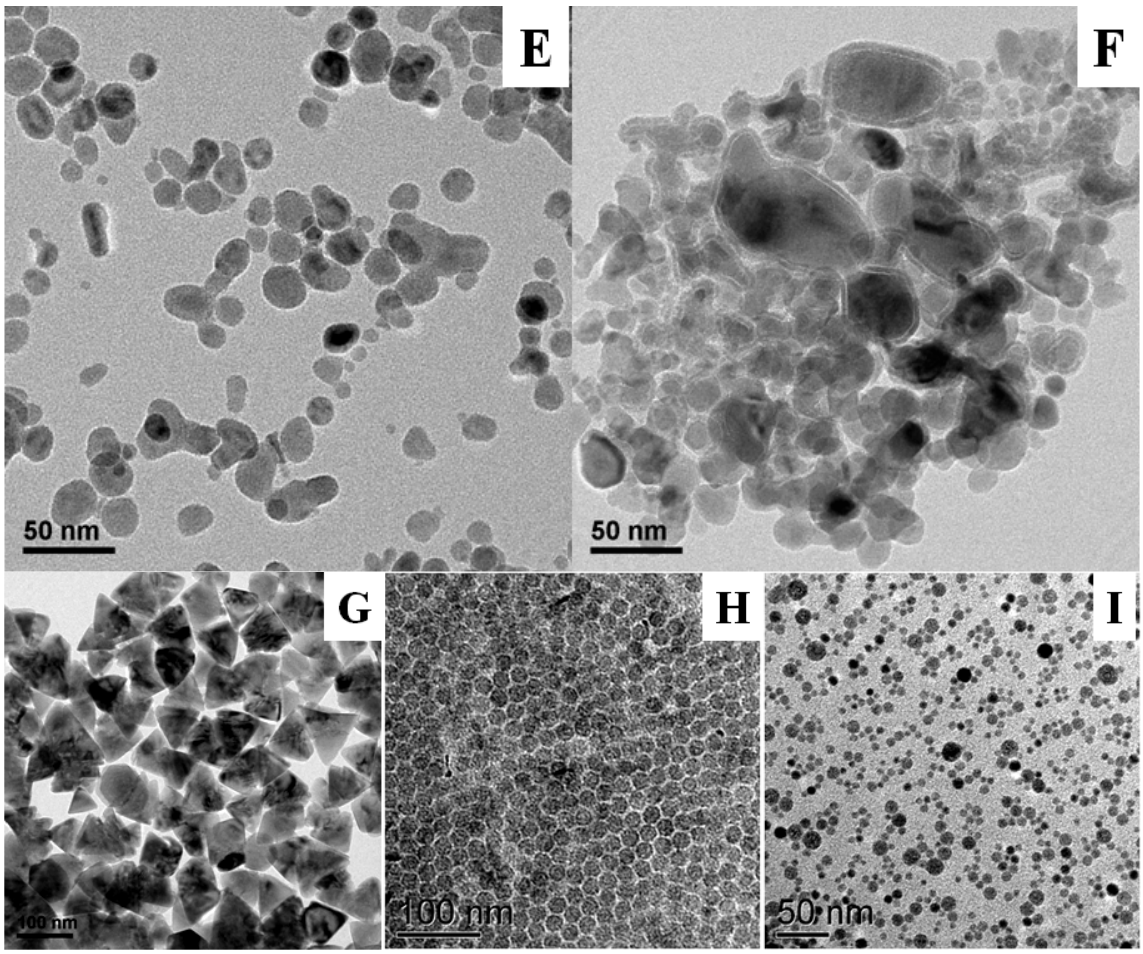

Figure A4. A and **B** are TEM images of OM and TEG coated ZnO nanoparticles; **C** and **D** are TEM images of OM and TEG coated Fe_3O_4 nanoparticles prepared using $Fe(ac)_2$ precursor; **E** and **F** are TEM images of OM coated Fe_3O_4 nanoparticles prepared using $Fe(cit)_3$ and Fe(hyd) precursor, respectively; **G, H** and **I** are OM coated CoO, Y_2O_3:Eu and $NaYF_4$:Yb,Er nanoparticles, respectively.

A2.3. Magnetic properties

Figure A5 A, B and C show the magnetization (M-H) curves of OM coated ZnO, Fe_3O_4 and CoO nanoparticles, respectively. The corresponding saturation magnetization (M_S) were measured at 20 kOe as ~5×10^{-3}, 64 and ~ 1 emu/g, respectively. Figure 5 A depicts the ferromagnetic nature of the ZnO nanoparticles while Figure A5 C indicates the combined paramagnetic and ferromagnetic behavior of CoO nanoparticles.

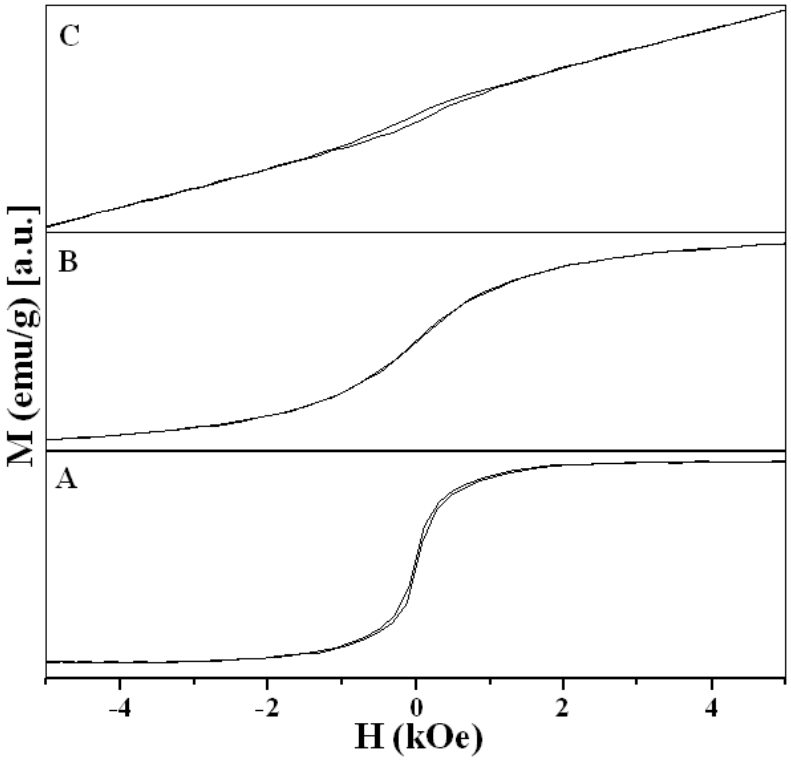

Figure A5. A. Room temperature M-H curves of OM coated **A.** ZnO, **B.** Fe_3O_4 and **C.** CoO nanoparticles, respectively.

A2.4. Luminescence properties

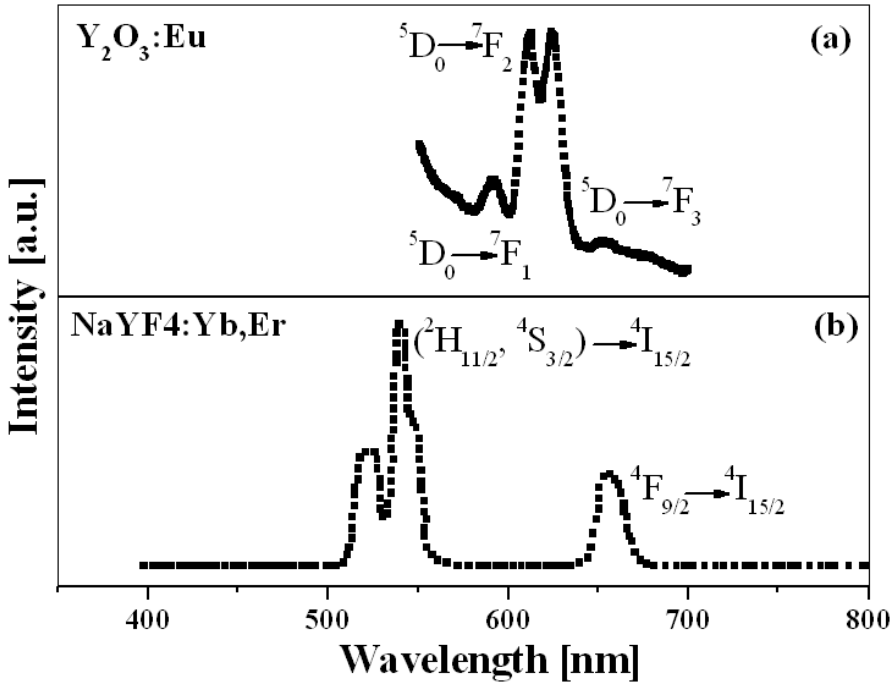

Figure A6. Room temperature luminescence emission spectra of (a) Y_2O_3:Eu and (b) $NaYF_4$:Yb,Er nanoparticles.

Figure A6 (a) and 5 (b) show the fluorescence spectra of Y_2O_3:Eu and $NaYF_4$:Yb,Er nanoparticles, respectively. The emission peaks of the Y_2O_3:Eu nanoparticles at about 591, 611-624, and 653 nm are due to the $^5D_0 \rightarrow {}^7F_1$, $^5D_0 \rightarrow {}^7F_2$ and $^5D_0 \rightarrow {}^7F_3$ transitions while the emission peaks of $NaYF_4$:Yb,Er nanoparticles at about 522, 540 and 656 nm are due to the $^2H_{11/2} \rightarrow {}^4I_{15/2}$, $^4S_{3/2} \rightarrow {}^4I_{15/2}$ and $^4F_{9/2} \rightarrow {}^4I_{15/2}$ transitions, respectively [1, 2].

A3. Conclusions

Highly dispersed hydrophobic and hydrophilic nanoparticles with diverse morphologies can be successfully prepared by the STD thermolysis of appropriate organometallic precursors in the OM and TREG medium, respectively.

A4. References

1. R. Si, Y-W. Zhang, H-P. Zhou, L-D. Sun, C-H. Yan, Chem. Mater. 19 (2007) 18.

2. J-C. Boyer, F. Vetrone, L. A. Cuccia, J. A. Capobianco, J. Am. Chem. Soc. 128 (2006) 7444.
3. W.S. Seo, J.H. Shim, S.J. Oh, E.K. Lee, N.H. Hur, J.T. Park, J. Am. Chem. Soc. 127 (2005) 6188.
4. J.R. Dyer, Applications of Absorption Spectroscopy of Organic Compounds, Prentice-Hall, Inc. (1965).
5. D. Maity, D.C. Agrawal, J. Magn. Magn. Mater. 308 (2007) 46.
6. D. Maity, S.-G. Choo, J. Yi, J. Ding, J.-M. Xue, J. Magn. Magn. Mater. 321 (2009) 1256.